

# **Quantum Mechanical Modelling of Engineering Nanostructures for CO<sub>2</sub> Adsorption and Dissociation**



**Francis Maduabuchi Enujekwu (AFHEA)  
BEng, MEng (Chemical Eng.)**

Thesis submitted to the University of Nottingham for  
the degree of Doctor of Philosophy

**May 2022**

## Abstract

Carbon dioxide (CO<sub>2</sub>) emission from anthropogenic sources has become the major source of greenhouse gases that have caused global climate change in recent times. Hence, much attention has been given to developing highly effective capture materials that can overcome the cost implications of existing technologies. This doctoral project centres on the development of two-dimensional (2D) nanostructured materials, which are extremely selective, stable, and sensitive to CO<sub>2</sub> capture and improve catalytic efficiency to achieve viable transformation of CO<sub>2</sub> on an industrial scale. The 2D nanostructure materials studied include graphene and molybdenum disulphide (MoS<sub>2</sub>) monolayers, graphene-MoS<sub>2</sub> confinements, and a series of defect-free monolayer MoS<sub>2</sub> as well as MoS<sub>2</sub> surface with different types of vacancies (single and double vacancies) with and without N-doping.

A comprehensive analysis of CO<sub>2</sub> adsorption energies ( $E_{AE}$ ) at various interlayer spacing of different multilayer structures comprising graphene/graphene (GrapheneB) and MoS<sub>2</sub>/MoS<sub>2</sub> (MoS<sub>2</sub>B) bilayers as well as graphene/MoS<sub>2</sub> (GMoS<sub>2</sub>) and MoS<sub>2</sub>/graphene (MoS<sub>2</sub>G) hybrids is performed to obtain the most stable adsorption configurations. It was found that 7.5 Å and 8.5 Å interlayer spacing is the most stable conformation for CO<sub>2</sub> adsorption on the bilayer and hybrid structures, respectively. Adsorption energies of the multilayer structures decreased in the following trend: MoS<sub>2</sub>B > GrapheneB > MoS<sub>2</sub>G > GMoS<sub>2</sub>. By incorporating van der Waals (vdW) interactions between the CO<sub>2</sub> molecule and the surfaces, we find that CO<sub>2</sub> binds more strongly on these multilayer structures. Bader charge analysis shows that the interaction between CO<sub>2</sub> and these surfaces causes charge transfer and redistributions. By contrast, the density of state (DOS) plots shows that

CO<sub>2</sub> physisorption does not have a substantial effect on the electronic properties of graphene and MoS<sub>2</sub>.

A DFT study was also conducted to analyse CO<sub>2</sub> adsorption on defective and non-defective MoS<sub>2</sub> surfaces with or without nitrogen doping. Results showed the dissociative chemisorption of CO<sub>2</sub> on the MoS<sub>2</sub>\_1V<sub>s</sub> and a significantly enhanced physisorption of CO<sub>2</sub> on the MoS<sub>2</sub>\_1V<sub>Mo</sub>\_3N<sub>S</sub>, which displays adsorption energy of -1.818 eV compared with -0.139 eV of the pristine MoS<sub>2</sub> surface. Meanwhile, the MoS<sub>2</sub>\_1V<sub>s</sub> exhibits excellent selective adsorption of CO<sub>2</sub> over N<sub>2</sub> and H<sub>2</sub>O, with the highest adsorption ratio of 5.1 and 3.5, respectively. Partial dissociation of CO<sub>2</sub> to CO over the MoS<sub>2</sub>\_1V<sub>s</sub> is also observed and attributed to increased covalent attractions at the vacant site, while the improved CO<sub>2</sub> physisorption over the MoS<sub>2</sub>\_1V<sub>Mo</sub>\_3N<sub>S</sub> is attributed to the enhanced electrostatic interactions at the vacancy site due to N doping. These are confirmed by the computed vibrational frequencies of CO<sub>2</sub> bound on these surfaces.

Furthermore, the adsorption and dissociation of CO<sub>2</sub> and H<sub>2</sub>O on MoS<sub>2</sub> monolayers with defects and N-doped vacancy sites are investigated. The calculations reveal that the MoS<sub>2</sub>\_1V<sub>Mo</sub>\_3N<sub>S</sub> are the most catalytically active sites. The interactions with CO<sub>2</sub> and H<sub>2</sub>O are enhanced by the larger electron distribution with N dopants and neighbouring S atoms. Climbing image nudged elastic band (CI-NEB) and *ab initio* molecular dynamics (AIMD) analyses indicate that the interactions are exothermic and result in spontaneous molecular dissociation. Here, CO<sub>2</sub> dissociates into CO\* and O\* on two N atoms with no barrier, while H<sub>2</sub>O dissociates via two mechanisms: 1) into adsorbed OH\* and H\* species ( $E_a = 0.21$  eV), and 2) into adsorbed O, H, and H atoms ((activation energy ( $E_a$ ) = 0.10 eV). The computed  $E_a$  values are significantly lower than the threshold energy barrier for chemical reactions

at room temperature (0.8 eV), which also indicates that CO<sub>2</sub> and H<sub>2</sub>O dissociation is spontaneous at ambient temperature. Given the ease of formation of CO\*, O\*, OH\* and H\* radicals.

Finally, the adsorption of different gas molecules (CO<sub>2</sub>, CH<sub>4</sub>, N<sub>2</sub>, H<sub>2</sub> and H<sub>2</sub>O) on the MoS<sub>2</sub>\_1V<sub>s</sub> surface is investigated using first-principles calculations and Grand Canonical Monte Carlo (GCMC) simulations. DFT and GCMC simulation results demonstrated that MoS<sub>2</sub>\_1V<sub>s</sub> enhances the adsorption of CO<sub>2</sub>, and H<sub>2</sub>O at 1 bar, 298 K, and H<sub>2</sub> at 1 bar, 77 K relative to that of the pure surface. CO<sub>2</sub> loadings of 2.49 wt.% and 0.55 wt.%, H<sub>2</sub>O loadings of 55.27 wt.% and 44.25 wt.%, and H<sub>2</sub> loadings of 0.29 wt.% and 0.20 wt.%, for the MoS<sub>2</sub>\_1V<sub>s</sub> and PMoS<sub>2</sub> surfaces, respectively, were observed. In addition, optimized MoS<sub>2</sub>\_1V<sub>s</sub> configuration stipulates that adsorption of CO<sub>2</sub>, H<sub>2</sub> and H<sub>2</sub>O was via dissociative chemisorption, in contrast to optimized PMoS<sub>2</sub> configuration, for which physisorption was the only adsorption mechanism. CI-NEB analysis in agreement with DFT results from geometry optimization shows that the partial CO<sub>2</sub> and H<sub>2</sub>O dissociation and complete H<sub>2</sub> splitting processes exhibited energy barriers of 1.11 eV, 0.65 eV and 0.18 eV. The computed free energy of activation ( $\Delta G_a$ ) for the partial and complete dissociation of CO<sub>2</sub> and H<sub>2</sub>O, and H<sub>2</sub> are 0.35 eV, 0.30 eV, and -0.66 eV. These values are lower than the threshold energy barrier for chemical reactions at room temperature (0.8 eV), which reveals that the dissociation is spontaneous at ambient temperature.

## Publications

The following peer-reviewed journal articles either have been published or are in preparation to be published because of the work undertaken as part of this thesis:

1. “Insights into the effect of vacancy defects and nitrogen doping on the adsorption and dissociation of CO<sub>2</sub> and H<sub>2</sub>O over MoS<sub>2</sub> monolayers” **Francis M. Enujekwu**, Yue Zhang, Collins I. Ezeh, Mengxia Xu, Hainam Do, and Tao Wu, *Applied Surface Science*, 577 (2022) 151908 DOI: 10.1016/j.apsusc.2021.151908 (2022). Presented in **Chapter 6**.
2. “N-doping enabled defect-engineering of MoS<sub>2</sub> for enhanced and selective adsorption of CO<sub>2</sub>: A DFT approach” **Francis M. Enujekwu**, Yue Zhang, Collins I. Ezeh, Haitao Zhao, Mengxia Xu, Elena Besley, Michael W. George, Nicholas A. Besley, Hainam Do, and Tao Wu, *Applied Surface Science*, 542 (2021) 148556 DOI: 10.1016/j.apsusc.2020.148556 (2021). Presented in **Chapter 5**.
3. “New insights into the effect of vacancy defects and nitrogen doping on the adsorption and dissociation of CO<sub>2</sub> and H<sub>2</sub>O over MoS<sub>2</sub> monolayers” **Francis M. Enujekwu**, Yue Zhang, Collins I. Ezeh, Mengxia Xu, Hainam Do, and Tao Wu. **In preparation**. Presented in **Chapter 7**.
4. “A comparative study of mechanisms of the adsorption of CO<sub>2</sub> confined within graphene–MoS<sub>2</sub> nanosheets: a DFT trend study” **F.M. Enujekwu**, C.I. Ezeh, M.W. George, M. Xu, H. Do, Y. Zhang, H. Zhao, T. Wu, *Nanoscale Adv.*, 2019, 1, 1442-1451 DOI 10.1039/C8NA00314A, rsc.li/nanoscale-advances (2019). Presented in **Chapter 4**.
5. “Mechanism of Hg<sup>0</sup> and O<sub>2</sub> Interaction on the IrO<sub>2</sub> (110) Surface: A Density Functional Theory Study” Haitao Zhao, Shuai Liu, Wentao Li, **Francis Enujekwu**, Chenghang Zheng, Shuyin Yu, Xiang Gao, and Tao W, *Energy & Fuels* 2019 33 (2), 1354-1362 DOI: 10.1021/acs.energy&fuels.8b03600 (2019).

## Conference/Meetings Attended

1. The 4<sup>th</sup> Zhejiang-Kyoto-Ajou Joint Symposium on Energy Science Dec 1<sup>st</sup> 2020 (Virtual) Online. **Contributed Talk Entitled:** New insights on the role of vacancy defect and nitrogen doping on gaseous adsorption and potential CO<sub>2</sub> reduction and water splitting over MoS<sub>2</sub> edges.
2. Royal Society of Chemistry (RSC), Theoretical Chemistry Group Graduate Meeting, University of Nottingham, United Kingdom, July 2019. **Contributed Talk Entitled:** New insights on the role of a single sulphur vacancy on gaseous adsorption and potential water splitting over MoS<sub>2</sub> edges.
3. Digital Research Compute Day: UoN HPC Conference, University of Nottingham, UK, May 2019 (Poster Presented).
4. Faculty of Science and Engineering 1st Annual PGR Research Poster Showcase, University of Nottingham, Ningbo China, April 2018 (Poster Presented).
5. The Fourth Post Graduate Research International Conference, University of Nottingham, Ningbo China, November 2017. **Contributed Talk Entitled:** Graphene-MoS<sub>2</sub> Nanosheets: DFT Comparative Study of Gas Adsorption Mechanism.

## **Author's Declaration**

The material contained within this thesis has not previously been submitted for a degree at the University of Nottingham or any other university. The research reported within this thesis has been conducted by the author unless otherwise indicated.

## **Copyright Notice**

The copyright of this thesis rests with the author. No quotation from it should be published without their prior written consent and information derived from it should be acknowledged.

For Jacqueline, Collins, Joy and Joyce



## **Dedication**

This thesis is dedicated to God Almighty, Who granted me the grace and mercies to fulfil this dream. It is also dedicated to My Dad and Mum who I am always in their thoughts and prayers. Their patience and perseverance in raising me have always been the motivation for me to aim at getting to the top and never give up no matter the challenges, thereby putting effort to make that one more attempt.

Finally, this work is specially dedicated to Professor Nicholas A. Besley who died on 27 June 2021 after a bike accident in Wollaton Park Nottingham, UK. Nick was extremely nice to me; his immense support, encouragement and guidance were greatly instrumental to my PhD success. I will miss him solely. May his soul Rest in Peace. My prayer and thoughts are with his wife Professor Elena Besley and their daughter Emily Besley.

## **Acknowledgements**

I am deeply grateful to God Almighty for His inspiration and strength He gave me to complete my study in good health. I return all glory and honour to Him for making this doctoral work possible.

I would like to gratefully acknowledge the financial support from the New Materials Institute (NMI) and Graduate School of the University of Nottingham Ningbo China (UNNC) for providing scholarships and stipends. The Zhejiang Provincial Department of Science and Technology is acknowledged for this research under its Provincial Key Laboratory Program (2020E10018). Ningbo Bureau of Science and Technology is thanked for sponsoring the Municipal Key Laboratory of Clean Energy Conversion Technologies; Ningbo Bureau of Education is appreciated for its funding to Municipal Comprehensive Collaborative Innovation Centre. Department of Science and Technology of Ningxia Hui Autonomous Region is thanked for sponsorship (2019BCH01001). National Key Research We are also grateful for the access to the University of Nottingham High-Performance Computing (HPC) facility in both Ningbo China and Nottingham UK (UNUK).

I would like to express my deepest gratitude to my supervisors Prof. Tao Wu, Prof. Michael W. George, Dr Hainam Do and Dr Mengxia Xu, for providing both the freedom required to explore topics that I found fascinating and the support necessary to help guide my pursuits and err on the side of caution. Their unflinching support, guidance, patience and trust at all times during my PhD was a pillar of strength. They kept me on a loose leash and let me break things, which was indeed an enriching experience to learn research ingredients through their lens. Thank you for having faith in me.

I would like to thank all members of the Computational Chemistry Group (compchemsupergroup) at UNUK for helping with different computational chemistry skills. I especially thank the late Prof. Nicholas A. Besley that introduced me to Qchem and other computational chemistry tools that became greatly instrumental to my PhD success. I am grateful to Prof. Elena Besley and Dr Joseph Glover for the short quantum chemistry meeting and for providing lessons for GCMC simulations using RASPA. I am deeply indebted to Prof. Jonathan Hirst for his helpful discussions and insight into this work, and Dr Linbin Yao for some of the graphical work. I was fortunate enough to learn the design and development of novel materials, their synthesis and characterization under Prof. Andrei N. Khlobystov and Dr Luke Norman guidance at the Nanoscience and Nanotechnology Centre group of UNUK. Words fail to thank the following characters I met in the compchemsupergroup UK; Dr Steve Mason, Dr Steve Oatley (Big Steve), Dr Adam Fouda, Dr Ellen Guest, Dr Pritesh Tailor, Dr James Wakerley and Dr Josh Baptiste (the fun organizer). Thank you all for your help. In addition, I thank Professor Kieron Burke for his helpful insights on the issue of delocalization error found in PBE-GGA functional.

Finally, and importantly, my family. I thank my mother, Caroline and my father, Joseph. You have moved mountains to support my interests and studies, and I will be forever grateful for everything that you have sacrificed to ensure that I have the opportunities that you did not. I would like to thank my siblings and relatives. I made many very good friends at UNNC. My thanks go to all of them, with a special mention to Dr Collins Ezeh, my girlfriend Miss Jacqueline Mlind, and Dr Joyce Addae. Honestly, I am short of words for these acknowledgements, and none of these lists is complete. Everyone who has in one way or the other contributed to the success of this work. Thank you. God bless you.

## Abbreviations

Below is a list of some of the more commonly used abbreviations in this Thesis.

2D	Two-Dimensional
Å	Angstrom
AIMD	Ab Initio Molecular Dynamics
B3LYP	Becke-3-parameter-Lee-Yang-Parr exchange-correlation
CCS	CO <sub>2</sub> Capture and Storage
CH <sub>4</sub>	Methane
CI-NEB	Climbing Image Nudged Elastic Band
CO	Carbon Monoxide
CO <sub>2</sub>	Carbon Dioxide
DFT	Density Functional Theory
DFT-D2	DFT-Grimme's dispersion correction method-2
DOS	Density of State
eV	electron Volt
FS	Final States
fs	femtoseconds
G5x5	Graphene 4×4×1 supercell monolayer
GAMs	Gas-Adsorbent Materials
GCMC	Grand Canonical Monte-Carlo
GGA	Generalized Gradient Approximation
GMoS <sub>2</sub>	Graphene-Molybdenum Disulphide hybrid structure

GrapheneB	Graphene Bilayer
H <sub>2</sub>	Hydrogen gas
H <sub>2</sub> O	Water
HgO	Mercury Oxide
HPC	High-Performance Computer
IR	Infrared
IS	Initial States
M4x4	MoS <sub>2</sub> 4×4×1 supercell monolayer
MEPs	Minimum-Energy Reaction Paths
MoS <sub>2</sub> B	Molybdenum Disulphide bilayer
MoS <sub>2</sub> G	Molybdenum Disulphide- Graphene hybrid structure
MoS <sub>2</sub>	Molybdenum Disulphide
MP	Monkhorst-Pack grids
N <sub>2</sub>	Nitrogen gas
NO <sub>2</sub>	Nitrogen Dioxide
optB88	Optimized Becke-1988 exchange functional
optPBE	Optimized Perdew, Burke and Ernzerhof functional
PAW	Projector Augmented Wave
PBE	Perdew, Burke and Ernzerhof functional
PDOS	Partial Density of State
ppm	Parts per million
revPBE	revised Perdew, Burke and Ernzerhof functional
SO <sub>2</sub>	Sulphur Dioxide

TDOS	Total Density of State
TMD	Transition Metal Dichalcogenides
TS	Transition States
UNNC	University of Nottingham Ningbo China
UNUK	University of Nottingham United Kingdom
UoN	University of Nottingham
VASP	Vienna Ab initio Simulation Package
vdW	van der Waals
vdW-DF2	vdW-Density Functional-2 (Langreth and Lundqvist et al)
ZPE	Zero Point Energy

# Table of Content

Abstract.....	i
Publications.....	iv
Conference/Meetings Attended .....	v
Author’s Declaration.....	vi
Copyright Notice.....	vi
Dedication.....	viii
Acknowledgements.....	ix
Abbreviations.....	xi
Table of Content .....	xiv
List of Figures.....	xviii
List of Tables .....	xxiv
CHAPTER 1 .....	1
Introduction.....	1
1.1 Motivation.....	1
1.2 Objectives.....	5
1.3 Research Novelty .....	8
1.4 Thesis Organization.....	10
CHAPTER 2 .....	13
Literature Review.....	13
2.1 Introduction .....	13
2.2 Carbon Dioxide .....	14
2.2.1 Natural Sources of CO <sub>2</sub> .....	16
2.2.2 Anthropogenic Sources of CO <sub>2</sub> .....	16
2.2.3 Natural Benefits of CO <sub>2</sub> .....	18
2.2.4 Hazards from CO <sub>2</sub> Emissions .....	19
2.3 Available CO <sub>2</sub> Capture and Storage Techniques .....	20
2.3.1 CO <sub>2</sub> Capture and Storage Technologies .....	21
2.3.2 CO <sub>2</sub> Adsorption Materials.....	25
2.3.3 Modification of CO <sub>2</sub> Adsorption Materials for Enhanced CO <sub>2</sub> Adsorption.....	36
2.3.4 Graphene/MoS <sub>2</sub> Hybrid .....	48

2.3.5	Computational analysis on CO <sub>2</sub> adsorption .....	50
2.4	Summary and Conclusions.....	51
CHAPTER 3	.....	54
Computational Methods.....		54
3.1	Overview of all Computational Methods.....	54
3.2	Electronic Structure Computational Methods .....	55
3.2.1	The Schrödinger Equation .....	57
3.2.2	Born-Oppenheimer Approximation .....	58
3.2.3	Hartree-Fock Theory.....	59
3.3	Overview on General Density Functional Theory .....	60
3.3.1	Hohenberg-Kohn Theorems.....	61
3.3.2	Kohn-Sham Theorems .....	63
3.3.3	Exchange-Correlation Energy/Functional .....	64
3.4	DFT Calculation of Vibrational Frequency .....	66
3.5	Ab Initio Molecular Dynamics (AIMD) .....	69
3.6	Computational Methods .....	73
3.7	Surface and Surface Simulation Models .....	76
3.8	Output from the Calculations .....	79
3.8.1	Lattice Parameter .....	79
3.8.2	Adsorption Energies.....	79
3.8.3	Density Difference .....	81
3.9	Summary and Conclusions.....	83
CHAPTER 4	.....	84
A Comparative Study of Mechanisms of the Adsorption of CO <sub>2</sub> Confined within Graphene-MoS <sub>2</sub> Nanosheets .....		84
4.1	Introduction .....	84
4.2	Computational Methods and Models .....	85
4.2.1	Computational Models.....	86
4.2.2	Computational Methods.....	86
4.3	Results and Discussion.....	88
4.3.1	Bulk Structure Parameters .....	88
4.3.2	Effects of Interlayer Distance on CO <sub>2</sub> Adsorption .....	89
4.3.3	Effects of CO <sub>2</sub> Orientation and Position.....	93



4.3.4	Structural Parameters .....	105
4.3.5	Density of States (DOS) Plots.....	110
4.4	Summary and Conclusions.....	115
CHAPTER 5	.....	117
Investigating N-Doping Enabled Defect-Engineering of MoS <sub>2</sub> for Enhanced and Selective Adsorption of CO <sub>2</sub> .....		
5.1	Introduction .....	117
5.2	Computational Methods and Models .....	120
5.2.1	Computational Models.....	120
5.2.2	Computational Methods.....	122
5.2.3	Calculation Details.....	123
5.3	Results and Discussion.....	126
5.3.1	Structural Geometry of Pristine Monolayer MoS <sub>2</sub> and Formation of Vacancy Defects and Nitrogen Doped (N-Dope) Monolayer MoS <sub>2</sub> , with the N Dopant, filled into the Single or Double Sulphur/Molybdenum Vacancies .....	126
5.3.2	Properties of Simulated Surface Configurations.....	129
5.3.3	Investigating CO <sub>2</sub> Adsorption Performance Modified MoS <sub>2</sub> Monolayer.	143
5.4	Summary and Conclusions.....	175
CHAPTER 6	.....	177
Investigating the Effect of Vacancy Defects and Nitrogen Doping on the Adsorption and Dissociation of CO <sub>2</sub> and H <sub>2</sub> O over Mos <sub>2</sub> Monolayers.....		
6.1	Introduction .....	177
6.2	Computational Methods and Models .....	179
6.2.1	Computational Details .....	180
6.2.2	Calculation Details.....	181
6.2.3	Ab Initio Thermodynamic Calculation Details.....	182
6.3	Results and Discussion.....	184
6.3.1	Adsorption of CO <sub>2</sub> , N <sub>2</sub> , and H <sub>2</sub> O on MoS <sub>2</sub> _1V <sub>Mo</sub> _3N <sub>S</sub> .....	184
6.3.2	Dissociation of CO <sub>2</sub> and H <sub>2</sub> O on MoS <sub>2</sub> _1V <sub>Mo</sub> _3N <sub>S</sub> .....	194
6.3.3	C-NEB Analysis of CO <sub>2</sub> and H <sub>2</sub> O Dissociation on MoS <sub>2</sub> _1V <sub>Mo</sub> _3N <sub>S</sub> .....	198
6.3.4	Energy barrier after enthalpy correction .....	201
6.3.5	Finite Temperature Ab Initio Molecular Dynamics.....	203
6.3.6	Ab Initio Thermodynamic on the Surface Stability of MoS <sub>2</sub> _1V <sub>Mo</sub> _3N <sub>S</sub>	206

6.4	Summary and Conclusions.....	209
CHAPTER 7 .....		211
Investigating the Role of Single Sulphur Vacancy on Gaseous Adsorption and Potential Water Splitting over Mos <sub>2</sub> Edges.....		211
7.1	Introduction .....	211
7.2	Simulation Details .....	214
7.2.1	Density Functional Theory Calculations .....	216
7.2.2	Force Field-Based Calculations .....	216
7.3	Results and Discussion.....	219
7.3.1	Adsorption Geometries and Energetics from DFT Calculations .....	219
7.3.2	Adsorption Isotherms from GCMC Simulations .....	224
7.3.3	C-NEB Analysis of Dissociative Adsorption of CO <sub>2</sub> , H <sub>2</sub> and H <sub>2</sub> O on Mos <sub>2</sub> _1V <sub>S</sub> Site .....	228
7.3.4	Energy Barrier after Enthalpy Correction.....	231
7.4	Summary and Conclusions.....	233
CHAPTER 8 .....		235
Conclusions and Future Work .....		235
8.1	Conclusions .....	235
8.2	Recommended Future Work .....	238
REFERENCES .....		240

## List of Figures

Figure 2.1: The three main approaches to capture CO <sub>2</sub> [50].	22
Figure 2.2: (a) Molecules of CO <sub>2</sub> and H <sub>2</sub> , (b-d) some of the most known groups of nanostructured gas-adsorbents [10].	27
Figure 2.3: Isolated Graphene Sheet Schematic Representation [89].	29
Figure 2.4: A pictorial view of the structures of (a) Single-walled nanotube (SWNT) [89], (b) Multiple-walled nanotube (MWNT) (where each colour is related to different SWNTs which make up the MWNT structure [89] and (c) C <sub>60</sub> Fullerene [90].	30
Figure 2.5: (A) Aromatic Hydrocarbon non-periodic models of graphene used in quantum calculations (Benzene, Coronene and Circumcoronene) and a supercell of 32 carbon atoms from a periodic graphene model, with a unit cell, highlighted in red. (B) Simulation boxes for empirical models containing finite graphene and a periodic graphene sheet with a small adsorbed RNA molecule respectively [95, 96].	31
Figure 2.6: A diagram of a crystal structure of monolayer MoS <sub>2</sub> showing molybdenum atoms (blue) sandwiched between two layers of sulphur atoms (yellow) [110].	35
Figure 2.7: A diagram of band structure of bulk (left) and monolayer (right) MoS <sub>2</sub> showing the crossover from indirect to direct bandgap followed by a widening of the bandgap [110].	36
Figure 2.8: Binding energies of CO <sub>2</sub> and N <sub>2</sub> with functionalized benzenes obtained using DFT [146].	44
Figure 2.9: Building van der Waals multilayer heterostructure materials.	49
Figure 3.1: Representation of common levels of $E_{xc}$ approximation within density functional theory together with some general features. Regions coloured in red indicate "High" and in blue "Low". The typical size of the systems that can be handled with those approaches are indicated on the right margin of the figure.	66
Figure 3.2: Schematic illustration of a CPMD trajectory along a single spatial coordinate. The smooth curve denotes the exact electronic ground state energy, while the symbols indicate the electronic energy calculated by the CPMD method at each time step of an MD simulation.	71
Figure 3.3: Schematic diagram for simulation algorithm in VASP.	75
Figure 3.4: Top views of a (001) surface (a) graphene and (b) MoS <sub>2</sub> . (c) Supercell model, including slabs and vacuum.	77
Figure 3.5: Vacancy defects and Nitrogen doping formation in MoS <sub>2</sub> monolayer.	78

Figure 4.1: CO<sub>2</sub> adsorption energy as a function of interlayer distance. Adsorption energy as a function of the interlayer distance between the two monolayers for all the studied multilayer structures..... 93

Figure 4.2: Relaxed geometric structures of CO<sub>2</sub> adsorption on possible initial graphene/MoS<sub>2</sub> (GMoS<sub>2</sub>) and MoS<sub>2</sub>/graphene (MoS<sub>2</sub>G) hybrid configurations. Position and orientation of CO<sub>2</sub> with respect to the surface are: (a) Centre/parallel, (b) Edge/parallel, (c) Centre/perpendicular, (d) Edge/perpendicular, (e) Centre/parallel (rotated 30°), (f) Edge/parallel (rotated 30°), (g) Centre/parallel (rotated 45°), and (h) Edge/parallel (rotated 45°). Energies are given in meV. Negative means heat release and blue, yellow, red and grey spheres depict Mo, S, O and C atoms, respectively..... 96

Figure 4.3: Relaxed geometric structures of CO<sub>2</sub> adsorption on possible initial bilayers of MoS<sub>2</sub> (MoS<sub>2</sub>B) and graphene (GrapheneB) configurations. Position and orientation of CO<sub>2</sub> with respect to the surface are: (a) Centre/parallel, (b) Edge/parallel, (c) Centre/perpendicular, (d) Edge/perpendicular, (e) Centre/parallel (rotated 30°), (f) Edge/parallel (rotated 30°), (g) Centre/parallel (rotated 45°), and (h) Edge/parallel (rotated 45°). Energies are given in meV. Negative means heat release and blue, yellow, red and grey spheres depict Mo, S, O and C atoms, respectively..... 97

Figure 4.4: Relaxed geometric structures of CO<sub>2</sub> adsorption on possible initial monolayers of graphene (G5x5) and MoS<sub>2</sub> (M4x4) configurations. Position and orientation of CO<sub>2</sub> with respect to the surface are: (a) Centre/parallel, (b) Edge/parallel, (c) Centre/perpendicular, (d) Edge/perpendicular, (e) Centre/parallel (rotated 30°), (f) Edge/parallel (rotated 30°), (g) Centre/parallel (rotated 45°), and (h) Edge/parallel (rotated 45°). Energies are given in meV. Negative means heat release and blue, yellow, red and grey spheres depict Mo, S, O and C atoms, respectively..... 98

Figure 4.5: The most stable configuration of the multilayered structures with adsorbed CO<sub>2</sub>. (a-d) are the top views of GMoS<sub>2</sub>, MoS<sub>2</sub>G, MoS<sub>2</sub>B and GrapheneB and (e-f) are side views of the same structures respectively. Colour code: Mo, blue, S, yellow, C, grey, and O, red. The lines define the interlayer distances, bond lengths, molecular distance while the curved lines define the bond angle. AA stacking type is chosen for both MoS<sub>2</sub>B and GrapheneB. This is because AA stacking of graphene has shown to be more preferable for intercalation of molecules according to ref [246] and ref [247]. Although the binding energy of AB stacking of graphene bilayer is lower than AA stacking, which makes AB stacking more stable than AA stacking, but AA stacking intercalation structures are more favourable than AB stacking ones ref [247]. For the hybrid structures, the stacking type is chosen according to ref [239], where one C atom in the unit cell of graphene sits exactly below a Mo atom. It is reported by ref [233] that another configuration called TS, where the stacking is such that a C atom sits below an S atom, is equivalent in both the binding and electronic properties..... 106

Figure 4.6: Top and side view of charge density difference plots for (a) Graphene/MoS<sub>2</sub> hybrid, (b) MoS<sub>2</sub>/Graphene hybrid, (c) MoS<sub>2</sub> bilayer, (d) graphene bilayer, (e) 4×4 supercell MoS<sub>2</sub> monolayer, and (f) 5×5 supercell graphene monolayer. The pink and green

distribution correspond to charge accumulation (electron excess) and depletion (electron loss) respectively. Isosurfaces:  $\pm 5 \times 10^{-5} e^{-1} \text{Å}^3$  ..... 109

Figure 4.7: Total DOS spectra before (1) and after (2) CO<sub>2</sub> adsorption. (a) 5×5 supercell graphene monolayer, (b) 4×4 supercell MoS<sub>2</sub> monolayer, (c) graphene bilayer, (d) MoS<sub>2</sub> bilayer, (e) graphene/MoS<sub>2</sub> hybrid, and (f) MoS<sub>2</sub>/graphene hybrid. The dashed line represents the Fermi level. .... 113

Figure 4.8: Projected DOS spectra before (a) and after (b) CO<sub>2</sub> adsorption. (G5×5) 5×5 supercell graphene monolayer, (M4×5) 4×4 supercell MoS<sub>2</sub> monolayer, (GrapheneB) graphene bilayer, (MoS<sub>2</sub>B) MoS<sub>2</sub> bilayer, (GMoS<sub>2</sub>) graphene/MoS<sub>2</sub> hybrid, and (MoS<sub>2</sub>G) MoS<sub>2</sub>/graphene hybrid. The dashed line represents the Fermi level. .... 114

Figure 5.1: Relaxed local geometric configurations of MoS<sub>2</sub> (a) pristine (b) one S atom substituted with an N atom (c) two S atoms substituted with two N atoms (d) three S atoms substituted with three N atoms (e) one Mo atom substituted with one N atoms (f) Mo and S atoms substituted with two N atoms (g) MoS<sub>2</sub> with 1 S-vacancy (h) one S atom substituted with one N atoms in MoS<sub>2</sub> with 1 S-vacancy (i) three neighbouring S atoms in a unit cell substituted with three N atoms in 1 Mo-vacancy defect and (j) 1Mo and 1S vacancy-defected MoS<sub>2</sub>. Colour code: Mo, blue, S, yellow, and N, green. The lines define the lengths given in Å. .... 128

Figure 5.2: (a) Top and side views of Isosurfaces of spin density difference of (a) 1 S-vacancy and double MoS vacancy with isosurface taken as  $\pm 0.00015 e/\text{Bohr}^3$ . The light blue and pink colours represent the increase and decrease of electron density, respectively. (b) The TDOS (top panel) and PDOS (bottom panel) projected on the p and d orbitals of respective S and Mo atoms near the MoS and S vacancy sites. The positive and negative values of DOS illustrate the spin-up and spin-down states, respectively. The vertical dashed line corresponds to the Fermi level. .... 133

Figure 5.3: Top and side views of isosurfaces of spin density difference for the defect surfaces with isosurface taken as  $\pm 0.005 e/\text{Bohr}^3$ . The light blue and pink colours represent areas with an increase and decrease of electron density, respectively. The colour codes for Mo, S and N atoms are the same as in Figure 5.1..... 140

Figure 5.4: (a) The TDOS of the defect-free and N doped monolayer MoS<sub>2</sub>. (b) The PDOS projected on the 3p orbitals of N dopants and the 3p and 4d orbitals of their neighbouring S and Mo atoms, respectively. The positive and negative values of DOS illustrate the spin-up and spin-down states, respectively. Green, orange and blue lines represent 4d, 2p and 3p orbitals, respectively. The Fermi level is represented by the vertical dashed line..... 142

Figure 5.5: The schematic structure of the most stable adsorption configurations for CO<sub>2</sub> molecule adsorbed on the pristine and defect (vacancy or N-substitutional doping) monolayer MoS<sub>2</sub> from the top (upper panel) and side (lower panel) views. The full descriptions of a-i have been given in Figure 5.1. The colour codes for Mo, S and N atoms are the same as in Figure 5.1, while, O and C atoms are shown in red and grey, respectively. The lines define the equilibrium molecular height between the central carbon atom of the CO<sub>2</sub> molecule and a reference atom of the MoS<sub>2</sub> surface in the basal plane in the z-direction

yielded by optimization (i.e. N atom for N doped MoS <sub>2</sub> surface and average z plane of S atoms, for non-doped MoS <sub>2</sub> surface given in Å.....	146
Figure 5.6: Adsorption energy versus molecular height. Adsorption energy as a function of molecular height for CO <sub>2</sub> adsorption on the most stable local geometric configurations for each model. The molecular height is the distance between the central carbon atom of the adsorbed CO <sub>2</sub> molecule and a reference atom of the MoS <sub>2</sub> surface in the basal plane in the z-direction (That is, N atom, for N doped MoS <sub>2</sub> surface and average z plane of top S-layer atom, for non-doped MoS <sub>2</sub> surface).....	149
Figure 5. 7: (a) The TDOS and (b) The PDOS projected on the p and d orbitals of respective S and Mo atoms near to the MoS and S vacancy sites, p orbital of N dopants and the s and p orbitals of the physisorbed CO and CO <sub>2</sub> molecules, and lattice embedded O atom. MoS <sub>2</sub> _1Vs, MoS <sub>2</sub> _1V <sub>Mo</sub> _1Vs and MoS <sub>2</sub> _1V <sub>Mo</sub> _3Ns represent 1 S-vacancy, 1Mo- and 1S-vacancy, and tertiary nitrogen-doped 1 Mo-vacancy MoS <sub>2</sub> monolayers, respectively. The vertical dashed line corresponds to the Fermi level.....	155
Figure 5. 8: Top and side views of isosurfaces of spin density difference of (a) 1 S-vacancy, (b) 1 Mo and 1 S vacancy and (c) tertiary nitrogen-doped 1 Mo-vacancy, with isosurface taken as ±0.00015 e/Bohr <sup>3</sup> . The light blue and pink colours represent the increase and decrease of electron density, respectively.....	157
Figure 5. 9: Investigation of CO <sub>2</sub> adsorption selectivity over N <sub>2</sub> and the effect of moisture content (a) The adsorption energies of CO <sub>2</sub> , N <sub>2</sub> and H <sub>2</sub> O molecules for the most stable adsorption configurations compared at 2.5 Å molecular height, (b) ratio and difference of adsorption energies between CO <sub>2</sub> and N <sub>2</sub> molecules, (c) ratio and difference of adsorption energies between CO <sub>2</sub> and H <sub>2</sub> O molecules.....	169
Figure 5. 10: Adsorption energy versus molecular height. Adsorption energy as a function of molecular height for (a) N <sub>2</sub> and (b) H <sub>2</sub> O molecules adsorbed on all the studied most stable local geometric configurations calculated by the same method applied for CO <sub>2</sub> as represented in Figure 5. [Here, molecular height is the distance between a reference atom of the MoS <sub>2</sub> surface in the basal plane in the z-direction (i.e. N atom, for N doped MoS <sub>2</sub> surface and average z plane of top S-layer atom for non-doped MoS <sub>2</sub> surface) and the (a) nearest N atom of the adsorbed N <sub>2</sub> molecule, and (b) central O atom of the adsorbed H <sub>2</sub> O molecule, respectively. Molecular Height is the same as explained in Figure 5.6. ....	170
Figure 6.1: The most stable adsorption configurations for the adsorption of CO <sub>2</sub> , N <sub>2</sub> and H <sub>2</sub> O molecules on MoS <sub>2</sub> _1V <sub>Mo</sub> _3Ns (a-c) and PMoS <sub>2</sub> (d-f). Colour code: Mo, blue, S, yellow, and N, green. O, C and H atoms are shown in red, grey and white, respectively. The lines define the equilibrium molecular height between the reference atoms of the molecules (CO <sub>2</sub> (carbon), H <sub>2</sub> O (oxygen), N <sub>2</sub> (nitrogen)) and a reference atom of the MoS <sub>2</sub> surface in the basal plane in the z-direction yielded by optimization (i.e. N atom for MoS <sub>2</sub> _1V <sub>Mo</sub> _3Ns surface and average z plane of S atoms, for PMoS <sub>2</sub> surface given in Å.....	186
Figure 6.2: Top and side views of isosurfaces of spin density difference for CO <sub>2</sub> , N <sub>2</sub> and H <sub>2</sub> O molecules adsorbed on MoS <sub>2</sub> _1V <sub>Mo</sub> _3Ns (a-c) and PMoS <sub>2</sub> (d-f). Each isosurface was	

taken as  $\pm 0.00015$  e/Bohr<sup>3</sup>. The light blue and pink colours represent an increase and decrease of electron density, respectively..... 193

Figure 6.3: Top (upper panels) and side (lower panels) views of a dissociated CO<sub>2</sub> and H<sub>2</sub>O molecules on MoS<sub>2</sub>\_1V<sub>Mo</sub>\_3N<sub>S</sub> site obtained from conjugate gradient energy minimization (a) CO<sub>2</sub> is partially dissociated into CO and O fractions that remain chemisorbed at two N atoms of the vacancy site, (b) first H<sub>2</sub>O dissociation state, where H<sub>2</sub>O dissociated into OH and H species that bound to two surface N atoms and (c) final H<sub>2</sub>O dissociation state, where H<sub>2</sub>O completely dissociated into O, H and H species that bound to two N atoms and one S atom of the surface..... 195

Figure 6.4: Energy diagram including reaction pathway and reaction barrier of single (a) CO<sub>2</sub> and (b) H<sub>2</sub>O dissociation on tertiary nitrogen doped Mo vacancy MoS<sub>2</sub> (MoS<sub>2</sub>\_1V<sub>Mo</sub>\_3N<sub>S</sub>) from climbing image nudged elastic band (CI-NEB) simulation. Inserts are the top and side views of the initial state (IS), Transition state (TS) and final state (FS) configurations along the MEP. The colour codes for Mo, S, N, O, H and C atoms are the same as explained in Figure 6.1..... 201

Figure 6.5: Reaction mechanism of single (a) CO<sub>2</sub> and (b) H<sub>2</sub>O dissociation on MoS<sub>2</sub>\_1V<sub>Mo</sub>\_3N<sub>S</sub> during AIMD simulations at 300 K. The MD reaction paths are similar to the reaction paths obtained in CI-NEB simulations..... 205

Figure 6.6: T-P phase diagram of CO<sub>2</sub>, N<sub>2</sub> and H<sub>2</sub>O molecules adsorption on nitrogen doped single Mo vacancy site (MoS<sub>2</sub>\_1V<sub>Mo</sub>\_3N<sub>S</sub>). The points on black, red and blue curves represent temperature as a function of partial pressure above which the adsorption of respective CO<sub>2</sub>, N<sub>2</sub> and H<sub>2</sub>O on MoS<sub>2</sub>\_1V<sub>Mo</sub>\_3N<sub>S</sub> site is stable. Line A is the partial pressure line fixed at 1 atmospheric pressure, while Line B, Line C and Line D are the temperature lines for CO<sub>2</sub>, N<sub>2</sub> and H<sub>2</sub>O, respectively. The partial pressure and temperature lines correspond to critical point lines above which the molecules desorb into the gas phase. .... 208

Figure 7.1: Single sulphur formation..... 215

Figure 7.2: The schematic structure of DFT strongest most stable adsorption configurations for CO<sub>2</sub>, CH<sub>4</sub>, N<sub>2</sub>, H<sub>2</sub>, H<sub>2</sub>O molecules adsorbed on PMoS<sub>2</sub> (a-e) and MoS<sub>2</sub>\_1V<sub>S</sub> (f-j) surfaces from top (upper panel) and side (lower panel) views. Colour code: Mo, pink, S, yellow, O, red, C, light blue, N, dark blue and H, white. .... 223

Figure 7.3: Ratio of adsorption energies between CO<sub>2</sub> and other molecules for pristine (PMoS<sub>2</sub>) and S vacancy (MoS<sub>2</sub>\_1V<sub>S</sub>) MoS<sub>2</sub> monolayers. .... 224

Figure 7.4: The gravimetric adsorption isotherms for (a) CO<sub>2</sub>, (b) CH<sub>4</sub>, (c) N<sub>2</sub>, and (d) H<sub>2</sub>O uptake on S vacancy (MoS<sub>2</sub>\_1V<sub>S</sub>) and pristine (PMoS<sub>2</sub>) MoS<sub>2</sub> monolayers at 298 K. .. 226

Figure 7.5: The gravimetric adsorption isotherms for H<sub>2</sub> uptake on S vacancy (MoS<sub>2</sub>\_1V<sub>S</sub>) and pristine (PMoS<sub>2</sub>) MoS<sub>2</sub> monolayers at (a) 298 K and (b) 77 K. .... 227

Figure 7.6: The gravimetric adsorption isotherms for (a) CO<sub>2</sub>, (b) H<sub>2</sub>O, and (c) H<sub>2</sub> uptake on S vacancy (MoS<sub>2</sub>\_1V<sub>S</sub>) and pristine (PMoS<sub>2</sub>) MoS<sub>2</sub> monolayers at 298 and 77 K, calculated at 0-1 bar pressure range..... 228

Figure 7.7: Energy diagram including reaction pathway and reaction barrier of single (a) CO<sub>2</sub>, (b) H<sub>2</sub> and (c) H<sub>2</sub>O dissociation on MoS<sub>2</sub>\_1V<sub>S</sub> from climbing image nudged elastic band (CI-NEB) simulation. Inserts are the top views of the initial state (IS); Transition state (TS) and final state (FS) configurations along the MEP. The colour codes for Mo, S, O, H and C atoms are the same as explained in Figure 7.2. .... 231



## List of Tables

Table 2.1: Summary of CO <sub>2</sub> Gas Physical-Chemical Properties [29].	15
Table 2.2: Typical Gas Conditions.	24
Table 2.3: Binding energies of CO and CO <sub>2</sub> on various adsorbents namely: (i) Pristine Graphene, (ii) Vacancy-defected Graphene, and (iii) Stone-wales-defected Graphene. E <sub>F</sub> is Fermi energy with respect to vacuum level, E <sub>bind</sub> is the binding energy of the molecule both in eV unit. “D” is the molecular-to-surface distance in Å units (Adapted with permission from [119]).	39
Table 2.4: Adsorption Minima of Ar, CH <sub>4</sub> , N <sub>2</sub> , CO <sub>2</sub> , and H <sub>2</sub> O Adsorptions on Nanographenes. Reprinted with permission from [142].	41
Table 2.5: Physical Properties of Selected Flue Gas [145].	43
Table 2.6: Adsorption energies (E <sub>ads</sub> ) and contribution of dispersion forces (E <sub>vdw</sub> ) of the G-adsorbate and FeG-adsorbate systems. Energies are in eV [156].	46
Table 4.1: Adsorption energies of CO <sub>2</sub> per carbon atom on different structures determined from different interlayered distance using PBE of GGA [215].	91
Table 4.2: Adsorption energies of possible initial configurations of CO <sub>2</sub> adsorption on perfect multilayer and monolayer structures using PBE [215].	99
Table 4.3: Adsorption energies at EDDIF=10 <sup>-4</sup> and EDDIG=-0.03, NSW=300, ENCUT=500, 5×5×1 KPOINT.	100
Table 4.4: Adsorption energies at EDDIF=10 <sup>-6</sup> and EDDIG=-0.01, NSW=500, ENCUT=500, 5×5×1 KPOINT.	100
Table 4.5: Adsorption energies at EDDIF=10 <sup>-6</sup> and EDDIG=-0.03, NSW=500, ENCUT=600, 6x6x1.	101
Table 4.6: Adsorption energies at EDDIF=10 <sup>-6</sup> and EDDIG=-0.03, NSW=500, ENCUT=700, 7x7x1.	101
Table 4.7: Comparison of adsorption energies (E <sub>AE</sub> , meV) of CO <sub>2</sub> on bilayer, hybrid and monolayer structures determined from different methods.	104
Table 4.8: Amount of charge transferred to CO <sub>2</sub> molecule (single atom and CO <sub>2</sub> molecule), amount of charge transferred from adjacent Mo, S and C atoms on the surface nearer to adsorbed CO <sub>2</sub> molecule, and the change in bond length and bond angle after CO <sub>2</sub> adsorption (length and angle, with angle change in parentheses) <sup>a</sup> .	107
Table 5.1: Structural geometry of pristine monolayer MoS <sub>2</sub> .	127
Table 5.2: Summary of calculated results for Vacancy defect MoS <sub>2</sub> configurations.	131
Table 5.3: Summary of N-doped MoS <sub>2</sub> configurations.	136

Table 5.4: Summary of adsorption energies of possible initial configurations of CO <sub>2</sub> adsorption on different surfaces.....	144
Table 5.5: Summary of calculated results for adsorption of CO <sub>2</sub> on most stable configurations of different surfaces at 2.5 Å initial molecular height. ....	150
Table 5.6: Calculated Vibrational Frequencies (cm <sup>-1</sup> ) for CO <sub>2</sub> molecule adsorption on MoS <sub>2</sub> _1V <sub>S</sub> , MoS <sub>2</sub> _1V <sub>Mo_1V<sub>S</sub></sub> and MoS <sub>2</sub> _1V <sub>Mo_3N<sub>S</sub></sub> sites. Calculated and Experimental values of gas-phase CO <sub>2</sub> molecule are included for comparison.....	165
Table 5.7: Summary of calculated results for adsorption of N <sub>2</sub> on most stable configurations of different surfaces at 2.5 Å initial molecular height. ....	171
Table 5.8: Summary of calculated results for adsorption of H <sub>2</sub> O on most stable configurations of different surfaces at 2.5 Å initial molecular height. ....	173
Table 6.1: Summary of the physisorption of CO <sub>2</sub> , N <sub>2</sub> and H <sub>2</sub> O molecules on MoS <sub>2</sub> _1V <sub>Mo_3N<sub>S</sub></sub> and PMoS <sub>2</sub> . ....	185
Table 6.2: Calculated geometry and vibrational frequencies (cm <sup>-1</sup> ) for adsorption of CO <sub>2</sub> , N <sub>2</sub> and H <sub>2</sub> O molecules on MoS <sub>2</sub> _1V <sub>Mo_3N<sub>S</sub></sub> sites. Calculated and experimental values of gas-phase molecules are included for comparison. The bond lengths and bond angles are in Å and degrees, respectively. ....	190
Table 6.3: Summary of calculated results for dissociation of CO <sub>2</sub> and H <sub>2</sub> O molecules on MoS <sub>2</sub> _1V <sub>Mo_3N<sub>S</sub></sub> sites. The values of charge transfer for the atoms of molecules and the total charge gained by the surface N atoms (Q <sub>N</sub> ) are included for comparison. The bonding of the dissociated atoms is as follows: CO <sub>2</sub> (N1=C1=O2 and N3=O1), H <sub>2</sub> O <sup>a</sup> (N3-H1 and N2-O1-H2) and H <sub>2</sub> O <sup>b</sup> (N3-H1, N2-O1 and S-H2). The total charge obtained by the N atoms of the surface before adsorption is 2.21 e (see Table 5.3 of Chapter 5).....	198
Table 7.1: Adsorption Energies and Orientations for the gas molecules (CO <sub>2</sub> , CH <sub>4</sub> , N <sub>2</sub> , H <sub>2</sub> and H <sub>2</sub> O) in the four reference positions. ....	215
Table 7.2: Summary of adsorption energies (E <sub>AE</sub> ), fully relaxed distances and angles of CO <sub>2</sub> , CH <sub>4</sub> , N <sub>2</sub> , H <sub>2</sub> and H <sub>2</sub> O gas molecules on PMoS <sub>2</sub> and MoS <sub>2</sub> _1V <sub>S</sub> surface, for the most favourable adsorption configurations. Notations: h <sub>mol-suf</sub> is the equilibrium molecular height, i.e. fully relaxed distance between the reference atom of the molecule and Mo atom. For CO <sub>2</sub> , CH <sub>4</sub> and H <sub>2</sub> O, the reference atoms are the central C and O, respectively, while the lowest N and H atoms are the reference atoms for N <sub>2</sub> and H <sub>2</sub> , respectively. l and θ are the bond distances and angles, respectively. The adsorption energies, distances and angles are in eV, Å and degrees (°), respectively.....	222

# CHAPTER 1

## Introduction

The introduction and general background for research activities presented in this thesis are detailed in this chapter. The chapter is divided into subsections to address the research motivations, objectives, author's achievements as well as thesis organizations. Firstly, in subsection 1.1, the motivation for this study is provided, while the objective of the study, research outcomes and thesis organization are provided in subsections 1.2, 1.3 and 1.4, respectively.

### 1.1 Motivation

CO<sub>2</sub> is a naturally occurring gas that is colourless, odourless and inflammable under normal atmospheric conditions, and it is about 60% denser than air [1]. CO<sub>2</sub> is thermodynamically stable and chemically inert, making it difficult to be activated under ambient conditions [2]. However, in the earth's atmosphere, CO<sub>2</sub> is one of the most long-lived significant greenhouse gases and in recent decades its concentration has increased due to anthropogenic emissions (like industrial emissions, fossil fuels and deforestation etc.) [3]. Another problem posed by CO<sub>2</sub> emission is ocean acidification because of its capability of dissolving in water at mild pressure and temperature to form carbonic acid which greatly affects aquatic lives [3]. In addition, CO<sub>2</sub> is categorized as a strong asphyxiate and an inhalation toxicant and is known to cause hypercapnia, which is one of the factors that causes sudden infant death syndrome [4]. Further, it is recognized to be hazardous to

human health in many other ways, for instance, it causes wheezing (>2000 ppm), tremors and loss of consciousness (>100000 ppm), and death (>250000 ppm) [5, 6]. Early detection of CO<sub>2</sub> gas is crucial since it helps overcome natural and anthropogenic hazards. In this framework, over the last decades, a surge in research activities towards developing cost-effective and highly sensitive CO<sub>2</sub> gas capture materials has been observed.

The use of commercially available CO<sub>2</sub> capturing and separating techniques have been widespread, however, the efficiency of these processes seem to pose a serious challenge [7]. There are some disadvantages associated with these technologies when they are employed beyond laboratory conditions as they tend to suffer from cross-sensitivity issues when interfering with effluent and earth abundant compounds (for example, NO<sub>2</sub>, SO<sub>2</sub>, HgO, N<sub>2</sub> and H<sub>2</sub>O) are present in the environment or sample [8]. Additionally, the existing CO<sub>2</sub> capture technologies exhibit a high range of cost estimates, which depends on process type, separation technology, CO<sub>2</sub> transport technique and storage site, and typically require skilled operators to supervise their operation [9].

In this context, the current research trend is focused on the development of novel material adsorbents for cost-effective and energy-efficient CO<sub>2</sub> gas capture and other gases adsorption and activation, as they have the potential to overcome the shortcomings that are associated with conventional CO<sub>2</sub> capture and storage (CCS) techniques. In addition, the development of these novel materials for environmental based catalysis aims to bridge the gap between innovative research, development, and application of these materials. Among the various types of gas-adsorbent materials (GAMs) developed, nanostructured CO<sub>2</sub> capture materials have been widely documented as they exhibit high surface to volume ratio, regular atomic composition, tunable reactivity, effective transport properties and

assembling affinity to form supramolecular systems, have warranted their applications to CO<sub>2</sub> capture technologies [10]. Despite the exceptional adsorption performance of nanostructured GAMs, they have certain disadvantages such as high working temperature (e.g. insufficient stability at >400 K) and complex material fabrication processes, thus contributing to their limited applications. To an extent, these inadequacies can be overcome by the use of two-dimensional (2D) nanomaterials like graphene and transition metal dichalcogenides (TMD) (e.g. Monolayer molybdenum disulphide (MoS<sub>2</sub>)) sheet. This is due to 2D nanomaterial sensitive layers being easy to fabricate, their extraordinary properties attributed to their ultrathin thickness, which is related to quantum effects [11-13]. In addition, their stability and simplistic operational requirements allow flexibility in design and enable superior sensing phenomenon that occurs on their sensitive surface in presence of target gas. These 2D nanomaterials vary in terms of their electronic properties and functionality. For instance, graphene is a low-work function metallic electrode, and MoS<sub>2</sub> is generally an n-type semiconductor (a very active potential site for CO<sub>2</sub> capture). However, their synergetic function is more attractive for technological applications. These merits are achieved but at the cost of poor selectivity, low stable and sensitivity. The lack of bandgap and inertness to reaction, which are the main characteristics of pristine graphene, limits its application in the field of semiconductors, sensors and gas adsorbents. In addition, the low electron transfer of the basal plane of MoS<sub>2</sub> can lead to sluggish catalytic kinetics [14, 15]. Pristine MoS<sub>2</sub> are less reactive than the modified MoS<sub>2</sub> like pristine graphene. This is because of the chemical activity and thus the sensitivity of nanomaterial-based gas sensors. However lately many works of literatures have been documented on overcoming these hurdles [16-20]. This includes controllable synthesis of

2D nanomaterials such as the introduction of point defects [21], to achieve desired morphologies. Also, the functionalization by incorporating nitrogen into the surface framework [19, 22, 23] or introducing a promoter cation like metal oxides and noble metals [24, 25], for synergistic and unique catalytic properties. In parallel with the efforts on graphene-like materials, recent studies have focused on the advantage of merging individual properties of different 2D materials. To this end, multilayer heterostructure materials are produced by stacking of 2D-crystals of each nanomaterial [26], bonded by relatively weak vdW like forces. However, little effort has been placed on the development of novel materials, for example, the possibility of making graphene/MoS<sub>2</sub> bilayer heterostructure for CO<sub>2</sub> adsorption. Interestingly, it was observed that the CO<sub>2</sub> based adsorbent materials studies reported in the literature lack critical atomic level understanding of the adsorption mechanisms. These include:

- ❖ The effects of interlayer distance on adsorption mechanisms of CO<sub>2</sub> confined within the graphene-MoS<sub>2</sub> nanosheets.
- ❖ The synergistic effect of molecular (nitrogen) doping and vacancy defects to enhance selective adsorption of CO<sub>2</sub> over adsorption of nitrogen (N<sub>2</sub>) and water (H<sub>2</sub>O) molecules
- ❖ The effect of vacancy defect and nitrogen doping on adsorption performance in terms of sensitivity, selectivity and stability, and dissociation of CO<sub>2</sub> and H<sub>2</sub>O.
- ❖ How N atoms surrounding a single Mo vacancy site facilitates CO<sub>2</sub> and H<sub>2</sub>O dissociations that occurs spontaneously at room temperature
- ❖ How sulphur vacancy defects affect the adsorption of CO<sub>2</sub>, CH<sub>4</sub>, N<sub>2</sub>, H<sub>2</sub> and H<sub>2</sub>O on MoS<sub>2</sub>.

Addressing the above knowledge gap was the critical motivating factor in carrying out the current challenging task of first principle understanding of the development of CO<sub>2</sub> sensitive materials, which are extremely selective, stable and sensitive for a wide range of applications.

## 1.2 Objectives

This thesis work is aimed at the design and development of finely tailored 2D nanomaterials that will describe the behaviour of CO<sub>2</sub> on the adsorption sites, which are sensitive and selective to CO<sub>2</sub>. Two 2D nanomaterials namely graphene and MoS<sub>2</sub> monolayers were studied as case theoretical models to achieve the primary objective. In an attempt to add more knowledge to this cutting-edge of applied materials design, the theoretical analysis using density functional theoretical (DFT), implemented in the Vienna *ab initio* simulation package (VASP) will correspond favourably with the experimental results. The critical literature review revealed several major first principle understanding of 2D materials that needed to be investigated, which are briefly discussed below:

- ❖ To comparatively investigate the adsorption mechanisms of CO<sub>2</sub> confined within the interlayer of 2D nanosheets, which is an intriguing confinement environment for molecular interactions but its atomic level understanding is still limited. Preferably, a nanoconfinement of graphene and MoS<sub>2</sub> hybrid having a smaller lattice mismatch for CO<sub>2</sub> adsorption mechanisms.
- ❖ To investigate different dispersion schemes to understand the effects of vdW forces on the adsorption of CO<sub>2</sub>, which will be presented as an accurate guide for future work involving the adsorption of molecules.

- ❖ To improve the adsorption strength and catalytic activity of the pristine MoS<sub>2</sub> layer by fine-tuning the physical and chemical properties. This is currently a major concern and postulated to be alleviated to an extent by developing highly engineered MoS<sub>2</sub> nanosheets with sufficient active sites for enhanced CO<sub>2</sub> adsorption capacity.
- ❖ To investigate the pristine MoS<sub>2</sub> layer for adsorption performance in terms of sensitivity and selectivity under different initial molecular height as a function of vacancies as well as non-defective MoS<sub>2</sub> planes and their decoration with N atoms by substitution route to form N-doped MoS<sub>2</sub> systems in different types, to determine the region of the optimum performance condition.
- ❖ To investigate the infrared (IR) spectroscopy of molecules adsorbed on the surface by calculating the vibrational frequencies of the molecules adsorbed on the most stable adsorption configuration. This is important because the phonon calculation in conjunction with the experimental measurements can provide a valuable approach to probe the structure of the surface adsorbates.
- ❖ To investigate the developed N-doping enabled defect engineering of MoS<sub>2</sub> model for performance in terms of sensitivity as a function of CO<sub>2</sub> gas adsorption and cross-interference in presence of competitive gaseous molecules, to determine the selective adsorption scope of the adsorbent under study.
- ❖ To determine the reliability of N-doped defective MoS<sub>2</sub> developed in terms of its dissociative properties by studying the temperature effect on the thermodynamic and kinetic properties, and the dynamic evaluation of the adsorption system.



- ❖ To investigate the adsorption performance under non-zero temperature and pressure of the surrounding atmosphere, to analyse the thermodynamic stability of the considered most stable adsorption surface when exposed to a given environment.
- ❖ Obtain partial charge distribution of MoS<sub>2</sub> surfaces that will be presented as an accurate guide for future work involving adsorption isotherm predictions using statistical-based method (GCMC).

Further, long-term repeatability is highly dependent on the reversible reactions taking place on the surface of the sensitive adsorbent material following the successive CO<sub>2</sub> gas adsorptions. Hence, it is important to investigate the adsorbent material layer before and after adsorption for changes in the crystal structure, electronic properties and chemical composition changes. To achieve this, various computational chemistry techniques such as conjugate gradient geometry relaxation method (to determine adsorption energies and structural properties), Bader charge analysis and spin-polarized density difference (to determine electrostatic interaction between the molecules) and the adsorption systems, and phonon analysis are employed. Furthermore, to provide further insight into the electronic properties of the systems the total DOS (TDOS) and partial DOS (PDOS) calculations are also employed. It is envisaged that these results will aid in the fundamental understanding of the type of adsorption (physisorption or chemisorption) taking place at the defective and non-defective graphene-MoS<sub>2</sub> monolayer and the nanoconfinement bilayer and hybrid heterostructures used in the body of the work. Additionally, the evaluation of minimum-energy reaction paths (MEPs) and the transition states (TS) are performed to determine the activation barrier for the dissociation reaction. The finite temperature analysis of the

dissociative adsorption system at 300 K are undertaken to determine the dynamic nature of the adsorption system. Moreover, the ab initio thermodynamics method is applied to investigate and analyse the thermodynamic stability of the system exposed to a given environment. This helps confirm the spontaneous nature of the dissociation at ambient temperature.

### **1.3 Research Novelty**

The investigation of CO<sub>2</sub> gas-based 2D nanostructure resulted in several novel outcomes during this thesis work, which is anticipated to add a major contribution to the existing gas adsorbent materials research field.

Two 2D nanostructure layered materials namely graphene and MoS<sub>2</sub> with four novel materials for CO<sub>2</sub> adsorption (graphene/MoS<sub>2</sub> (GMoS<sub>2</sub>) and MoS<sub>2</sub>/graphene (MoS<sub>2</sub>G) hybrids, N atoms surrounding a single Mo vacancy site (MoS<sub>2</sub>\_1V<sub>Mo</sub>\_3N<sub>S</sub>) and single sulphur vacancy MoS<sub>2</sub> were developed. The adsorption performance and catalytic activity of the developed gas adsorbent material were investigated towards CO<sub>2</sub> adsorption and activation in some instant at various temperatures and pressures. The cross-sensitivity performance of the developed adsorbent models was tested thoroughly to determine the selective adsorption and practicability of the developed gas adsorbent model could be served as useful guidance in the experimental investigation for potential industrial use. To the best of the author's knowledge, this thesis work resulted in the following key novelties:

- ❖ The space within the interlayer of 2-dimensional (2D) nanosheets have provided new and intriguing confinement environments for molecular interactions. However,

- atomic-level understanding of the adsorption mechanisms of CO<sub>2</sub> confined within the interlayer of 2D nanosheets is still limited in the literature. This is a highly significant contribution as it provided a comparative study of the adsorption mechanisms of CO<sub>2</sub> confined within the graphene-MoS<sub>2</sub> nanosheets using the DFT. Furthermore, it demonstrated for the first time that the employment of 7.5 Å and 8.5 Å interlayer spacing is the most stable conformation for CO<sub>2</sub> adsorption on the bilayer and hybrid structures, respectively and molecular orientations resulted in enhanced CO<sub>2</sub> adsorption.
- ❖ N-doping enabled defect engineering of MoS<sub>2</sub> to introduce desirable properties was proposed for the first time as an effective approach for the enhanced selective adsorption of CO<sub>2</sub>.
  - ❖ The single S vacancy defect is identified for dissociative chemisorption of CO<sub>2</sub> at the vacant site during CO<sub>2</sub> adsorption to yield lattice-embedded oxygen and CO molecule that desorb from the surface. This can be associated with the perpendicular orientation of the CO<sub>2</sub> molecule and the increased covalent attractions, which were not considered in, previously reported studies.
  - ❖ The enhanced adsorption of CO<sub>2</sub> on N-doped vacancy-containing MoS<sub>2</sub> surface was tested for cross-interference in presence of N<sub>2</sub> and H<sub>2</sub>O. This was crucial since the adsorption phenomenon of vacancy defect and nitrogen doping facilitates CO<sub>2</sub> and H<sub>2</sub>O dissociations at room temperature leading to the formation of CO\* and O\*, and OH\* and H\* radicals. This technique was only conducted for carbon surfaces (e.g. graphene).

## 1.4 Thesis Organization

This thesis contains eight Chapters with relevant references that provide a rational sequence of the research conducted during this research work. It details the advancement in the field of CO<sub>2</sub> gas adsorbent materials, resulting from a rigorous atomistic investigation done throughout this program.

The thesis begins with **Chapter 1**, which is the introductory chapter and contains general background for research activities in this work. Also, the author's motivation to embark on the research in the field of CO<sub>2</sub> gas adsorbent materials is detailed. In addition, this chapter also includes the research objectives of the thesis work. Finally, contributions to the current body of knowledge and the author's achievements are stated.

In **Chapter 2**, the literature review is presented, which outlines the importance of CO<sub>2</sub> gas adsorbent material and the current state of the techniques available for capturing and activation. Furthermore, this chapter details the knowledge gap in this area and justifies the rationale to carry out the current research.

In **Chapter 3**, calculation methods and the supercell models of the monolayer nanostructured used as CO<sub>2</sub> adsorbent materials are provided. Different computational methods are discussed also. In addition, a brief description of the information intended to be acquired from some of the computational techniques used for binding energy, structural and electronic investigations is provided.

In **Chapter 4**, a comparative study of mechanisms of the adsorption of CO<sub>2</sub> confined within graphene-MoS<sub>2</sub> nanosheets using DFT trend study is presented. This chapter also includes

the effect of interlayer spacing and molecular orientations on CO<sub>2</sub> adsorption energies ( $E_{AE}$ ) in a bid of finding the most stable conformation for CO<sub>2</sub> adsorptions. In addition, the effect of different dispersion schemes on adsorption is provided to understand the effects of vdW forces on the adsorption of CO<sub>2</sub>.

In **Chapter 5**, novel N-doping enabled defect engineering of MoS<sub>2</sub> for enhanced and selective adsorption of CO<sub>2</sub> using a DFT approach is presented. N doping is adopted to engineer defects on MoS<sub>2</sub> to introduce desirable properties. A new insight into CO<sub>2</sub> adsorption on N-doped defective MoS<sub>2</sub> surface is revealed and N-doped MoS<sub>2</sub> with Mo single vacant defects is found the best for CO<sub>2</sub> adsorption. In addition, phonon analysis is carried out to probe the structure of the surface adsorbates and confirms C=O bonds weakened upon CO<sub>2</sub> adsorption on the vacancy. It is discovered that CO<sub>2</sub> adsorption is enhanced through covalent and electrostatic interactions. Finally, the N-doping enabled defect engineering of MoS<sub>2</sub> is proved an effective approach for the enhanced selective adsorption of CO<sub>2</sub>.

**Chapter 6** starts with a comparison of adsorption of stable CO<sub>2</sub>, N<sub>2</sub> and H<sub>2</sub>O on N-doped vacancy-containing MoS<sub>2</sub> surface, which motivated to study dissociation of CO<sub>2</sub>, and H<sub>2</sub>O at room temperature. New insights on the effect of vacancy defect and nitrogen doping on the adsorption and dissociation of CO<sub>2</sub> and H<sub>2</sub>O over the MoS<sub>2</sub> monolayer is revealed. After different DFT calculation methods, it was discovered that N atoms surrounding a single Mo vacancy site (MoS<sub>2</sub>\_1V<sub>Mo</sub>\_3Ns) facilitate CO<sub>2</sub> and H<sub>2</sub>O dissociations and that dissociation of CO<sub>2</sub> and H<sub>2</sub>O, which occurs spontaneously at room temperature leads to the formation of CO\* and O\*, and OH\* and H\* radicals. This study shows the great potential of MoS<sub>2</sub>\_1V<sub>Mo</sub>\_3Ns in the sustainable production of fuels and chemicals via CO<sub>2</sub> and H<sub>2</sub>O

splitting processes. Finally, after thorough ab initio thermodynamics analysis, MoS<sub>2</sub>-1V<sub>Mo</sub>-3N<sub>S</sub> was tested for stability over a temperature range of between 200 K and 1200 K and the pressure range between 1.5 x 10<sup>5</sup>atm and 10<sup>-35</sup> atm, to include experimental pressure range (1 atm and 10<sup>-14</sup> (ultrahigh vacuum, UHV) and any variation in pressure.

**Chapter 7** presents new insights on the role of a single sulphur vacancy on gaseous adsorption and potential water splitting over MoS<sub>2</sub> edges. First-principles simulations were performed to understand and differentiate how sulphur vacancy defects affect the adsorption of CO<sub>2</sub>, CH<sub>4</sub>, N<sub>2</sub>, H<sub>2</sub> and H<sub>2</sub>O on MoS<sub>2</sub>. Classical Grand Canonical Monte-Carlo (GCMC) simulations were carried out using RASPA 2.0 to simulate adsorption isotherms between 0 – 100 bar for MoS<sub>2</sub> with and without single vacancy defects. Adsorption isotherms were simulated from 0 – 100 bar for CO<sub>2</sub>, CH<sub>4</sub>, N<sub>2</sub>, H<sub>2</sub>, H<sub>2</sub>O.

Finally, **Chapter 8** includes a summary of the thesis and concluding remarks. The scope for future research work on CO<sub>2</sub> gas adsorbent materials is also discussed in this chapter.

## CHAPTER 2

### Literature Review

#### 2.1 Introduction

This chapter details available experimental and computational techniques that are actively employed in the investigations of the separation of CO<sub>2</sub> from the gaseous products of the combustion of fossil fuels. An overview of both natural and anthropogenic sources of CO<sub>2</sub> and its impact on the environment is briefly discussed. It also shows the logical rationale put forth for the computational analysis using DFT to depict molecular interactions with the adsorbent surface. This chapter further emphasizes the importance of graphene/molybdenum disulphide (MoS<sub>2</sub>) modification by chemical exfoliation of graphite and bulk MoS<sub>2</sub> followed by metal doping and polymer functionalization in producing effective adsorbents for CO<sub>2</sub> uptake and promoting their intrinsic catalytic characteristics. Theoretical studies on the replacement of surface atoms in the graphene/MoS<sub>2</sub> hexagonal or other carbon-based structures (such as fullerenes) with foreign atoms like Boron nitride (BN), Boron (B) or precious metals, as active sites for CO<sub>2</sub> fixation and activation are also discussed.

## 2.2 Carbon Dioxide

CO<sub>2</sub> consists of a carbon atom that forms two linear covalent double bonds with two atoms of oxygen with the structural formula of O=C=O. It has a 116.3 pm linear carbon-oxygen bond length (180° bond angle) that is significantly shorter than the bond length of a C-O single bond and even shorter than most other C-O multiply-bonded functional groups [27]. CO<sub>2</sub> is an odourless linear acidic toxicant and non-polar molecule and is hard to activate due to its high thermodynamic stability. However, if the structural linearity of CO<sub>2</sub> is transferred into a bent structure, there will be a significant reduction in the activation energy barrier [28]. According to National Oceanic and Atmospheric Administration (NOAA) in its monthly report in March 2017, CO<sub>2</sub> was found to have an average concentration of about 0.0407% (407ppm) by volume of the Earth's atmosphere and thus considers as a trace since it only contributed less than 1% by volume of the Earth's atmosphere. At pressure below 5.11 atm, it has no liquid state; it is highly soluble in ethanol and acetone, and it dissolves in water (H<sub>2</sub>O) to form carbonic acid at a gaseous state. Likewise, it spontaneously reacts with alkalis to form carbonates and bicarbonates at normal temperature and pressure, although the reaction mechanism is highly dependent on the concentration of alkali solution. The reactivity of CO<sub>2</sub> depends mostly on its properties like every other molecule and some of these important physical properties of CO<sub>2</sub> gas are listed in the table (**Table 2.1**) below.



**Table 2.1:** Summary of CO<sub>2</sub> Gas Physical-Chemical Properties [29].

Properties (unit)	Values
Molar mass (g/mol)	44.0095
Density (g/L)	1600 (solid), 771 (liquid), 1.98 (gas)
Sublimation point (°C) at 5.185 bar	-56.6
Solubility in water (g/L) at 25°C, 100 kpa	1.45
Acidity (pKa)	6.35 and 10.33
Viscosity (cP) at -78°C	0.07
Linear Bond length (pm)	116.3
Linear Bond angle (°)	180

CO<sub>2</sub> gas can be emitted by natural and anthropogenic sources. Emissions from natural sources are absorbed back by the natural sinks, which is not true in the case of anthropogenic sources. Although anthropogenic emissions are small compared to natural emissions, still they add up heavily to the CO<sub>2</sub> concentration in the atmosphere. Hence, when higher amount of CO<sub>2</sub> is released outside the naturally occurring carbon cycle, nearly 40% of extra CO<sub>2</sub> is absorbed and the rest is accumulated in the earth's atmosphere. This is primarily attributed to the absence of anthropogenic sinks and natural absorptions only having a limited ability to process the extra amount of CO<sub>2</sub> emitted in the atmosphere [30]. Recently, it was reported that CO<sub>2</sub> concentration rose from a pre-industrial level of about 265 ppm to 407 ppm (in March 2017) [3] and reports suggest that by 2050, this value will have increased to 710 ppm [31].

### **2.2.1 Natural Sources of CO<sub>2</sub>**

Naturally, sources like volcanoes, hot springs and geysers have been found to produce CO<sub>2</sub>. It can also be released from carbonate rocks by dissolving in water and acids. Because of its ability to dissolve in water, it can be found naturally in groundwater, rivers etc. Also, it can be found present in crude products like petroleum and natural gas [32]. According to the United States Environmental Protection Agency (USEPA), the CO<sub>2</sub> exchange between ocean and atmosphere contributes around 42.84% whereas soil, plant and animals contribute around 57.12% [30, 33]. The ocean-atmosphere exchange is part of the famous carbon cycle, in the sense that, the CO<sub>2</sub> present in the ocean is released into the air through the surface by evaporation, thus creating 330 billion tons of CO<sub>2</sub> emissions annually; the same amount of CO<sub>2</sub> is absorbed back into the ocean through the process of diffusion. Similarly, CO<sub>2</sub> emissions from living beings are respiration and soil processes such as respiration and decomposition account for 440 billion tons per year. These emissions are again balanced by natural vegetation and land process. The volatile eruptions (volcanoes, hot springs and geysers) create about 0.26 billion tons annually [34], during which gases such as CO<sub>2</sub> and SO<sub>2</sub> are released in addition to water vapour into the atmosphere. The emissions released into the atmosphere are absorbed continuously by the respective natural sinks, thus being nature's way of maintaining the CO<sub>2</sub> levels in a safe range.

### **2.2.2 Anthropogenic Sources of CO<sub>2</sub>**

The utilization of traditional fossil fuels for the production of energy and chemicals has been the primary cause of the constant rise in anthropogenic CO<sub>2</sub> concentration during the industrial era [3, 35]. Other sources arise from the combustion of wood and other organic

materials. The rapid use of these products as a source of energy has induced climate variation since thermodynamically stable CO<sub>2</sub> is the most significant long-lived greenhouse gases. The industrial revolution (1760-1840, England) not only developed new technologies and improved the living standard but also showed adverse effects on nature. The downside of the industrial revolution includes rapid deforestation, drastic climate changes referred to as global warming. As one of the greenhouse gases, its emissions from anthropogenic sources such as the burning of fossil fuels, coal and gas accounts for about 87%, creating more than 33.2 billion tons per year [36]. Further, deforestation and land-use changes (9%, 3.3 billion tons per year) and other industrial processes (4%, 1.7 billion tons per year) contribute to the remaining emissions [37] Major economic sectors that utilize energy obtained from the burning of fuels include electricity, transportation and other industries. Interestingly, the first two sectors contribute the majority of the total global anthropogenic CO<sub>2</sub> emissions, while the remaining is balanced from other industries. Rapid conversion of forestland for use as human settlements or construction is termed as land-use change. This land change has resulted in the release of an estimated 396-690 billion tons of CO<sub>2</sub> gas into the atmosphere, owing to tremendous increases in the perpetual elimination of standing forests, either by cutting and burning, thus significantly increasing CO<sub>2</sub> emissions. Deforestation further increases soil erosion and leaching of valuable nutrients thus decreasing the ability of the land to act as a carbon sink. Industrial processes such as cement, petrochemicals, steel, and mining emit substantial quantities of CO<sub>2</sub> gas directly or indirectly as a ramification of various inevitable chemical reactions that are allowed during material production. Overall, the total amount of CO<sub>2</sub> emissions from anthropogenic sources are very small compared to natural sources, but they contribute

substantially to the earth's atmosphere as there is no artificial sink to absorb back the emissions, thereby enhancing ocean acidification and the greenhouse effect (global warming) which has now been linked to the increase in global natural disasters.

### **2.2.3 Natural Benefits of CO<sub>2</sub>**

Atmospheric CO<sub>2</sub> remains the primary carbon source for plants on earth and this importance is competently shown in the carbon cycle [38]. In the pre-industrial era in the late Precambrian period, its concentration in the atmosphere has been regulated by a photosynthetic organism and geological phenomena. During photosynthesis plants and anaerobic organisms use light energy to produce carbohydrates from the reaction of CO<sub>2</sub> and water, giving out the oxygen (O<sub>2</sub>) as a secondary product [38]. On the other hand, aerobic organisms produce CO<sub>2</sub> while metabolizing carbohydrates and lipids to produce energy by respiration. This cycle sees the air-breathing land animals (including humans) and photosynthetic organisms exchange O<sub>2</sub> and CO<sub>2</sub>. Interestingly, the availability of CO<sub>2</sub> gas in the earth's atmosphere has helped maintain the temperature above sub-zero. Industrially, CO<sub>2</sub> plays important role in food, oil and chemical productions. For instance, it is a very important material used as an inert gas in welding and fire extinguishers and as a pressurizing gas in air guns and oil recovery. It has also been used as a chemical feedstock and in liquid form as a solvent in decaffeination coffee and supercritical drying. In drinking and carbonated beverages including beer and sparkling wine, it serves as a preservative agent. Furthermore, the effects and benefits due to CO<sub>2</sub> on human health are innumerable. For example, in the case of vasodilation (expansion of arteries), recently it was found that the low CO<sub>2</sub> concentration in the arterial blood constricts blood vessels and leads to

decreased perfusion of all vital organs [39]. Additionally, cell oxygen levels are controlled by alveolar CO<sub>2</sub> and breathing, oxygen transport, bronchodilation and inflammatory response depends on breathing. Interestingly, nerve stabilization occurs due to the sedative effects of CO<sub>2</sub> on nervous cells. This reason perfectly explains the lack of CO<sub>2</sub> in the brain leads to "spontaneous and asynchronous firing of neurons" thus leading to mental and psychological abnormalities [39].

#### **2.2.4 Hazards from CO<sub>2</sub> Emissions**

Despite its numerous commercial uses, the amount of CO<sub>2</sub> that is released into the atmosphere is enormous [3, 35]. Without instituting corrective measures, this will further exacerbate the greenhouse effect [24]. CO<sub>2</sub> contributes approximately 60% to the overall climate change taking place around the globe [40]. Another problem posed by CO<sub>2</sub> emission is ocean acidification [41] because of its capability of dissolving in water to form carbonic acid which greatly affects aquatic lives. Exposure to increased CO<sub>2</sub> gas concentration results in serious effects such as a slight increase in breathing rate (1%), headache and dizziness (2%), weakly narcotic (3%), slight choking (4-5%), loss of consciousness (5-10%), unconsciousness within a few minutes (~15%) and death (17-30%) are observed [42]. CO<sub>2</sub> is an inhalation toxicant and strong asphyxiate (O<sub>2</sub><16%). Acute high-levels of CO<sub>2</sub> exposure in the presence of low-level O<sub>2</sub> can produce significant persistent adverse health effects including headaches, attacks of vertigo, poor memory and ability to concentrate, difficulty sleeping, tinnitus, double vision, photophobia, loss of eye movement, visual field defects, enlargement of blind spots, deficient dark adaptation, and personality changes. However, prolonged exposure to low levels of CO<sub>2</sub> produces short-

term health effects such as changes in bone metabolism and calcium concentrations in blood. The last few decades have witnessed serious hazards of CO<sub>2</sub> at the workplace and hence recently, it has been declared as an occupational hazard at high concentrations (>5000 ppm). Stringent laws have been enforced to curb anthropogenic CO<sub>2</sub> emissions all over the world to provide a safer working environment. For example, in Great Britain, CO<sub>2</sub> is classed as a 'substance hazardous to health' under the Control of Substances Hazardous to Health Regulations 2002 (COSHH) [43]. According to Health and Safety Executive (HSE), the workplace exposure limits (WELs) calculated by taking an average over a specified period for CO<sub>2</sub> are, 5000 ppm over long-term exposure limits of the 8-hr reference period and 15000 ppm over a short-term exposure period of 15 minutes [44]. In addition, Occupational Safety and Health Administration (OSHA), National Institute for Occupational Safety and Health (NIOSH) and Association Advancing Occupational and Environmental Health (ACGIH) occupational exposure standards are 0.5% CO<sub>2</sub> (5000 ppm) averaged over a 40 hour week, 3% (30000 ppm) average for a short-term (15 min) exposure and 4% (40000 ppm) as the maximum instantaneous limit considered immediately dangerous to life and health [39, 45].

### **2.3 Available CO<sub>2</sub> Capture and Storage Techniques**

To effectively mitigate the above-mentioned hazards, the amount of CO<sub>2</sub> emissions into the atmosphere at every possible site have to be controlled. Hence, there is a crucial need to identify and develop stable systems with improved selective CO<sub>2</sub> capture and storage. In addition, it is essential to develop sustainable and energy-saving platforms that can convert captured CO<sub>2</sub> into fuels and/or produce valuable chemicals for other uses. On this

account, this subsection focuses on a few available experimental and computational techniques that are actively employed in the investigation of the separation of CO<sub>2</sub> from the gaseous products of the combustion of fossil fuels. These methods are based on four physical and chemical separation processes, i.e., adsorption, absorption, cryogenic distillation and membrane separation. The latter methods are of challenges in processing low concentrations of CO<sub>2</sub> in the flue gases due to the low CO<sub>2</sub> partial pressure [46], which results in an inefficient separation of CO<sub>2</sub>. On the other hand, absorption has been investigated extensively and is considered as suitable approach for the removal of CO<sub>2</sub> [47]. Using suitable aqueous solutions, the CO<sub>2</sub> absorption capacity is highly efficient. However, it is associated with some operating limitations, such as high-energy consumption of the desorption process, a requirement of a large volume of absorbent and severe corrosion of the equipment [47-49]. Some of these issues can be addressed by the use of solid adsorbents.

### **2.3.1 CO<sub>2</sub> Capture and Storage Technologies**

CO<sub>2</sub> capture and storage (CCS) technologies are being studied and developed in various fields to control and limit the increase of CO<sub>2</sub> emissions. CCS technologies are dedicated to CO<sub>2</sub> capture followed by compression, transport and storage when implemented in modern power plants. In general, CCS systems can be grouped into three technologies namely, pre-combustion, post-combustion and oxyfuel-combustion. **Figure 2.1** summarises the basic principles of the capture component of these systems, which uses either one or a combination of the following physical and chemical separation processes mentioned earlier.

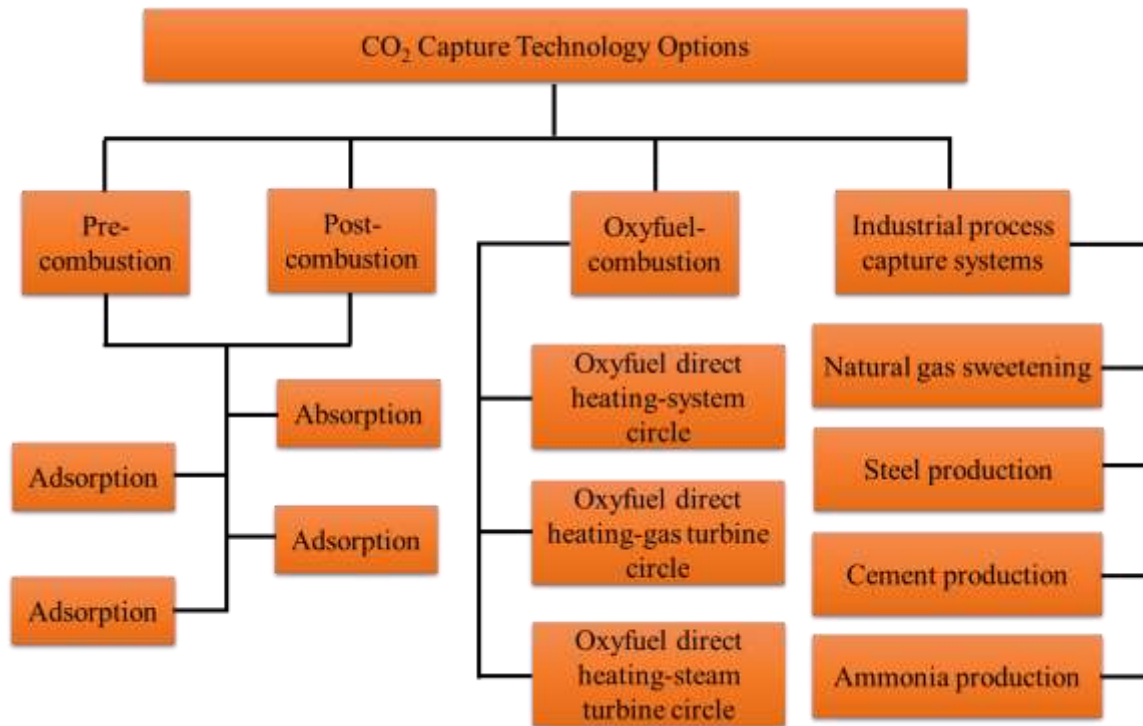


**Figure 2.1:** The three main approaches to capture CO<sub>2</sub> [50].

The choice of a suitable CO<sub>2</sub> capture technology depends on the characteristics (temperature, total pressure and partial pressure) of the gas stream from which CO<sub>2</sub> is to be separated (**Table 2.2**). This mainly depends on the power plant technology. The CO<sub>2</sub> content ranges from 3% to 15%, the lower end of this range (3-5%) is typical for gas-fired plants while the upper end (12-15%) for coal-fired plants [50]. In the pre-combustion capture, the carbon content of the fuel is stripped off before combustion by reacting it with steam (known as steam reforming) or oxygen (known as partial oxidation or gasification). This process produces syngas composed mainly of CO and H<sub>2</sub>. Subsequently, the products react with steam (through a water-gas shift reaction), giving rise to the generation of additional H<sub>2</sub> and the oxidization of CO to CO<sub>2</sub>, which in turn is ready for capture. While in the post-combustion capture technologies, CO<sub>2</sub> removal from the flue gas occurs after



the burning of the fossil fuels in ambient air (normal combustion). This system leads to a flue gas with a diluted stream of CO<sub>2</sub> mixed with a large amount of N<sub>2</sub> and small proportions of H<sub>2</sub>O, O<sub>2</sub>, and CO. The flue gas is then removed by scrubbing using solvents (e.g., amine) [51]. On the other hand, in oxyfuel-combustion systems, the combustion is performed in pure oxygen instead of air leading to a flue gas that primarily consists of CO<sub>2</sub> and H<sub>2</sub>O [52-54].

Among the three approaches, oxyfuel-combustion is a near-zero emission technology for both new and existing pulverized fossil-fired power stations [52]. However, oxy-combustion options are still under development and will require significantly more effort to reach operational and commercial readiness [54]. In contrast, both pre-combustion and post-combustion capture are technically feasible and have the potential to reduce CO<sub>2</sub> emissions by a gigaton or more per year [55]. **Table 2.2** shows the typical gas conditions for the pre-, and post-, and oxy-fuel combustion carbon capture.

**Table 2.2:** Typical Gas Conditions.

	Pre-combustion capture (before water gas shift) <sup>a</sup>	Post combustion Capture <sup>b</sup>	Oxy-fuel combustion Capture <sup>c</sup>
<b>Gas composition</b>			
CO <sub>2</sub>	35.5 %	15-16 %	87.95 mol%
H <sub>2</sub> O	0.2 %	5-7 %	3.51 mol%
H <sub>2</sub>	61.5 %	-	-
O <sub>2</sub>	-	3-4 %	8.54 mol%
CO	1.1 %	20 ppm	-
N <sub>2</sub>	0.25 %	70-75 %	-
SO <sub>x</sub>	-	800 ppm	-
NO <sub>x</sub>	-	500 ppm	-
H <sub>2</sub> S	1.1 %	-	-
<b>Conditions</b>			
Temperature (°C)	40	50-75	247 oC
Pressure (bar)	50-60	1	17

<sup>a</sup> [56]   <sup>b</sup> [57]   <sup>c</sup> [58]

Each of these capture scenarios entails different gas separation requirements and constraints mainly due to variations in the flue gas composition and operating environment as well as inconsistency in physical properties (i.e., effective kinetic diameter, dipole moment, quadrupole moment and polarization) of the gases involved (see **Table 2.2**). Although the implementation of CCS in modern power plants is estimated to reduce CO<sub>2</sub> emission by 80-90% [59], existing CCS technologies are mostly associated with an increased process energy requirement by 25-40% and are therefore not cost-effective [48, 59-61]. Hence, research is needed to develop highly effective capture materials that are beneficial for offsetting the cost implication of the existing capture technologies.

### **2.3.2 CO<sub>2</sub> Adsorption Materials**

Adsorption, on the other hand, is an attractive option to curb CO<sub>2</sub> emissions because of its comparatively fewer energy requirements and many other competitive advantages (including simplicity of operation, applicability over a relatively wide range of temperature and pressure conditions, and low capital investment costs) [46, 62]. Adsorption is a surface phenomenon wherein the adsorbate forms a film on the surface of the adsorbent via either chemisorption or physisorption. A good adsorbent must be thermodynamically stable and have high adsorption /desorption capacity over a wide operating temperature window. Although a huge number of CO<sub>2</sub> adsorbent materials have been computationally and experimentally studied in the past, nanostructured materials are at the cutting-edge of potentially revolutionary advancements in fast-growing technological fields such as; molecular sensing, energy storage and harvesting, environmental and sustainability engineering etc. This has led to the rapid increase in the development of novel

nanostructured materials. Their properties which include high surface to volume ratio, regular atomic composition, tunable reactivity, effective transport properties and assembling affinity to form supramolecular systems, have warranted their applications to CO<sub>2</sub> capture technologies. This subsection discusses some of these novel CO<sub>2</sub> adsorbent materials with more emphasis on two-dimensional nanostructured materials.

### **2.3.2.1 Graphene/Carbon-based nanomaterials**

Carbon-based nanomaterials have gained much attention due to their exceptional properties that have made them have a unique place in nanoscience. Their exceptional electrical, thermal, chemical and mechanical properties have been recognized and applied in vast areas like material science, electronics and nanotechnology as Gas Adsorption Material (GAM), composite materials, energy storage and conversion, sensors, drug delivery, field emission devices and nanoscale electronic components. This group of nanostructured gas adsorbents includes carbon nanotubes (CNT), sheets, met-cars, graphite intercalation compounds, pristine graphene and frameworks of organic pillared graphene and fullerenes (see **Figure 2.2**).

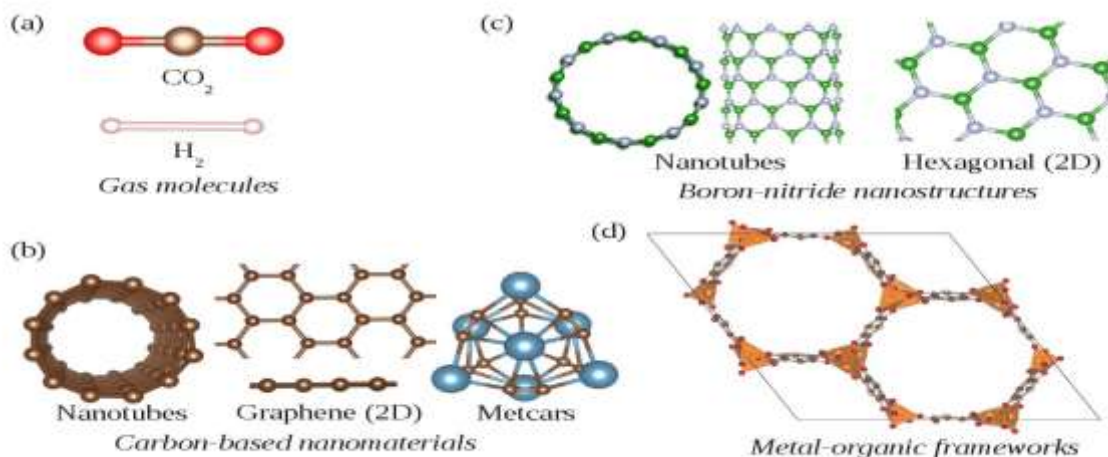


**Figure 2.2:** (a) Molecules of CO<sub>2</sub> and H<sub>2</sub>, (b-d) some of the most known groups of nanostructured gas-adsorbents [10].

Carbon nanotubes (CNT) chemistry, control over electronic properties and the assembly of nanotube devices are active areas of research that have affected many fields and the number of potential applications continues to grow. Work in fullerenes has renewed vigour with significant advances in the field of superconductivity, thin films and supramolecular assembly being made over the last few years. Although graphene is the newest of the carbon-based nanomaterials it promises to be a very active research field in gas adsorption especially CO<sub>2</sub> due to its unique adsorption properties. Already, since its isolation in 2004, it has grabbed the attention of the chemistry, materials and physics communities. Faraday discussion in 2014 showed that graphene promises to rival carbon nanotubes in terms of properties and applications with an escalation of publications from ca. 130 in 2005 to ca. 2,800 in 2010 [63]. This interest has made researchers carry out a great deal of research to determine the potential of graphene to adsorb CO<sub>2</sub> and this reason practically made graphene the right carbon-based nanomaterial candidate to be of interest in this present research.

Interestingly, the adsorption of CO<sub>2</sub> molecules on carbon-based GAM can be of physisorption or chemisorption type depending on whether the material surfaces are smooth, contain defects or are chemically functionalized. In the case of non-defective surfaces, the interactions with the gas molecules are dominated by dispersion forces thereby the gas is retained on the adsorbent material very weakly [64]. In 2006, Xu et al. were the first in carrying out nonstandard DFT calculations on the binding of CO<sub>2</sub> molecules to pristine graphene [65]. By using the hybrid ONIOM [B3LYP: DFTB-D] method, they found that the corresponding gas-adsorption energy was  $E_{\text{bind}} = -0.03$  eV.

Although there are adsorption of gas (CO<sub>2</sub>) molecules on other carbon-based materials studied using DFT techniques, our emphasis is largely on graphene-based materials. For example, carbon nanotubes (CNT) has been thoroughly analysed by Quiñonero et al. with dispersion-corrected DFT methods (i.e., B97-D/SVP) [66]. By considering different types of CNT, diameters, and binding sites, Quiñonero et al. have concluded that CO<sub>2</sub>-adsorption is energetically more favourable in the interior than in the exterior of nanotubes, in marked disagreement with previous reports [67, 68]. From these DFT studies, it can be seen that carbon-based materials are good candidate materials for CO<sub>2</sub> adsorption more especially graphene and this prove the reason why we are interested to explore more benefit of this special material (graphene) in studying the CO<sub>2</sub> adsorption mechanism on its surface using the ever-efficient DFT approach.

In recent years, graphene has been studied extensively as a promising adsorbent for CO<sub>2</sub> adsorption. Single-layer graphene is composed of a single layer of graphite [69, 70] and has a high transmittance value of *ca.* 98% indicating it is very transparent. However, the transmittance value tends to decrease by a factor of 2.3% with each additional graphite

layer [69, 71]. In addition, the material is highly durable [72], flexible [73, 74] and has high conductivity [75, 76], which make it applicable in a wide range of applications, such as in energy storage [77, 78] and molecular separation [79, 80]. Moreover, due to its high specific surface area and porosity, graphene is highly important for gas adsorption and storage [81, 82]. This is in addition to its tailorable interlayer distance between 0.7 – 1.0 nm, which is sufficient for the penetration of gaseous molecules [83]. In addition to its extraordinary properties, most of its properties are sensitive to structural defects and the number of layers [84-87]. Despite these extraordinary properties and great application potential, the lack of bandgap and inertness to reaction, which are the main characteristics of pristine graphene, limits its application in the field of semiconductors, sensors and gas adsorbents. Accordingly, much research has gone into opening a tunable gap in graphene.

Structurally, graphene is a two-dimensional (2D) allotrope of carbon ( $1s^22S^22P^2$ ) that consists mainly of a hexagonal (honeycomb) lattice of covalently bond  $sp^2$  carbon atoms [88] that are interposed between two  $\pi$ -electron clouds. Graphene can be said to be an infinitely extending sheet of benzene molecules fused at the positions the hydrogen atoms would occupy as shown in **Figure 2.3**.

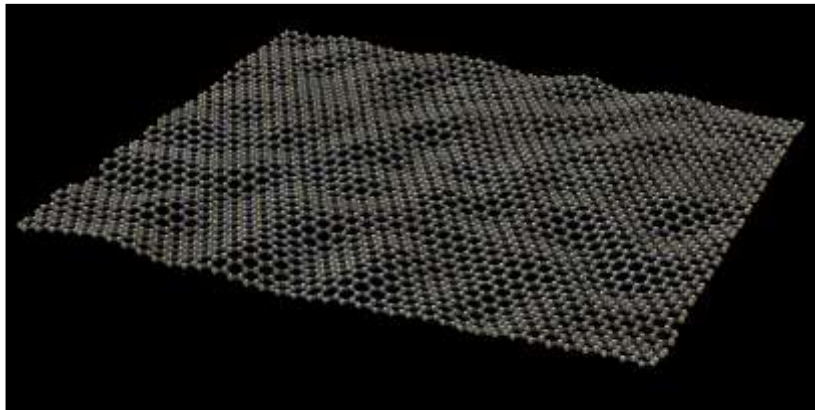


**Figure 2.3:** Isolated Graphene Sheet Schematic Representation [89].

Furthermore, bulk graphite (three-dimensional) are formed by multiple layers of graphene and it is the building block for several carbon nanotubes (one-dimensional). Single-walled carbon nanotubes (SWNT) is formed by a single graphene sheet that is rolled up while multi-walled carbon nanotube (MWNT) is formed by rolling up multiple sheets of graphene as shown in **Figure. 2.4a** and **Figure. 2.4b** respectively. Fullerenes (zero-dimensional) consist of carbon atoms arranged at the vertices of a truncated icosahedron (**Figure 2.4c**). The van der Waals forces holding these layers together in graphite are weak while the covalent in-plane  $\sigma$  bonds between each carbon atom holding each graphene sheet together are extremely hard to break which is attributed to the remarkable physical properties of many graphenes. This was exploited to enable the first isolation of graphene since the individual graphene sheets can be pulled apart easily using adhesive tape [88].

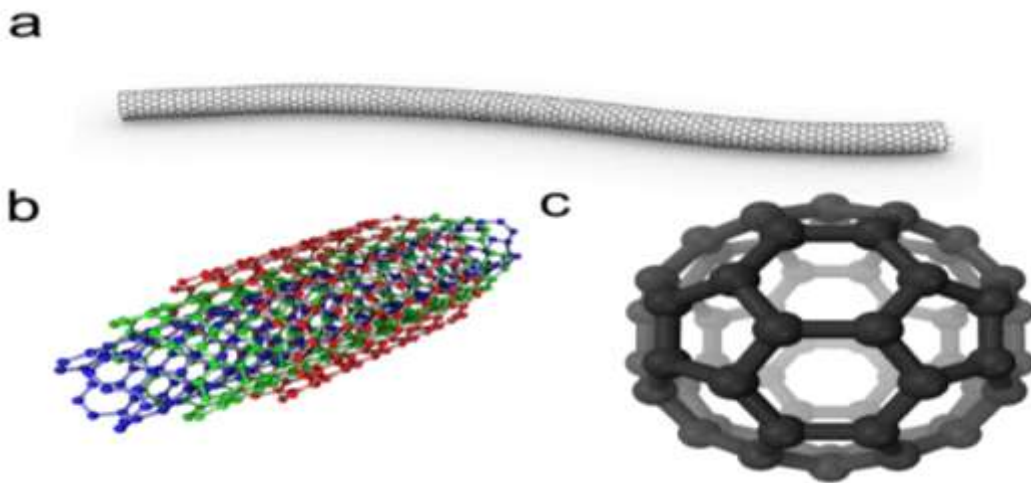


**Figure 2.4:** A pictorial view of the structures of (a) Single-walled nanotube (SWNT) [89], (b) Multiple-walled nanotube (MWNT) (where each colour is related to different SWNTs which make up the MWNT structure [89] and (c) C60 Fullerene [90].



There are two major models used to model graphene surfaces namely, finite molecular and periodic (infinite) models. These models have different methods and help to give an in-depth understanding of the nature and strength of interactions between graphene and guest molecules. Finite molecular models (**Figure 2.5**) are the non-periodic models commonly used to model graphene in quantum calculations [91-94]. These models are polycyclic aromatic hydrocarbons (PAH) models such as benzene ( $C_6H_6$ ), coronene ( $C_{24}H_{12}$ ) or circumcoronene ( $C_{54}H_{18}$ ) as shown in **Figure 2.5**. An important advantage of using finite molecular models is that they can be studied using a wide portfolio of electronic structure methods developed for molecular systems. The only limitations come from the size of the system that can be treated in a reasonable timeframe with specific methods, and the available computational power.

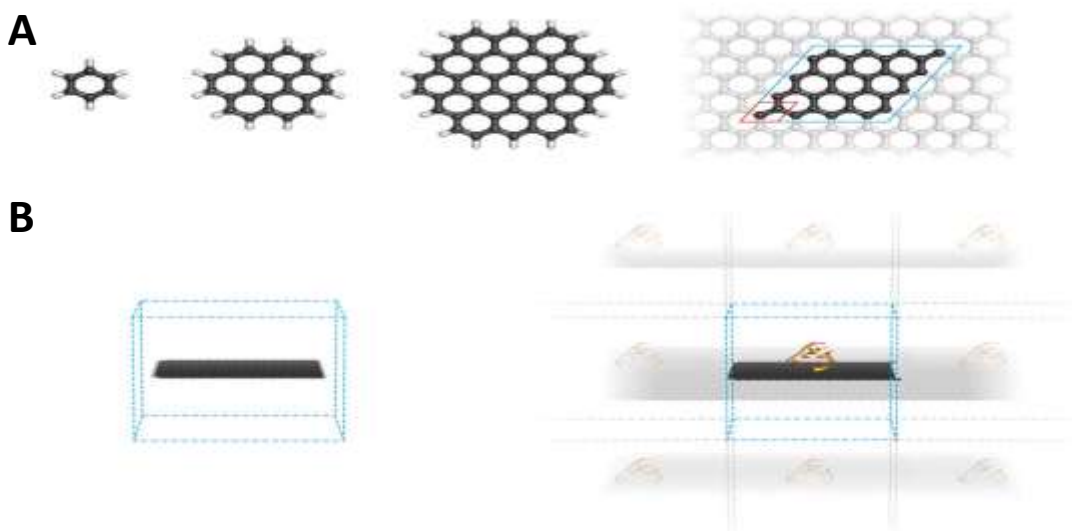


**Figure 2.5:** (A) Aromatic Hydrocarbon non-periodic models of graphene used in quantum calculations (Benzene, Coronene and Circumcoronene) and a supercell of 32 carbon atoms from a periodic graphene model, with a unit cell, highlighted in red. (B) Simulation boxes for empirical models containing finite graphene and a periodic graphene sheet with a small adsorbed RNA molecule respectively [95, 96].

On the other hand, ideal (pristine) graphene is an infinite two-dimensional (2D) sheet with a regular lattice structure that can be straightforwardly modelled using periodic boundary conditions (**Figure 2.3**). In these models, a unit cell includes two carbon atoms that are replicated across space. This periodic graphene model can be studied using numerous methods, most of which are based on DFT and were developed by solid-state physicists to model the physical features of crystals. When studying the adsorption of guest molecules (adsorbates) to graphene, the size of a replicating cell, which is known as the supercell, is dictated by the size and target concentration of the adsorbate because it is important to avoid unwanted interactions between replicas. Since the periodic boundary conditions are typically implemented over the three-dimensional (3D) space, graphene (which is generally assumed to lie in the XY plane) and its complexes are modelled using 3D unit cells in a large vacuum (vertical length of approximately 1.5 nm) to avoid spurious vertical interactions between replicas. Spurious interactions could be particularly problematic if the supercell contains polar molecules or ions, because of the slow decay of Coulombic forces. It should be noted that the attractive vdW forces in nanomaterials act over longer distances than was originally assumed [97]. The electronic band structure of graphene and its derivatives can only reasonably be studied using periodic models because models that do not account for the inherent extended nature of graphene neglect correlation contributions from the bands close to the Dirac point. Notwithstanding, the infinite model may better describe the situations encountered in some experiments, such as those involving measurements on spots of graphene flakes that may be multiple micrometres in diameter. In such cases, the presence of edge effects in a simulated finite sheet could introduce undesirable bias. An infinite periodic boundary condition (PBC) model was used to study

the mechanism by which graphene dispersions are stabilized in the presence of lipids, revealing that the lipids present a kinetic barrier to graphene aggregation by forming reverse micelles on the graphene surface [98]. On the other hand, PBC models may be less suitable for studying phenomena such as surface corrugation because the box size limits the scale on which corrugation effects can be studied. Another potential drawback of the periodic model that may be encountered with certain simulation configurations relates to sandwiched structures in which two graphene sheets are separated by a fixed distance; this can lead to unphysical conditions such as unreasonable pressures.

Both finite and infinite (periodic) graphene models can be described using either quantum chemical (electronic structure) or molecular mechanical (empirical) methods as mentioned above. The potential applications of each are delineated by the Born–Oppenheimer approximation, which enables the separation of electronic and nuclear motions inside a molecular system. Phenomena involving changes in electronic states should be modelled using electronic structure methods that explicitly account for electronic motions. Molecular mechanics can be used to model phenomena in which the electronic structure does not change or changes only slightly, such as changes in conformational states or physisorption.

### **2.3.2.2 Molybdenum Disulphide /Transition Metals Dichalcogenides**

The hexagonal structure of graphene has opened new prospects for the exploration of properties of other layered two-dimensional (2D) materials. Recently, several new classes of 2D nanostructures like transition metal dichalcogenides (TMDs) have been studied and grouped among the most promising alternative candidates for the next-generation gas capturing materials. Generally, TMDs consist of a transitional metal and a chalcogen (S,

Se or Te). The material of this class is represented in a chemical formula of  $\text{MX}_2$ , where M is the transitional metal (Groups 4-12 in the periodic table) and X is a chalcogen (Group 16). Within a single TMD layer, repeating units of  $\text{MX}_2$  are held by strong covalent bonds. These layers are loosely stacked together by weak vdWs' forces. This nature of bonding enables TMDs to be conveniently thinned down into individual sheets [99] and renders them highly anisotropic; especially in their mechanical, electrical and electrochemical aspects. These materials have become new alternative materials to CCS technologies that are being investigated because, they exhibit a number of interesting properties such as high catalytic activity [100], bandgap variation with a number of layers [101, 102], high carrier mobility [103, 104] and gas sensing capability. The discovery of these materials resulted in a fundamental change in the research and technology of gas sensors, which have made them be widely used in the adsorption of gas molecules especially toxic gases [105-107].

Monolayer molybdenum disulphide ( $\text{MoS}_2$ ) belonging to Group 6 TMDs, is one of the 2D TMD that have gained numerous attention over the past two decades [108]. Similar to other 2D materials, monolayer  $\text{MoS}_2$  is of the potential to be used as an alternative material for  $\text{CO}_2$  capture because of its extraordinary physical and chemical properties such as a large surface to mass ratio, good catalytic activity, etc. [13]. To date, layered TMDs have garnered much success in fields such as electronics, energy storage, sensing, and photoluminescence [109].

$\text{MoS}_2$  consists of one Mo atom and two S atoms positioned at alternating hexagonal structures [108]. These triple plans stack on top of each other and within the layers, the atoms are held by strong covalent bonds, whereas the adjacent layers are weakly bonded

by vdWs' forces. This allows them to be mechanically separated to form 2D sheets of MoS<sub>2</sub> as shown in **Figure 2.6**.

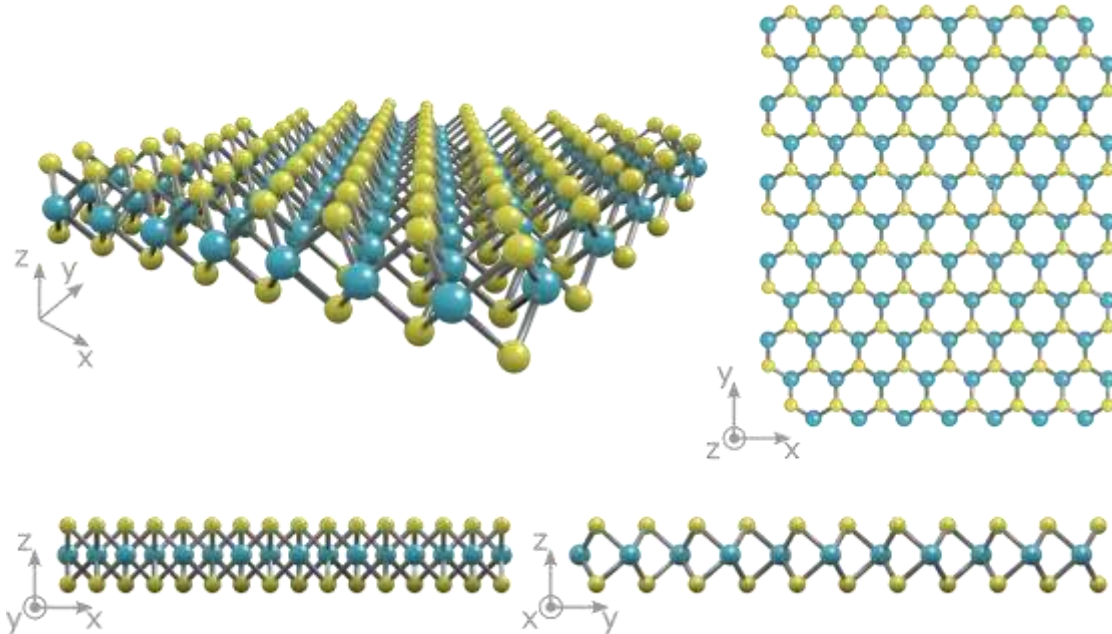


**Figure 2.6:** A diagram of a crystal structure of monolayer MoS<sub>2</sub> showing molybdenum atoms (blue) sandwiched between two layers of sulphur atoms (yellow) [110].

Unlike graphene with a zero bandgap, MoS<sub>2</sub> is a semiconducting layered material with a bandgap that changes from 1.2 eV (indirect) for bulk [19] to 1.9 eV (direct) for monolayer [110] as shown in **Figure 2.7**. The change in bandgap gives rise to the novel photoluminescence and electronic properties of the MoS<sub>2</sub> monolayer. Another important feature is the massive surface area created when the bulk is thinned into layers. Such a large surface area of exfoliated MoS<sub>2</sub> carries a high density of edges that are potential active sites for the electrochemical applications in sensing and energy storage, in particular for CO<sub>2</sub> storage [108, 109].

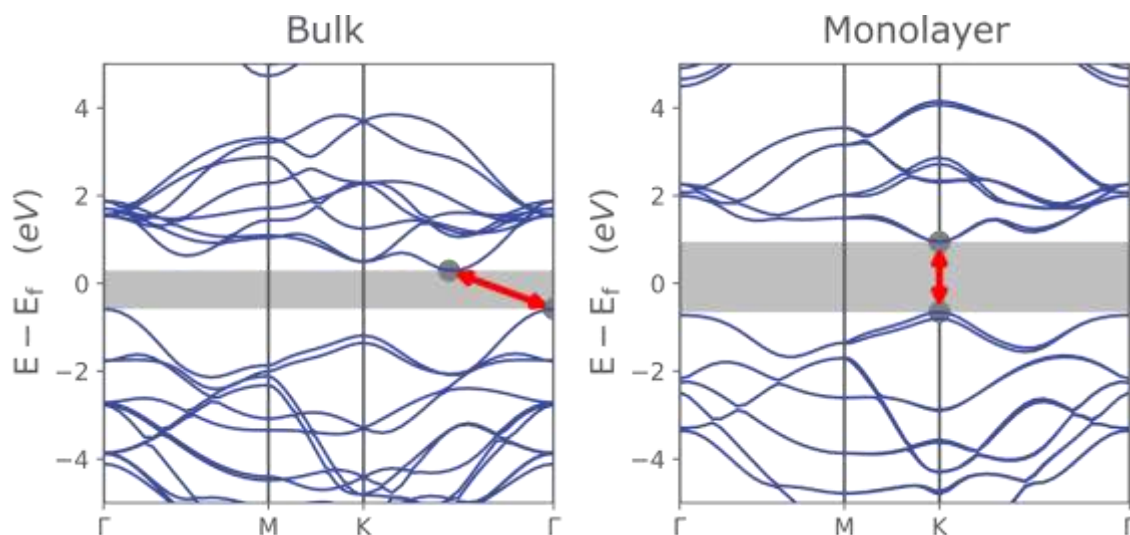


**Figure 2.7:** A diagram of band structure of bulk (left) and monolayer (right) MoS<sub>2</sub> showing the crossover from indirect to direct bandgap followed by a widening of the bandgap [110].

### 2.3.3 Modification of CO<sub>2</sub> Adsorption Materials for Enhanced CO<sub>2</sub> Adsorption

The modification of gas adsorption material surfaces has given rise to numerous research interests because this results in the enhancement of their unique properties for increased performance where it is applied. There are many methods used for graphene and MoS<sub>2</sub> modifications such as in-plane defects which are symmetry-breaking and includes point defects (substitutional, interstitial and vacancies cluster defects), grain or sample boundaries or edges which also behave like a defect in lowering the symmetry of infinite crystals, covalent and non-covalent functionalization, intercalation and electrostatic tuning etc. These modifications change either the electronic structure or molecular properties or both in some cases. For instance, covalent or non-covalent modification or functionalization has effects on the physicochemical properties of the material. This can be

either by forming a chemical bond between the adsorbent and some functional groups or modifiers like carbonyl, carboxylic or amine groups etc. (covalent modification) which significantly changes the structure and hybridization of their surface atom, or adsorption of modifiers onto the adsorbent surface through vdWs' forces (non-covalent modification) which has a lesser effect on the changes of the structure and properties of the material [111, 112]. DFT has emerged as the most frequently used theoretical technique because it is appropriate to study the ground-state properties, for instance, adsorption of molecules on surface problems. This section discusses the computational and experimental investigation of the modified CO<sub>2</sub> adsorption materials for enhanced adsorption and catalytic performance.

### **2.3.3.1 Graphene Modification**

Graphene exhibits excellent properties for diverse applications as mentioned early. In addition, it is cheap, easy to handle and modify. Despite these extraordinary properties and great application potentials, the lack of bandgap and inertness to reaction found in pristine graphene weakens its competitive strength in the field of semiconductors, sensors and gas adsorbents. Thus, many efforts to open a tunable gap in graphene have been devoted. CO<sub>2</sub> is slightly acidic and thus basicity of adsorbents in surface chemistry plays an important role in achieving high CO<sub>2</sub> capture performance [113]. Recently, for adsorption of various atmospheric gases, including CO<sub>2</sub> on functionalized graphene, carbon nanotubes (CNTs), graphene nanoribbons (GNRs) and graphene oxide have been experimentally and theoretically studied on various materials as candidates of adsorbent beds [114-123].

**Vacancies:** Vacancies are common defects in crystalline solids that affects their physical properties. A vacancy is the removal of one carbon atom (monovacancy or VI) [124] or two carbon atoms (double vacancy with two pentagonal rings and one octagonal ring known as 5-8-5 defect, and the 5-7-7-5 known as Stone-Wales (SW) defects with two heptagonal rings [124, 125], from the hexagonal ring. Very low concentrations of vacancy defects occur in graphite [126] during growth and at thermal equilibrium at ambient conditions. These defects are much more prevalent in electron or ion irradiated materials and are believed to be the predominant defects on irradiated graphitic surfaces [127]. CO<sub>2</sub> adsorption on defected graphene through molecular simulation was first reported by Cabrera-Sanfeliix [128]. The DFT results showed that the adsorption of CO<sub>2</sub> on defective graphene sheets having a monovacancy have higher chemical reactivity for small molecules compared with defect-free (pure) graphene. Liu and Wilcox later applied the plane-wave DFT calculations to develop a more rigorous understanding of the underlying mechanism of CO<sub>2</sub> adsorption on defective graphene surfaces [129]. The physisorption energy of CO<sub>2</sub> on the defective graphene site with one carbon atom missing (i.e. monovacancy) was four times as strong as that on a perfect defect-free graphene surface ( $\sim 20.3 \text{ kJ mol}^{-1}$  on the monovacancy site at a molecular height of 3.45 Å compared to  $\sim 4.8 \text{ kJ mol}^{-1}$  on pristine graphene). Recently, Tit *et al.* reported ab initio investigation of adsorption of CO and CO<sub>2</sub> molecules on graphene to further explain the role of intrinsic defects on gas sensing [119]. The results, summarized in **Table 2.3**, showed that CO<sub>2</sub> exhibits both chemisorption and physisorption adsorption on the vacancy graphene (vG) whereas CO exhibits only physisorption. For their findings, it is worth mentioning that the



potential range of applications for graphene in CO<sub>2</sub> adsorption and activation can be enhanced enormously by the controlled introduction of vacancy defects.

**Table 2.3:** Binding energies of CO and CO<sub>2</sub> on various adsorbents namely: (i) Pristine Graphene, (ii) Vacancy-defected Graphene, and (iii) Stone-wales-defected Graphene.  $E_F$  is Fermi energy with respect to vacuum level,  $E_{bind}$  is the binding energy of the molecule both in eV unit. “D” is the molecular-to-surface distance in Å units (Adapted with permission from [119]).

Adsorbent	CO molecule		CO <sub>2</sub> molecule	
	$E_F$ (eV)	$E_{bind}$ (eV) (D)(Å)	$E_F$ (eV)	$E_{bind}$ (eV) (D)(Å)
Pristine Graphene	-4.650	-0.125 (3.467)	-4.144	-0.184 3.345
Vacancy-defected Graphene	-4.652	-5.063 (chemisorption)	-4.655	-0.685 (3.30)
SW-defected Graphene	-4.661	-1.301 (3.00)	-4.655	-1.371 (2.96)

**Boundaries and edges:** Boundaries and edges [130-140] have been reported to be attractive sites for CO<sub>2</sub> adsorption. These sites also behave like defects because they tend to lower the symmetry of the infinite crystal allowing CO<sub>2</sub> adsorption. Montoya and co-workers suggested that a broad spectrum of active binding sites, such as edge sites, pre-adsorbed alkali metals and defects occur because of variation in the adsorption energy from ~3.7 eV to ~200 meV of the experimental and theory (using DFT at the B3LYP/Basis level of theory) when they investigated the mechanism of CO<sub>2</sub> chemisorption on graphene sheets [141]. They reported that the most stable complex formed by the chemisorption of CO<sub>2</sub> on the graphene edge sites was the lactone group on the armchair edge, with an adsorption energy of 3.68 eV. Also, the adsorption energy drops to hundreds of meV as the CO<sub>2</sub> coverage increases because active sites were already occupied, so further CO<sub>2</sub> molecules could only be physisorbed on the graphene plans. The first and perhaps the only simulation-based work on edge effects of nanographene on CO<sub>2</sub> adsorption was the work of Ohba and Kanoh [142]. With the fact that nanographene layers have a large number of edges that predominantly influence their chemical and physical properties, they investigated the differences in the interaction potential of edge sites and basal planes of nanographene for Carbon dioxide and Nitrogen gases adsorption using GCMC. Their results showed that CO<sub>2</sub> and N<sub>2</sub> preferred to be adsorbed on the edge sites and basal plans respectively. The reason for this preference is the fact that the edge sites of nanographene layers have very strong columbic interactions because of the presence of the partial charges at the edges, but basal plans have no partial electronic charges at the edges and thus barely have columbic interactions. Therefore, the separation ability of CO<sub>2</sub> is higher than that of N<sub>2</sub> in the low-pressure region where CO<sub>2</sub> exhibits a very high quadrupole moment than N<sub>2</sub>. Their results

provided preliminary evidence of the adsorption capacity of graphene edge sites for flue gas mixture (**Table 2.4**) and encouraged the building of adsorbents for selective adsorption, reaction and separation of CO<sub>2</sub> from a mixture of flue gases after combustion by precise tuning graphene edge.

**Table 2.4:** Adsorption Minima of Ar, CH<sub>4</sub>, N<sub>2</sub>, CO<sub>2</sub>, and H<sub>2</sub>O Adsorptions on Nanographenes. Reprinted with permission from [142].

Adsorbates	Adsorption potential/kJmol <sup>-1</sup>		
	E <sub>edge</sub>	E <sub>plane</sub>	(E <sub>edge</sub> – E <sub>plane</sub> )/E <sub>plane</sub>
Ar	6.5	9.4	-0.31
CH <sub>4</sub>	8.1	11.1	-0.27
N <sub>2</sub>	7.8	10.0	-0.02
CO <sub>2</sub>	19.2	17.6	0.09
H <sub>2</sub> O	8.7	7.3	0.18

**Functionalization:** Functionalization of graphene including reactions of graphene and its derivatives with organic and inorganic molecules is another efficient way of improving the properties of graphene. The functionalization modes can be grouped based on the method and materials used which can be covalent or non-covalent. In gas adsorption processes, properties of the gases like polarizability and quadrupole moment, which makes some molecules, have higher adsorption enthalpy than others, determine the separation. As mentioned early, CO<sub>2</sub> is slightly acidic thus has higher quadrupole, moments than other

flue associative gases like N<sub>2</sub>, O<sub>2</sub> and H<sub>2</sub>, which are barely polar (Table 2.5). Therefore, to achieve a high CO<sub>2</sub> capture performance, the basicity of CO<sub>2</sub> adsorbents is imperative. In a nutshell, the addition of functional groups having high affinity for CO<sub>2</sub> to graphene will improve its adsorption capacity and selectivity. It has been proven experimentally and theoretically that grafting functional groups like carboxyl, carbonyl, epoxy and hydroxyl on graphene rings enhances its CO<sub>2</sub> adsorption. By studying the interaction of CO<sub>2</sub>, H<sub>2</sub>O, Li, Mg, Li<sup>+</sup> and Mg<sup>2+</sup> with polycyclic aromatic hydrocarbon using DFT, Umadevi and Sastry [143] showed  $\pi$ - $\pi$  stacking interactions are of special interest due to the extended  $\pi$  orbitals of graphene. Also, it has shown that functional groups attached to an aromatic molecule affect the nature and magnitude of interactions between the molecule and graphene [144]. Their results proved that CO<sub>2</sub> was greatly adsorbed on the edges with polar functional groups, which indicates that, the presence of these polar groups can significantly enhance CO<sub>2</sub> binding by activating exposed edges and terraces to introduce additional binding sites making the edges potentially viable gas binding sites.

**Table 2.5:** Physical Properties of Selected Flue Gas [145].

Flue Gas	Polarizability ( $10^{-25} \text{ cm}^3$ )	Dipole moment ( $10^{-18} \text{ esu}^{-1} \text{ cm}^{-1}$ )	Quadrupole moment ( $10^{-26} \text{ esu}^{-1} \text{ cm}^{-1}$ )
N <sub>2</sub>	17.4	0	1.52
CO <sub>2</sub>	29.1	0	4.30
O <sub>2</sub>	15.8	0	0.39
H <sub>2</sub> O	14.5	1.85	-
H <sub>2</sub>	8.0	0	6.62

Recently, Dasgupta et al., further demonstrated the strength of edge functionalized graphene nanoribbons on CO<sub>2</sub> capture by examining the influence of particular functional moieties (-OH, -NH<sub>2</sub>, -NO<sub>2</sub>, -CH<sub>3</sub>, and -COOH) on the selective separation of CO<sub>2</sub> from its mixtures with N<sub>2</sub> by combining first principle (ab initio) and Monte Carlo simulations [146]. The results showed that CO<sub>2</sub> binds strongly to the -COOH functional group with higher binding energy (-5.84 kJ/mol) compared to other functional groups (-NH<sub>2</sub> (-4.79 kJ/mol), -CH<sub>3</sub> (-2.93 kJ/mol), -OH (-2.20 kJ/mol) and -NO<sub>2</sub> (-0.84 kJ/mol) whereas N<sub>2</sub> showed a strong affinity with the sides with -COOH and OH groups (**Figure 2.8**). This can be presumed due to the overall increase in vdW interactions because of the C=O bond present in the -COOH group. These studies showed that site-specific functionalization with -COOH has a prominent effect on the local gas adsorption characteristics and may be used as a potential route to manipulate graphene sheets for high CO<sub>2</sub> capacity and selectivity.

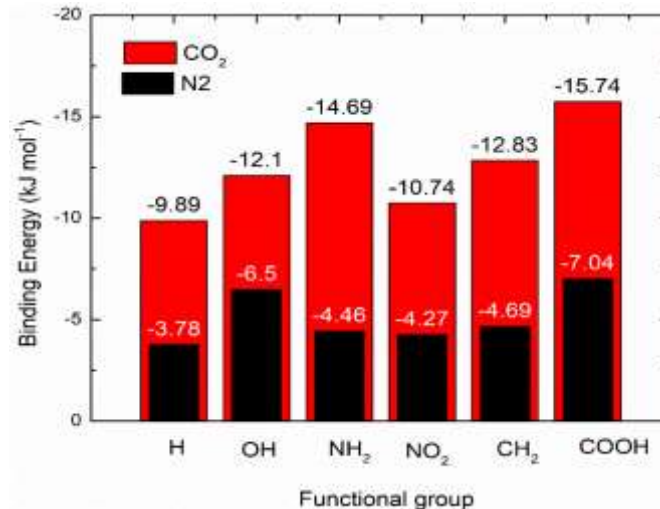


**Figure 2.8:** Binding energies of CO<sub>2</sub> and N<sub>2</sub> with functionalized benzenes obtained using DFT [146].

**Doping:** Another method employed to enhance the properties of graphene is a modification by chemical or substitutional doping with foreign atoms [147]. Generally, the type of dopant (depending on its electrophilic character) used determines the nature of the graphene as a p- or n-type semiconductor. The use of these dopants shown to inject either electrons or holes in the system changing its electronic properties, with the advantage that they can also play the role of adsorption sites. Experiments have shown that B and N atoms are the natural dopants for graphene and other carbon materials because of their similar atomic size as that of C (carbon atom) and their hole acceptor and electron donor characters for substitutional B- (electron-less) and N-(electron-rich) doping respectively. It has been proved theoretically that doping graphene with B-, N-, and Bi-dopants can open its bandgap and enhance its electronic properties [148-152]. With these advanced achievements made by many researchers in modifying graphene through doping for application in electronic devices, environmental engineers and material scientists have gone further up to apply it in the adsorption of gas molecules. For instance, it has been shown theoretically that, N-

doping plays a critical role in regulating the electronic and chemical properties of carbon materials. This is because it has a comparable atomic size and five valence electrons available to form strong valence bonds with carbon atom; making the carbon atom adjacent to the nitrogen atom (which is electron-rich and highly electron-negative) possess a higher positive charge due to low electron-negativity in the carbon atom [153]. This result in a positive shift of Fermi energy at the top of the Brillion zone of graphene [154]. In other words, there is a change in its transport properties compared to that of intrinsic graphene when the Dirac point moved from positive gate voltage ( $V_g$ ) to negative  $V_g$  indicating the transition of graphene from p-type to n-type after annealing in  $NH_3$ ; which makes N-graphene a promising material for multiple applications [155].

Cortés-Arriagada et al recently investigated the effect of Fe-doped monovacancy graphene (FeG) nanosheet on adsorbing harmful gas molecules ( $CO$ ,  $CO_2$ ,  $SO_2$  and  $H_2S$ ) and co-adsorption in  $O_2$  environments using DFT [156]. **Table 2.6** compares adsorption energies of gases adsorbed on pristine and doped graphene. The effect of replacing carbon atoms in graphene with foreign atoms on the structure of graphene is obvious from the difference in the adsorption energies of both structures. Specifically,  $CO_2$  and other gas pollutants were chemisorbed onto FeG with binding energies of the range of 0.54-1.80 eV, improving the adsorption strength by at best 39% compared to those onto pristine graphene.

**Table 2.6:** Adsorption energies ( $E_{ads}$ ) and contribution of dispersion forces ( $E_{vdw}$ ) of the G-adsorbate and FeG-adsorbate systems. Energies are in eV [156].

System	$E_{ads}$	$E_{vdw}$
<b>With Pristine Graphene (G)</b>		
G-CO	0.08	0.15
G-CO <sub>2</sub>	0.11	0.19
G-H <sub>2</sub> S	0.15	0.19
G-SO <sub>2</sub>	0.28	0.29
<b>With Fe-doped Graphene (FeG)</b>		
G-CO	1.60	0.12
G-CO <sub>2</sub>	0.54	0.20
G-H <sub>2</sub> S	1.19	0.18
G-SO <sub>2</sub>	1.80	0.26

### 2.3.3.2 MoS<sub>2</sub> Modification

Although, MoS<sub>2</sub> has recently emerged as a promising energy storage and catalyst system due to its layered structure and unique electronic configuration [157, 158]. However, the low electron transfer of the basal plane of MoS<sub>2</sub> results in low energy storage activities and sluggish catalytic kinetics [14, 15]. To date, numerous strategies have been employed for the fine-tuning of the physical and chemical properties of MoS<sub>2</sub> and other TMD materials [16-19]. Both experimental and theoretical studies have been used to investigate the point



defects in MoS<sub>2</sub> monolayer [159, 160] and revealed that point defects are usually more reactive than the sites on a perfect surface, among which single sulphur vacancy (S-vacancy) is easily formed than anti-site defects [159] and the edge is usually less stable and more prone to doping [161]. The results showed that the defective MoS<sub>2</sub> surface improved adsorption strength and catalytic activity of the MoS<sub>2</sub> layer [160, 161].

Another way to improve CO<sub>2</sub> uptake capacity and intrinsic catalytic characteristics is to create basic or redox-active surface sites by incorporating nitrogen into a surface framework or introducing a promoter cation [24, 25]. These manipulate its conductivity and charge density to trigger the inert S atoms in the basal plane, thus, promote the transfer of electrons [19, 22, 23, 162]. This promotes the transfer of electrons between the surface and CO<sub>2</sub>, therefore enhancing the energy storage and catalytic activities [162]. A recent DFT simulation study proposed that nitrogen doping in monolayer MoS<sub>2</sub> leads to a high electronic state density around N and Mo atoms and therefore enhance its electronic conductivity [19]. Allegedly, the synergistic effect of molecular doping and vacancy defects may further enhance the CO<sub>2</sub> adsorption activity of MoS<sub>2</sub>.

Besides, theoretical and experimental evidence has revealed that TM-doped MoS<sub>2</sub> with the TM preferentially substituting the Mo atom at the S edge has significantly improved its energy storage and catalytic efficiency [161]. However, the improved catalytic activity varies with the nature of the constituting TM and its composition [163]. Hence, the intrinsic CO<sub>2</sub> reduction and H<sub>2</sub>O splitting features of MoS<sub>2</sub> can be readily tuned by incorporating specific TMs to enhance the catalytic activity and selectivity of these chemical reactions. For instance, Cu-based materials are the only known TM catalysts that produce a wider range of hydrocarbons with high FE [164]. Also, Co-based materials have exhibited

significantly enhanced catalytic activities towards CO<sub>2</sub> reduction and water splitting [165-167]. These TM materials possess abundant surface defects, disordered lattice, and low-coordinated sites, which are closely correlated to the number of active sites and the reaction energy barrier of catalytic CO<sub>2</sub> reduction and water splitting under ambient conditions [165, 166]. Also, Metal (Fe-, Co, Ni and Cu) dopants are rationally anchored into the vacancy site of MoS<sub>2</sub> lattice architecture to provide an additional dimension to tune the electronic structure of MoS<sub>2</sub>.

In this regard, DFT has provided an opportunity to investigate the chemical environment between the foreign TM atoms and the host crystal at the atomic level [24, 25, 165]. Therefore, a deeper understanding of the promotional effects could be established for developing high-performance CO<sub>2</sub> reduction and water splitting at a low cost. Moreover, the configuration of MoS<sub>2</sub> should be delicately designed to ensure good electronic conductivity and maximize the exposed active sites.

### **2.3.4 Graphene/MoS<sub>2</sub> Hybrid**

In parallel with the efforts on graphene-like materials, recent studies have focused on the advantage of merging individual properties of different 2D materials. These 2D nanomaterials vary in terms of their electronic properties and functionality. For instance, graphene is a low-work function metallic electrode, hBN is an insulator, and MoS<sub>2</sub> is generally an n-type semiconductor (a very active potential site for CO<sub>2</sub> capture). However, their synergetic function is more attractive for technological applications. To this end, multilayer heterostructure materials are produced by stacking of 2D-crystals of each nanomaterial [26], bonded by relatively weak vdW like forces (**Figure 2.9**).

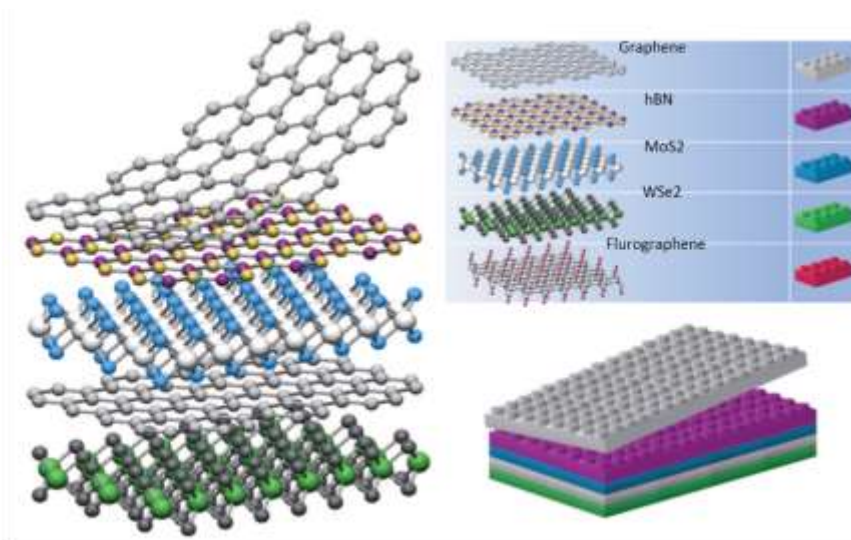


**Figure 2.9:** Building van der Waals multilayer heterostructure materials.

Recently, interesting physics have already been observed in many hybrid systems, such as Ni(OH)<sub>2</sub>/graphene hybrid [168], SnO<sub>2</sub>/graphene hybrid [169] and so forth. Specifically, recently, the possibility of making graphene/MoS<sub>2</sub> bilayer heterostructure has been demonstrated experimentally. Experimental findings show that synthesized materials are more thermally stable with high adsorption capacity [170]. Chang et al. [171] first reported a facile in situ solution-phase reduced method for growing MoS<sub>2</sub> layers on graphene to form MoS<sub>2</sub>/graphene hybrid. Their experimental results indicated that MoS<sub>2</sub> growth on the surface of graphene increases its electron conductivity and electrochemical performance.

Moreover, the space within the interlayer separation of these 2D nanosheets has often provided new and intriguing confinement environments for molecular interactions due to the nanoconfinement effect [172-175]. The confined space between layers of these nanosheets has provided lower loss and stronger localization of active sites. In addition,

the tunability of this spacing can enhance the physicochemical properties of these nanostructures. Examples of these properties include surface area, penetration depth, adsorption capacity and catalytic activity. Therefore, understanding the underlying principles of CO<sub>2</sub> adsorption mechanisms within this nanoconfinement will provide in-depth knowledge into the material science involving stacking routes of 2D nanomaterials (see **Chapter 4**).

### **2.3.5 Computational analysis on CO<sub>2</sub> adsorption**

The recent increase in computational chemistry has provided great and valuable insights into the interaction of adsorbate molecules with the adsorbent surface using molecular simulations, which has enhanced the ability of material scientists and engineers to interpret experimental observations at the atomistic level [176]. This in-depth understanding of the fundamentals of an adsorbent's molecular structure and with the experimental data is particularly important for the rational design of new adsorbents scaled to meet the intended operating conditions. Also, molecular simulations constitute an extremely powerful tool for rapid and systematic screening of both existing and hypothetical adsorbents, necessitating experimental validation of only those that demonstrate the highest level of performance, which have saved time and resources [177]. With regards to numerous benefits, it is worth mentioning that there is an increase in interest in applying molecular simulation techniques to assess and predict CO<sub>2</sub> adsorption materials.

## 2.4 Summary and Conclusions

The rapid increase in anthropogenic CO<sub>2</sub> emission primarily causing induced climate variation has surged research efforts into the design and development of highly efficient and selective gas adsorption systems. Based on the critical literature review, in addition to the adoption of renewable sources of energy, carbon capture and storage (CCS) has become one of many measures deployed to circumvent excessive emissions of CO<sub>2</sub>. However, the existing CO<sub>2</sub> capture technologies mostly require increased process energy, which makes their application not cost-effective. On the other, nanostructured GAMs with high efficiency and low costs have been investigated largely for CCS. Due to their diverse properties, graphene and MoS<sub>2</sub> materials have attracted more interest for CCS. This material has been reported to have a specific surface area, stability (thermal and chemical), tailorable surface chemistry and unique nano-structural configuration which makes it suitable for various forms of modifications. Modified graphene and MoS<sub>2</sub> monolayer materials clearly showed several advantages over their bulk and pristine 2D structures due to the high density of edges and more reactive sites, respectively. Nanostructuring and modification of their properties, especially the surface area, enhance the practical applicability of these materials and their composites. Further, these materials do not require expensive technologies such as pre-combustion, post-combustion and oxyfuel-combustion, which makes their application easy of processing and cost-effective.

Before this thesis work, a large number of novel CO<sub>2</sub> gas-adsorbent materials have been computationally and experimentally reported. However, these studies lacked a few crucial investigations such as atomic-level understanding of the adsorption mechanisms of CO<sub>2</sub>

confined within the interlayer of 2D nanosheets. Also, comprehensive analysis of CO<sub>2</sub> adsorption at various interlayer spacing of different multilayer structures comprising graphene-graphene and MoS<sub>2</sub>-MoS<sub>2</sub> bilayers as well as graphene-MoS<sub>2</sub> hybrids, and the effect of conformational anisotropy on adsorption and electronic properties is still limited. Further, despite the numerous investigations on gas molecules interaction with pristine [178, 179] and defective [160, 161] monolayer MoS<sub>2</sub>, there is no extensive study on the synergistic effect of nitrogen doping and vacancy defects engineering of MoS<sub>2</sub> monolayer for enhanced CO<sub>2</sub> adsorption activity. Selective performance of CO<sub>2</sub> on N-doped defective MoS<sub>2</sub> in presence of earth-abundant molecules such as H<sub>2</sub>O and N<sub>2</sub> were rarely given importance. In addition, a single S vacancy in MoS<sub>2</sub> monolayer reported study suggested that CO<sub>2</sub> tends to run away from the vicinity of single S vacancy defect of MoS<sub>2</sub> monolayer and can only be less attracted to the S vacant site. This is due to CO<sub>2</sub> molecule orientation and the effect of lateral interaction between the O of CO<sub>2</sub> pointing towards the S vacant site and the surface. Theoretical studies also showed that pristine graphene and MoS<sub>2</sub> monolayer are poor adsorbents for CO<sub>2</sub> irrespective of these sites. These limitations hinted at the potential use of proper molecule orientation and lateral spacing, and tailored modifications of the adsorbent surface for improvement in adsorption performance.

Some modification methods adopted include in-plane defects (substitutional, interstitial and vacancies cluster), covalent and non-covalent functionalization, intercalation and electrostatic tuning. These materials are investigated for gas storage both experimentally and computationally. This is particularly important for the rational design of new adsorbents scaled to meet the intended operating conditions. Based on the modification process, different reasons for improved sorption were obtained. In particular, experimental

CO<sub>2</sub> adsorption data are comparatively analysed for various graphene-based materials at various operating conditions. However, at elevated pressures, the adsorption capacity of graphene-based materials showed tremendous improvement. Nonetheless, this is still subject to further studies. Moreover, integrating graphene with other materials of good sorption capacity such as MoS<sub>2</sub>, improved the adsorption capacity of the graphene-based material. However, the modification of interlayer spacing and structural configuration during the synthesis route is the key to enhancing the adsorption performance of these nanocomposites. This is attainable given the improving successes in atomic-level studies and the combination of design of experiments like nanoparticle tracking analysis. Furthermore, an extensive study on N atom doped MoS<sub>2</sub> for CO<sub>2</sub> adsorptions will pave the way towards developing an engineered MoS<sub>2</sub> nanosheet with sufficient active sites for enhanced CO<sub>2</sub> adsorption capacity and catalytic activity. Additionally, insight on the effect of vacancy defect and molecular doping on the adsorption and dissociation of CO<sub>2</sub> and H<sub>2</sub>O over MoS<sub>2</sub> monolayer needs to be investigated computationally. This will be well suited for acquiring green and sustainable energy resources and will initiate several experimental studies. The knowledge gaps observed here were taken into consideration that eventually motivated the computational investigation of tailored nanostructures for enhanced and selective adsorption of CO<sub>2</sub>, which can catalytically activate CO<sub>2</sub> conversion and water splitting processes for a better catalysts design.

# CHAPTER 3

## Computational Methods

### 3.1 Overview of all Computational Methods

The optimal functioning of a gas adsorbent involves considerations from rational design standpoints to guide experimental design. Computational chemists are concerned with models, which mimic real chemical systems or reactions. Any successful model must ultimately find its basis in quantum mechanics and solve the Schrödinger equation (or Dirac equation in relativistic quantum chemistry) [180]. It is a well-known fact that the computational design of gas adsorbent materials at the atomistic level is based on the general quantum chemistry that applies quantum mechanics to address problems in chemistry. Quantum mechanics describes a system by a wave-function that completely characterizes all of the physical properties of the system [180]. In this thesis, we employ a range of computational chemistry tools, including DFT [181], GCMC, ab Initio Molecular Dynamics (AIMD), ab Initio thermodynamics method [182, 183], Infrared (IR) Spectroscopy and Climbing Image Nudged Elastic Band (CI-NEB) method [184] to investigate the adsorption properties of pristine and defective graphene and Molybdenum disulphide ( $\text{MoS}_2$ ) surfaces. In this chapter, a description of these methods is presented, with more focus on DFT, as this is the main method employed in this thesis. Furthermore, an attempt has been made to describe the rational design approaches that are employed to investigate the interactions between gas molecules and the host sorbents.



## 3.2 Electronic Structure Computational Methods

The governing interaction principles of electrons and atomic nuclei systems are electrostatic in nature. The Coulomb interaction, although simple in its form, becomes very complicated to handle already for a few particle ensembles and soon impossible to treat exactly with the current computational resources; thus approximations are called for. The ionic and electronic masses differ by a factor over three orders of magnitude so the ionic movement is much slower than the electronic and the nuclei are much more localized than the electronic wave function; therefore the nuclei move slowly in the instantaneous potential created by surrounding, more delocalized electrons[185]. With the advent of high-speed computers being readily available, electronic structure computations have become an important component of theoretical and experimental chemical research. Calculations may be performed on highly reactive molecules and transition states as reliably as on stable molecules. There are several commercially available software with excellent graphics that allow for excellent viewing of three-dimensional structure, electron densities, and dipole moments. Thermodynamic information such as heats of formation and strain energies can be readily obtained from such software. Reaction dynamics can also be obtained such as transition state structures. Electronic structure approximation methods include the following, the Born-Oppenheimer approximation,  $H_2^+$  Molecule approximation, Molecular Mechanics methods, ab initio and semi-Empirical Methods [180]. The underlying principle of these electronic structure computation methods is finding solutions to the fundamental equation that describes quantum behaviour of atoms and molecules, the Schrödinger equation, in settings of practical values; thus the total many-body wave function can be

factorized into one-electron (body) wave functions for ease of solving the Schrödinger equation.

Computational procedures exist which approach the exact result but are too demanding for all except few-atom systems; in the physics community the Quantum Monte Carlo (QMC) [186-189] and in the quantum chemistry community the Configuration Interaction (CI) [190, 191], which is used to accurately model the wave function and used within the wave method to solve the Schrödinger equation, have existed already for decades but still have their limitations. In the QMC method, the many-body electron wave function is probed stochastically and the physical observables are obtained as statistical averages. Different algorithms exist, of different accuracy: the Variational Monte Carlo (VMC), the Diffusion Monte Carlo (DMC) and the Green's Function Monte Carlo (GFMC). The so-called sign problem [192, 193] arises from the fermionic exclusion principle and makes the methodology much more difficult than for bosons. The quantum Monte Carlo algorithms have progressed in recent years in the speed for calculation [194-196], but are not broadly used for studies of realistic materials due to the higher complexity in the practical implementation than for instance, in the ab initio (first-principle) density functional calculations and thus making DFT the most used approach in physics and physical chemistry nowadays, which justifies the reason for using it in this work. Any successful model must ultimately find its basis in quantum mechanics and the starting point of any discussion of quantum mechanics is, of course, the Schrödinger.

### 3.2.1 The Schrödinger Equation

The mainspring of modern theoretical chemistry is the time-independent Schrödinger wave equation [197], which was proposed by Austrian physicist Erwin Schrödinger in 1926. It accounts for the quantum mechanical behaviour of atoms and molecules in mathematical form

$$\hat{H}\Psi_T = E\Psi \quad 3.1$$

Where  $\hat{H}$  is the Hamiltonian operator for the system,  $E$  is the energy of the system, and  $\Psi$  is the wavefunction or eigenfunction of an N-electron system that contains all its physical information.

The form of the molecular Hamiltonian is given by the sum of the nuclear and electronic kinetic energies,  $\hat{T}_N$  and  $\hat{T}_e$ , together with nuclei-nuclei repulsion,  $\hat{V}_{NN}$ , electron-nuclei attraction,  $\hat{V}_{eN}$ , and electron-electron repulsion,  $\hat{V}_{ee}$ , potential energies,

$$\hat{H} = \hat{T}_e + \hat{T}_N + \hat{V}_{NN} + \hat{V}_{eN} + \hat{V}_{ee} \quad 3.2$$

Which gives a full non-relativistic Hamiltonian in atomic units that can be written as

$$\hat{H} = - \sum_{i=1}^N \frac{1}{2} \nabla_i^2 - \sum_{A=1}^M \frac{1}{2M_A} \nabla_A^2 + \sum_{A=1}^M \sum_{B>A}^M \frac{Z_A Z_B}{R_{AB}} - \sum_{i=1}^N \sum_{A=1}^M \frac{Z_A}{r_{iA}} + \sum_{i=1}^N \sum_{j>i}^N \frac{1}{r_{ij}} \quad 3.3$$

$r_{ij}$ ,  $r_{iA}$ , and  $R_{AB}$ , represent the difference between the particles position vectors given as  $r_{iA} = |\mathbf{r}_i - \mathbf{R}_A|$ , and  $\mathbf{R}_A = (R_{Ax}, R_{Ay}, R_{Az})$ , the summations run over the N electrons and M nuclei of the system,  $Z_A$  and  $M_A$  are the respective nuclear charges and masses, and the Laplace operator,  $\nabla^2$ , can be defined in Cartesian coordinates by

$$\nabla^2 = \frac{\partial^2}{\partial x^2} + \frac{\partial^2}{\partial y^2} + \frac{\partial^2}{\partial z^2} \quad 3.4$$

### 3.2.2 Born-Oppenheimer Approximation

The molecular wavefunction,  $\Psi$ , is a complex mathematical function of the positions of all electrons and nuclei within a given system and in most cases is unknown. The Born-Oppenheimer approximation [198] allows de-coupling of the electronic and nuclear degrees of freedom in the electronic and nuclear structure problems based on the assumption that the electrons can respond to changes in the nuclear potentials instantaneously, and that the nuclei in a molecule are at stationary positions compared the electrons, hence,

$$E = E_{elec} + E_{nuc} \quad 3.5$$

Where

$$\Psi = \Psi_{elec} + \Psi_{nuc} \quad 3.6$$

Now the electronic degrees of freedom can be solved with the nuclei held fixed and electrons in the electronic wavefunction can be regarded as classical point charges. Therefore, the Hamiltonian operator ( $\hat{H}$ ) obtained after applying the Born-Oppenheimer approximation is the electronic Schrödinger equation which has only three terms: the kinetic energy of the electron ( $\hat{T}_e$ ), electron-electron ( $\hat{V}_{ee}$ ) and external field ( $\hat{V}_{ext}$ ) which accounts for electron-nucleus interactions

$$\hat{H} = \hat{T}_e + \hat{V}_{eN} + \hat{V}_{ext} \quad 3.7$$

The Born-Oppenheimer approximation is often a precise treatment but sometimes it notoriously fails for the nuclei of the light atoms, especially hydrogen. Despite these simplifications, the electron structure is a many-body problem, and thus still not exactly solvable in a reasonable time. Quantum chemistry is predominantly concerned with the solution of the electronic Hamiltonian. Therefore, techniques for calculating the electronic energy within this approximation is very important.

### 3.2.3 Hartree-Fock Theory

The fact that the molecular wavefunction,  $\Psi$ , depends on the coordinates of all the electrons in the molecule, Hartree proposed the separation of variables whereby the electronic wavefunction can be separated into a product of functions that depend only on one electron or orbital [199]. This made Hartree-Fock theory one of the simplest quantum chemical methods for solving the so-called electronic Schrödinger equation for many-electron systems. These orbitals are dependent on both spatial and spin components, although the majority of studies considered closed-shell systems that have electrons of opposite spin paired together with the same spatial components, hence we will exclusively consider it.

$$\psi^\uparrow(X) = \phi(r)\alpha(\omega) \quad 3.8$$

$$\psi^\downarrow(X) = \phi(r)\beta(\omega) \quad 3.9$$

Hartree-Fock theory can be summarized in full electronic wavefunction and may be expressed as

$$\Psi_H(r_1, r_2, r_3, \dots, r_N) = \phi_1(r_1)\phi_2(r_2)\phi_3(r_3) \dots \phi_N(r_N) \quad 3.10$$

Where the system contains N-electrons.

This wavefunction can be reformulated to reflect the Pauli principle by constructing it from Slater determinants as explained in the literature [200, 201]. The equations that arise in Hartree-Fock theory are solved in an iterative process that minimizes the energy, allowing an approximate wave function and electronic energy to be determined. However, an implicit assumption in Hartree-Fock theory is that electrons only see an averaged potential of the other electrons, which introduces a small error known as the correlation energy,  $E_C$

$$E_C = E_{exact} + E_{HF} \quad 3.11$$

Where  $E_{exact}$  is the exact non-relativistic energy within the basis set used and  $E_{HF}$  is the Hartree-Fock energy.

Despite accounting for around 1 % of the total energy, the correlation energy can be an important quantity correctly accounting for chemical behaviour. While several methods exist to go beyond the Hartree-Fock approximation and calculate the correlation energy using the wavefunction, the remaining chapters of this work will focus on the use of density functional theory (DFT) to account for electron correlation.

### **3.3 Overview on General Density Functional Theory**

DFT is one of the first-principle (also called *ab initio*) methods of obtaining an approximate solution to the Schrödinger equation of a many-body system. Consequently, DFT has become one of the most popular, powerful, versatile and successful quantum chemical/mechanical modelling methods. DFT has been found to accurately predict adsorption energies of adsorbent-adsorbate interactions by eliminating the issue of transferability and as such provided reaction schemes and models that are interesting

targets for experimental validation studies. DFT is commonly employed in practice to investigate the electronic, magnetic, structural and vibrational properties of molecules, materials and defects. It has practical utility and is highly valuable to most electronic structure calculations in quantum chemistry and condensed matter physics. It was formulated by Hohenberg, Kohn, and Sham and aims to describe the ground state properties of many-electron systems in terms of the electronic charge density. Its approaches accurately obtain directly the interactions between atoms by applying the principles of quantum mechanics to the electrons and nuclei, which eliminates the issue of transferability. It is being used for calculating the binding energy of molecules in chemistry and the electronic and phononic band structures of solids in physics. In the present thesis, DFT calculations are performed to investigate ground state electronic and structural properties of two-dimensional systems. Hence, the description of the method and an explanation of its features are necessary for the correct interpretation of the results obtained from band structure calculations.

### **3.3.1 Hohenberg-Kohn Theorems**

DFT fundamental principle lies in the principle of Hohenberg-Kohn theorem [202] in solving the so-called Schrödinger equation of the form of Eq. (3.1) using the electron density. The Hohenberg-Kohn Theorems of 1964 proved that the ground state electronic energy of any system is uniquely determined by a functional of the electron probability density which gives total energy ( $E[\rho]$ ) equation that has only three terms: the kinetic energy ( $T[\rho]$ ), electron-electron ( $E_{ee}[\rho]$ ) interaction energy and external field ( $E_{ext}[\rho]$ ) which accounts for electron-nuclei interaction energy,

$$E[\rho] = T[\rho] + E_{ee}[\rho] + E_{ext}[\rho] \quad 3.12$$

Where in atomic units

$$T[\rho] = -\frac{1}{2} \sum_i \nabla_i^2 \quad 3.13$$

And

$$E_{ee}[\rho] = \frac{1}{2} \iint \frac{\rho(r_1, r_2)}{r_{12}} dr_1 r_2 \quad 3.14$$

$$E_{ext}[\rho] = \langle \psi \left| \sum_{i=1}^n \phi(r_i) \right| \psi \rangle = \int \rho(r) \phi(r) dr \quad 3.15$$

The Hamiltonian within the Born-Oppenheimer is far simpler than the original, but still far too difficult to solve. The Hohenberg-Kohn theorem is one of the several methods to reduce Eq. (3.12) to an approximate but treatable form.

The conventional formulation of Hohenberg and Kohn theorems states that the total energy and other ground-state properties of a material are determined by its charge density ( $n(r)$ ) as an unknown functional. This means that the total ground state energy of a many-electron system is represented as a functional of the density. Therefore, knowing the electron density functional, the total energy of the system in terms of ion-electron potential energy, ion-ion potential energy, electron-electron energy and kinetic energy can be determined. Thus, each term of Eq. (3.12) can be written as a functional of  $n$

$$\Psi_H | \hat{H}[n] | \Psi_H = \Psi_H \left| T[n] + E_{ee}[n] + \sum_{i=1}^n \phi(r_i) \right| \Psi_H \quad 3.16$$



Hohenberg-Kohn theorems show that it is possible to use ground state density the physical properties of a system, however, it does not tell us how to calculate  $\hat{H}[n]$  from  $n$ . It also does not tell us how to find  $n$  without first finding the wavefunction. This difficulty is overcome by the Kohn-Sham equation, which leads to the discussion of the Kohn-Sham method [203].

### 3.3.2 Kohn-Sham Theorems

In an attempt to make additional progress, Kohn and Sham [203] introduced correlation energy as part of the total energy absent in the Hartree-Fock solution. They considered that the interacting electron density  $\rho(r)$ , could be constructed from a set of auxiliary non-interacting electron orbitals

$$\rho(r) = \sum_{i=1}^n \phi_i^*(r)\phi_i(r) \quad 3.17$$

They rewrote the total energy  $E = T + V$  by re-separating total energy functional into the following part

$$E[\rho] = T_S[\rho] + E_{ext}[\rho] + E_J[\rho] + E_{XC}[\rho] \quad 3.18$$

Where  $E_J$  and  $E_{ext}$  are similar to Eq. (3.14) and (3.15), respectively. The remaining unknown components of the density functional can then be collected into a single exchange-correlation term,  $E_{XC}[\rho]$  and the resulting energy expression in Eq. 1.31, can be solved using a Slater determinant and self-consistent method (SCF) procedure similar to Hartree-Fock theory [200, 201].

Kohn-Sham method represents an exact description of the ground-state properties of many-body systems. However, the exchange-correlation functional is unknown and demands further approximation. The accuracy of the electronic energy calculated in this way for a given basis set depends on how accurately the unknown terms for the exchange and correlation energies can be approximated. As DFT normally includes an approximation for the electron correlation energy missing from Hartree-Fock theory, DFT calculations can be highly accurate while having a comparable computational cost to a Hartree-Fock calculation. This has led to the development of a wide range of approximate exchange-correlation functionals, with various approximations leading to differing accuracies for different chemical problems. While many functionals are used in this work, they can loosely be grouped according to the types of information they contain as gradient-corrected and hybrid functionals.

### **3.3.3 Exchange-Correlation Energy/Functional**

The exchange-correlation energy has a purely quantum mechanical origin and can be defined as the interaction energy difference between a many-electron quantum system and its classical aspect. This is because electrons are indistinguishable particles that are known as fermions and therefore, when two particles exchange orbital states, there must be a sign change in the wave function describing an ensemble of the electrons. This antisymmetric in quantum always leads to an effective repulsion between electrons known as Pauli repulsion, which helps in lowering their total Coulomb energy.

As stated earlier,  $E_{xc}$  is very difficult to calculate and it represents a relatively small fraction of the total energy, but it is an extremely important quantity for all the physical aspects of materials and molecules because it acts directly on the bonding of atoms. The difficultness in calculating  $E_{xc}$  increases when it involves the n-electron system, which is quite often encountered. This is because; the exchange correlation functional of the many-body system (n-electron-system),  $E_{xc} [n]$  is unknown thus leading to its approximation in a practical sense. This is the only source of fundamental error in using DFT methods and depending on the approximation that is used the resulting approach may turn out to be valid or not for describing the systems and phenomena of interest.

There are many popular  $E_{xc} [n]$  approximations that are currently used in computational studies of Gas-Adsorbent Materials (GAM) but the most commonly used approximate functionals are those developed in the Local Density Approximations (LDA) [203] or Generalized Gradient Approximations (GGA) [204]. The LDA and GGA bring in a nonphysical electron self-interaction energy [205-209] which has been successful in cancelling the self-interaction energy between the different calculations that are combined into a property. Meanwhile, this error cancellation can no longer be relied upon when it comes to dealing with the prediction of relative energies of compounds with varying electronic environments that are significantly more challenging. Although, efforts have been made by several researchers to introduce advanced functionals that will mitigate the self-interaction error. However, the major problem lies in the relative degree of accuracy and computational expense associated with those DFT approaches [10] as shown in Figure 3.1.

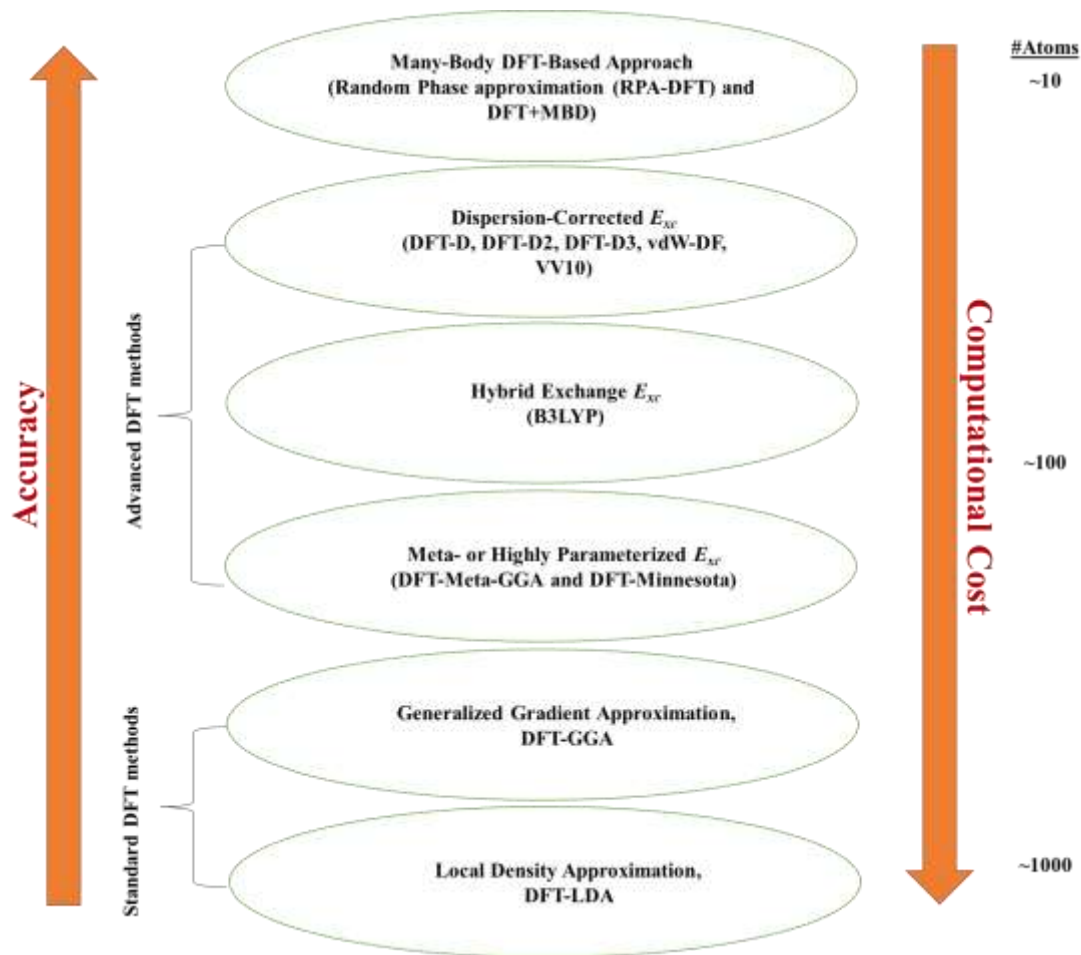


**Figure 3.1:** Representation of common levels of  $E_{xc}$  approximation within density functional theory together with some general features. Regions coloured in red indicate “High” and in blue “Low”. The typical size of the systems that can be handled with those approaches are indicated on the right margin of the figure.

### 3.4 DFT Calculation of Vibrational Frequency

Despite the very satisfying prediction of properties of a wide variety of interesting materials, in DFT calculations using improved exchange correlations functionals, there is a common issue about DFT calculations: namely, that it is a zero temperature approach. What is meant by this is that the calculations tell us about the properties of material in which the atoms

are localized at “equilibrium” or “minimum energy” positions. In classical mechanics, this corresponds to a description of a material at 0 K (zero-point energy (ZPE)). This criticism implies that it may be interesting to know about how materials would appear at 0 K, but real life happens at finite temperatures. This subsection aims to show how DFT calculations can give useful information about materials at nonzero temperatures. As a starting point, imagine a material that is cooled to 0 K. In the context of classical mechanics, the atoms in the material will relax to minimize the energy of the material. This will refer to the coordinates of the atoms in this state as the equilibrium positions. One of the simplest things that happen (again from a classical perspective) if the material is raised to a nonzero temperature is that the atoms in the material will vibrate about their equilibrium positions. From a more correct quantum mechanical perspective, the vibrations that are possible around an atom’s equilibrium position contribute to the material’s energy even at 0 K via zero-point energies. In many instances, these vibrations can be measured experimentally using spectroscopy, so the frequencies of vibrations are often of great interest. In this subsection, a look at how DFT calculations can be used to calculate vibrational frequencies is discussed briefly.

The vast majority of vibrational calculations are based on the harmonic approximation since to go beyond this approximation requires significantly greater sampling of the nuclear potential energy surface, and the calculations soon become prohibitively expensive as the number of atoms increases. Of the electronic structure methods available, DFT is potentially the most useful for the evaluation of nuclear force fields. This is because its relatively low computational cost makes accurate calculations possible for large systems, albeit with a wide choice of approximate exchange and correlation functionals [210].

In the harmonic approximation, the potential energy surface around an equilibrium structure is approximated by its second-order Taylor series with initial and equilibrium bond lengths ( $b$  and  $b_0$ ).

$$E = E_0 + \frac{1}{2}(b - b_0)^2 \left[ \frac{d^2E}{db^2} \right]_{b=b_0} \quad 3.19$$

Treating the nucleus of the atoms of the molecule AB ( $m_A$ ,  $m_B$ , the mass of atom A and B, respectively) following Newton's force law and a little algebra shows that the bond length oscillates with a characteristic vibrational frequency

$$\nu = \frac{\omega}{2\pi} = \frac{1}{2} \sqrt{\alpha \left( \frac{m_A + m_B}{m_a m_b} \right)} \quad 3.20$$

$$\alpha = \left[ \frac{d^2E}{db^2} \right]_{b=b_0} \quad 3.21$$

Using DFT, vibrational frequencies and normal modes can then be obtained simply by diagonalizing the mass-weighted Hessian matrix, which requires only the second derivatives of the energy with respect to the nuclear coordinates to be evaluated. While this model provides an effective general treatment of the vibrational structure, the specific anharmonicity in the fundamental frequencies is inherently ignored. Hence, an empirical linear frequency-scaling factor is introduced as a further correction. Unfortunately, plane-wave DFT calculations do not routinely evaluate an analytical expression for the second derivatives of the energy with respect to atomic positions. However, a good estimate of the second derivative can be obtained using a finite-difference approximation. Normally, for the 0.005–0.04 Å range of displacement, the calculated vibrational frequency is relatively insensitive to the value of finite-difference displacement. For larger and smaller

displacements, however, this situation changes markedly. In practice, it is a good idea to choose displacements that result in energy differences about 0.01–0.10 eV since these energy differences can be calculated accurately without requiring extraordinary care. For most materials, these energy differences correspond to finite-difference displacements in the range of 0.03–0.1 Å. As with any DFT calculation, it is wise to perform a series of calculations testing the consistency of your numerical results as a function of finite-difference displacements when you begin to examine the vibrational properties of new material (see **Chapters 5, 6 and 7**).

### 3.5 Ab Initio Molecular Dynamics (AIMD)

The basic concept of AIMD is that the natural use of DFT calculations might be to perform molecular dynamics (MD) by calculating total potential energy,  $U(r_1, \dots, r_{3N})$  with DFT. That is, the potential energy of the system of interest can be calculated “on the fly” using quantum mechanics, unlike in the classical MD that emphasized that the dynamics of atoms can be described if the potential energy,  $U(r_1, \dots, r_{3N})$  of the atoms is known as a function of the atomic coordinates. Hence, the Lagrangian for AMID approach can be written as

$$L = K - U = \frac{1}{2} \sum_{i=1}^{3N} m_i v_i^2 - E[\varphi(r_1, \dots, r_{3N})] \quad 3.22$$

Where  $K$  and  $U$  are the kinetic and potential energies,  $m_i$  and  $v_i$  and mass and velocities of each atom, respectively.  $\varphi(r_1, \dots, r_{3N})$ , represents the full set Kohn–Sham one-electron wave functions for the electronic ground state of the system. This Lagrangian suggests that calculations be done sequentially: first, the ground-state energy is calculated; then the

positions of the nuclei are advanced using one step of MD; then the new ground-state energy is calculated; and so on. We will refer to any method that advances the positions of nuclei along trajectories defined by classical mechanics from forces calculated from DFT as *ab initio* MD. Because of the limited size of time steps that can be taken with MD, finding methods to perform these calculations with great efficiency was extremely important for making them feasible for physically interesting problems. A key breakthrough that changed *ab initio* MD from simply an interesting idea to a powerful and useful method was made by Car and Parrinello. They introduced an algorithm in which the separate tasks of following the motion of nuclei and finding the electronic ground state given the nuclear positions are treated in a unified way through an extended Lagrangian. The central idea in this approach is to define equations of motion for both the nuclei and the electronic degrees of freedom that are simultaneously followed using molecular dynamics. Car and Parrinello's extended Lagrangian is cleverly constructed with nuclear equations of motion similar to Eq. (3.23) and the introduction of the electronic degrees of freedom as fictitious dynamical variables. Schematically, this extended Lagrangian is

$$L = \frac{1}{2} \sum_{i=1}^{3N} m_i v_i^2 - E[\varphi(r_1, \dots, r_{3N})] + \frac{1}{2} \sum_j 2\mu \int dr |\dot{\varphi}_j(r)|^2 + L_{ortho} \quad 3.23$$

The first two terms on the right-hand side are the same as in Eq. (3.22), while the last two terms introduce fictitious degrees of freedom. The third term that has the form of kinetic energy introduces a fictitious mass,  $\mu$ , while the final term above is required to keep the one-electron wave functions orthogonal. When the velocities associated with the dynamics based on Eq. (3.23) are used to assign a temperature and scaled to bring  $T \rightarrow 0$ , the equilibrium state of minimal  $E$  is reached and the Lagrangian describes a real physical



system on the potential energy surface. This method is referred to as Car–Parrinello molecular dynamics (CPMD). Because the nuclear and electronic degrees of freedom are propagated simultaneously during a CPMD calculation, the total energy that is calculated at each time step does not correspond exactly to the true Born–Oppenheimer potential energy surface for the nuclear coordinates. This idea is illustrated in **Figure 3.2**, which schematically shows the instantaneous electronic energy observed during a CPMD simulation. It is also important to realize that the dynamics of the electronic degrees of freedom during CPMD cannot be interpreted physically as the dynamics of electrons; the equations of motion for the electrons are merely a mathematical device to allow the dynamics of the nuclei to be generated in a numerically efficient way.

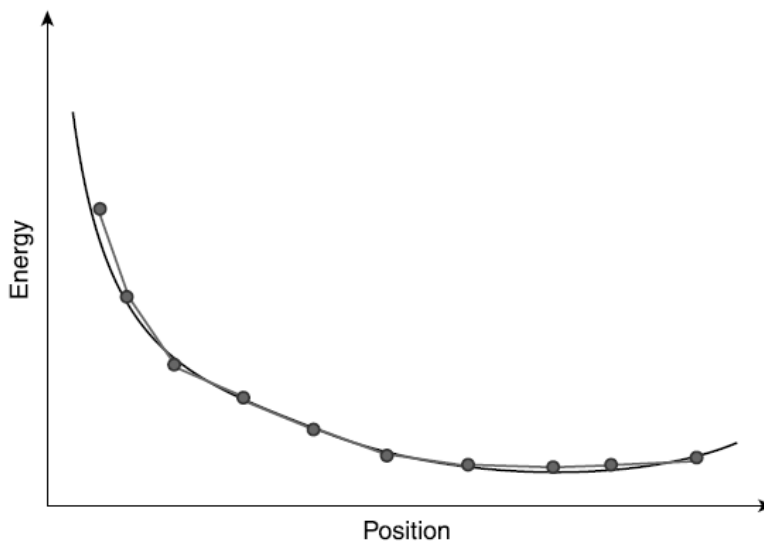


**Figure 3.2:** Schematic illustration of a CPMD trajectory along a single spatial coordinate. The smooth curve denotes the exact electronic ground state energy, while the symbols indicate the electronic energy calculated by the CPMD method at each time step of an MD simulation.

At the time it was introduced, the Car–Parrinello method was adopted for ab initio molecular dynamics as well as for determination of the Kohn–Sham ground state (because their technique was faster than contemporary methods for matrix diagonalization). This situation changed in the 1990s, as a variety of efficient numerical methods for solving the Kohn–Sham equations based on iterative linear algebra methods were developed and widely applied. When used appropriately, the electronic information from a previous MD step can provide a good initial approximation for the ground state of the updated nuclear positions, enabling the energy and forces for a new time step to be computed efficiently. MD methods based on this approach are often referred to as Born–Oppenheimer molecular dynamics (BOMD) because they directly explore the dynamics of nuclei on the Born–Oppenheimer potential energy surface. Although the extended Lagrangian approach of Car and Parrinello remains influential, calculations based on direct minimization of the Kohn–Sham equations at each time step are now more widely used. To conclude our brief overview of ab initio MD, we note that the dynamics defined by Eq. (3.22) define a microcanonical ensemble. That is, trajectories defined by this Lagrangian will conserve the total energy of the system. Similar to the situation for classical MD simulations, it is often more useful to calculate trajectories associated with dynamics at a constant temperature. One common and effective way to do this is to add additional terms to the Lagrangian so that calculations can be done in the canonical ensemble (constant  $N$ ,  $V$ , and  $T$ ) using the Nose–Hoover thermostat as demonstrated in **Chapters 6 and 7**.

## 3.6 Computational Methods

For this thesis, the DFT [181] implemented in Vienna ab initio simulation package (VASP) [211, 212] has been used for all calculations. The reason for this is that VASP uses periodic structures; hence, a plan-wave as a basis set for calculating the central quantities is the best choice as it is cheap. Also, it is known for its balanced computational efficiency and accuracy. In all calculations, the Projector Augmented Wave (PAW) [213, 214] potential as implemented in VASP is employed to describe the core-valance electron interaction of the atoms. This is largely due to its potentials in approximating the model of atomic-like core wavefunctions and actively calculating the valence electron states.

In all calculations, the Perdew, Burke and Ernzerhof (PBE) [215] version of the generalised gradient approximation is used to find the exchange correlation functional. In **Chapter 4**, different dispersion schemes are employed to understand the effects of vdW forces on the adsorption properties for pristine and modified surfaces. Firstly, we include Grimme's [216] DFT-D2 method, which adds a semi empirical pairwise force field to conventional DFT calculations. Then, we employ the vdW-DF functional of Langreth and Lundqvist et al, which adds a nonlocal correlation functional that approximately accounts for dispersion interaction [217-219]. The vdW-DFT methods with exchange-correlation energy given by revPBE [217], the opt functionals (optPBE and optB88) [220] for accurate exchange functionals for vdW correlation, and vdW-DF2 of Langreth and Lundqvist groups, [221, 222] are considered. In **Chapters 5-7** the simulation calculations are founded on spin-polarized DFT-D2 calculations using Grimme's [216] method. This calculation approach adds a semi-empirical pairwise force field to the conventional first-principles plane-wave

DFT calculations. This considers dispersion force, as it accurately describes the interactions for adsorption systems [223] from the benchmark study in **Chapter 4**.

In all cases, the test for cutoff energy and k-point grid is required for convergence. To achieve this, three denser  $\Gamma$ - centre meshes (5x5x1, 6x6x1 and 7x7x1) Monkhorst-Pack grids [224] k-point and cutoff energy (500, 600 and 700 eV) were tested for all the simulated systems. Finer k-points are used for sampling the Brillouin zone density of state calculations to ensure accurate prediction of the DOS of the semiconductors. The Gaussian smearing width was set to 0.2 eV. For geometry relaxation, we used the method of conjugate gradient energy minimization. The convergence criterion for energy is chosen to be  $10^{-6}$  eV between two consecutive steps, and the maximum Hellmann-Feynman force exerting on each atom is less than 0.01 eV/Å upon ionic relaxation. **Figure 3.3** summarises the simulation algorithm in VASP used for geometry relaxation and energy minimization. Using Bader charge analysis, charge transfer between molecules and the substrate is obtained [225]. All calculations are performed under the same relaxation criteria.

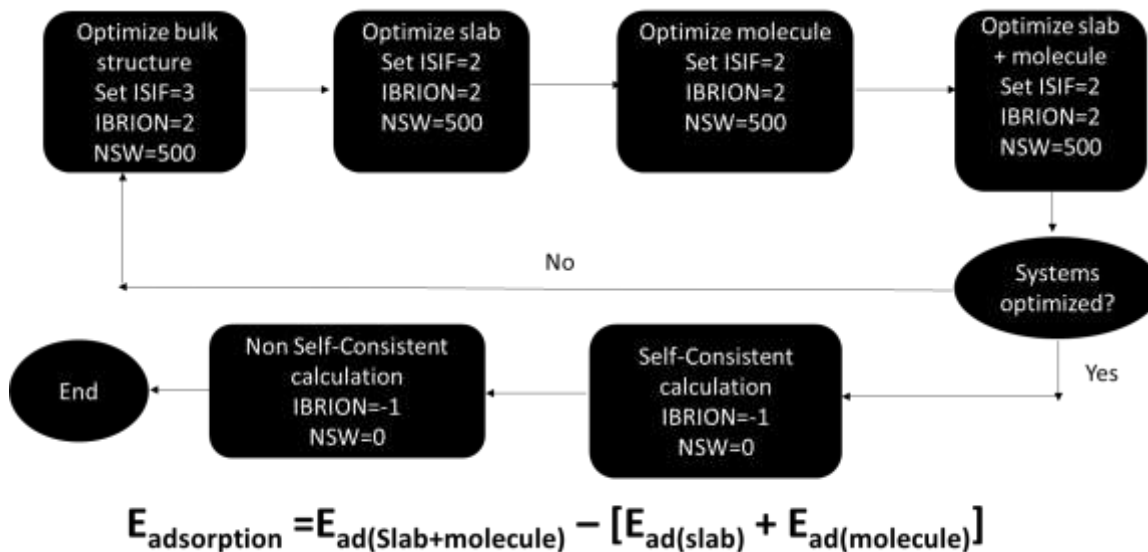


**Figure 3.3:** Schematic diagram for simulation algorithm in VASP.

Furthermore, Infrared (IR) spectroscopy was performed to probe the structure of the surface adsorbates in **Chapters 5 and 6**. Frequencies of phonon modes for the surface adsorbates have been calculated through the finite difference method using a displacement of 0.015, by fixing all the atoms of the surface. In **Chapter 6** the activation energies for the CO<sub>2</sub> reduction and water dissociation reactions on N doped defected MoS<sub>2</sub> surface were determined using the climbing image nudged elastic band (CI-NEB) methods [184]. Subsequently, Finite temperature effects were analysed through ab initio molecular dynamics (AIMD) to study the reactions. Also, using the ab initio thermodynamics method [182, 183], the thermodynamic stability of the considered most stable adsorption surfaces, when exposed to a given environment were analysed.

Finally, in **Chapter 7** First-principles and Classical GCMC Monte-Carlo simulations were carried out using VASP and RASPA 2.0 simulations, respectively, to understand and differentiate how Sulphur vacancy defects affect the adsorption of CO<sub>2</sub>, N<sub>2</sub>, H<sub>2</sub>, CH<sub>4</sub> and

H<sub>2</sub>O on MoS<sub>2</sub>. Classical GCMC Monte-Carlo simulations were performed to simulate adsorption isotherms between 0 – 100 bar for MoS<sub>2</sub> with and without single vacancy defects. Single-molecule NVT Monte-Carlo simulations were also carried out to visualize the strongest adsorption sites, which can be, compared to ab initio data.

### 3.7 Surface and Surface Simulation Models

To study the surface and molecules interactions, there is a need to summarize how to construct surface models within the context of periodic boundary condition electronic structure calculations, and which geometric structure quantities of surfaces are used in our analysis. Surfaces are generated when a bulk crystal is split. The created surface is the place where molecules from the gas phase or a liquid meet the material. Atoms at the surface will have lower coordination than those in the bulk. Because of the changed coordination, the surface geometry will relax or possibly even reconstruct to let surface atoms find their new equilibrium positions. There are two groups for ideal surfaces of cubic crystals, namely: low Miller index (flat) and high Miller index (stepped) surfaces. Low Miller index (flat) includes (100) and its equivalents ((010) and (001), (111) and (110)). Because graphene and MoS<sub>2</sub> have a crystal lattice easily described with Cartesian coordinates, we have used the (001) surface in this thesis as shown in **Figure 3.4**.

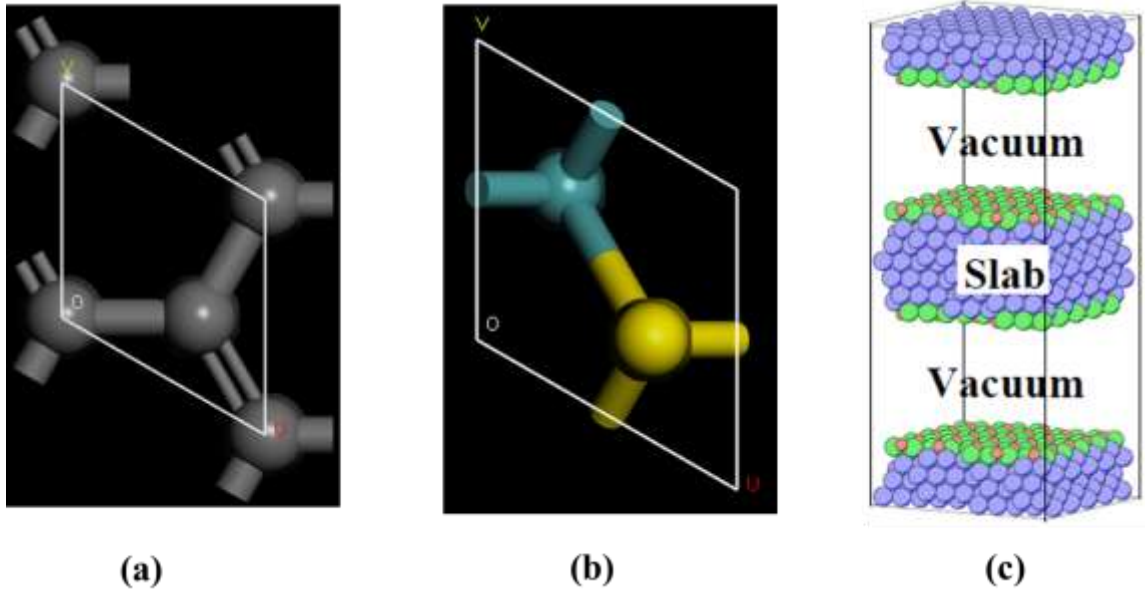


**Figure 3.4:** Top views of a (001) surface (a) graphene and (b) MoS<sub>2</sub>. (c) Supercell model, including slabs and vacuum.

About surface simulations, different models can be used, most notably the cluster model and the supercell model. Cluster models treat the surface as a small isolated cluster of atoms, one facet of which has the same symmetry and atomic arrangement. This model is useful for materials with more localized wavefunctions, such as insulators like MgO. For metal and semiconductor surfaces with more localized wavefunctions as the crystal surface intended to study, however, it is not suitable, and the supercell model (Figure 3.3c) including slabs and vacuum is more preferred. The slab in the supercell is infinite and periodic in the directions parallel to the surface, but finite in the direction perpendicular to the surface. Such a setup thus enables band formation with the correct dispersions. Two important things should be kept in mind using a supercell model: The vacuum thickness should be large enough to avoid surfaces of consecutive slabs seeing each other, and the thickness of the slab should be thick enough to avoid interaction between the two surfaces

of one slab. This normally also ensures that the middle layer of the slab exhibits bulk-like properties. In all calculations in this thesis, a large vacuum layer of 15 Å is used in the direction to the interface as an isolated slab boundary condition to avoid interlayer interactions. All calculations are performed with a simulation box of a periodic 4×4×1 supercell of monolayer MoS<sub>2</sub> containing (16 Mo atoms and 32 S atoms) and 5×5×1 supercell of monolayer graphene containing 50 C atoms for the monolayers as an initial computational model. The positions of all the atoms in the supercell were fully relaxed during structural optimization and were conducted for all the supercells with or without defects. In **Chapter 5**, the influences of different types of vacancies and level of N doping on the structural and electronic property of MoS<sub>2</sub> monolayer was investigated. In addition, how N doping and various types of vacancies govern the electron transfer rate, as well as the efficacy for CO<sub>2</sub> adsorption, were explored. **Figure 3.5** shows the vacancy defects and Nitrogen doping formation used in **Chapters 5 and 7**.

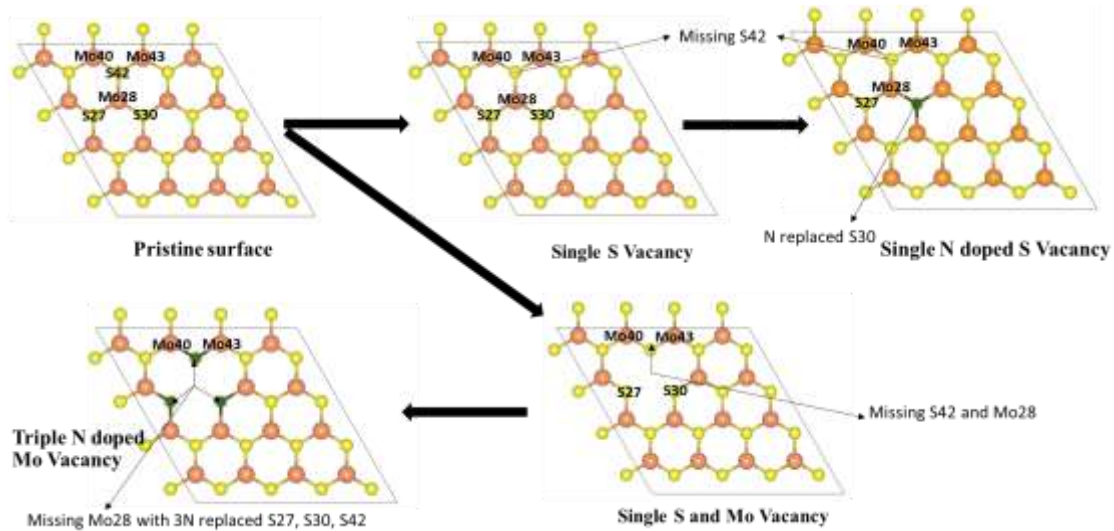


**Figure 3.5:** Vacancy defects and Nitrogen doping formation in MoS<sub>2</sub> monolayer.



## 3.8 Output from the Calculations

In this section, an effort is made to briefly explain the interpretation of the calculations in our analysis and what information can be won from the resulting output.

### 3.8.1 Lattice Parameter

The lattice constant is in principle the value that minimizes Gibbs's free energy but due to the exchange-correlation term, the theoretical lattice constant is not the same as from the experiments. Usually, the temperature and zero point (ZPE) effects are also not included; these would increase the lattice constant typically less than once per cent. In **Chapter 4**, the lattice constant of bulk and pristine graphene and MoS<sub>2</sub> sheets using a unit cell were calculated and compared with the literature to validate this method and its pseudopotentials.

### 3.8.2 Adsorption Energies

The binding energy of an adsorbate to a surface is not always uniquely determined, as its value depends on the energy reference. For instance, atoms that form strongly bound molecules can overcome the repulsion, which reigns between the adsorbed atoms and the surface. Hence, the value of binding energy obtained from calculations should account for a larger portion of the potential energy surface than only at the immediate vicinity of adsorption sites. The adsorption energy of CO<sub>2</sub> molecule on multilayer and monolayer structures in **Chapter 4** is calculated as:

$$E_{AE} = E_{Surf+CO_2} - (E_{surf} + E_{CO_2}) \quad (3.24)$$

Where  $E_{Surf+CO_2}$  is the total energy of the optimized structure with an adsorbed CO<sub>2</sub> molecule and  $E_{surf}$  and  $E_{CO_2}$  are the total energies of the pristine structure and isolated CO<sub>2</sub> molecule, respectively. A negative value of  $E_{AE}$  indicates that the adsorption is exothermic which means that, the adsorption of CO<sub>2</sub> molecules on the surface of the structures is favoured energetically.

Whereas, in **Chapter 5**, the binding energies of N atom(s),  $E_{bN}$ , on MoS<sub>2</sub> surface were calculated according to the reference [226].

$$E_{bN} = E_{N+MoS_2} - (E_N + E_{PMoS_2}) \quad (3.25)$$

where,  $E_{N+MoS_2}$  is the optimized total energy of the system N atom(s) + (4×4×1) supercell of MoS<sub>2</sub> monolayer (pristine MoS<sub>2</sub>),  $E_N$  is the ground-state energy of the free N atom(s) calculated in the same supercell with the same parameters and  $E_{PMoS_2}$  is the total energy of the (4×4×1) supercell of MoS<sub>2</sub> monolayer (pristine MoS<sub>2</sub>). A negative  $E_{bN}$  value indicates an exothermic process. The higher the value, the stronger the binding of the N atom(s) on the (4×4×1) supercell of the MoS<sub>2</sub> monolayer.

On the contrary, the binding energies of N atom(s) on the vacancy defect MoS<sub>2</sub> surface will be affected strongly by vacancy formation energy  $E_v$  and can be calculated using Eq. (3.26 and 3.27).

$$E_{bN} = (E_{N+MoS_2} - (E_N + E_{PMoS_2})) - E_v \quad (3.26)$$

$$E_v = E_x + E_{MoS_{2+x}} - E_{PMoS_2} \quad (3.27)$$

$E_v$  was calculated using the approach defined in Ref. [226]. That is, by subtracting the total energy of the pristine structure (without any vacancy) ( $E_{PMoS_2}$ ) from the sum of the total energy of a structure with a particular type of vacancy ( $E_{MoS_{2+x}}$ ) and the total energy (ies) of the removed atom ( $E_x$ , x is the removed atom, S or Mo). Negative  $E_v$  indicates stability. Similarly, the adsorption energy ( $E_{AE}$ ) of MoS<sub>2</sub> surfaces in this chapter is calculated using Eq. (3.24).

### 3.8.3 Density Difference

The density differences describe the charge transfer in the system upon a change in the atomic configuration. The change here comprises extraction or inclusion of atoms or molecules: the positions of the corresponding atoms in different calculations have to be the same, that is, they must not be relaxed except in one case and the coordinates to the other calculations are taken from the relaxed one. Generally, the system we are interested in is an adsorbate on a surface, and although we refer to the density difference as arising from the adsorption, the geometry is taken from the final state, that is, the adsorbed system. Thus, the density difference in this characteristic case would be obtained by the formula:

$$\Delta\rho = \rho_{mole+surf} - (\rho_{mole} + \rho_{surf}) \quad (3.28)$$

Where  $\rho_{mole+surf}$ ,  $\rho_{mole}$  and  $\rho_{surf}$  are the charge densities of non-interacting components (molecule and surfaces), isolated molecule and pure surface of the structures, respectively.

In **Chapter 5** the isosurfaces of the spin-charge density difference for the defective MoS<sub>2</sub> monolayer,  $\Delta\rho_s$ , was obtained using Eq. (3.29):

$$\Delta\rho_s = \Delta\rho_{N+MoS_2} - (\Delta\rho_N + \Delta\rho_{MoS_2}) \quad (3.29)$$

where  $\Delta\rho_N$  and  $\Delta\rho_{MoS_2}$  is the charge densities of the free N atom (s) and defect MoS<sub>2</sub> monolayer without N atom (s), respectively, and  $\Delta\rho_{N+MoS_2}$  is the total charge density of defect MoS<sub>2</sub> monolayer with N atom (s).

### **3.9 Summary and Conclusions**

In summary, this chapter detailed computational techniques such as DFT, molecular dynamics and grand canonical Monte Carlo. The new techniques that have been developed to computationally study adsorbent-adsorbate interactions at the atomistic level have been detailed. In conclusion, DFT is accurate, if we know how to derive necessary relations between density and energy. Unfortunately, energy functionals relating electronic density to energy are unknown, and there is no general way to improve them besides trying new ones and judging their quality by the results. However, DFT provides hope for an accurate method which scales with the fourth power of molecular size in the worst case, and possibly linearly for larger molecules [227].

## CHAPTER 4

# A Comparative Study of Mechanisms of the Adsorption of CO<sub>2</sub> Confined within Graphene-MoS<sub>2</sub> Nanosheets

### 4.1 Introduction

Results presented in this chapter focus on gaps in the literature discussed in **Chapter 2**. As mentioned in **Chapter 2**, an essential goal for carbon capture and storage technologies is identifying stable systems with improved CO<sub>2</sub> capture has become [228, 229]. One of the ways of improving CO<sub>2</sub> capture is using the space within the interlayer of 2-dimensional (2D) nanosheets, which have provided new and intriguing confinement environments for molecular interactions due to the nanoconfinement effect [172-175]. However, atomic-level understanding of the adsorption mechanisms of CO<sub>2</sub> confined within the interlayer of 2D nanosheets is still limited.

Motivation to carry out this present study stems from the impact of interlayer orientation on electronic properties and binding energy of substrate-grown monolayers [230, 231] and multi-layered structures of the same material [232]. Also, experiments have shown that combining Molybdenum disulphide (MoS<sub>2</sub>) and graphene provides tremendous active sites for molecule adsorption that could responsibly remove smoke particles, CO and other toxic volatiles [170]. Therefore, it is possible to attune structural parameters of these sites to facilitate CO<sub>2</sub> adsorption. Moreover, experimental and theoretical studies have shown that this nano-space presents new and extraordinary behaviours for molecular intercalations

[172] and catalytic activities [173-175]. In this chapter, the effect of interlayer distance between 2D materials, graphene/graphene (GrapheneB) and MoS<sub>2</sub>/MoS<sub>2</sub> (MoS<sub>2</sub>B) bilayers as well as graphene/MoS<sub>2</sub> (GMoS<sub>2</sub>) and MoS<sub>2</sub>/graphene (MoS<sub>2</sub>G) hybrids, on CO<sub>2</sub> adsorption mechanisms from first principles was investigated, to find the most stable conformation for CO<sub>2</sub> adsorptions. A comprehensive analysis of CO<sub>2</sub> adsorption energies ( $E_{AE}$ ) at a various interlayer spacing of different multilayer structures is performed to obtain the most stable adsorption configurations and the result is presented in **section 4.3.2**. The orientations and binding energies of CO<sub>2</sub> molecule on these surfaces are determined as well (**section 4.3.3**).

## 4.2 Computational Methods and Models

This section details all the calculation methods and the supercell models of the monolayer nanostructured used as CO<sub>2</sub> adsorbent materials. Additionally, the construction of the bilayer and hybrid structures utilizing the counterparts of each of the monolayers and addition of the lattice mismatch to impose a commensurability condition between the monolayers is discussed.

### 4.2.1 Computational Models

Calculations are performed with a  $4\times 4\times 1$  supercell of monolayer  $\text{MoS}_2$  (1H- $\text{MoS}_2$ ) containing (16 Mo atoms and 32 S atoms) and  $5\times 5\times 1$  supercell of monolayer graphene containing 50 C atoms for the monolayers. The  $\text{MoS}_2$  bilayer contains two  $4\times 4\times 1$  supercells of monolayer  $\text{MoS}_2$  (32 Mo atoms and 64 S atoms) while the graphene bilayer contains two  $5\times 5\times 1$  supercell monolayers of graphene (100 C atoms). For the hybrid structure, a supercell containing  $5\times 5\times 1$  lateral periodicity of graphene and  $4\times 4\times 1$  lateral periodicity of  $\text{MoS}_2$  monolayer (16 Mo atoms, 32 S atoms and 50 C atoms) were employed which includes 1.9% lattice mismatch [233] to impose a commensurability condition between the graphene and  $\text{MoS}_2$  monolayer. To illustrate the fundamental properties of graphene- $\text{MoS}_2$  hybrid, we chose a lateral lattice parameter for the triangular lattice  $a = 12.34 \text{ \AA}$  that was optimized for isolated graphene which is in agreement with graphene-based hybrid systems investigated previously [233] to ensure a smaller lattice mismatch. A large vacuum layer of  $15 \text{ \AA}$  is used in the direction to the interface as an isolated slab boundary condition to avoid interlayer interactions.

### 4.2.2 Computational Methods

All calculations are carried out using DFT as explained in Section 3.6 (Chapter 3). Valence electrons for Mo and S are generated in  $4p^6 5s^1 4d^5$  and  $3s^2 3p^4$  respectively, while valence electron for C is generated in  $2s^2 2p^2$ . Different dispersion schemes are employed to understand the effects of vdW forces on the adsorption of  $\text{CO}_2$ , which is detailed in Section 3.6 (Chapter 3). The test for cutoff energy and k-point grid is required for convergence. The Gaussian smearing width was set to 0.2 eV. The total energy was



converged to <10 meV for a plane-wave cutoff of 500 eV and 5×5×1 Monkhorst-Pack (MP) [224] k-point sampling for the Brillouin zone. Because of the large quasiparticle dynamics of graphene [234], the Brillouin zone sampling of electronic states was performed using a finer MP mesh with a size of 40×40×1 per unit cell. The tetrahedron method with Blöchl corrections for pure graphene monolayer and bilayer DOS was also adopted. Finer MP mesh and Fermi smearing width of 0 eV was used to ensuring accurate prediction of the DOS of semiconductors like graphene. For geometry relaxation, we used the method of conjugate gradient energy minimization. The convergence criterion for energy is chosen to be 10<sup>-4</sup> eV between two consecutive steps, and the maximum Hellmann-Feynman force exerting on each atom is less than 0.03 eV/Å upon ionic relaxation. Using Bader charge analysis, charge transfer between the substrate and the adsorbate is obtained [225].

The adsorption energy of CO<sub>2</sub> molecule on multilayer and monolayer structures are investigated. Adsorption energy is calculated as:

$$E_{AE} = E_{Surf+CO_2} - (E_{surf} + E_{CO_2}) \quad (4.1)$$

Where  $E_{Surf+CO_2}$  is the total energy of the optimized structure with an adsorbed CO<sub>2</sub> molecule and  $E_{surf}$  and  $E_{CO_2}$  are the total energies of the pristine structure and isolated CO<sub>2</sub> molecule respectively. A negative value of  $E_{AE}$  indicates that the adsorption is exothermic which means that, the adsorption of CO<sub>2</sub> molecule on the surface of the structures is favoured energetically.

## 4.3 Results and Discussion

This section discusses the CO<sub>2</sub> adsorption mechanisms results for monolayers, bilayers and hybrid structures. Firstly, the bulk structure parameters were calculated and the results were compared with previous studies. The result of the effect of interlayer spacing on CO<sub>2</sub> adsorption is also discussed, to find the most stable conformation for CO<sub>2</sub> adsorptions. Thereafter, the orientations and binding energies of CO<sub>2</sub> molecule on these surfaces are comparatively discussed in detail.

### 4.3.1 Bulk Structure Parameters

Graphene and MoS<sub>2</sub> have hexagonal structures consisting of C-C and S-Mo-S layers respectively. Bulk graphene has two layers and each layer known as a unit cell consists of a central carbon atom connected to three carbon atoms with an adjacent carbon atom on both sides of the layers. Bulk MoS<sub>2</sub> also has two such layers, with molybdenum (Mo) atoms of one layer directly above the sulphur (S) atoms of the other layer and vice versa. The lattice constant of pristine graphene and MoS<sub>2</sub> sheets using a unit cell was calculated and compared with to literature to validate this method and its pseudopotentials. Calculated values are 2.468 Å and 3.186 Å for graphene and MoS<sub>2</sub> respectively, which are in excellent agreement with previous theoretical results of 2.463 Å and 3.20 Å [235]. Based on this agreement, all other calculations were carried out, which are discussed in the subsequent sections.

### 4.3.2 Effects of Interlayer Distance on CO<sub>2</sub> Adsorption

To obtain a clear understanding of the effect of the multilayer structures on CO<sub>2</sub> adsorption, the adsorption energies of CO<sub>2</sub> ( $E_{AE}$ ) at various interlayer distances of multilayer structures comprising graphene/graphene bilayer (GrapheneB), MoS<sub>2</sub>/MoS<sub>2</sub> bilayer (MoS<sub>2</sub>B), graphene/MoS<sub>2</sub> hybrid (GMoS<sub>2</sub>) and MoS<sub>2</sub>/graphene (MoS<sub>2</sub>G) hybrid were computed and the results are reported in **Table 4.1**. At the start of each geometry optimization procedure, the CO<sub>2</sub> molecule is placed horizontally along the z-axis, at the middle distance between the two surface layers. This is assumed to avoid the repulsive effect between the electrons of the surface atoms and the lower oxygen atom of the CO<sub>2</sub> molecule. Such repulsive effect was commonly encountered in a configuration where the CO<sub>2</sub> molecule is perpendicularly oriented to the surface. This was one of the initial configurations proposed for CO<sub>2</sub> physisorption on pristine graphene [236] and defected (0001) graphene sheet [237].

As shown in **Table 4.1**, a more negative value means stronger CO<sub>2</sub> adsorption. The positive values at separations below 6.0 Å indicate that the spacing between layers is so small that overlapping with CO<sub>2</sub> occurred. Hence, energy is required to promote CO<sub>2</sub> adsorption. According to Ataca et al [235], an interlayer spacing of 6.145 Å was estimated via DFT to be suitable spacing for molecule interaction in MoS<sub>2</sub> interlayer. Below this, no adsorption (NA) will be observed, which corresponds to the results for MoS<sub>2</sub>B in **Table 4.1**. Similarly, the most-suitable interlayer distance that permits molecule adsorption in GrapheneB has been determined to be between 7 Å to 10 Å [83]. However, unlike MoS<sub>2</sub>B, energy is required to facilitate adsorption below this interlayer distance. This is attributed to the structural flexibility of graphene, in contrast to MoS<sub>2</sub>. Furthermore, it can be stipulated that

the required interlayer distance for CO<sub>2</sub> adsorption in GMoS<sub>2</sub> hybrid should be the sum of the equilibrium distance between GMoS<sub>2</sub> substrate and the kinetic diameter of CO<sub>2</sub> (3.30 Å [238]). The equilibrium distance between GMoS<sub>2</sub> substrate in different arrangements was measured to be around 3.32 Å [233, 239]. Hence, energy is demanded for CO<sub>2</sub> adsorption at interlayer distances less than 6.62 Å for the GMoS<sub>2</sub> hybrid. Considering the CO<sub>2</sub> molecule has a kinetic diameter of 3.30 Å [238], it is expected that CO<sub>2</sub> intercalation should enlarge the distance between the graphene sheet and MoS<sub>2</sub> surface and that of the bilayer surfaces. By expanding the vdW gap between the two sheets, a charge transfer between the guest and the host surface is expected to occur with a very large repulsive energy [240].

**Table 4.1:** Adsorption energies of CO<sub>2</sub> per carbon atom on different structures determined from different interlayered distance using PBE of GGA [215].

Interlayer Distance (Å)	Adsorption Energies E <sub>AE</sub> (meV)			
	<b>GMoS<sub>2</sub></b>	<b>MoS<sub>2</sub>G</b>	<b>MoS<sub>2</sub>B</b>	<b>GrapheneB</b>
3.5	237.20	27.98	(NA)	179.98
6.0	61.10	44.87	(NA)	67.54
7.0	-17.10	-9.01	-36.00	-10.50
7.5	-23.55	-24.00	-38.00	-32.00
8.5	-24.11	-25.09	-28.25	-17.15
9.5	-15.76	-15.45	-16.90	-12.99
10.5	-8.90	-9.00	-8.13	-4.57
11.5	-9.76	-6.28	-4.76	-1.03
12.5	-2.54	-1.84	-2.30	0.68
13.5	-0.49	-0.55	-1.36	1.17

NA: Not Adsorbed

**Figure 4.1** demonstrates the variation of interlayer spacing with CO<sub>2</sub> adsorption energies. This figure shows that 7.5 Å and 8.5 Å interlayer spacing is the most stable conformation for CO<sub>2</sub> adsorption on the bilayer and hybrid structures respectively. Also, as the interlayer distance increases, the CO<sub>2</sub> binding energy increases as well, but come to a local minimum at 7.5 Å and 8.5 Å for bilayer and hybrid structures respectively. It is estimated that GrapheneB has the least total adsorption capacity given the considered range of interlayer

distance. It can be assumed that the presence of MoS<sub>2</sub> in the hybrid buttressed CO<sub>2</sub> adsorption beyond interlayer spacing greater than 8.0 Å. The plot for the GMoS<sub>2</sub> hybrid structure is in good agreement with the work of Ma et al [233], although only graphene adhesion on MoS<sub>2</sub> was considered. The peak binding energies per C atom for GMoS<sub>2</sub>, MoS<sub>2</sub>G, MoS<sub>2</sub>B and GrapheneB are -24.11 meV, -25.09 meV, -38.00 meV and -32.00 meV respectively. Moreover, the adsorption energies of these multilayer structures seem to be a simple sum of the contributions from the constituents with decreasing binding energies in the order: MoS<sub>2</sub>B > GrapheneB > MoS<sub>2</sub>G > GMoS<sub>2</sub>. These values are low which correspond to the weak interaction between the layers and the CO<sub>2</sub> molecule. This is due to the inability of conventional DFT approaches to describe dispersion force in adsorption systems. These values were improved when factors like CO<sub>2</sub> orientation and the addition of vdW interactions between the CO<sub>2</sub> molecule and the surfaces were considered. Furthermore, two different configurations of the bilayer heterostructure were considered. This is to explain the effect of structural anisotropy on adsorption energies of heterostructures. In the first structure, graphene is the substrate (GMoS<sub>2</sub>) while in the second case MoS<sub>2</sub> is the substrate (MoS<sub>2</sub>G). Optimization results depict that there is a discrepancy in the binding energies of CO<sub>2</sub> adsorption on these hybrid structures (GMoS<sub>2</sub> and MoS<sub>2</sub>G). This can be ascribed to the modality of the atom arrangement (C-Mo-S-O and Mo-S-O-C) just like in the case of zigzag and armchair arrangement of bilayer graphene [232] and interlayer orientation effect on bilayer heterostructures. This indicates that conformational anisotropy of this structure determines to a certain degree its CO<sub>2</sub> adsorption energy. The most appropriate orientation of this hybrid for optimal adsorption performance is subject to further investigation.

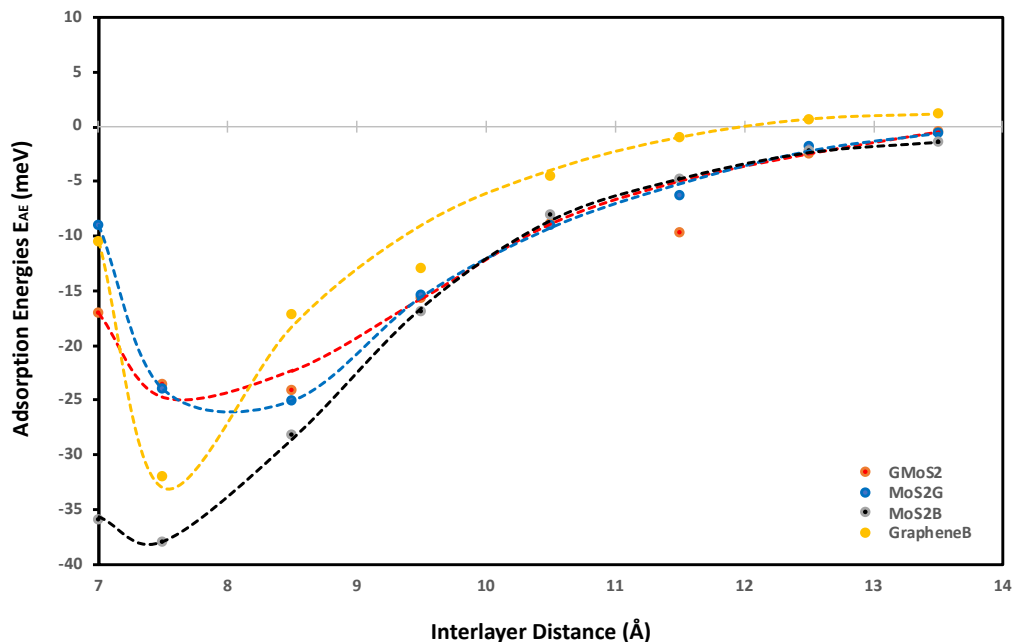


**Figure 4.1:** CO<sub>2</sub> adsorption energy as a function of interlayer distance. Adsorption energy as a function of the interlayer distance between the two monolayers for all the studied multilayer structures.

### 4.3.3 Effects of CO<sub>2</sub> Orientation and Position

To further understand the interaction of CO<sub>2</sub> within these multilayer structures, we calculated CO<sub>2</sub> adsorption energy at different CO<sub>2</sub> orientations and positions (see **Figure 4.2-4.4**) using the same optimum interlayer distance presented earlier. **Table 4.2** summarises the calculated adsorption energies per carbon atom for the most stable adsorption configuration of the multilayer structures in comparison with the most stable monolayers. In all calculations, CO<sub>2</sub> was placed at the mid-point of the interlayer distance for the multilayer structure and the same value was chosen for the monolayers for proper comparison. Also, since the test for cutoff energy and k-point grid is required for convergence, we calculated total energies using different cutoff and k-points and the result

is summarized in **Table 4.3-4.6**. The total energy was converged to <10 meV for a plane wave cutoff of 500 eV and  $5 \times 5 \times 1$  Monkhorst-Pack [224] k-point sampling for the Brillouin zone. The adsorption energies of the multilayer structures also seem to be a simple sum of the contributions from the constituents. The structures displayed low energies, which explains the difficulty of conventional DFT approaches to accurately reflect vdW force in the adsorption system. Our goal here is to gain insight into the surface most active site, which is the CO<sub>2</sub> adsorption energies with respect to its positions and orientation on the surface. From obtained results, it is evident that the CO<sub>2</sub> molecule prefers to interact with a parallel or inclined orientation with the adsorbent surface than the perpendicular orientation. For instance, considering the edge position of GrapheneB bilayer, the adsorption energy for parallel and 30° parallel-rotation are -27.05 and -23.62 meV respectively, but the value is -5.65 meV for the perpendicular attack of CO<sub>2</sub> at the same position. This is due to the repulsive effect between the electrons in C-atoms (graphene) and the lower O-atom (CO<sub>2</sub> molecule). Consequently, the molecule stays less bound to the surface compared to the optimum adsorption site. The same effect was addressed by Cabrera-Sanfeliix when CO<sub>2</sub> was placed initially perpendicular on defected graphene sheet [237]. CO<sub>2</sub> parallel attack at the edge position is observed to be the most favourite adsorption site for GMoS<sub>2</sub>, MoS<sub>2</sub>B and MoS<sub>2</sub>G composites with stable adsorption energies of -27.16, -40.37 and -27.07 meV respectively, while the centre position was the most favourable adsorption site for GrapheneB (-32.37 meV). GMoS<sub>2</sub> and MoS<sub>2</sub>G retained this position as its active site for CO<sub>2</sub> inclined (30° and 45° respectively) attack on the surface (**Figure 4.2**), in contrary to GrapheneB, which favoured centre position as the favourite adsorption site (**Figure 4.3**). These differences can be attributed to changes in the electronic



environment causing charge redistribution culminating in variation in adsorption capabilities. In addition, the adsorption capacity derived from the edge site of MoS<sub>2</sub> [241, 242] can contribute to these changes. For instance, MoS<sub>2</sub> monolayer (M4×4) favoured the edge position as the favourite adsorption site while graphene monolayer (G5×5) favoured the centre position as the favourite adsorption site (**Figure 4.4**). Therefore, it is expected that the edge position will be most favourite adsorption site for the GMoS<sub>2</sub> and MoS<sub>2</sub>G due to the inclusion of the MoS<sub>2</sub> layer, whose catalytic activity occurs at the edge sites. Also, since M4×4 has higher adsorption energy (-20.33 meV) than G5×5 (-16.38 meV), it is expected that M4×4 will determine to a certain extent the adsorption properties of the hybrid structures (GMoS<sub>2</sub> and MoS<sub>2</sub>G).

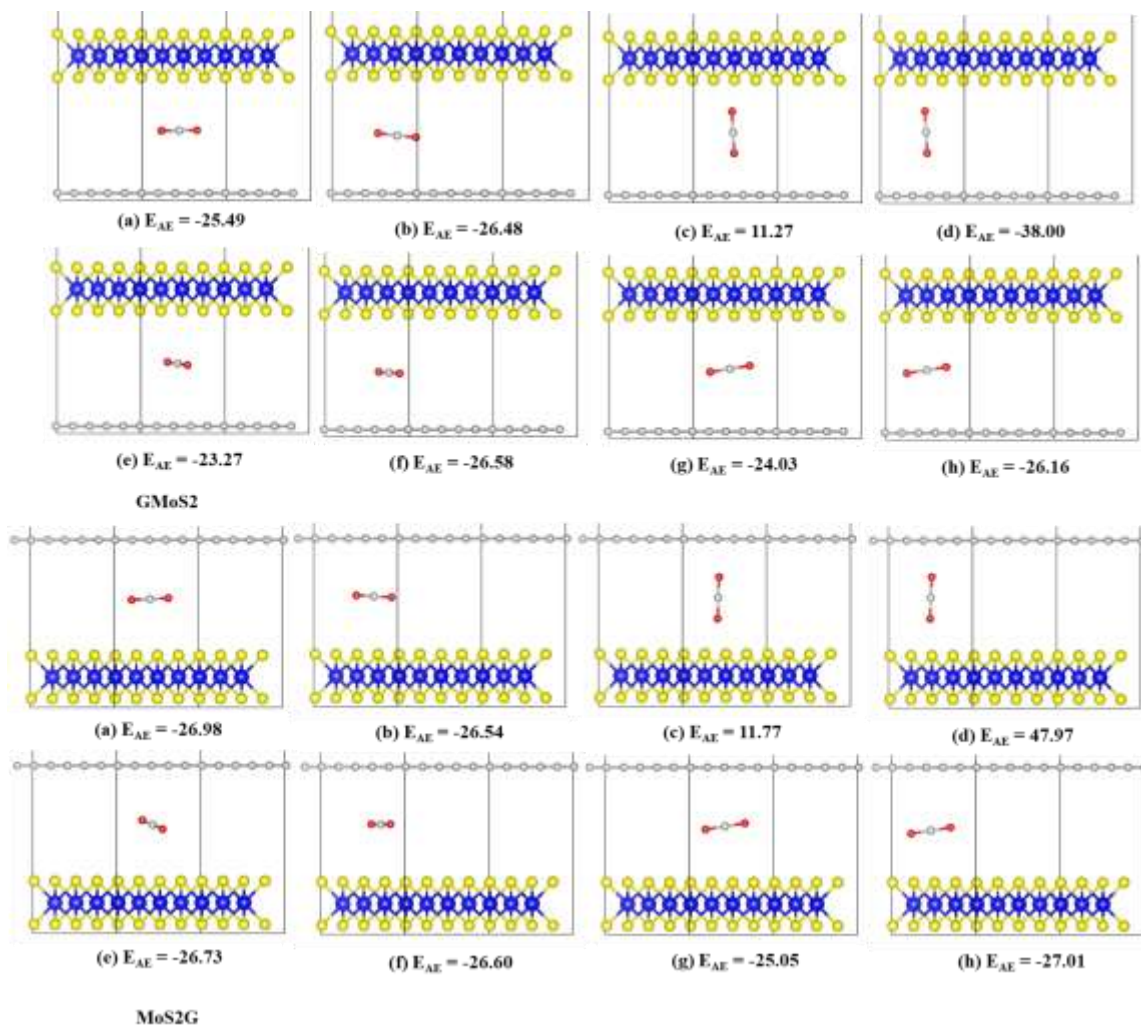


**Figure 4.2:** Relaxed geometric structures of CO<sub>2</sub> adsorption on possible initial graphene/MoS<sub>2</sub> (GMoS<sub>2</sub>) and MoS<sub>2</sub>/graphene (MoS<sub>2</sub>G) hybrid configurations. Position and orientation of CO<sub>2</sub> with respect to the surface are: (a) Centre/parallel, (b) Edge/parallel, (c) Centre/perpendicular, (d) Edge/perpendicular, (e) Centre/parallel (rotated 30°), (f) Edge/parallel (rotated 30°), (g) Centre/parallel (rotated 45°), and (h) Edge/parallel (rotated 45°). Energies are given in meV. Negative means heat release and blue, yellow, red and grey spheres depict Mo, S, O and C atoms, respectively.

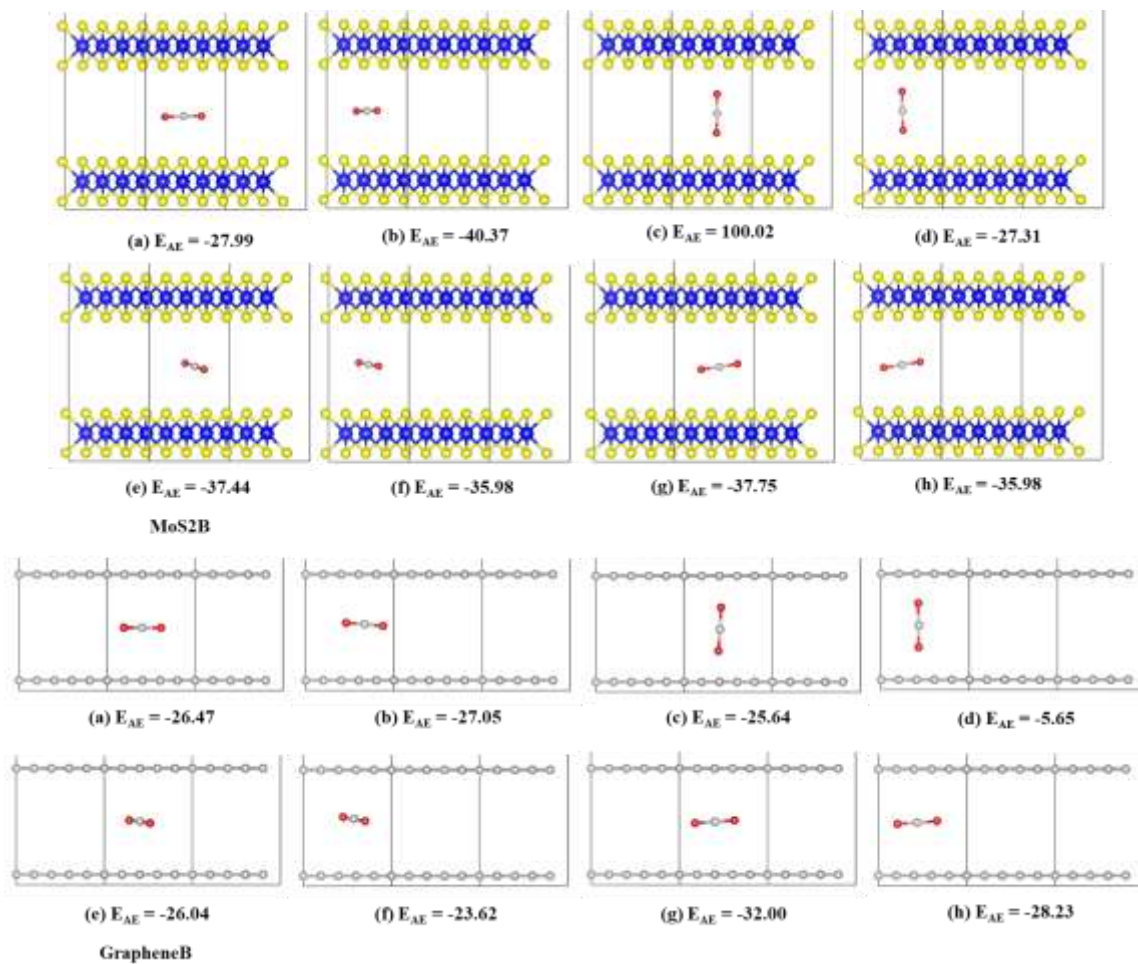


**Figure 4.3:** Relaxed geometric structures of CO<sub>2</sub> adsorption on possible initial bilayers of MoS<sub>2</sub> (MoS<sub>2</sub>B) and graphene (GrapheneB) configurations. Position and orientation of CO<sub>2</sub> with respect to the surface are: (a) Centre/parallel, (b) Edge/parallel, (c) Centre/perpendicular, (d) Edge/perpendicular, (e) Centre/parallel (rotated 30°), (f) Edge/parallel (rotated 30°), (g) Centre/parallel (rotated 45°), and (h) Edge/parallel (rotated 45°). Energies are given in meV. Negative means heat release and blue, yellow, red and grey spheres depict Mo, S, O and C atoms, respectively.

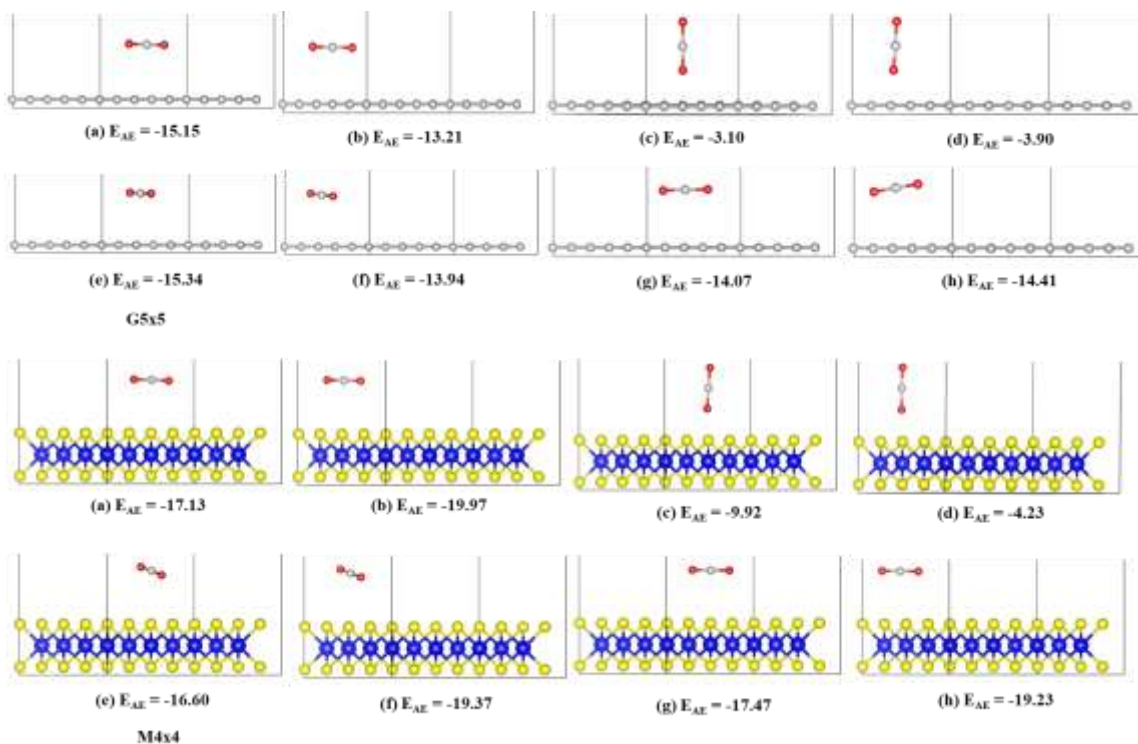


**Figure 4.4:** Relaxed geometric structures of CO<sub>2</sub> adsorption on possible initial monolayers of graphene (G5x5) and MoS<sub>2</sub> (M4x4) configurations. Position and orientation of CO<sub>2</sub> with respect to the surface are: (a) Centre/parallel, (b) Edge/parallel, (c) Centre/perpendicular, (d) Edge/perpendicular, (e) Centre/parallel (rotated 30°), (f) Edge/parallel (rotated 30°), (g) Centre/parallel (rotated 45°), and (h) Edge/parallel (rotated 45°). Energies are given in meV. Negative means heat release and blue, yellow, red and grey spheres depict Mo, S, O and C atoms, respectively.

**Table 4.2:** Adsorption energies of possible initial configurations of CO<sub>2</sub> adsorption on perfect multilayer and monolayer structures using PBE [215].

Position/Orientation to the Surface	Adsorption Energies $E_{AE}$ (meV)					
	GMoS <sub>2</sub>	MoS <sub>2</sub> G	MoS <sub>2</sub> B	GrapheneB	G5x5	M4x4
Centre/Parallel	-25.49	-26.98	-27.99	-26.47	-15.15	-17.13
Edge/Parallel	-26.48	-26.54	-40.37	-27.05	-13.21	-20.33
Centre/Perpendicular	11.27	11.77	100.02	-25.64	-3.10	-9.92
Edge/Perpendicular	38.00	47.97	-27.31	-5.65	-3.90	-4.23
Centre/Parallel (rotated 30°)	-23.27	-26.73	-37.44	-26.04	-16.38	-16.60
Edge/Parallel (rotated 30°)	-27.16	-26.60	-35.98	-23.62	-13.94	-19.37
Centre/Parallel (rotated 45°)	-24.03	-25.05	-37.75	-32.37	-14.07	-17.47
Edge/Parallel (rotated 45°)	-26.16	-27.07	-35.98	-28.23	-14.41	-19.23

G5×5 and M4×4 are 5×5 and 4×4 supercells of Graphene and MoS<sub>2</sub> monolayers respectively.

**Table 4.3:** Adsorption energies at EDDIF= $10^{-4}$  and EDDIG=-0.03, NSW=300, ENCUT=500,  $5 \times 5 \times 1$  KPOINT.

Structure	Adsorption Energies $E_{AE}$ (meV)
Edge/Parallel (rotated $30^\circ$ ) (6GMoS <sub>2</sub> )	-26.58
Edge/Parallel (rotated $45^\circ$ ) 7MoS <sub>2</sub> G	-27.01
Edge/Parallel (3MoS <sub>2</sub> )	-40.37
Centre/Parallel (rotated $45^\circ$ ) (8Graphene)	-32.00
Centre/Parallel (rotated $30^\circ$ ) (5G5x5)	-15.34
Edge/Parallel (3M4x4)	-19.97

**Table 4.4:** Adsorption energies at EDDIF= $10^{-6}$  and EDDIG=-0.01, NSW=500, ENCUT=500,  $5 \times 5 \times 1$  KPOINT.

Structure	Adsorption Energies $E_{AE}$ (meV)
Edge/Parallel (rotated $30^\circ$ ) (6GMoS <sub>2</sub> )	-26.44
Edge/Parallel (rotated $45^\circ$ ) 7MoS <sub>2</sub> G	-26.84
Edge/Parallel (3MoS <sub>2</sub> )	-39.85
Centre/Parallel (rotated $45^\circ$ ) (8Graphene)	-32.01
Centre/Parallel (rotated $30^\circ$ ) (5G5x5)	-15.35
Edge/Parallel (3M4x4)	-19.65

**Table 4.5:** Adsorption energies at  $EDDIF=10^{-6}$  and  $EDDIG=-0.03$ ,  $NSW=500$ ,  $ENCUT=600$ ,  $6 \times 6 \times 1$ .

Structure	Adsorption Energies $E_{AE}$ (meV)
Edge/Parallel (rotated $30^\circ$ ) (6G $MoS_2$ )	-27.16
Edge/Parallel (rotated $45^\circ$ ) 7Mo $S_2$ G	-27.07
Edge/Parallel (3Mo $S_2$ )	-39.59
Centre/Parallel (rotated $45^\circ$ ) (8Graphene)	-32.28
Centre/Parallel (rotated $30^\circ$ ) (5G $5 \times 5$ )	-15.53
Edge/Parallel (3M $4 \times 4$ )	-19.37

**Table 4.6:** Adsorption energies at  $EDDIF=10^{-6}$  and  $EDDIG=-0.03$ ,  $NSW=500$ ,  $ENCUT=700$ ,  $7 \times 7 \times 1$ .

Structure	Adsorption Energies $E_{AE}$ (meV)
Edge/Parallel (rotated $30^\circ$ ) (6G $MoS_2$ )	-27.14
Edge/Parallel (rotated $45^\circ$ ) 7Mo $S_2$ G	-27.61
Edge/Parallel (3Mo $S_2$ )	-39.63
Centre/Parallel (rotated $45^\circ$ ) (8Graphene)	-32.37
Centre/Parallel (rotated $30^\circ$ ) (5G $5 \times 5$ )	-16.38
Edge/Parallel (3M $4 \times 4$ )	-20.33

Improved adsorption energies were obtained when the dispersion correction to DFT is considered. To consider dispersion force, we carried out a spin-polarized calculation using different dispersion force methods and compared the results with conventional DFT approaches. The adsorption energies significantly improved by incorporating vdW interactions between the CO<sub>2</sub> molecule and the surfaces as shown in **Table 4.7**. However, there is no detailed experimental or computational data for CO<sub>2</sub> adsorption on hybrid and bilayer structures so far. Based on previous calculations of CO<sub>2</sub> adsorption on pristine monolayer graphene [236, 243] and MoS<sub>2</sub> [178], the results obtained using optPBE functional for the monolayers should be reliable. In addition, we find that CO<sub>2</sub> binds strongly to these multilayer structures. In fact, graphene bilayer gives the highest CO<sub>2</sub> adsorption energy among the multilayer structures when vdW-DF2 interactions are included, in contrast to conventional PBE results. This is contrary to the previous suggestion from conventional PBE results that the adsorption energy of the bilayers is approximately a simple sum of the contributions from the constituents. In addition, it is expected that the adsorption energy of CO<sub>2</sub> on perfect graphene and MoS<sub>2</sub> sheets to be lower because of the lack of dispersive interactions in DFT. Due to the addition of vdW interactions, there is a tendency for overestimation of molecule adsorption [68, 244]. For instance, vdW-DF2 correlation overestimates the adsorption energy of graphene bilayer, while revPBE and optPBE correlations overestimate the adsorption energy of MoS<sub>2</sub> bilayer. Furthermore, it is observed that CO<sub>2</sub> adsorption energies obtained when revPBE and optPBE correlations are included are similar. Likewise, there are similarities in the adsorption energies calculated using DFT-D2 and vdW-DF2 correlations except for the adsorption energy of bilayer graphene, which is overestimated, by vdW-DF2 correlation.



Also, the results of these correlations for the MoS<sub>2</sub> monolayer are in good agreement with the previous calculation [178]. On the other hand, the stronger binding between CO<sub>2</sub> and graphene monolayer when using DFT-D2 correlation is in agreement with reported values given for CO<sub>2</sub> adsorption on perfect monolayer graphene, ~147-151 meV [68, 244]. Generally, the increase in CO<sub>2</sub> adsorption energies with the introduction of vdW interactions indicates that vdW interaction dominates during the adsorption process. This is comparable with previous theoretical results that incorporated vdW interaction [178, 228].

**Table 4.7:** Comparison of adsorption energies ( $E_{AE}$ , meV) of CO<sub>2</sub> on bilayer, hybrid and monolayer structures determined from different methods.

Structures	This Work						Reference <sup>a</sup>	
	PBE	DFT-D2	revPBE	optPBE	optB88	vdW-DF2	PBE	DFT-D2
GMoS <sub>2</sub>	-27.16	-145.17	-321.73	-333.01	-242.13	-161.31	-	-
MoS <sub>2</sub> G	-27.07	-169.14	-300.47	-313.54	-254.74	-186.46	-	-
MoS <sub>2</sub> B	-40.37	-195.33	-1157.28	-1069.94	-829.09	-232.65	-	-
GrapheneB	-32.37	-241.34	-405.23	-450.26	-368.47	-1694.0	-	-
G5x5	-16.38	-153.30	-209.58	-249.98	-224.41	-160.21	-	-60 [228]
							17.10[236]	
M4x4	-20.33	-126.30	-201.25 (-210[178])	-232.40 (-253[178])	-204.50	-152.38	-4.00[178]	-139.0[178]

<sup>a</sup> The corresponding values of previous calculations for monolayer graphene and MoS<sub>2</sub> are given for the sake of comparison. The PBE adsorption energy of ref [178] for MoS<sub>2</sub> monolayer appears to be too small, this is because ref [178] did not consider CO<sub>2</sub> orientation, a similar value was obtained when we considered CO<sub>2</sub> orientation (**Table 4.2**). Similarly, the DFT-D2 adsorption energy of ref [228] for graphene monolayer is too small due to the same reason. But the revPBE and optPBE adsorption energies of the MoS<sub>2</sub> monolayer are in good agreement with the adsorption energy of ref [178].

#### 4.3.4 Structural Parameters

The optimized adsorption configuration of CO<sub>2</sub> on the most stable multi-layered structures determined by PBE calculations and the stacking type of the structures are shown in **Figure 4.5**. The bond length (C=O), angle of CO<sub>2</sub> molecule, interlayer distances, C=C, Mo=S bond lengths and the molecular distance are presented in this figure. To further understand the interaction between CO<sub>2</sub> and the surface, several structural parameters are calculated and compared with previous studies. Calculated bond length and angle for free CO<sub>2</sub> molecule are 1.177 Å and 179.87° respectively, which is in line with 1.16 Å and 180° from experiment [245], and 1.175 Å and 178° from previous theoretical calculation [236]. Based on experimental values, bond angles of adsorbed CO<sub>2</sub> decreased by about 0.05° - 0.13°, depending on the structures of the nanocomposite (**Table 4.8**). There is no chemical bonding observed, and interactions are dominated by weak vdW forces. In other words, the entire adsorption is purely physisorption due to small adsorption energy and large separation height (molecular distance). Moreover, only the stable configurations obtained from PBE calculations are presented. This is because the inclusion of vdW interactions slightly changes the stable configurations.

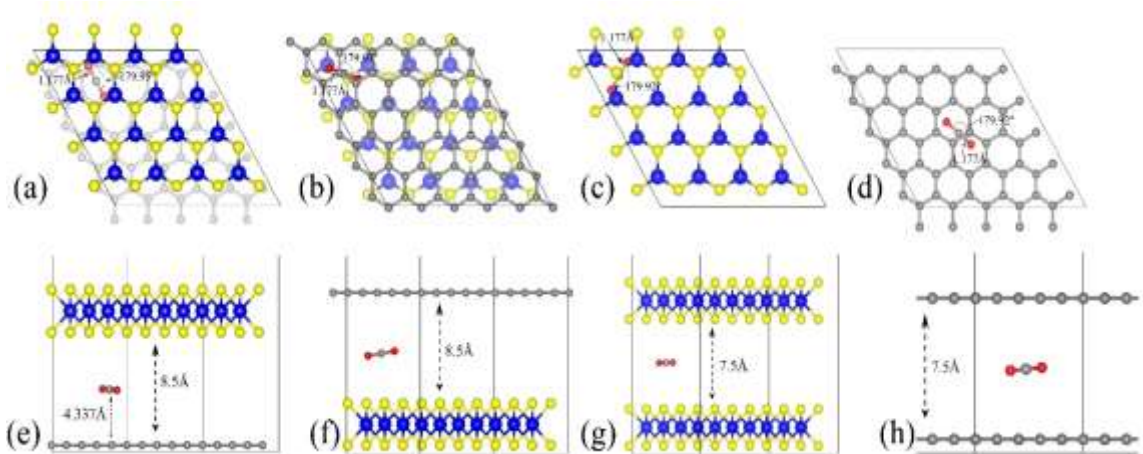


**Figure 4.5:** The most stable configuration of the multilayered structures with adsorbed CO<sub>2</sub>. (a-d) are the top views of GMoS<sub>2</sub>, MoS<sub>2</sub>G, MoS<sub>2</sub>B and GrapheneB and (e-f) are side views of the same structures respectively. Colour code: Mo, blue, S, yellow, C, grey, and O, red. The lines define the interlayer distances, bond lengths, molecular distance while the curved lines define the bond angle. AA stacking type is chosen for both MoS<sub>2</sub>B and GrapheneB. This is because AA stacking of graphene has shown to be more preferable for intercalation of molecules according to ref [246] and ref [247]. Although the binding energy of AB stacking of graphene bilayer is lower than AA stacking, which makes AB stacking more stable than AA stacking, but AA stacking intercalation structures are more favourable than AB stacking ones ref [247]. For the hybrid structures, the stacking type is chosen according to ref [239], where one C atom in the unit cell of graphene sits exactly below a Mo atom. It is reported by ref [233] that another configuration called TS, where the stacking is such that a C atom sits below an S atom, is equivalent in both the binding and electronic properties.

**Table 4.8:** Amount of charge transferred to CO<sub>2</sub> molecule (single atom and CO<sub>2</sub> molecule), amount of charge transferred from adjacent Mo, S and C atoms on the surface nearer to adsorbed CO<sub>2</sub> molecule, and the change in bond length and bond angle after CO<sub>2</sub> adsorption (length and angle, with angle change in parentheses)<sup>a</sup>

Structures	Amount of charge transferred (e)							Bond Length (Å)	Angle (deg)
	O1	C	O2	CO <sub>2</sub>	Mo	S	Cg	C=O	O=C=O
GMoS <sub>2</sub>	-0.001	-0.018	-0.009	-0.028	0.001	-0.002	-0.001	1.18	179.95 (0.05)
MoS <sub>2</sub> G	0.804	0.036	-0.030	0.810	0.000	0.000	-0.003	1.18	179.93 (0.07)
MoS <sub>2</sub> B	0.035	-0.033	0.015	0.017	0.000	0.000	N/A	1.18	179.92 (0.08)
GrapheneB	0.021	-0.012	-0.016	-0.007	N/A	N/A	-0.004	1.18	179.92 (0.08)
G5x5	0.001	0.020	-0.015	0.006	N/A	N/A	-0.004	1.18	179.89 (0.11)
M4x4	0.035	-0.047	0.002	-0.010	0.000	0.084	N/A	1.18	179.87 (0.13)

<sup>a</sup> Bader charge analysis is used for the charge transfer calculations. Cg is the adjacent carbon atom of graphene surface that is nearer to the adsorbed CO<sub>2</sub> molecule, while Mo and S are adjacent molybdenum and sulphur atoms of MoS<sub>2</sub> surface that are nearer to the adsorbed CO<sub>2</sub> molecule. The adjacent atoms were chosen arbitrary based on their proximity to the adsorbed CO<sub>2</sub> molecule. The negative charge denotes electron gain.

Bader charge analysis shows that the interaction between CO<sub>2</sub> and these surfaces causes charge transfer and redistributions (**Figure 4.6**). The amount of charge transferred from the Bader charge analysis is summarized in Table 4. It can be seen that while 0.028 e of charge is transferred to CO<sub>2</sub> in GMoS<sub>2</sub> surface where graphene is the bottommost layer, 0.810 e of charge is transferred from CO<sub>2</sub> to MoS<sub>2</sub> where MoS<sub>2</sub> is the topmost layer. This could indicate that the modality of the atom arrangement (C-Mo-S-O and Mo-S-O-C) in both structures affects the charge transfer between the molecule and surface atoms. In other words, the conformational anisotropy of this structure determines to a certain point the charge transfer and redistribution just like in its CO<sub>2</sub> adsorption energy. Meanwhile, in some cases, the adjacent S atom of MoS<sub>2</sub> and C atom of graphene nearer to the adsorbed CO<sub>2</sub> gain electrons, while the Mo atom loses an electron in all cases. This is because of the more electronegativity of S and C atoms compared to the Mo atom. **Figure 4.6** presents the charge density difference plots for CO<sub>2</sub> molecule-surfaces, obtained by the formula:

$$\Delta\rho = \rho_{mole+surf} - (\rho_{mole} + \rho_{surf}) \quad (4.2)$$

Where  $\rho_{mole+surf}$ ,  $\rho_{mole}$  and  $\rho_{surf}$  are the charge densities of non-interacting components (CO<sub>2</sub> and surfaces), isolated CO<sub>2</sub> molecule and pure surface of the structures, respectively.

The pink region shows the charge accumulation (electron excess) while the green region indicates the charge depletion (electron loss). In all the structures, it can be shown there is a noticeable polarization of the surfaces upon CO<sub>2</sub> adsorption, and electrostatics interaction plays a role in the attractive interaction. Moreover, there is charge accumulation on GMoS<sub>2</sub>, MoS<sub>2</sub>G, MoS<sub>2</sub>B, GrapheneB, G5×5 and M4×4 upon CO<sub>2</sub> adsorption, which suggests that

CO<sub>2</sub> also has a charge-donor characteristic. In addition, polarization in GrapheneB and MoS<sub>2</sub>B structures showed to be stronger than in MoS<sub>2</sub>G, G5×5, GMoS<sub>2</sub> and MoS<sub>2</sub> structures, which gives rise to larger adsorption energies. This explains why GrapheneB and MoS<sub>2</sub>B displayed larger adsorption energies (-241 and -195 meV, respectively) than the MoS<sub>2</sub>G, G5×5, GMoS<sub>2</sub> and MoS<sub>2</sub> (-169, -153, -145, and -126 meV, respectively) after spin-polarized DFT-D2 calculations mentioned earlier.

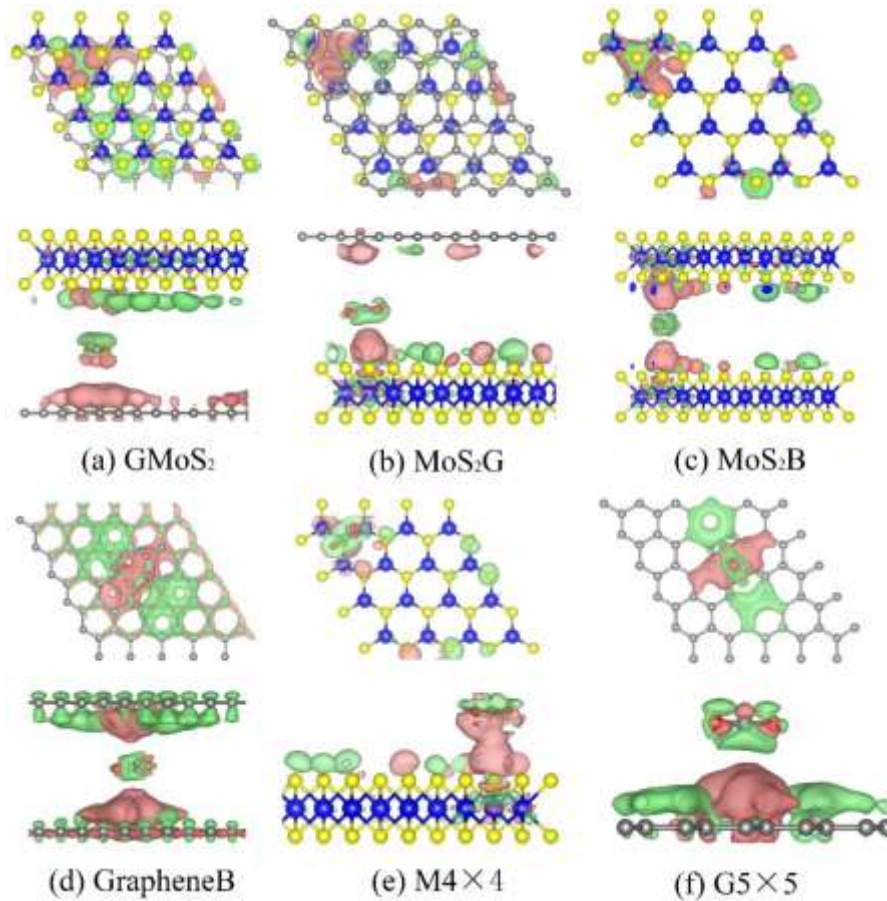


**Figure 4.6:** Top and side view of charge density difference plots for (a) Graphene/MoS<sub>2</sub> hybrid, (b) MoS<sub>2</sub>/Graphene hybrid, (c) MoS<sub>2</sub> bilayer, (d) graphene bilayer, (e) 4×4 supercell MoS<sub>2</sub> monolayer, and (f) 5×5 supercell graphene monolayer. The pink and green distribution correspond to charge accumulation (electron excess) and depletion (electron loss) respectively. Isosurfaces:  $\pm 5 \times 10^{-5} e^{-1} \text{Å}^3$ .

### 4.3.5 Density of States (DOS) Plots

To analyse the electronic properties of adsorbed CO<sub>2</sub> interaction on the multilayer structures, the total and projected electronic density of state (TDOS) and (PDOS) were studied for graphene and MoS<sub>2</sub> monolayer and bilayer surfaces before and after CO<sub>2</sub> adsorption. **Figure 4.7** and **Figure 4.8** shows that the DOS spectra for either valence or conduction band of the monolayers and bilayers surfaces do not have significant changes before and after adsorption. This indicates that the CO<sub>2</sub> interaction with these surfaces is purely physisorption, involving weak interaction forces such as vdW and Lewis acid-base interaction. Subsequently, this will not affect the electronic structure of surface atoms significantly. Although, it is observed that the adsorption of CO<sub>2</sub> introduces several distinct states at the lower-lying valence bands within the energy level of -22 eV to -25 eV, and offsets some peaks at the conduction bands within energy levels 2.5 – 5.0 eV. However, there is no noticeable modification of the DOS near the Fermi level, which also concludes that CO<sub>2</sub> physisorption does not have a substantial effect on the electronic properties of graphene and MoS<sub>2</sub>. DOS spectra of graphene (G5×5) and MoS<sub>2</sub> (M4×4) monolayer, bilayers (GrapheneB and MoS<sub>2</sub>B) and hybrid (GMoS<sub>2</sub> and MoS<sub>2</sub>G) structures were compared. It is observed that the DOS spectra of the monolayer and bilayer structures are nearly the same. MoS<sub>2</sub> (monolayer and bilayer) displayed a spectrum of an intrinsic semiconductor with a direct bandgap of 1.66 eV before and after CO<sub>2</sub> adsorption, which fairly correspond with both previous experimental (1.80 eV) and computational (1.58 eV) results obtained for pure MoS<sub>2</sub> monolayer, whereas graphene (monolayer and bilayer) exhibited a semi-metal spectrum with a small overlap between the valence and conduction band (zero bandgap material) [110, 226]. However, it is noted here that 5×5×1 K-point



mesh produced an un-converged sampling of Brillouin zone for pure graphene, and introduced small peaks around the Fermi level. This is attributed to the large quasiparticle dynamics of graphene [234], particularly at fewer K-point meshes like  $5 \times 5 \times 1$ . To correct this anomaly, a very fine K-point mesh without increasing the computational cost was proposed. Accordingly, a finer MP mesh of size  $40 \times 40 \times 1$  in the unit cell and the tetrahedron method with Blöchl corrections was used to reproduce the Brillouin zone sampling of electronic states. The  $40 \times 40 \times 1$  K-point mesh centred at  $\Gamma$  gave a faster convergence and accurately predicted the DOS of pure graphene. It also eliminated the small peaks around the Fermi level. As shown in **Figure 4.7**, the Dirac cone was obtained in pure graphene monolayer and bilayer, which is unaffected after  $\text{CO}_2$  adsorption. The plots are in good agreement with the work of ref [248], which tested different K-point meshes to generate DOS of graphene monolayer and bilayer structures. However, the DOS spectra of the bilayer heterostructure seem to be a simple sum of those of each constituent with a shift of the valence and conduction band. The conduction band shifted closer to the Fermi level, a characteristic of an n-type semiconductor. There is a noticeable modification of DOS spectra near the Fermi level, as the conduction band shifted closer to the Fermi level. This indicates a small bandgap opening due to the variation of on-site energy induced by  $\text{MoS}_2$  that is found in graphene/ $\text{MoS}_2$  bilayer heterostructures [233]. As shown in **Figure 4.7** (1 and 2), the calculated bandgap is 0.04 eV irrespective of the modality of the atom arrangement in both structures. This specifies that graphene monolayer in the heterostructure loses its metallic, with massless electrons characteristic and become more semiconducting with a direct narrow bandgap; while significantly increasing the conductivity of  $\text{MoS}_2$  monolayer. This is comparable with other hybrid structures [233]. It is also observed that the DOS spectra of the

hybrid structures are the same, which indicates that the conformational anisotropy does affect the DOS spectra bilayer heterostructures unlike in its CO<sub>2</sub> adsorption energy.

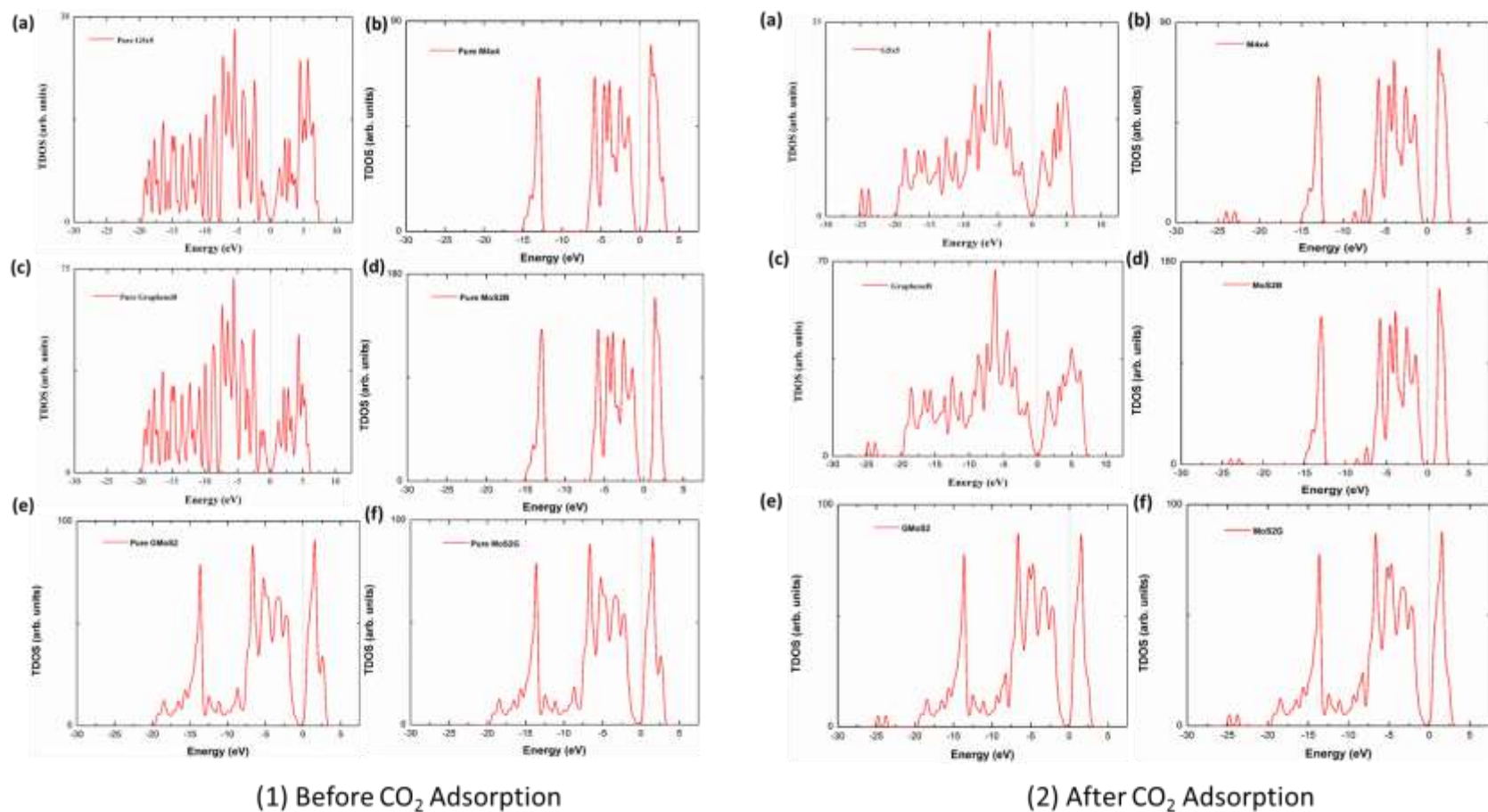


**Figure 4.7:** Total DOS spectra before (1) and after (2) CO<sub>2</sub> adsorption. (a) 5×5 supercell graphene monolayer, (b) 4×4 supercell MoS<sub>2</sub> monolayer, (c) graphene bilayer, (d) MoS<sub>2</sub> bilayer, (e) graphene/MoS<sub>2</sub> hybrid, and (f) MoS<sub>2</sub>/graphene hybrid. The dashed line represents the Fermi level.

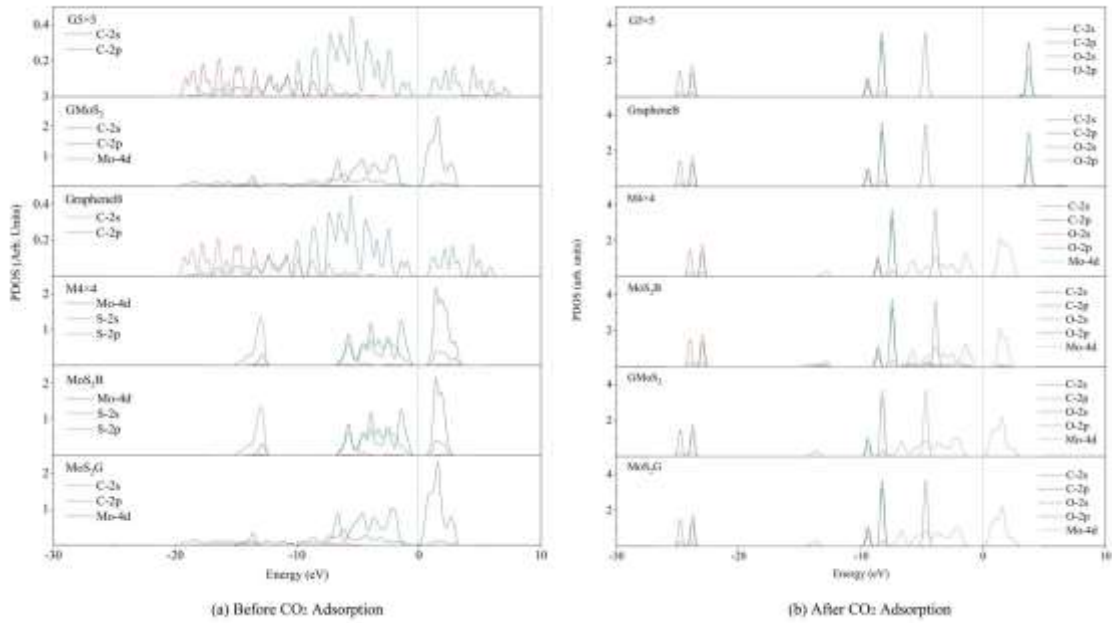


**Figure 4.8:** Projected DOS spectra before (a) and after (b) CO<sub>2</sub> adsorption. (G5×5) 5×5 supercell graphene monolayer, (M4×5) 4×4 supercell MoS<sub>2</sub> monolayer, (GrapheneB) graphene bilayer, (MoS<sub>2</sub>B) MoS<sub>2</sub> bilayer, (GMoS<sub>2</sub>) graphene/MoS<sub>2</sub> hybrid, and (MoS<sub>2</sub>G) MoS<sub>2</sub>/graphene hybrid. The dashed line represents the Fermi level.

## 4.4 Summary and Conclusions

In this chapter, a comprehensive first-principles study of CO<sub>2</sub> adsorption mechanism on graphene/graphene, MoS<sub>2</sub>/MoS<sub>2</sub> bilayers and graphene/MoS<sub>2</sub>, MoS<sub>2</sub>/graphene hybrids using GGA-PBE is presented. CO<sub>2</sub> adsorption energies, indicative of adsorption capacity, were calculated at various interlayer spacing. 7.5 Å and 8.5 Å interlayer spacing are the most stable conformation for CO<sub>2</sub> adsorption on the bilayer and hybrid structures respectively, with the bilayers displaying higher adsorption capacities. Beyond interlayer spacing of 8.0 Å, CO<sub>2</sub> adsorption was promoted by the presence of MoS<sub>2</sub> in the hybrid. However, this varied with the configuration of the bilayer structure. Moreover, the most active adsorption site was determined by varying CO<sub>2</sub> molecule orientations. A parallel CO<sub>2</sub> attack at the edge position of the surface exhibited the most adsorption energies. Parallely inclined orientations also showed promising adsorption potential, however, this varied in attack positions for each nanocomposite. The total electronic density of state analysis reveals that CO<sub>2</sub> interaction with these surfaces is purely physisorption, which mainly involves weak interaction forces. The Bader charge analysis indicates that there is charge transfer and redistribution between the substrate and the adsorbate. In addition, it was demonstrated that conformational anisotropy could affect CO<sub>2</sub> adsorption and other properties due to the modality of the atom arrangement (C-Mo-S-O and Mo-S-O-C) in both heterostructures.

In general, the modification of interlayer spacing and structural configuration during the synthesis route is the key to enhancing the adsorption performance of these nanocomposites. This is attainable given the improving successes in atomic-level studies

and the combination of design of experiments like nanoparticle tracking analysis. Finally, the incorporation of vdW interactions boosted the adsorption energies; thus, portraying the importance of doping and functionalization in improving the adsorption performance of these composites and the monolayer structures (**See Chapter 5**).

## CHAPTER 5

# Investigating N-Doping Enabled Defect-Engineering of MoS<sub>2</sub> for Enhanced and Selective Adsorption of CO<sub>2</sub>

### 5.1 Introduction

The previous chapter detailed an excellent CO<sub>2</sub> adsorption performance on pristine monolayer graphene and MoS<sub>2</sub> when different dispersion schemes are employed. However, in a bid to mitigate global climate change caused by anthropogenic CO<sub>2</sub> emission [24], there is a need to continue with the quest to develop highly effective capture materials that can overcome the cost implications of existing capture technologies [9]. It was realized from a recent literature review regarding the growing efforts in utilizing the two-dimensional (2D) transition-metal dichalcogenides (TMD) as they involve a comparatively simple molecular combination and can be fine-tuned to improve its sensing performance towards analyt gas [249-251]. Additionally, TMDs are innately suitable for electronic applications because of low power consumption and have extraordinary physical, optical and electrical properties like maximum surface to mass ratio, low noise, high sensitivity and increased selectivity [13]. In spite of numerous reports available in context to pristine TMDs based CO<sub>2</sub> adsorbent materials; there is a sparse number of reports regarding the development of CO<sub>2</sub> sensitive materials, which are extremely selective, stable and sensitive. Monolayer molybdenum disulphide (MoS<sub>2</sub>) is one of the two-dimensional (2D) transition-metal dichalcogenides (TMD) that have been the focus of considerable interest over the

past two decades [108] due to much success in applications in electronics, energy storage, sensing, and photoluminescence [109]. As in the well-studied cases of graphene and graphene oxide (GO) [252-256], the high surface to volume ratio of mono and a few layers of TMD can be exploited for gas sensing applications. Detection of CO<sub>2</sub> using highly reduced GO flakes has been shown to be effective as the low adsorption strength of CO<sub>2</sub> on GO flakes surface results in easy desorption of gas molecules without light assistance [257]. Unlike graphene which has a zero bandgap, MoS<sub>2</sub> is a semiconductor with a bandgap ranging from 1.2 eV (indirect) in bulk [19] to 1.9 eV (direct) in monolayer [110]. This change in band gap gives rise to the novel photoluminescence and electronic properties of the MoS<sub>2</sub> monolayer and might unlock the potential of this material as a gas sensor and as an alternative material for CO<sub>2</sub> capture.

Calculations based on density functional theory (DFT), show that pollutant gases such as NO<sub>2</sub>, NO and SO<sub>2</sub>, can strongly interact with MoS<sub>2</sub> surfaces owing to the charge transfer mechanism between gas molecules and MoS<sub>2</sub>, which explains its gas sensing properties [258, 259]. DFT calculations also show that MoS<sub>2</sub> adsorbs H<sub>2</sub> molecules, which prefer to bind with the S atoms of the monolayer thus enhancing its conductivity [260]. For non-polar gas molecules, like CO<sub>2</sub> and CH<sub>4</sub>, the perfect MoS<sub>2</sub> surface cannot offer strong adsorbing sites, and the presence of defects, especially S vacancies, is essential to result in the possibility for these molecules to adsorb on MoS<sub>2</sub> [20]. Another important feature is the large surface area created when the bulk is thinned into layers, with the surface area of exfoliated MoS<sub>2</sub> flakes having a high density of edges which are potential active sites for electrochemical applications in sensing and energy storage, in particular for CO<sub>2</sub> storage



[108, 109]. As the edge sites of MoS<sub>2</sub> flakes are more reactive than the surface, the orientation of the flakes can be used to tune their response to target specific gases.

To date, numerous strategies have been employed for the fine-tuning of the physical and chemical properties of MoS<sub>2</sub> and other TMD materials [16-19]. Both experimental and theoretical studies have been used to investigate point defects in the MoS<sub>2</sub> monolayer [159, 160]. These studies have revealed that point defects are usually more reactive than the sites present on a perfect surface. The single sulphur vacancy (S-vacancy) point defect is more easily formed than anti-site defects [159] and the edge is usually less stable and more prone to doping [161]. The results showed that the defective MoS<sub>2</sub> surface improved the adsorption strength and catalytic activity of the MoS<sub>2</sub> layer [160, 161].

An alternative way to improve CO<sub>2</sub> uptake capacity is to create basic or redox-active surface sites by incorporating nitrogen into the surface framework, which manipulates its conductivity and charge density [19, 22, 23]. This promotes the transfer of electrons between the surface and CO<sub>2</sub>, therefore enhancing the energy storage activities [162]. A recent DFT study proposed that nitrogen doping in monolayer MoS<sub>2</sub> leads to a high electronic state density around the N and Mo atoms and therefore enhancing its electronic conductivity [19]. The synergistic effect of molecular doping and vacancy defects may further enhance the CO<sub>2</sub> adsorption activity of MoS<sub>2</sub>. However, despite the numerous investigations on molecules interacting with pristine [178, 179] and defective [160, 161] monolayer MoS<sub>2</sub>, there has not been an extensive study on CO<sub>2</sub> adsorption on N atom doped MoS<sub>2</sub>, which has the potential to pave the way towards developing an engineered MoS<sub>2</sub> nanosheet with sufficient active sites for enhanced CO<sub>2</sub> adsorption capacity.

In this chapter, a fundamental understanding of exploiting nitrogen doping (N-doping) for the preparation of defect-rich MoS<sub>2</sub> with enhanced CO<sub>2</sub> adsorption capacity is presented. The first-principles DFT study was carried out to investigate CO<sub>2</sub> adsorption on defect-free monolayer MoS<sub>2</sub> as well as MoS<sub>2</sub> surface with different types of vacancies (single and double vacancies) with and without N-doping. The influence of different types of vacancies and levels of N-doping on the structural and electronic properties of the MoS<sub>2</sub> monolayer was investigated. In addition, how N-doping and various types of vacancies govern the electron transfer rate, as well as the efficacy for CO<sub>2</sub> adsorption, were explored. Infrared (IR) spectroscopy was also performed to probe the structure of the surface adsorbates. The adsorption of nitrogen and water molecules was investigated to ascertain the selective adsorption of CO<sub>2</sub>.

## **5.2 Computational Methods and Models**

This section details the simulation models and methods employed to obtain the single and double vacancies as well as non-defective MoS<sub>2</sub> planes and their decoration with N atoms by substitution route to form N-doped MoS<sub>2</sub> systems in different types. The binding energy of the N atom(s) on the MoS<sub>2</sub> surface and adsorption energy as well as other calculation details are also discussed.

### **5.2.1 Computational Models**

A simulation box of a periodic (4×4×1) supercell of the MoS<sub>2</sub> monolayer (PMoS<sub>2</sub>) previously used in Section 4.2.1 (Chapter 4) is used as an initial computational model.

The lateral value of the box is  $12.76 \text{ \AA} \times 12.76 \text{ \AA}$  [261]. A large vacuum layer of  $15 \text{ \AA}$  in the direction to the interface is used as an isolated slab boundary condition to avoid interlayer interactions. The positions of all the atoms in the supercell were fully relaxed during structural optimization for all the supercells with or without defects.

In order to simulate the vacancy defect MoS<sub>2</sub> systems, one or two adjacent Mo or S atoms were removed to create a stable single or double vacancy-defected MoS<sub>2</sub> (**Figure 5.1**) consistent with the literature [226]. Also, Mo or S atoms were substituted with N atom (s) to simulate N-doped MoS<sub>2</sub> defect complex systems as shown in **Figure 5.1**. Also, 10 different simulation boxes consisting of non-defective and defective periodic (4×4×1) supercell of MoS<sub>2</sub> monolayer, starting with pristine MoS<sub>2</sub> (PMoS<sub>2</sub>) are investigated. Five different N substitutional alone systems are created by substituting S, Mo, or S and Mo atoms with N atom (s). First, one, two or three S atoms are replaced by a corresponding number of N atoms to form single S (MoS<sub>2</sub>\_1N<sub>S</sub>), double S (MoS<sub>2</sub>\_2N<sub>S</sub>) or triple S (MoS<sub>2</sub>\_3N<sub>S</sub>) N substitutional sites, respectively. A Mo atom is substituted by an N atom to create single Mo (MoS<sub>2</sub>\_1N<sub>Mo</sub>) N substitutional sites. In addition, Mo and S atoms are replaced by two N atoms to form a MoS double (MoS<sub>2</sub>\_1N<sub>Mo</sub>\_1N<sub>S</sub>) N substitutional site. Subsequently, S single (MoS<sub>2</sub>\_1V<sub>S</sub>) or MoS double (MoS<sub>2</sub>\_1V<sub>Mo</sub>\_1V<sub>S</sub>) vacancy is created by removing one S or adjacent Mo and S atoms from the supercell. Finally, we create N substitutional S or Mo vacancy defect complex, namely S and Mo sites. S sites are created by substituting one S atom in a single S vacancy with an N atom (MoS<sub>2</sub>\_1V<sub>S</sub>\_1N<sub>S</sub>). It is worth mentioning that Mo vacancy (single and double) and double S vacancies are not considered in this study. A theoretical study has shown that 1 Mo-vacancy is not an active site for CO<sub>2</sub> molecule and double S vacancy bears close semblance to 1 S-vacancy in terms

of CO<sub>2</sub> adsorption [18]. The Mo site is formed by replacing three neighbouring S atoms in a unit cell with three N atoms and removing adjacent Mo atoms (MoS<sub>2</sub>\_1V<sub>Mo</sub>\_3N<sub>S</sub>). It should be noted that single Mo vacancy, double S vacancy and other possible N-doping sites were tested, but the stable structures are presented in **Figure 5.1**. Four different CO<sub>2</sub> orientations were also considered for CO<sub>2</sub> adsorption on the structures, which is presented in **Table 5.4**.

### 5.2.2 Computational Methods

The simulations use spin-polarized DFT-D2 calculations using Grimme's [216] method, as implemented in the *Vienna ab initio simulation package* (VASP) [211, 212]. This approach explained in Section 3.6 (**Chapter 3**), adds as a semi-empirical pairwise force field to the conventional first-principles plane-wave DFT calculations. The reason for using spin-polarized DFT-D2 correlation is that is in agreement with experimental values given for CO<sub>2</sub> adsorption on perfect monolayer MoS<sub>2</sub> from the benchmark studies on different dispersion schemes to understand the effects of vdW forces on the adsorption properties in Section 4.3 (**Chapter 4**). Hence, it takes dispersion interactions into consideration, and it accurately describes the interactions for adsorption systems [223]. The exchange-correlation potential is treated with the generalized gradient approximation (GGA) functional of Perdew, Burke and Ernzerhof (PBE) [215]. A 500 eV cutoff energy was used for the plane-wave basis set.  $\Gamma$ -centre meshes of 5x5x1 and 9x9x1 Monkhorst-Pack [224] k-point are used for sampling the Brillouin zone during geometry optimization and density of state calculations, respectively. The Gaussian smearing width was set to 0.2 eV. For geometry relaxation, we used the method of conjugate gradient energy minimization with

convergence criterion for the energy of  $10^{-6}$  eV between two consecutive steps, and the maximum Hellmann-Feynman force exerting on each atom less than  $0.01$  eV/Å upon ionic relaxation. In order to test for cutoff energy and k-point grid is required convergence, two denser Monkhorst-Pack grids ( $6 \times 6 \times 1$  and  $7 \times 7 \times 1$ ) and cutoff energy (600 and 700 eV) were tested for all the simulated systems. The results were compared for several selected parameters. It was found that the results from  $5 \times 5 \times 1$  Monkhorst-Pack grids were very similar to those for the  $6 \times 6 \times 1$  and  $7 \times 7 \times 1$  Monkhorst-Pack grids. The total energy was converged to  $<10$  meV. Hence, we believe that  $5 \times 5 \times 1$  Monkhorst-Pack is dense enough for a  $4 \times 4 \times 1$  MoS<sub>2</sub> monolayer and that 500 eV cutoff energy is suitable for the plane-wave basis set. Using Bader charge analysis, charge transfer between molecules and the substrate is obtained [225]. All calculations are performed under the same relaxation criteria.

The frequencies of the phonon modes for the physisorbed and dissociated state have been calculated through the finite difference method using a displacement of 0.015, and by fixing all of the atoms of the MoS<sub>2</sub> monolayer. This approach has shown to introduce little or no error in the computed frequencies and intensities of the adsorbed molecules and results in a significant reduction in computational cost [262]. The vibrational modes of the molecules in the gas phase were also computed to compare with the different adsorption configurations.

### 5.2.3 Calculation Details

The binding energies of N atom(s),  $E_{bN}$ , on the MoS<sub>2</sub> surface were calculated according to the reference [226].

$$E_{bN} = E_{N+MoS_2} - (E_N + E_{PMoS_2}) \quad (5.1)$$

where,  $E_{N+MoS_2}$  is the optimized total energy of the system N atom(s) + (4×4×1) supercell of MoS<sub>2</sub> monolayer (pristine MoS<sub>2</sub>),  $E_N$  is the ground-state energy of the free N atom(s) calculated in the same supercell with the same parameters and  $E_{PMoS_2}$  is the total energy of the (4×4×1) supercell of MoS<sub>2</sub> monolayer (pristine MoS<sub>2</sub>). A negative  $E_{bN}$  value indicates an exothermic process. The higher the value, the stronger the binding of the N atom(s) on the (4×4×1) supercell of the MoS<sub>2</sub> monolayer.

On the contrary, the binding energies of N atom(s) on the vacancy defect MoS<sub>2</sub> surface will be affected strongly by vacancy formation energy  $E_v$  and can be calculated using Eq. (5.2).

$$E_{bN} = (E_{N+MoS_2} - (E_N + E_{PMoS_2})) - E_v \quad (5.2)$$

$$E_v = E_x + E_{MoS_{2+x}} - E_{PMoS_2} \quad (5.3)$$

$E_v$  was calculated using the approach defined in Ref. [226]. That is, by subtracting the total energy of the pristine structure (without any vacancy) ( $E_{PMoS_2}$ ) from the sum of the total energy of a structure with a particular type of vacancy ( $E_{MoS_{2+x}}$ ) and the total energy (ies) of the removed atom ( $E_x$ , x is the removed atom, S or Mo). Negative  $E_v$  indicates stability.

The isosurfaces of the spin-charge density difference for the defective MoS<sub>2</sub> monolayer,  $\Delta\rho_s$ , was obtained using Equation (5.4):

$$\Delta\rho_s = \Delta\rho_{N+MoS_2} - (\Delta\rho_N + \Delta\rho_{MoS_2}) \quad (5.4)$$

where  $\Delta\rho_N$  and  $\Delta\rho_{MoS_2}$  is the charge densities of the free N atom (s) and defect MoS<sub>2</sub> monolayer without N atom (s), respectively, and  $\Delta\rho_{N+MoS_2}$  is the total charge density of defect MoS<sub>2</sub> monolayer with N atom (s).

The adsorption energy ( $E_{AE}$ ) is calculated as,

$$E_{AE} = E_{Surf+CO_2} - (E_{surf} + E_{CO_2}) \quad (5.5)$$

Where,  $E_{surf}$  and  $E_{Surf+CO_2}$  are the total energies of the surface (pristine or the defect monolayer MoS<sub>2</sub>) and that with the adsorbed CO<sub>2</sub> molecule respectively, and  $E_{CO_2}$  is the total energy of the isolated CO<sub>2</sub> molecule. A negative value of  $E_{AE}$  indicates that the adsorption is exothermic, which means that the adsorption of CO<sub>2</sub> molecule on the surface of the structure is favoured energetically, vice versa.

To analyse the electronic property of the defect structures upon CO<sub>2</sub> adsorption, the charge density difference,  $\Delta\rho_{df}$ , were calculated using Equation (5.6)

$$\Delta\rho_{df} = \Delta\rho_{Surf+CO_2} - (\Delta\rho_{Surf} + \Delta\rho_{CO_2}) \quad (5.6)$$

Where  $\Delta\rho_{Surf+CO_2}$ ,  $\Delta\rho_{Surf}$  and  $\Delta\rho_{CO_2}$  are the charge density of CO<sub>2</sub>-MoS<sub>2</sub> adsorption system, MoS<sub>2</sub> substrate and CO<sub>2</sub> molecule, respectively.

## 5.3 Results and Discussion

This section discusses the influences of different types of vacancies and levels of N doping on the structural and electronic property of the MoS<sub>2</sub> monolayer. In addition, how N doping and various types of vacancies govern the electron transfer rate, as well as the efficacy for CO<sub>2</sub> adsorption, were explored. Infrared (IR) spectroscopy was also performed to probe the structure of the surface adsorbates. Thereafter, the adsorption of nitrogen and water molecules was investigated to ascertain the selective adsorption of CO<sub>2</sub>.

### 5.3.1 Structural Geometry of Pristine Monolayer MoS<sub>2</sub> and Formation of Vacancy Defects and Nitrogen Doped (N-Dope) Monolayer MoS<sub>2</sub>, with the N Dopant, filled into the Single or Double Sulphur/Molybdenum Vacancies

The structural parameters of the optimized pristine monolayer MoS<sub>2</sub> in the present work is in fair agreement with the experimental value and previous theoretical values as shown in **Table 5.1**. The slight discrepancy is due to the pseudopotential used in this work.



**Table 5.1:** Structural geometry of pristine monolayer MoS<sub>2</sub>.

Structural geometry	Experimental	Theoretical (DFT GGA)	Current work
a=b (Å)	3.20 [263]	3.12 [179], 3.18 [160, 178, 264], 3.19 [17, 265], 3.20 [226], 3.22 [261]	3.19
band gap (E <sub>g</sub> ), eV	1.9 [110]	1.70 [17], 1.58 [226]	1.79
S-S bond length (Å)		3.13 [17, 226],	3.11
Mo-S bond length (Å)		2.42 [17, 226]	2.41
S-Mo-S bond angle (°)		80.65 [17], 80.65 [226]	80.39

In total, 10 possible surface configurations consisting of non-defective and defective periodic (4×4×1) supercell of the MoS<sub>2</sub> monolayer were investigated. The corresponding stable localized configurations for N doping and vacancies are shown in **Figure 5.1**.

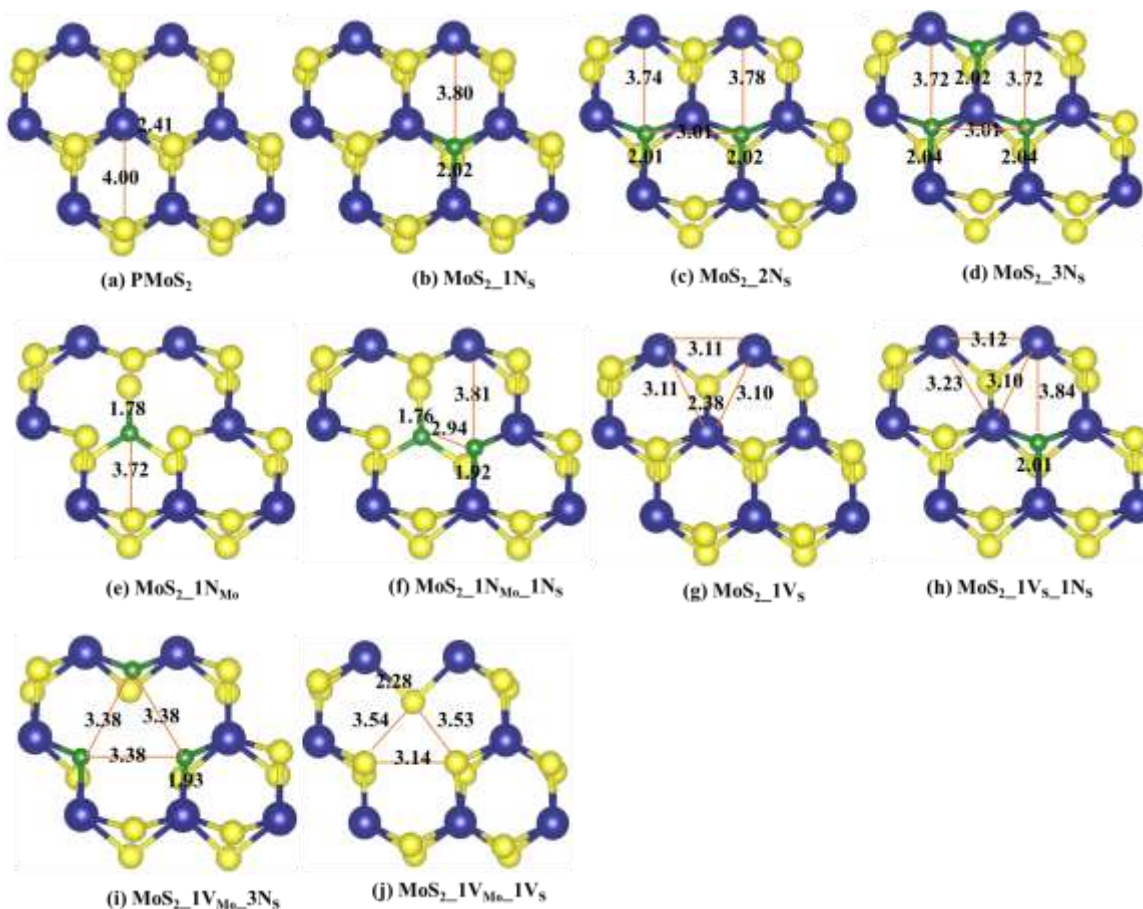


**Figure 5.1:** Relaxed local geometric configurations of  $\text{MoS}_2$  (a) pristine (b) one S atom substituted with an N atom (c) two S atoms substituted with two N atoms (d) three S atoms substituted with three N atoms (e) one Mo atom substituted with one N atoms (f) Mo and S atoms substituted with two N atoms (g)  $\text{MoS}_2$  with 1 S-vacancy (h) one S atom substituted with one N atoms in  $\text{MoS}_2$  with 1 S-vacancy (i) three neighbouring S atoms in a unit cell substituted with three N atoms in 1 Mo-vacancy defect and (j) 1Mo and 1S vacancy-defected  $\text{MoS}_2$ . Colour code: Mo, blue, S, yellow, and N, green. The lines define the lengths given in Å.

## 5.3.2 Properties of Simulated Surface Configurations

This section discusses the relative properties (atomic, electronic and magnetic) of the simulated surface configurations prior to evaluating the adsorption of CO<sub>2</sub>. Firstly, the simulation results of the single (MoS<sub>2</sub>\_1V<sub>S</sub>) and double vacancy (MoS<sub>2</sub>\_1V<sub>Mo</sub>\_1V<sub>S</sub>) defect systems are discussed. To reveal the effects of N atoms and vacancy defects on the structural properties of the adsorbent, the results of the N substitutional and N-doped vacancy (Mo and S) defect systems are compared with that of the optimized MoS<sub>2</sub> monolayer.

### 5.3.2.1 Vacancy Energies (E<sub>V</sub>), Atomic, Electronic and Magnetic Properties of Vacancy Defect MoS<sub>2</sub> Configurations

This subsection details the changes in the atomic, electronic and magnetic properties of MoS<sub>2</sub> configuration due to vacancy defects, that is, MoS double vacancy defect (MoS<sub>2</sub>\_1V<sub>Mo</sub>\_1V<sub>S</sub>) and S single vacancy defect (MoS<sub>2</sub>\_1V<sub>S</sub>). The results were compared with the previous theoretical results in order to validate vacancy defects on the MoS<sub>2</sub> monolayer

#### 5.3.2.1.1 Vacancy Energies (E<sub>V</sub>) and Atomic Properties

In **Table 5.2**, the calculated results for the vacancy formation energies E<sub>V</sub>, atomic, electronic and magnetic properties of the vacancy defect structure are presented. Eq. (5.3) and (5.6) in subsection 5.2.3 were employed to calculate E<sub>V</sub>, charge transfer and spin density charge difference in order to examine the magnetic properties at the proximity of MoS and S vacancies. The calculated vacancy energies, E<sub>V</sub>, are in good agreement with

the previous theoretical study [226]. **Table 5.2** shows that Mo atoms around the MoS vacancy ( $\text{MoS}_2\text{-1V}_{\text{Mo-1V}_\text{S}}$ ) gained more electrons than the ones around the S vacancy ( $\text{MoS}_2\text{-1V}_\text{S}$ ). Also, the S atoms around the MoS vacancy gained more electrons than the S atom around the S vacancy. However, in comparison with the Mo atom around MoS vacancy, the amount of charge transferred to Mo atoms around the MoS vacancy is higher than the charge received by the surrounding S atoms. This is because, after reconstruction around the vacancy upon optimization, the five S atoms having dangling bonds are less negatively charged, and the surrounding Mo atoms without dangling bonds are less positively charged compared to those in the pristine  $\text{MoS}_2$  sheet. Unlike in the MoS vacancy, the three unsaturated Mo atoms without dangling bonds and the surrounding S atoms lose their electrons to the vacancy sites, which becomes more negatively charged. Mo atoms become more positively charged while the S atoms become less negatively charged. This explains why  $\text{CO}_2$  strongly binds on  $\text{MoS}_2\text{-1V}_\text{S}$  site than on  $\text{MoS}_2\text{-1V}_{\text{Mo-1V}_\text{S}}$  as stated in subsection **5.3.3.2**. This statement is in good agreement with the work of ref [18], which proposed that a monolayer of  $\text{MoS}_2$  with point defects can be used as the sorbent for non-polar gas molecules adsorption.

The calculated Mo-S bond length for the vacancy defect sheets are in good agreement with Ref. [160]. The S-S height, which is that height between two opposite S atoms in a unit cell closer to the defect sites, increases from 3.117 Å to 3.120 Å in  $\text{MoS}_2\text{-1V}_\text{S}$ , but decreased to 3.098 Å in  $\text{MoS}_2\text{-1V}_{\text{Mo-1V}_\text{S}}$ . Also, the results of the electronic structure calculations show that MoS and S vacancy defects do not induce magnetism or reconstruction, with a total magnetic moment of 0.00  $\mu_\text{B}$ , agreeing well with previous theoretical studies [160, 226]. This is because, charge transfer in the close range of S and

MoS vacancies are insignificant as compared to those of the perfect structures, and thus, do not induce any magnetic moment.

**Table 5.2:** Summary of calculated results for Vacancy defect MoS<sub>2</sub> configurations.

Model	MoS <sub>2</sub> _1V <sub>S</sub>	MoS <sub>2</sub> _1V <sub>Mo</sub> _1V <sub>S</sub>	Reference <sup>g</sup>
E <sub>v</sub> , eV	<b>5.90</b>	<b>13.79</b>	<b>5.89/17.39</b> [226]
Q <sub>S</sub> <sup>a</sup> , e	<b>0.02</b>	<b>-0.04</b>	
Q <sub>Mo</sub> <sup>b</sup> , e	<b>0.07</b>	<b>-0.06</b>	
M <sup>c</sup> , μ <sub>B</sub>	<b>NM</b>	<b>NM</b>	<b>NM</b> [160, 226]
E <sub>g</sub> <sup>d</sup> (eV)	<b>1.05</b>	<b>0.46</b>	
h <sub>S-S</sub> <sup>e</sup> , Å	<b>3.12</b>	<b>3.10</b>	
d <sub>Mo-S</sub> <sup>f</sup> , Å	<b>2.38</b>	<b>2.34</b>	<b>2.38</b> [160]

<sup>a</sup> Q<sub>S</sub> and <sup>b</sup> Q<sub>Mo</sub> stands for the average total charge obtained by the S and Mo atoms, respectively, nearer to the vacancy sites. Negative charge means charge the S and Mo atoms gains electron from the vacancy defect site.

<sup>c</sup>M, is the net magnet moment

<sup>d</sup>E<sub>g</sub>, is the direct energy band-gap.

<sup>e</sup> d<sub>Mo-S</sub>, is average distance between the Mo and S atoms close to the vacancy defect site, <sup>f</sup> h<sub>S-S</sub>, is height between two opposite S atoms in the unit cell around the vacancy defect.

<sup>g</sup> Reference, are the results for MoS<sub>2</sub>\_1V<sub>S</sub> and MoS<sub>2</sub>\_1V<sub>Mo</sub>\_1V<sub>S</sub> models, respectively, from Ref. [160, 226].

\*NM, means nonmagnetic state, which shows that MoS and S vacancy defects exhibit a nonmagnetic state with total magnetic moment ( $\mu = 0 \mu_B$ ).

### 5.3.2.1.2 Electronic and Magnetic Properties

Furthermore, electronic structure calculations also show that vacancy defects give rise to states in the bandgap that localized at atoms around the vacancy (see **Figure 5.2a**). Both the bandgap and the electronic properties of monolayer MoS<sub>2</sub> are modified by these atoms. The calculated direct energy bandgap ( $E_g$ ) for MoS<sub>2</sub>\_1V<sub>S</sub> is 1.05 eV, which is narrower than the 1.79 eV of the pristine structure due to the defective states mainly introduced by the three unsaturated Mo atoms near the 1 S-vacancy. This is similar to the bandgap result in Ref. [160]. However, a much narrower direct energy bandgap of 0.46 eV is obtained in the MoS<sub>2</sub>\_1V<sub>Mo</sub>\_1V<sub>S</sub> structure, due to an increase in the defective states introduced by the five unsaturated S atoms having dangling bonds near the MoS vacancy (**Figure 5.2b**).

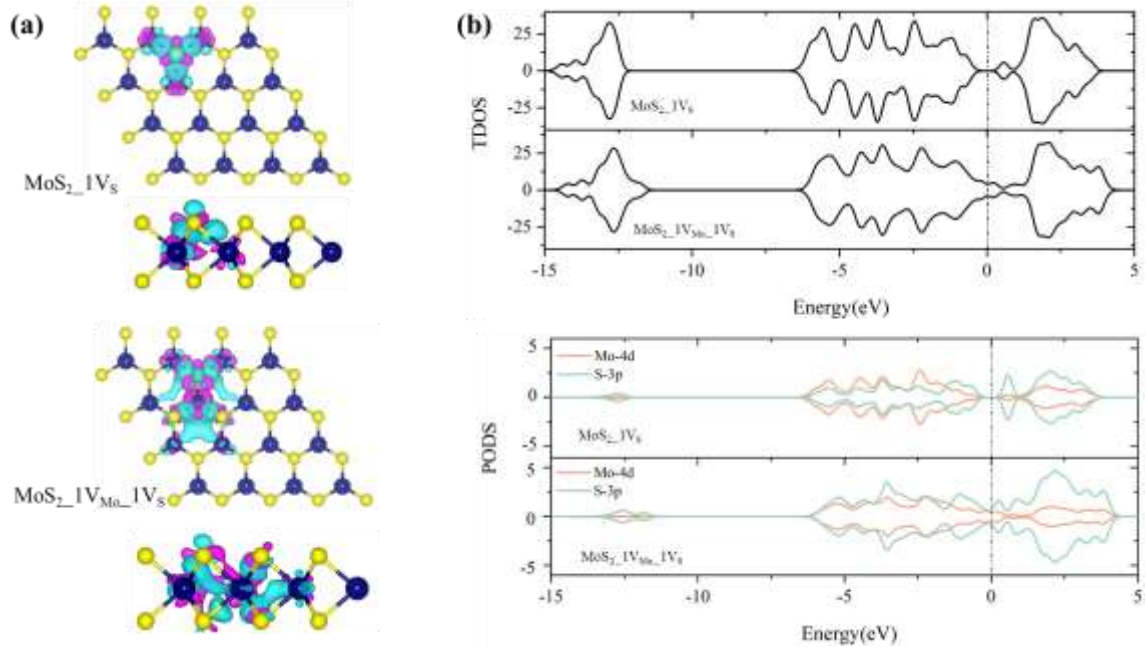


**Figure 5.2:** (a) Top and side views of Isosurfaces of spin density difference of (a) 1 S-vacancy and double MoS vacancy with isosurface taken as  $\pm 0.00015$  e/Bohr<sup>3</sup>. The light blue and pink colours represent the increase and decrease of electron density, respectively. (b) The TDOS (top panel) and PDOS (bottom panel) projected on the p and d orbitals of respective S and Mo atoms near the MoS and S vacancy sites. The positive and negative values of DOS illustrate the spin-up and spin-down states, respectively. The vertical dashed line corresponds to the Fermi level.

### 5.3.2.2 Properties of N-Doped Defective and Non-Defective MoS<sub>2</sub> Monolayer

This subsection discusses the novelties of the modified MoS<sub>2</sub> monolayer and the changes in its structural and electronic property due to modification. The optimum binding energies of the N dopants were determined from a comprehensive analysis aided by geometry optimization and energy minimization explained in Section 5.2.2.

### 5.3.2.2.1 Binding Energies and Atomic Properties

The binding energy and bond length of N-doped monolayer MoS<sub>2</sub> at different sites using the DFT calculations illustrated in **Figure 5.1** are presented in **Table 5.3**. The binding energies of N atom(s) on the MoS<sub>2</sub> surface were calculated using Eq. (5.1), while the binding energies of N atom(s) on the vacancy defect MoS<sub>2</sub> surface were calculated using Eq. (5.2) and (5.3) as explained in subsection **5.2.3**. The binding energies of all N-doped MoS<sub>2</sub> surfaces are negative (exothermic process), which suggests that it is viable for N atoms to be filled into the MoS<sub>2</sub> surfaces. Among the N-doped MoS<sub>2</sub> monolayers, the MoS<sub>2</sub>\_1N<sub>Mo</sub>\_1N<sub>S</sub> displayed the highest binding energy of -11.49 eV upon optimization. Similarly, the MoS<sub>2</sub>\_1N<sub>Mo</sub> showed a relatively high binding energy (-8.07 eV), but lower than that of MoS<sub>2</sub>\_1N<sub>Mo</sub>\_1N<sub>S</sub> due to fewer N atoms. The reason is that the replacement of Mo and/or S atoms in the MoS<sub>2</sub> sheet by N atoms (MoS<sub>2</sub>\_1N<sub>Mo</sub>\_1N<sub>S</sub> and MoS<sub>2</sub>\_1N<sub>Mo</sub>), further creates a local reconstruction on the S layer in adjacent site (**Figure 5.1**) in an energetically favourable manner during optimization.

The relatively large binding energy and stable localized configurations of MoS<sub>2</sub>\_1N<sub>Mo</sub>\_1N<sub>S</sub> and MoS<sub>2</sub>\_1N<sub>Mo</sub> when compared with that of 1 S-vacancy MoS<sub>2</sub> monolayer, MoS<sub>2</sub>\_1V<sub>S</sub>\_1N<sub>S</sub> (1.92 eV) can be explained by the designed optimization principle. While the vacancy in MoS<sub>2</sub>\_1V<sub>S</sub>\_1N<sub>S</sub> configuration was intentionally created before optimization, the vacancies in MoS<sub>2</sub>\_1N<sub>Mo</sub>\_1N<sub>S</sub> and MoS<sub>2</sub>\_1N<sub>Mo</sub> configurations were systematically induced after structural optimization. In other words, the vacancies in MoS<sub>2</sub>\_1N<sub>Mo</sub>\_1N<sub>S</sub> and MoS<sub>2</sub>\_1N<sub>Mo</sub> configurations occurred during structural relaxation without any missing atoms. As a result, the binding energy (computed from Eq. (5.1)) for the latter will be larger than the former (computed from Eq. (5.2)) since Eq. (5.1) does not account for vacancy



formation energy. Although the vacancies in  $\text{MoS}_2\text{-1N}_{\text{Mo-1N}}\text{S}$  and  $\text{MoS}_2\text{-1N}_{\text{Mo}}$  configurations occurred without any missing atoms, however, the breakage of the Mo-S covalent bond led to the formation of 2S, 1N and 3S unsaturated atoms having dangling bonds in their respective systems. Thus, the reconstruction around N-substitutional atoms upon optimization occurred at high exothermic energy. Furthermore, it was observed that the binding energy increased with the number of N-substitutional atoms. This can be attributed to the enhanced electrostatic attraction from the introduction of the N atom, which is more electronegative than Mo and S atoms. **Table 5.3** also depicts that the binding energy (and thus the electrostatic attractions) was higher in vacancy defect N-doped configurations than in configurations without defects. This posits that the absence of vacancy defect lessens the electrostatic component of the interaction.

Larger binding energy was obtained when the vacancy is created along the S atom of the  $\text{MoS}_2$  than the Mo atom. This is because the S atom is above the Mo atom and slightly lower than the N atom in the electronegativity trend. Hence, the absence of S atom in the  $\text{MoS}_2$  layer will lessen the repulsive component of the attraction. Subsequently, this tends to increase the electrostatic attraction between the defected nanosheet and relatively higher electronegative N atom. As a result, it is expected that the S vacancy  $\text{MoS}_2$  systems will form more stable configurations [160]. The impact of the vacant site on the binding energy was elucidated by comparing the binding energy for configuration with single S and Mo vacancies. Specifically, higher binding energy was obtained in configurations with single S vacancy (such as  $\text{MoS}_2\text{-1N}_{\text{Mo}}$ ) than in configurations with Mo vacancy (such as  $\text{MoS}_2\text{-1V}_{\text{Mo-3N}}\text{S}$ ), even though  $\text{MoS}_2\text{-1N}_{\text{Mo-1N}}\text{S}$  had a lesser number of N atoms. The

comprehensive details of why S vacancy MoS<sub>2</sub> systems form a more stable structure than MoS vacancy systems have been given elsewhere [226].

**Table 5.3:** Summary of N-doped MoS<sub>2</sub> configurations.

Model	$E_{bN}$ , eV	$E_g^a$ , eV	$Q_N^b$ , e	$M_N^c$ , $\mu_B$	$d_{Mo-S}^d$ , Å	$d_{N-Mo}^e$ , Å	$h_{N-S}^f$ , Å
MoS <sub>2</sub> _1N <sub>S</sub>	<b>-0.88</b>	<b>1.71</b>	<b>-0.81</b>	<b>0.23 (0.83)</b>	<b>2.45</b>	<b>2.02</b>	<b>2.69</b>
MoS <sub>2</sub> _2N <sub>S</sub>	<b>-1.63</b>	<b>1.67</b>	<b>-1.56</b>	<b>0.00 (*NM)</b>	<b>2.44</b>	<b>2.02</b>	<b>2.68</b>
MoS <sub>2</sub> _3N <sub>S</sub>	<b>-2.47</b>	<b>1.62</b>	<b>-2.23</b>	<b>0.00 (NM)</b>	<b>2.43</b>	<b>2.04</b>	<b>2.66</b>
MoS <sub>2</sub> _1N <sub>Mo</sub>	<b>-8.07</b>	<b>1.18</b>	<b>-0.84</b>	<b>0.34 (0.82)</b>	<b>2.39</b>	<b>1.78</b>	<b>3.11</b>
MoS <sub>2</sub> _1N <sub>Mo</sub> _1N <sub>S</sub>	<b>-11.49</b>	<b>0.94</b>	<b>-1.72</b>	<b>0.00 (NM)</b>	<b>2.35</b>	<b>1.92</b>	<b>2.74</b>
MoS <sub>2</sub> _1V <sub>S</sub> _1N <sub>S</sub>	<b>-1.92</b>	<b>0.90</b>	<b>-0.95</b>	<b>0.17 (0.61)</b>	<b>2.38</b>	<b>2.01</b>	<b>2.70</b>
MoS <sub>2</sub> _1V <sub>Mo</sub> _3N <sub>S</sub>	<b>-8.05</b>	<b>0.91</b>	<b>-2.21</b>	<b>0.20 (2.20)</b>	<b>2.43</b>	<b>1.93</b>	<b>2.63</b>

<sup>a</sup>  $E_g$  is the calculated direct energy band gap

<sup>b</sup>  $Q_N$  stands for total charge obtained by the N atoms. Negative charge means charge was transferred from MoS<sub>2</sub> surface atoms to the N atom, and vice versa.

<sup>c</sup>  $M_N$  is the net magnetic moment of the N dopant atoms. The values in brackets are the net magnet moment of the entire structure.

<sup>d</sup>  $d_{Mo-S}$  is the average distance between Mo and S atoms close to the defect sites.

<sup>e</sup>  $d_{N-Mo}$  is the average distance between the N atom and its neighbouring Mo atoms.

<sup>f</sup>  $h_{N-S}$  is the height of the N atom with respect to the S plane (that is, S atom of the S-layer opposite to the layer doped with N atom).

\*NM, means nonmagnetic state, which shows that the investigated model exhibits a nonmagnetic state (i.e. total magnetic moment,  $\mu = 0 \mu_B$ ).

About the atomic properties, from **Table 5.3**, it can be observed that the average N-Mo bond length shows a small increase with the number of N dopants for both vacant and non-vacant systems. Specifically, the  $\text{MoS}_2\text{-1V}_s\text{-1N}_s$  system exhibited an N-Mo bond length of 2.01 Å, which is similar to that of non-defective configurations despite containing an S vacancy. This can be related to the characteristic stretching of the Mo-Mo distance within the vicinity of the S vacant site, which offers a cushioning effect on the N-Mo bond by the vacancy site upon optimization. On the contrary,  $h_{\text{N-S}}$  (the height of the nitrogen atom with respect to the S atoms) decreases with increasing numbers of N dopants for the systems.  $\text{MoS}_2\text{-1N}_{\text{Mo}}$  displayed the largest  $h_{\text{N-S}}$  value of *approx.* 3.11 Å, which is close to the interlayer S-S distance of pristine  $\text{MoS}_2$  (3.11 Å). This can be associated with the shortest  $d_{\text{N-Mo}}$  for  $\text{MoS}_2\text{-1N}_{\text{Mo}}$  when compared to the other structures. Overall, our results showed that the vacancy defects (single or double) created in  $\text{MoS}_2$  do not induce molecular structure reconstruction as witnessed in the case of carbon vacancy in graphene [236].

The Mo atoms close to the single S vacancy slightly relaxed towards the vacancy site. Furthermore,  $d_{\text{Mo-S}}$  decreased from 2.41 Å (pristine  $\text{MoS}_2$ ) to 2.39 Å, 2.38 Å and 2.35 Å in  $\text{MoS}_2\text{-1N}_{\text{Mo}}$ ,  $\text{MoS}_2\text{-1V}_s\text{-1N}_s$  and  $\text{MoS}_2\text{-1N}_{\text{Mo}}\text{-1N}_s$ , respectively, which are in agreement with literature [160]. However, the  $d_{\text{Mo-S}}$  was observed to increase to 2.43 Å in  $\text{MoS}_2\text{-1V}_{\text{Mo}}\text{-3N}_s$  due to the Mo vacancy, which has less effect on the surrounding Mo-S bonds than the S vacancy. The impact of the number of N dopants on  $d_{\text{Mo-S}}$  for  $\text{MoS}_2\text{-1V}_{\text{Mo}}\text{-3N}_s$  was similar to that for defect-free N doped systems. Mo-S bond length for these set of structures was observed to decrease, tending towards the  $d_{\text{Mo-S}}$  for  $\text{PMoS}_2$  (2.412 Å) with an increase in N dopant.

### 5.3.2.2.2 Electronic and Magnetic Properties

The electron transfer between the dopant and the surface was also investigated by examining the charge densities using Bader charge analysis [225]. As can be seen from **Table 5.3**, the values of  $Q_N$  are negative for all the considered surfaces, which indicates that the transfer of electrons occurred from the surficial atoms to the N atom. This is in line with the electronegative nature of the N atom [266]. The Pauling electronegativity of both Mo and S atoms of the surface are 2.16 and 2.58, respectively, which are smaller than 3.04 for the N atom. Hence, charge transfers from the Mo and S atoms to N dopant, which becomes more negatively charged. The charge transfer from the surface to the N dopant increased with the number of N atoms present in the structure and, there is charge transfer from the 1 S-vacancy sites to the N dopant. For instance, the N dopant gained more charge in  $\text{MoS}_2\text{-1V}_S\text{-1N}_S$  (0.95 e) and  $\text{MoS}_2\text{-1N}_{\text{Mo}}$  (0.84 e) due to the formation of vacancy and unsaturated dangling atoms than  $\text{MoS}_2\text{-1N}_S$  (0.81 e) with the same number of N atoms. This can also be seen in  $\text{MoS}_2\text{-1N}_{\text{Mo-1N}_S}$  (1.72 e) and  $\text{MoS}_2\text{-2N}_S$  (1.56 e). Furthermore, N dopants gained more electron from  $\text{MoS}_2\text{-3N}_S$  (2.23 e) than  $\text{MoS}_2\text{-1V}_{\text{Mo-3N}_S}$  (2.21 e). This is because the neighbouring S atoms around the Mo vacancy receive less charge (as shown in **Table 5.2**) due to the missing Mo atom. Therefore, less charge is transferred to the surrounding N dopant from the S atoms neighbouring the vacant Mo site. This is in good agreement with the previous theoretical study [226].

In addition, the results from **Table 5.3** show that  $\text{MoS}_2\text{-1N}_S$ ,  $\text{MoS}_2\text{-1V}_S\text{-1N}_S$ ,  $\text{MoS}_2\text{-1N}_{\text{Mo}}$  and  $\text{MoS}_2\text{-1V}_{\text{Mo-3N}_S}$  exhibit a magnetic moment. This is because of the fewer number of N atoms in  $\text{MoS}_2\text{-1N}_S$  and the vacancy in  $\text{MoS}_2\text{-1V}_S\text{-1N}_S$ ,  $\text{MoS}_2\text{-1N}_{\text{Mo}}$  and

MoS<sub>2</sub>\_1V<sub>Mo</sub>\_3N<sub>S</sub>. In contrast, MoS<sub>2</sub>\_2N<sub>S</sub>, MoS<sub>2</sub>\_3N<sub>S</sub> and MoS<sub>2</sub>\_1N<sub>Mo</sub>\_1N<sub>S</sub> (with a higher number of N atoms) exhibit a nonmagnetic moment despite having double the amount of charge transfer that could enable significant disturbance and spin polarization. It is also observed that the excess charge transfer around the N dopants is evenly distributed among the N atoms. This even distribution reduces the effect of spin polarization on the surface, and thus, do not induce a magnetic moment. The distribution of the magnetic moment can be clearly seen from **Figure 5.3**, which is the isosurfaces of the spin-charge density difference for the defective MoS<sub>2</sub> monolayer,  $\Delta\rho_s$ , and was obtained using Eq. (5.4) as explained in subsection **5.2.3**.

Specifically, the significant disturbance and spin polarization in the MoS<sub>2</sub>\_1N<sub>Mo</sub> system (with total magnetic moment = 0.82  $\mu_B$ ) originated from the p orbitals of three S atoms which have dangling bonds, with p orbitals of N atom contributing a magnetic moment of 0.34  $\mu_B$ . Concerning the MoS<sub>2</sub>\_1V<sub>S</sub>\_1N<sub>S</sub> system, the total magnetic moment of 0.61  $\mu_B$  originated equally from d<sub>yz</sub> and d<sub>zx</sub> orbitals of three unsaturated Mo atoms near the single S vacancy, with the p orbitals of N atom contributing a magnetic moment of 0.17  $\mu_B$ . Similarly, the high induced total magnetic moment of 2.20  $\mu_B$  in the MoS<sub>2</sub>\_1V<sub>Mo</sub>\_3N<sub>S</sub> system originated from the p orbitals of three S and three N atoms (0.20  $\mu_B$ ) which have dangling bonds. For the MoS<sub>2</sub>\_1N<sub>S</sub> system, p orbitals of the single N substitutional atom contributed a magnetic moment of 0.23  $\mu_B$ , while the rest of the magnetic moment originated equally from d<sub>yz</sub> and d<sub>zx</sub> orbitals of the Mo atoms and p orbitals S atoms that surround the N atom. Unlike in MoS<sub>2</sub>\_1N<sub>S</sub>, MoS<sub>2</sub>\_1V<sub>S</sub>\_1N<sub>S</sub>, MoS<sub>2</sub>\_1N<sub>Mo</sub> and MoS<sub>2</sub>\_1V<sub>Mo</sub>\_3N<sub>S</sub> systems, the charges in MoS<sub>2</sub>\_2N<sub>S</sub>, MoS<sub>2</sub>\_3N<sub>S</sub> and MoS<sub>2</sub>\_1N<sub>Mo</sub>\_1N<sub>S</sub>

systems are evenly distributed in the orbitals of Mo, S and N atoms, which resulted in the nonmagnetic state with a total magnetic moment,  $\mu = 0 \mu_B$ .

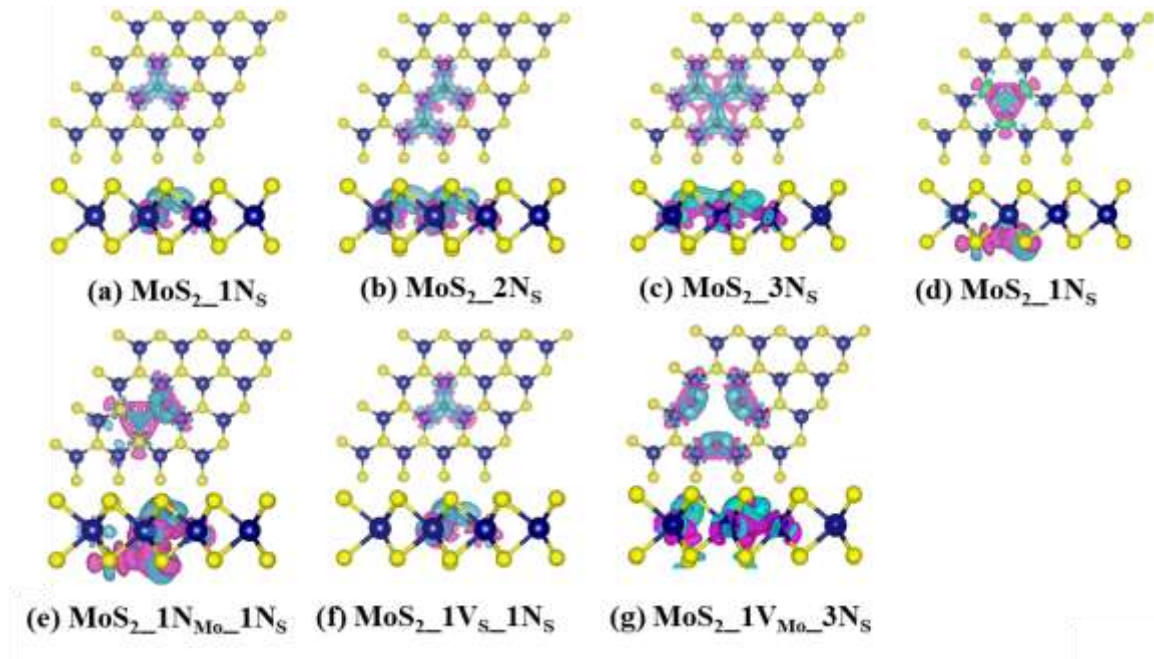


**Figure 5.3:** Top and side views of isosurfaces of spin density difference for the defect surfaces with isosurface taken as  $\pm 0.005 \text{ e/Bohr}^3$ . The light blue and pink colours represent areas with an increase and decrease of electron density, respectively. The colour codes for Mo, S and N atoms are the same as in **Figure 5.1**.

Finally, to provide more insight into the electronic properties of these sites, the total (TDOS) and partial (PDOS) density of state were calculated. **Figure 5.4** presents the characteristic TDOS and PDOS of the N-doped vacancy free and N-doped vacancy containing MoS<sub>2</sub> monolayers. N is expected to act as a source of p-type doping for the monolayer MoS<sub>2</sub> when it substitutes for S, due to that N has one p valence electron less than S. This leads to the generation of a hole in the valence band as shown in the DOS plots (**Figure 5.4**). The calculated direct energy bandgap ( $E_g$ ) for each structure is given in **Table 5.3**. From **Table**

**5.3**, the bandgaps become narrower as the number of N dopants increases for the N-doped vacancy-free systems. The narrow state of the bandgap compared with the pristine structure (1.79 eV) indicates a shift in the Fermi level is mainly due to the impurity state introduced by N atoms. The impurity states mainly come from the hybridization between the 2p orbitals of N and the 4d orbitals of its neighbouring Mo. The electron transfer due to the presence of nitrogen as a p-type dopant and the band bending induced by the formation of Mo-N covalent bond at the top-most layer, as well as the preferential sulphur removal, contribute to a band shift, which is commonly found in N doped MoS<sub>2</sub> [19, 267]. Furthermore, it is observed that much narrower band gaps are obtained in N doped single S or Mo vacancy defect complexes. This can be attributed to the combined effects of the impurity state introduced by the N atom as a p-type dopant and the defect states as a result of unsaturated S or Mo atoms near the single S or Mo vacancy, respectively [226]. A detailed explanation of the defect states in non-doped single S or Mo vacancy defects has been provided in subsection **5.3.2.1.2**.

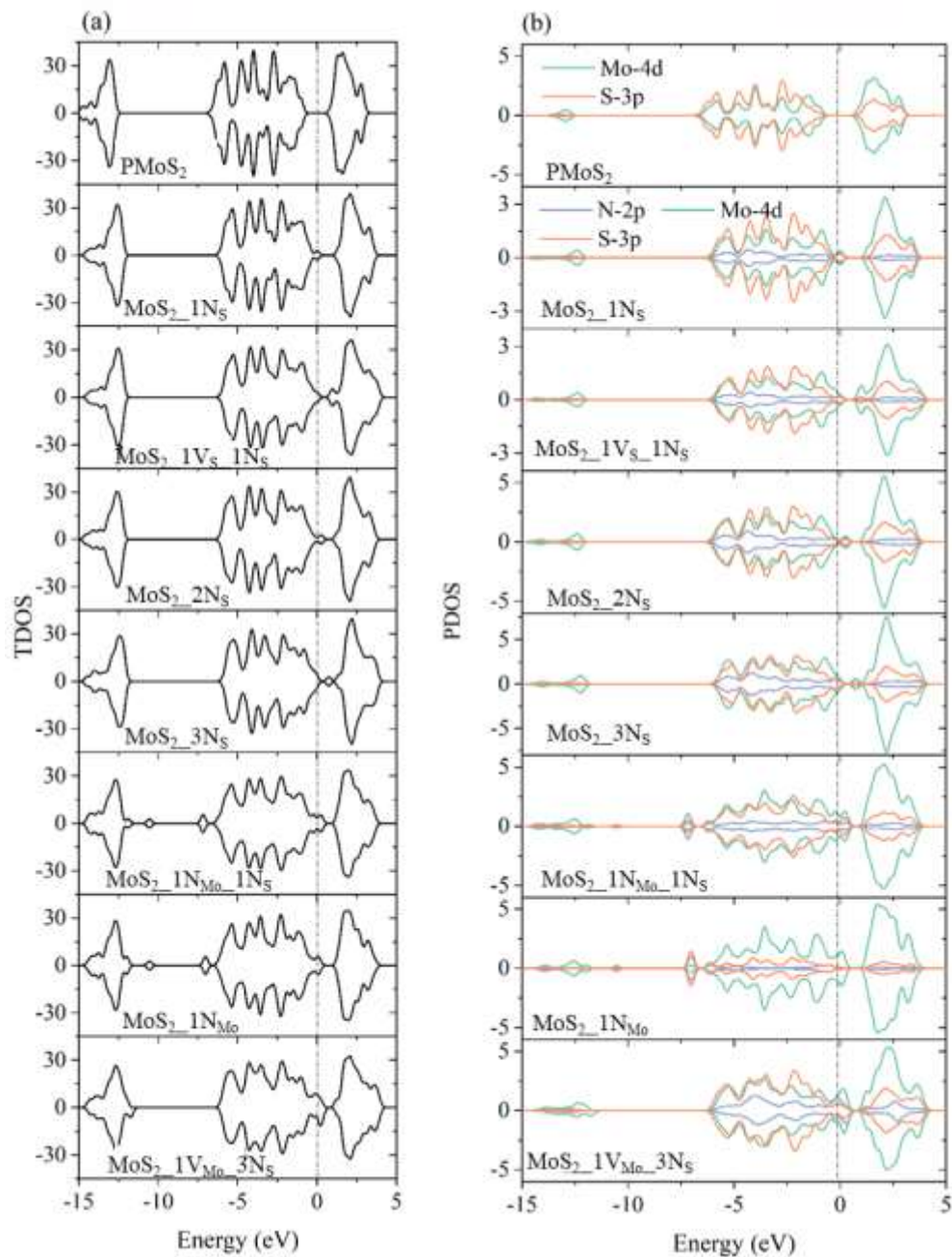


**Figure 5.4:** (a) The TDOS of the defect-free and N doped monolayer MoS<sub>2</sub>. (b) The PDOS projected on the 3p orbitals of N dopants and the 3p and 4d orbitals of their neighbouring S and Mo atoms, respectively. The positive and negative values of DOS illustrate the spin-up and spin-down states, respectively. Green, orange and blue lines represent 4d, 2p and 3p orbitals, respectively. The Fermi level is represented by the vertical dashed line.



### **5.3.3 Investigating CO<sub>2</sub> Adsorption Performance Modified MoS<sub>2</sub> Monolayer**

The evaluation of the adsorption of CO<sub>2</sub> on the pristine and modified MoS<sub>2</sub> monolayers as well as the effect of variation of initial molecular height on CO<sub>2</sub> adsorption energies are detailed in this subsection. Further, infrared (IR) spectroscopy of molecules adsorbed on the surface is discussed to analyse the structure of the surface adsorbates. Finally, how the N-doping enabled defect engineering of MoS<sub>2</sub> proved to be an effective approach for the enhanced selective adsorption of CO<sub>2</sub> is discussed.

#### **5.3.3.1 CO<sub>2</sub> Adsorption on the Considered MoS<sub>2</sub> Surfaces**

To investigate the adsorption of CO<sub>2</sub> on the pristine or defect (vacancy or N-substitutional doping) monolayer MoS<sub>2</sub>, the adsorption energy ( $E_{AE}$ ) is calculated using Eq. (5.5) as described in subsection 5.2.3. The molecular height is defined as the distance between the carbon atom of the CO<sub>2</sub> molecule and a reference atom of the MoS<sub>2</sub> surface in the basal plane in the z-direction (i.e. N atom for N doped MoS<sub>2</sub> surface and average z plane of S atoms, for non-doped MoS<sub>2</sub> surface). It should be pointed out that top (Mo or S), hollow or bridge sites of the MoS<sub>2</sub> monolayer were not emphasized in our calculations. The reason for this is that a theoretical study has shown that MoS<sub>2</sub> is a poor adsorbent for CO<sub>2</sub> irrespective of these sites, but defective MoS<sub>2</sub> is a good adsorbent, hence, our focus is to further enhance the adsorption by N doping [18]. In this regard, the CO<sub>2</sub> molecule was initially placed at a height of 2.5 Å from S or Mo at the vacancy site and doped N atom(s) for vacancy defect and N-doped monolayer MoS<sub>2</sub>, respectively. Different orientations of

the CO<sub>2</sub> molecule and lateral positions with respect to XYZ axes of the MoS<sub>2</sub> supercell (**Table 5.4**) were also considered to obtain the most stable CO<sub>2</sub> adsorption configurations.

**Table 5.4:** Summary of adsorption energies of possible initial configurations of CO<sub>2</sub> adsorption on different surfaces.

Model	Adsorption Energies E <sub>AE</sub> (eV)			
	Config. 1	Config. 2	Config. 3	Config. 4
PMoS <sub>2</sub>	<b>-0.139</b>	<b>-0.116</b>	<b>-0.134</b>	<b>-0.085</b>
MoS <sub>2</sub> _1N <sub>S</sub>	<b>-0.197</b>	<b>-0.197</b>	<b>-0.196</b>	<b>-0.106</b>
MoS <sub>2</sub> _2N <sub>S</sub>	<b>-0.191</b>	<b>-0.200</b>	<b>-0.187</b>	<b>-0.112</b>
MoS <sub>2</sub> _3N <sub>S</sub>	<b>-0.207</b>	<b>-0.205</b>	<b>-0.211</b>	<b>5.863</b>
MoS <sub>2</sub> _1N <sub>Mo</sub>	<b>8.484</b>	<b>12.28</b>	<b>11.655</b>	<b>8.853</b>
MoS <sub>2</sub> _1N <sub>Mo</sub> _1N <sub>S</sub>	<b>-0.161</b>	<b>-0.186</b>	<b>-0.176</b>	<b>1.106</b>
*MoS <sub>2</sub> _1V <sub>S</sub>	<b>0.004</b>	<b>0.003</b>	<b>0.003</b>	<b>-0.908</b>
MoS <sub>2</sub> _1V <sub>S</sub> _1N <sub>S</sub>	<b>-0.196</b>	<b>-0.184</b>	<b>-0.183</b>	<b>-0.125</b>
MoS <sub>2</sub> _1V <sub>Mo</sub> _3N <sub>S</sub>	<b>-1.406</b>	<b>-1.818</b>	<b>-0.213</b>	<b>-0.073</b>
MoS <sub>2</sub> _1V <sub>Mo</sub> _1V <sub>S</sub>	<b>-0.184</b>	<b>-0.252</b>	<b>-0.084</b>	<b>2.199</b>

\*MoS<sub>2</sub>\_1V<sub>S</sub>, the config. 4 results to the formation of CO gas, with one O atom of the CO<sub>2</sub> molecule forming Mo-O-Mo layer at the S vacancy site.

Based on these test calculations, only the most stable relaxed adsorption geometric structures and results are presented and discussed here. **Figure 5.5** presents the schematic structure of the most stable CO<sub>2</sub> adsorption configurations for the pristine or defect (vacancy or N-substitutional doping) monolayer MoS<sub>2</sub>. Except for the MoS<sub>2</sub>\_1V<sub>S</sub>, all other models exhibited stable CO<sub>2</sub> adsorption when the CO<sub>2</sub> molecule is oriented in parallel with the surface of the model. It is worth mentioning that MoS<sub>2</sub>\_1N<sub>Mo</sub> is not a stable adsorption configuration for CO<sub>2</sub> molecule due to high positive adsorption energy in all the considered configurations, therefore is not be discussed further.

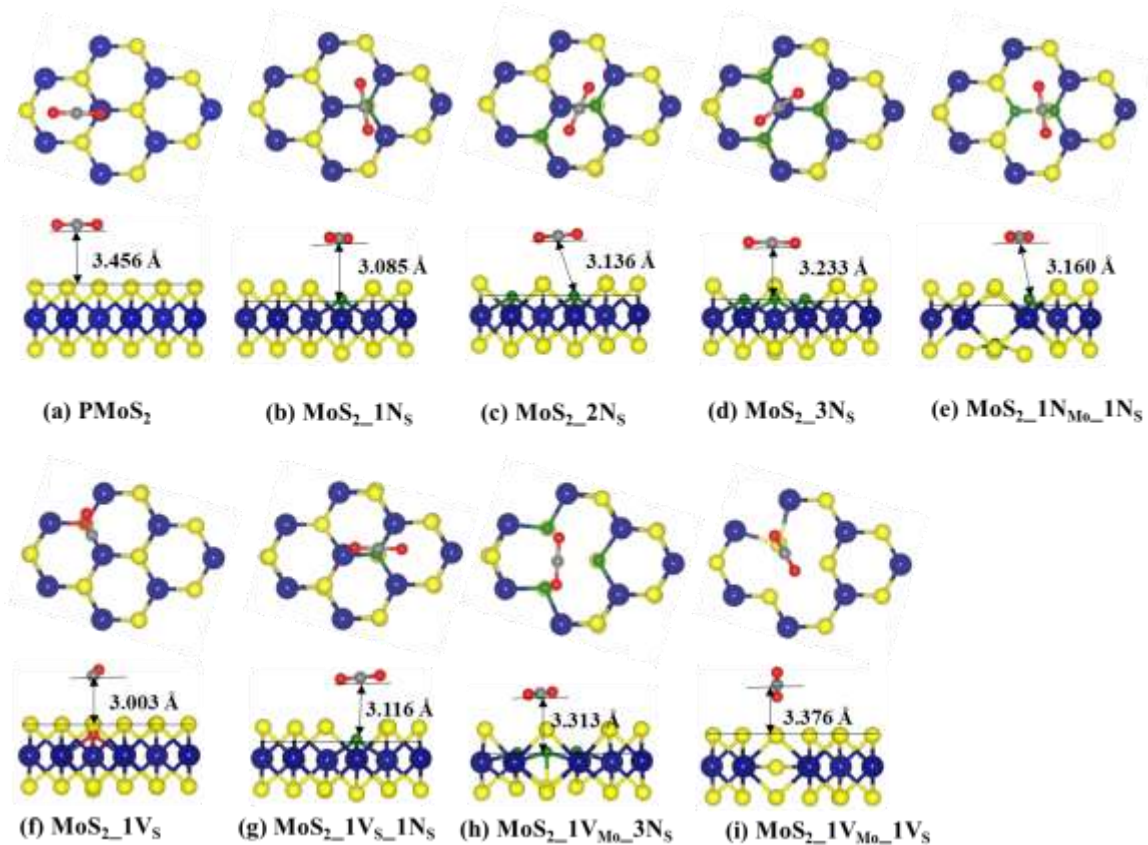


**Figure 5.5:** The schematic structure of the most stable adsorption configurations for CO<sub>2</sub> molecule adsorbed on the pristine and defect (vacancy or N-substitutional doping) monolayer MoS<sub>2</sub> from the top (upper panel) and side (lower panel) views. The full descriptions of a-i have been given in Figure 5.1. The colour codes for Mo, S and N atoms are the same as in Figure 5.1, while, O and C atoms are shown in red and grey, respectively. The lines define the equilibrium molecular height between the central carbon atom of the CO<sub>2</sub> molecule and a reference atom of the MoS<sub>2</sub> surface in the basal plane in the z-direction yielded by optimization (i.e. N atom for N doped MoS<sub>2</sub> surface and average z plane of S atoms, for non-doped MoS<sub>2</sub> surface given in Å).

To further understand the molecule-monolayer interaction and to ensure adequate optimization of possible stable configurations, the characteristic adsorption energy curves for all the studied local geometric configurations were calculated. Herein, the CO<sub>2</sub> adsorption energies at varied initial molecular heights from 1.0 - 6.5 Å were calculated. The corresponding results are presented in **Figure 5.6**. It can be seen that the highest adsorption energies for all the studied structures occurred at 2.5 Å initial molecular height except for MoS<sub>2</sub>\_1V<sub>S</sub>\_1N<sub>S</sub> and MoS<sub>2</sub>\_1V<sub>Mo</sub>\_3N<sub>S</sub> models with the highest adsorption energies at 1.5 to 2.0 Å molecular heights. It is shown that the curve for MoS<sub>2</sub>\_1V<sub>Mo</sub>\_3N<sub>S</sub> gives the highest adsorption energy, which is 13 times higher than that of pristine MoS<sub>2</sub> (PMoS<sub>2</sub>).

Further elaboration of the adsorption properties at 2.5 Å initial molecular height is given in **Table 5.5**. **Table 5.5** presents the equilibrium molecular distance between the adsorbate and the substrate yielded by optimization ( $h_{\text{mol-surf}}$ ), along with the corresponding adsorption energy ( $E_{AE}$ ) and characteristic parameters for the considered models such as the amount of charge transfer (from Bader charge analysis) between MoS<sub>2</sub> and CO<sub>2</sub> molecule ( $Q_{\text{CO}_2}$ ), and MoS<sub>2</sub> and the nitrogen atom of the dopant ( $Q_N$ ), characteristic surficial bond lengths ( $d_{\text{Mo-S}}$ ,  $d_{\text{N-Mo}}$  and  $h_{\text{N-S}}$ ), average bond lengths ( $l$ ) and bond angles ( $\theta$ ) of CO<sub>2</sub> after adsorption, and change in CO<sub>2</sub> bond angles ( $\Delta\theta$ ).  $\Delta\theta$  is the difference between the bond angle experimental value (180°) [245] and the value obtained from the structural optimization. For example, stable CO<sub>2</sub> adsorption on the MoS<sub>2</sub>\_1N<sub>S</sub> surface displayed an equilibrium height of 3.085 Å with an adsorption energy of -0.197 eV. All equilibrium heights obtained from the models are lower than that obtained in PMoS<sub>2</sub> (3.456 Å) with an adsorption energy of 0.139 eV. Also, CO<sub>2</sub> is considered to be physisorbed on all the

surfaces based on the large separation heights, except the for MoS<sub>2</sub>\_1V<sub>S</sub> surface, where the CO<sub>2</sub> molecule was found to undergo dissociative adsorption. A detailed discussion on dissociation is given in the subsequent section.

As mentioned earlier, a notable distinction was observed for the MoS<sub>2</sub>\_1V<sub>S</sub>\_1N<sub>S</sub> and MoS<sub>2</sub>\_1V<sub>Mo</sub>\_3N<sub>S</sub> models with maximum adsorption energies obtained at 1.5 and 2.0 Å above the surface, respectively (**Figure 5.6**). In these models, stable adsorption is characterized by dissociative chemisorption of CO<sub>2</sub> molecule with -0.614 and -2.136 eV adsorption energies, respectively. The results reveal that CO<sub>2</sub> dissociated into CO and O on these surfaces at these initial molecular heights, and this will be investigated in **Chapters 6 and 7**. However, a repulsive interaction, indicated by the endothermic adsorption energy, between the CO<sub>2</sub> molecule and all the surfaces was observed at initial molecular heights lower than 1.3 Å. MoS<sub>2</sub>\_1V<sub>S</sub> displayed the highest endothermic energy barrier of 18.415 eV (**Figure 5.6**). This result demonstrates the increased difficulty associated with CO<sub>2</sub> interaction at proximity to the vacancy site. Therefore, CO<sub>2</sub> cannot be attracted to the S vacancy site but physisorbed at a certain distance from the vacancy, this is a common phenomenon associated with 1 S-vacancy in MoS<sub>2</sub> nanostructures [160].

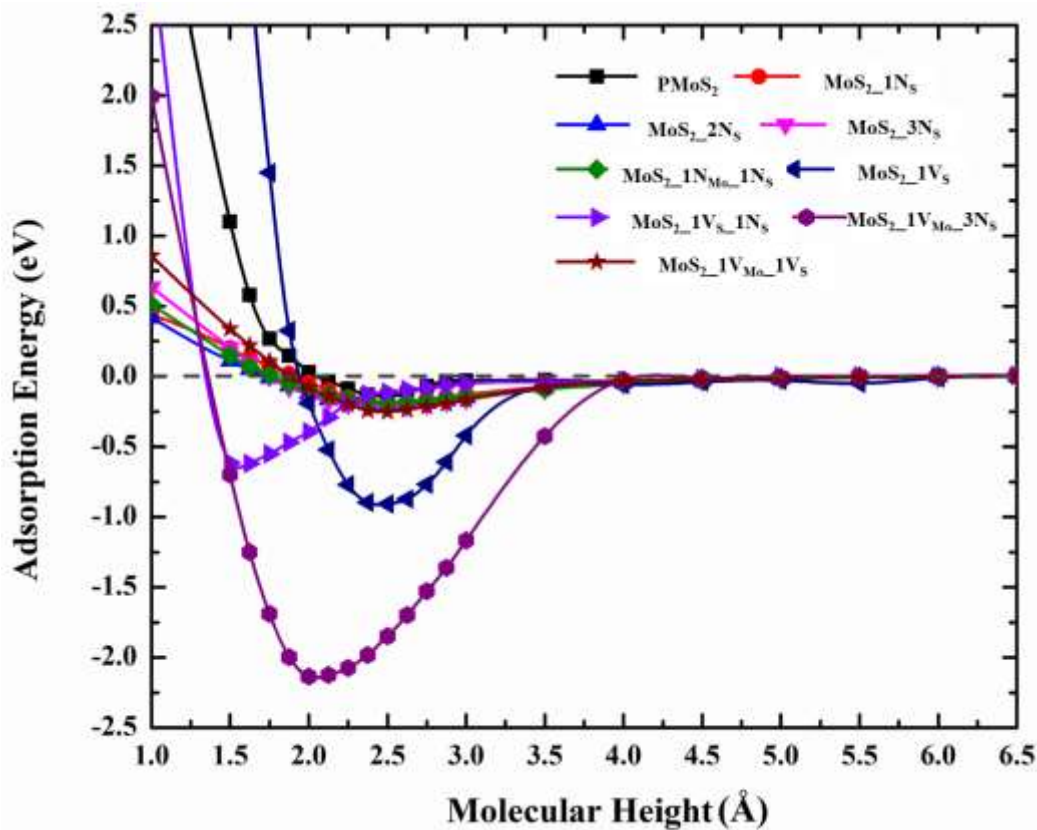


**Figure 5.6:** Adsorption energy versus molecular height. Adsorption energy as a function of molecular height for CO<sub>2</sub> adsorption on the most stable local geometric configurations for each model. The molecular height is the distance between the central carbon atom of the adsorbed CO<sub>2</sub> molecule and a reference atom of the MoS<sub>2</sub> surface in the basal plane in the z-direction (That is, N atom, for N doped MoS<sub>2</sub> surface and average z plane of top S-layer atom, for non-doped MoS<sub>2</sub> surface).

**Table 5.5:** Summary of calculated results for adsorption of CO<sub>2</sub> on most stable configurations of different surfaces at 2.5 Å initial molecular height.

Model	E <sub>AE</sub> , eV	Q <sub>CO<sub>2</sub></sub> <sup>a</sup> , e	Q <sub>N</sub> <sup>b</sup> , e	<sup>c</sup> M <sub>N</sub> , μ <sub>B</sub>	h <sub>mol-surf</sub> <sup>d</sup> , Å	d <sub>Mo-S</sub> <sup>e</sup> , Å	d <sub>N-Mo</sub> <sup>f</sup> , Å	h <sub>N-S</sub> <sup>g</sup> , Å	l, Å	θ, °	Δθ, °
PMoS <sub>2</sub>	<b>-0.139</b>	<b>-0.020</b>	-	-	<b>3.456</b>	<b>2.412</b>	-	-	<b>1.177</b>	<b>179.698</b>	<b>0.302</b>
MoS <sub>2</sub> _1N <sub>S</sub>	<b>-0.197</b>	<b>-0.017</b>	<b>-0.958</b>	<b>0.213</b>	<b>3.085</b>	<b>2.443</b>	<b>2.019</b>	<b>2.694</b>	<b>1.177</b>	<b>178.713</b>	<b>1.287</b>
				<b>(0.840)</b>							
MoS <sub>2</sub> _2N <sub>S</sub>	<b>-0.200</b>	<b>-0.017</b>	<b>-1.894</b>	<b>0.000</b>	<b>3.136</b>	<b>2.439</b>	<b>2.012</b>	<b>2.681</b>	<b>1.177</b>	<b>178.712</b>	<b>1.288</b>
				<b>(*NM)</b>							
MoS <sub>2</sub> _3N <sub>S</sub>	<b>-0.211</b>	<b>-0.015</b>	<b>-2.814</b>	<b>0.000</b>	<b>3.233</b>	<b>2.365</b>	<b>2.016</b>	<b>2.655</b>	<b>1.176</b>	<b>178.710</b>	<b>1.290</b>
				<b>(NM)</b>							
MoS <sub>2</sub> _1N <sub>Mo</sub> _1N <sub>S</sub>	<b>-0.186</b>	<b>-0.019</b>	<b>-1.702</b>	<b>0.000</b>	<b>3.160</b>	<b>2.351</b>	<b>1.926</b>	<b>2.754</b>	<b>1.176</b>	<b>178.720</b>	<b>1.280</b>
				<b>(NM)</b>							
MoS <sub>2</sub> _1V <sub>S</sub> <sup>*</sup>	<b>-0.908</b>	<b><sup>h</sup>-1.015</b>	-	-	<b><sup>i</sup>3.003</b>	<b>2.421</b>	-	-	<b>1.144</b>	-	-
		<b>(0.109)</b>									



MoS <sub>2</sub> _V <sub>S</sub> _1N <sub>S</sub>	<b>-0.196</b>	<b>-0.019</b>	<b>-0.962</b>	<b>0.089</b>	<b>3.116</b>	<b>2.384</b>	<b>2.016</b>	<b>2.699</b>	<b>1.176</b>	<b>178.975</b>	<b>1.025</b>
				<b>(0.544)</b>							
MoS <sub>2</sub> _1V <sub>Mo</sub> _3N <sub>S</sub>	<b>-1.818</b>	<b>-0.012</b>	<b>-2.557</b>	<b>0.027</b>	<b>3.313</b>	<b>2.365</b>	<b>2.046</b>	<b>‡1.776</b>	<b>1.177</b>	<b>178.581</b>	<b>1.419</b>
				<b>(0.256)</b>							
MoS <sub>2</sub> _1V <sub>Mo</sub> _1V <sub>S</sub>	<b>-0.252</b>	<b>-0.027</b>	<b>-</b>	<b>-</b>	<b>3.376</b>	<b>2.334</b>	<b>-</b>	<b>-</b>	<b>1.179</b>	<b>179.369</b>	<b>0.631</b>

<sup>a</sup> Q<sub>CO<sub>2</sub></sub> and <sup>b</sup> Q<sub>N</sub>, are total charge obtained by the CO<sub>2</sub> molecule and N atom of the dopant respectively. Negative charge means charge is transferred from MoS<sub>2</sub> surface atoms to the atoms of CO<sub>2</sub> molecule, and vice versa.

<sup>c</sup> M<sub>N</sub>, is the net magnetic moment of the N dopant atoms. The values in brackets are the net magnet moment of the entire structure.

<sup>d</sup> h<sub>mol-surf</sub>, is the equilibrium molecular height, the equilibrium molecular height is the height between the central carbon atom of the adsorbed CO<sub>2</sub> molecule and a reference atom of the MoS<sub>2</sub> surface in the basal plane in the z-direction yielded by optimization (That is, N atom, for N doped MoS<sub>2</sub> surface and average z plane of top S-layer atom, for non-doped MoS<sub>2</sub> surface).

<sup>e</sup> d<sub>Mo-S</sub>, is the average distance between Mo and S atoms close to the defect sites nearest to the adsorbed CO<sub>2</sub>.

<sup>f</sup> d<sub>N-Mo</sub>, is the average distance between the N atom and its neighbouring Mo atoms nearest to the adsorbed CO<sub>2</sub>.

<sup>g</sup> h<sub>N-S</sub>, is the height of the N atom with respect to the S plane (that is, S atom of the S-layer opposite to the layer doped with N atom).

\*MoS<sub>2</sub>\_1V<sub>S</sub> model, however might not be a stable system for sustainable CO<sub>2</sub> adsorption because of the strong tendency of one O atom of CO<sub>2</sub> to embed in the MoS<sub>2</sub> surface, thus creating Mo-O-Mo layer at the S vacancy site when the CO<sub>2</sub> molecule is oriented vertically leading to the formation of CO gas, therefore, the adsorption energy presented there is rather CO<sub>2</sub> dissociation energy.

<sup>h</sup> -1.015 (0.109) e, is the charge gained (lost) by the formed CO gas (O atom that bonded with the surface).

<sup>i</sup> 3.003 Å, is the distance between C atom of the formed CO gas and O atom that bonded with the surface.

<sup>‡</sup> 1.776 Å, is the average N-S triple bond length, that is, when CO<sub>2</sub> adsorbed on MoS<sub>2</sub>\_1V<sub>Mo</sub>\_3N<sub>S</sub> surface, triple bonds were formed between opposite dangling N and S atoms in the Mo vacancy.

\*NM, means nonmagnetic state, which shows that the investigated model exhibits a nonmagnetic state (i.e. total magnetic moment,  $\mu = 0 \mu_B$ ).

### 5.3.3.2 CO<sub>2</sub> Adsorption on Defective MoS<sub>2</sub> Monolayer

For MoS<sub>2</sub>\_1Vs, an improved adsorption efficiency of CO<sub>2</sub> is obtained with an adsorption energy of -0.908 eV. This energy is much stronger than those obtained for CO<sub>2</sub> interaction with some MOFs or carbon-based nanomaterials [268, 269]. As discussed earlier (subsection 5.3.3.1), only the MoS<sub>2</sub>\_1Vs model exhibited the dissociation of CO<sub>2</sub> to yield lattice-embedded oxygen and CO molecule that desorb from the surface at the considered molecular height (**Figure 5.5f**). The dissociative chemisorption of CO<sub>2</sub> on the single S vacancy defect can be associated with the perpendicular orientation of the CO<sub>2</sub> molecule and the increased covalent attractions. The covalent attraction was observed to be higher around the vacancy defect sites due to the three dangling Mo atoms. The O atom of the CO<sub>2</sub> molecule possesses an excess negative charge due to its higher electronegativity when compared to the central C atom. As a result, the O atom is strongly attracted to the more positively charged vacant site, due to the enhanced charge transfer from the excess positively charged dangling Mo atoms ( $Q_{Mo} = 0.07 e$ ) to the single S-vacancy defect sites (**Table 5.2**).

This explains why the CO<sub>2</sub> molecule tends to distance itself from the vicinity of single S vacancy defect of MoS<sub>2</sub> monolayer when linear CO<sub>2</sub> is placed horizontally along the z-axis since the positively charged central C atom of CO<sub>2</sub> is not electrostatically attracted to the positively charged dangling Mo atoms of single S vacancy defect. As a result, the large electropositive central C atom may make it difficult for CO<sub>2</sub> to grab electrons from the MoS<sub>2</sub>\_1Vs defect site and thus prevent the strong interaction between them. As shown in **Table 5.4**, the repulsive interaction between CO<sub>2</sub> and MoS<sub>2</sub>\_1Vs when linear CO<sub>2</sub>

molecule is horizontally oriented along the z-axis is reflected in the positive adsorption energy. This is one reason why the pristine MoS<sub>2</sub> surface does not strongly interact with CO<sub>2</sub> molecule as the layer of negatively charged S atoms shields the inner positively charged Mo atoms. Subsequently, a lesser interaction is observed on the pristine surface when CO<sub>2</sub> is perpendicularly oriented to the surface. The calculated energy of -0.908 eV is far larger than the value reported in Ref. [160] for CO<sub>2</sub> adsorption on the single SV defect site. This reported study suggested that CO<sub>2</sub> only physisorbed on MoS<sub>2</sub>\_1Vs. Part of the discrepancy can be attributed to the perpendicularly orientated CO<sub>2</sub> molecule and the effect of lateral interaction between the O of CO<sub>2</sub> pointing towards the S vacant site and the surface.

Furthermore, as shown in **Figure 5.5f**, the lattice-embedded oxygen and three dangling Mo atoms are linked by three newly formed O-Mo covalent bonds, whose average length is 2.081 Å, shorter than the Mo-S bond length. The formation of these bonds leads to the elongation of the surrounding Mo-S bonds from 2.412 to 2.421 Å as shown in **Table 5.5**. Bader Charge analysis shows 0.109 e charge transferred from the lattice-embedded oxygen to the detached CO, which obtained 1.015 e total electron charge. The distance between the C atom of the detached CO molecule and the lattice-embedded O atom is 3.003 Å. This value is smaller than 3.500 Å reported in Ref. [178] for CO physisorption on perfect MoS<sub>2</sub> surface, which indicates a strong physisorption state. The C-O bond length is calculated to be 1.114 Å, which is in excellent agreement with the experimental value of 1.13 Å [245].

Pertaining to MoS<sub>2</sub>\_1V<sub>Mo</sub>\_1Vs, the adsorption of CO<sub>2</sub> resulted in moderate adsorption energy of -0.252 eV, which corresponds to a physisorption process. CO<sub>2</sub> physisorption is therefore energetically favoured in MoS<sub>2</sub>\_1V<sub>Mo</sub>\_1Vs by -0.113 eV over the PMoS<sub>2</sub> and

notably lesser by -0.656 eV when compared to the dissociative adsorption on MoS<sub>2</sub>-1V<sub>S</sub>. The large difference in the adsorption energies between MoS<sub>2</sub>-1V<sub>S</sub> and MoS<sub>2</sub>-1V<sub>Mo</sub>-1V<sub>S</sub> can be attributed to the missing Mo atom in the MoS<sub>2</sub>-1V<sub>Mo</sub>-1V<sub>S</sub> surface, which reduces the electrostatic and covalent components of the interaction between the O atom of CO<sub>2</sub> and the vacant site. The adsorption distance of MoS<sub>2</sub>-1V<sub>Mo</sub>-1V<sub>S</sub> is 3.376 Å, which is also shorter than that obtained for PMoS<sub>2</sub>, and the CO<sub>2</sub> molecule adopts a tilted orientation, with O atom pointing to the MoS defect as shown in **Figure 5.5i**. The bond length of the physisorbed CO<sub>2</sub> slightly increased while the bond angle decreased by ~0.6° with respect to the linear CO<sub>2</sub> in the gas phase (**Table 5.5**). From the Bader charge analysis, 0.027 e charge is transferred from MoS<sub>2</sub>-1V<sub>Mo</sub>-1V<sub>S</sub> surface to CO<sub>2</sub> molecule, which is comparable to that obtained with the perfect surface. Thus, this proves that the CO<sub>2</sub> molecule gives a moderate interaction with the MoS<sub>2</sub>-1V<sub>Mo</sub>-1V<sub>S</sub> defect. The calculated adsorption energy of -0.252 eV is close to the value of -20.5 kJ/mol (-0.213 eV) reported by Ref. [18].

To analyse the electronic properties of the defect structures upon CO<sub>2</sub> adsorption, the density of state (DOS) and charge density difference were calculated. The charge density difference,  $\Delta\rho_{df}$ , is defined in subsection 5.2.3 Eq. (5.6). **Figure 5.7** presents the TDOS and PDOS of the adsorption system. The PDOS were projected on the relevant orbitals: p and d orbitals of the respective S and Mo atoms near the MoS and S vacancy sites, p orbital of N dopants, and the s and p orbitals of the CO and CO<sub>2</sub> molecules, and lattice embedded O atom. As can be seen in **Figure 5.7b**, when CO<sub>2</sub> is physisorbed on the MoS vacancy site (MoS<sub>2</sub>-1V<sub>Mo</sub>-1V<sub>S</sub>), there is an orbital coupling between the p orbital of CO<sub>2</sub> and the d orbital of the Mo atom, which is in agreement with a previous study [18]. There are no significant changes in the DOS spectra of either valence or conduction band of

MoS<sub>2</sub>\_1V<sub>Mo</sub>\_1V<sub>S</sub> upon CO<sub>2</sub> adsorption just like in the perfect surface. The narrower bandgap near the Fermi level, when compared to the pristine surface, is due to the defect states introduced because of vacancy formation (see **Figure 5.2b**). Contrarily, after CO<sub>2</sub> dissociated on MoS<sub>2</sub>\_1V<sub>Mo</sub>\_1V<sub>S</sub>, the lattice embedded O atom acts as coverage on the S vacancy site, thus there is a modification of the bandgap near the Fermi level (see **Figure 5.7a**). The defect states introduced because of unsaturated Mo atoms near the 1 S-vacancy is now eliminated by the lattice embedded O atom, forming 3 saturated Mo-O bonds. Hence, the bandgap near the Fermi level of this stable structure is normalized and compares with that of the perfect surface. This result agrees with reported studies that atmospheric oxygen heals vacancies and other defects resulting from a sulphur vacancy in MoS<sub>2</sub> [270, 271].

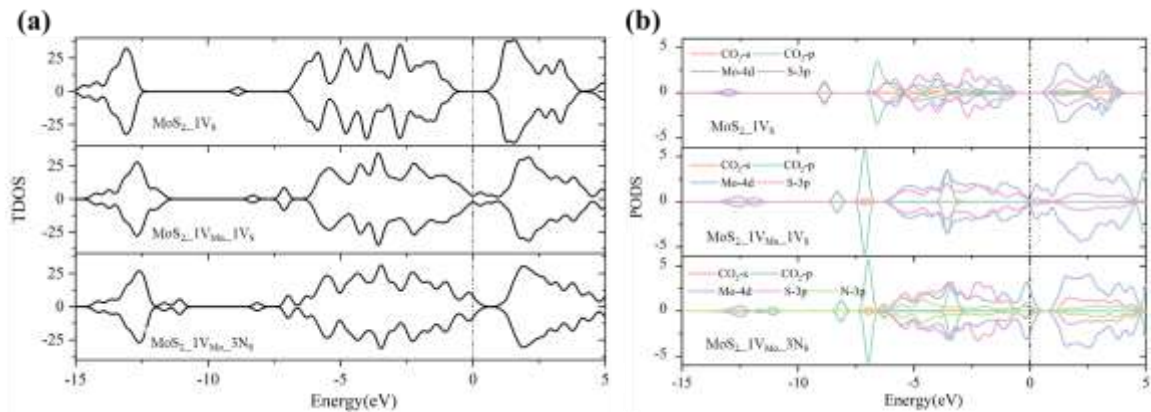


**Figure 5. 7:** (a) The TDOS and (b) The PDOS projected on the p and d orbitals of respective S and Mo atoms near to the MoS and S vacancy sites, p orbital of N dopants and the s and p orbitals of the physisorbed CO and CO<sub>2</sub> molecules, and lattice embedded O atom. MoS<sub>2</sub>\_1V<sub>S</sub>, MoS<sub>2</sub>\_1V<sub>Mo</sub>\_1V<sub>S</sub> and MoS<sub>2</sub>\_1V<sub>Mo</sub>\_3N<sub>S</sub> represent 1 S-vacancy, 1Mo- and 1S-vacancy, and tertiary nitrogen-doped 1 Mo-vacancy MoS<sub>2</sub> monolayers, respectively. The vertical dashed line corresponds to the Fermi level.

The isosurfaces of spin density difference for the CO<sub>2</sub> molecule adsorption on the defect surfaces (MoS<sub>2</sub>\_1V<sub>S</sub> and MoS<sub>2</sub>\_1V<sub>Mo</sub>\_1V<sub>S</sub>) are presented in **Figure 5.8**. There is a charge difference re-distribution in the middle region between the CO<sub>2</sub> molecule and MoS<sub>2</sub>\_1V<sub>Mo</sub>\_1V<sub>S</sub> substrate (**Figure 5.8b**), with much noticeable polarization of the MoS<sub>2</sub>\_1V<sub>Mo</sub>\_1V<sub>S</sub> sheet upon CO<sub>2</sub> adsorption. This indicates a stronger covalent character when compared to the perfect surface. This explains why the MoS<sub>2</sub>\_1V<sub>Mo</sub>\_1V<sub>S</sub> gives higher adsorption energy than the PMoS<sub>2</sub>. Meanwhile, there is more charge transfer and stronger interaction between the MoS<sub>2</sub>\_1V<sub>S</sub> surface with the lattice-embedded O atom and CO molecule (**Figure 5.8a**), which can be compared to that of Lewis acid interaction. The electrophilic C atom of CO makes the molecule Lewis acidic and interacts with lattice embedded O atom through electron acceptor-donor type interaction. A total electron charge of about 1.015 e is transferred from the surface to the CO molecule, with the embedded O atom contributing a considerable 0.109 e. The interaction of CO with the MoS<sub>2</sub>\_1V<sub>S</sub> is favoured by -0.968 e when compared to the total amount charge received by CO<sub>2</sub> molecule from both PMoS<sub>2</sub> and MoS<sub>2</sub>\_1V<sub>Mo</sub>\_1V<sub>S</sub> vacancy surfaces. The high amount of charge transfer to the CO molecule and the stability of the electronic structure of 1 S-vacancy MoS<sub>2</sub> due to the presence of O atom provides evidence of n-type doping and the effect of O atom on stabilizing the electronic properties of MoS<sub>2</sub>. Hence, this large electron transfer significantly changes the electronic transport properties of MoS<sub>2</sub>\_1V<sub>S</sub>.

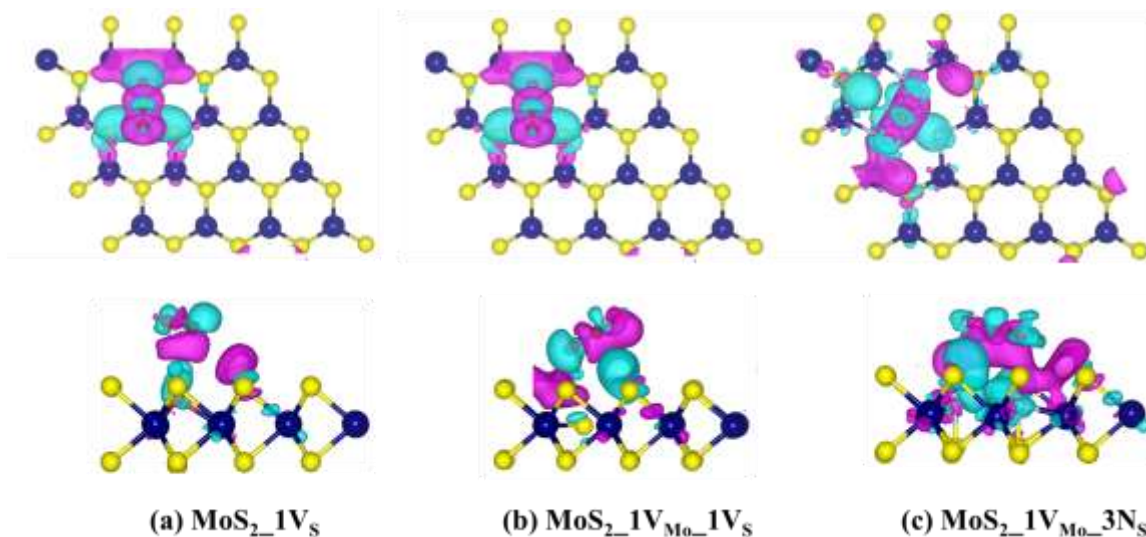


**Figure 5. 8:** Top and side views of isosurfaces of spin density difference of (a) 1 S-vacancy, (b) 1 Mo and 1 S vacancy and (c) tertiary nitrogen-doped 1 Mo-vacancy, with isosurface taken as  $\pm 0.00015 \text{ e/Bohr}^3$ . The light blue and pink colours represent the increase and decrease of electron density, respectively.

### 5.3.3.3 $\text{CO}_2$ Adsorption on N-doped Defected $\text{MoS}_2$ Monolayer

From the results presented in **Table 5.5**, it is evident that the  $\text{MoS}_2\text{-1V}_{\text{Mo-3N}_S}$  site possesses the highest activity for  $\text{CO}_2$  adsorption ( $E_{\text{AE}} = -1.818 \text{ eV}$ ) amongst all of the considered N-doped models, which is significantly higher than the defective  $\text{MoS}_2$  monolayers ( $\text{MoS}_2\text{-1V}_S$  and  $\text{MoS}_2\text{-1V}_{\text{Mo-1V}_S}$ ). Therefore, to understand the effect of nitrogen doping on vacancy  $\text{MoS}_2$ , the adsorption characteristic of  $\text{MoS}_2\text{-1V}_{\text{Mo-3N}_S}$  is investigated. Also, the adsorption properties of  $\text{CO}_2$  molecule on  $\text{MoS}_2\text{-1V}_{\text{Mo-3N}_S}$  sites are calculated and compared with that of the perfect  $\text{MoS}_2$  and non-doped vacancy surfaces. As shown in **Figure 5.5**,  $\text{CO}_2$  physisorbed on  $\text{MoS}_2\text{-1V}_{\text{Mo-3N}_S}$  has an equilibrium molecular height of  $3.313 \text{ \AA}$  with its molecular axis parallel to the  $\text{MoS}_2\text{-1V}_{\text{Mo-3N}_S}$  basal

plane. This parallel adsorption configuration is similar to that of CO<sub>2</sub> adsorption on the pristine MoS<sub>2</sub> surface, except that the CO<sub>2</sub> physisorbed on the perfect surface displayed an equilibrium molecular height of 3.456 Å. The physisorption of CO<sub>2</sub> molecule on the N doped vacancy site stretches out the surficial N atoms resulting in an increase in  $d_{N-Mo}$  from 1.93 Å (**Table 5.3**) to 2.046 Å (**Tables 5.5**).

The interaction between CO<sub>2</sub> and MoS<sub>2</sub>\_1V<sub>Mo</sub>\_3N<sub>S</sub> surface yields stronger CO<sub>2</sub>-surface interactions compared to pristine MoS<sub>2</sub> (PMoS<sub>2</sub>) or the other defect (vacancy or N-substitutional doping) sites. Specifically, the CO<sub>2</sub> adsorption physisorption energy is approximately 13 times as strong as that on a PMoS<sub>2</sub>. The superior adsorption performance is also illustrated by the difference in the equilibrium molecular height between MoS<sub>2</sub>\_1V<sub>Mo</sub>\_3N<sub>S</sub> and PMoS<sub>2</sub>. The difference can be explained by their bonding nature with CO<sub>2</sub>. The positively charged central carbon atom of the CO<sub>2</sub> molecule is attracted electrostatically to the negatively charged tertiary nitrogen atoms surrounding the Mo vacancy. The absence of a Mo atom lessens the repulsive component of the interaction. As shown in **Table 5.2**, the adsorption energetic configuration for the CO<sub>2</sub> molecule on MoS<sub>2</sub>\_1V<sub>Mo</sub>\_3N<sub>S</sub> is obtained when the linear CO<sub>2</sub> molecular axis is placed parallel to the surface. Less or repulsive interaction is observed when linear CO<sub>2</sub> is perpendicularly oriented to the surface, with the O atom pointing to the MoS<sub>2</sub> basal plane. The result indicates that for pristine MoS<sub>2</sub> surface, CO<sub>2</sub> physisorption mainly occurs on the basal plane through vdW interaction, whereas the N atoms surrounding the Mo vacancy site in MoS<sub>2</sub>\_1V<sub>Mo</sub>\_3N<sub>S</sub> promotes the physical interaction between CO<sub>2</sub> molecules through non-covalent interaction and enhanced electrostatic interaction on the N doped Mo vacancy sites. This result demonstrates that N doping could boost the effective surface for CO<sub>2</sub>



adsorption by facilitating both vdW and electrostatic interactions. This phenomenon is quite similar to CO<sub>2</sub> physisorption on N doped carbon surface [228].

Furthermore, the geometric structures of the CO<sub>2</sub> molecule adsorbed on MoS<sub>2</sub>\_1V<sub>Mo</sub>\_3N<sub>S</sub> were calculated to understand the surface-molecule interactions. The bond length and bond angle of the physisorbed CO<sub>2</sub> molecule were calculated and compared related to the values in the gas phase. As shown in **Table 5.5**, the bond angle of the physisorbed CO<sub>2</sub> molecule changed compared to the gas phase CO<sub>2</sub>. The calculated bond angle of physisorbed CO<sub>2</sub> is 178.68°, which decreased by 1.42° with respect to the gas phase CO<sub>2</sub> molecule [245]. The decrease in CO<sub>2</sub> bond angle makes the optimized state highly exothermic with a difference in adsorption energy of about -1.7 eV with respect to the pristine surface, where the bond angles remain almost unchanged after adsorption. **Table 5.5** also shows that the bond length of the physisorbed CO<sub>2</sub> molecule is unchanged compared to the gas phase CO<sub>2</sub> molecule. Therefore, the geometric structure of the CO<sub>2</sub> molecule is not affected when it is adsorbed on N doped 1 Mo-vacancy site, indicating only physical interaction.

Similar to the perfect and MoS<sub>2</sub>\_1V<sub>Mo</sub>\_1V<sub>S</sub> surfaces, the DOS analysis shows that there are no significant changes in the DOS spectra of either valence or conduction band of MoS<sub>2</sub>\_1V<sub>Mo</sub>\_3N<sub>S</sub> upon CO<sub>2</sub> adsorption. However, the bandgap near the Fermi level was observed to be narrower than that for the pristine surface since the introduction of the N atom and 1 Mo-vacancy induces impurity and defect state, respectively, as explained in subsection **5.3.2.2.2**. The only observed effect of the adsorption is the orbital coupling between the p orbital of the CO<sub>2</sub> molecule and the d orbital of the Mo atom, as shown in **Figure 5.7b**.

Bader charge analysis reveals that the interaction between the CO<sub>2</sub> molecule and MoS<sub>2</sub>-1V<sub>Mo</sub>-3N<sub>S</sub> surface also resulted in charge transfer and redistribution. As shown in **Table 5.5**, while 0.020 e is transferred to CO<sub>2</sub> on the pristine surface, only 0.012 e is transferred to CO<sub>2</sub> when 1 Mo-vacancy is doped with N atoms. The difference in the charge transfer supports the Lewis-acid interaction analogy between CO<sub>2</sub> and MoS<sub>2</sub>-1V<sub>Mo</sub>-3N<sub>S</sub> surface but is less noticeable when compared to the pristine and non-doped vacancy surfaces. Moreover, the reactive surface N atoms gain more electrons after CO<sub>2</sub> adsorption compared to the electrons gained by the N dopants before adsorption. Specifically, the total electron gained by the N dopant before and after CO<sub>2</sub> adsorption is 2.21 e (**Table 5.3**) and 2.557 e, respectively. Thus, the N dopants become more negatively charged after adsorption with an additional charge of 0.347 e. Also, as the surface N atoms become negatively charged, less charge is transferred to the CO<sub>2</sub> molecule and higher adsorption energy is obtained, different from the behaviour observed in pristine (PMoS<sub>2</sub>) and non-doped vacancy (MoS<sub>2</sub>-1V<sub>S</sub> and MoS<sub>2</sub>-1V<sub>Mo</sub>-1V<sub>S</sub>) surfaces. This is attributed to the electron transfer from the oxygen atom of CO<sub>2</sub> molecules and indicates that the CO<sub>2</sub> molecule binds strongly onto the N doped vacancy site by transferring some of the electrons of the O atom. These results further demonstrate that nitrogen doping of MoS<sub>2</sub> belongs to the p-type doping, which agrees with reference [267].

This conclusion drawn based on Bader charge analysis can be confirmed by the charge density difference,  $\Delta\rho_{df}$ . As shown in **Figure 5.8c**, charge difference redistributes in the middle region between CO<sub>2</sub> molecule and MoS<sub>2</sub>-1V<sub>Mo</sub>-3N<sub>S</sub> substrate, with much more noticeable polarization of the MoS<sub>2</sub>-1V<sub>Mo</sub>-3N<sub>S</sub> sheet upon molecules adsorption, indicating a stronger covalent character, when compared to the perfect surface and the

MoS<sub>2</sub>-1V<sub>Mo</sub>-1V<sub>S</sub>. The light blue and pink colours represent an increase and decrease of charge electron density, respectively. When CO<sub>2</sub> is physisorbed onto the surface, the reactive surface N atoms receive electrons from the region between the CO<sub>2</sub> central carbon atom and itself to strengthen the interaction between CO<sub>2</sub> and the surface. The increase in the pink colour (decrease of electron density) in the middle region between the CO<sub>2</sub> and MoS<sub>2</sub>-1V<sub>Mo</sub>-3N<sub>S</sub> surface compared to the cases of defect-free and non-doped defective surfaces, indicates less charge transfer to CO<sub>2</sub> upon the adsorption on MoS<sub>2</sub>-1V<sub>Mo</sub>-3N<sub>S</sub>. Also, the increase in the light blue colour (an increase of electron density) on the surface N atoms compared to MoS<sub>2</sub>-1V<sub>Mo</sub>-3N<sub>S</sub> surface before adsorption (**Figure 5.3**), shows the reactive surface N atoms gained more electrons after CO<sub>2</sub> adsorption. As a result, a large region of electron depletion appears near the oxygen atoms and there is lower electron density surrounding CO<sub>2</sub> compared to that of CO<sub>2</sub> on the perfect surface. For the magnetic properties, upon CO<sub>2</sub> adsorption, the magnetic moment of the surface N atom is significantly reduced to 0.027  $\mu_B$ , while the net magnetic moment locates on the adsorbed CO<sub>2</sub> molecule as shown in **Figure 5.8c**. This significant impact on the magnetic moment of MoS<sub>2</sub>-1V<sub>Mo</sub>-3N<sub>S</sub> upon CO<sub>2</sub> adsorption proposes MoS<sub>2</sub>-1V<sub>Mo</sub>-3N<sub>S</sub> as a suitable CO<sub>2</sub> sensing device. These results suggest that CO<sub>2</sub> interacts strongly with the Mo vacancy site when the surrounding S atoms are substituted with N atoms. In general, the adsorption efficacy of the MoS<sub>2</sub> surface can be promoted by any measure that can enhance the electrostatic interaction between the CO<sub>2</sub> molecule and the surface complex, other than vdW interactions. This can be revealed by the electron charge distribution and magnetic moment-induced polarization. The qualitative difference between adsorption mechanisms associated with CO<sub>2</sub> on the perfect surface and non-doped vacancy defect sites, and

nitrogen-doped Mo vacancy defect sites stresses the importance of nitrogen doping on vacancies for CO<sub>2</sub> adsorption in the MoS<sub>2</sub> system.

### **5.3.3.4 Infrared (IR) Spectroscopy of CO<sub>2</sub> Adsorption on MoS<sub>2</sub>\_1V<sub>S</sub>, MoS<sub>2</sub>\_1V<sub>Mo</sub>\_1V<sub>S</sub> and MoS<sub>2</sub>\_1V<sub>Mo</sub>\_3N<sub>S</sub> Surfaces**

Calculation of the infrared (IR) spectroscopy of molecules adsorbed on the surface in conjunction with the experimental measurements can provide a valuable approach to probe the structure of the surface adsorbates. The vibrational frequencies of the CO<sub>2</sub> molecule adsorbed on MoS<sub>2</sub>\_1V<sub>S</sub>, MoS<sub>2</sub>\_1V<sub>Mo</sub>\_1V<sub>S</sub> and MoS<sub>2</sub>\_1V<sub>Mo</sub>\_3N<sub>S</sub> surfaces were calculated and compared to the gas phase. As shown in **Table 5.6**, the vibrational frequencies of the asymmetric ( $\nu_3$ ) and symmetric ( $\nu_1$ ) stretching modes for gas phase CO<sub>2</sub> was calculated to be 2361 cm<sup>-1</sup> and 1328 cm<sup>-1</sup>, respectively. The bending frequencies ( $\nu_2$ ) for gas phase CO<sub>2</sub> is calculated to be 633 cm<sup>-1</sup>. The calculated value is in good agreement with the experimental value [245, 272]. The discrepancies between the DFT calculated vibrational frequencies and the true vibrational frequencies arise from the harmonic treatment of the DFT vibrations and the inexact nature of DFT in solving the Schrödinger equation, which are common in quantum chemistry calculations [273]. To correct the discrepancies, the DFT results are often multiplied by a scaling factor (in the range of 0.95-0.99 for typical GGA) to match the experimental measurements [273]. In this study, we used a scaling factor of 0.989.

The computed asymmetric stretching modes ( $\nu_3$ ) for physisorbed CO<sub>2</sub> molecule on MoS<sub>2</sub>\_1V<sub>Mo</sub>\_1V<sub>S</sub> and MoS<sub>2</sub>\_1V<sub>Mo</sub>\_3N<sub>S</sub> surfaces are 2353 cm<sup>-1</sup> and 2355 cm<sup>-1</sup>, respectively. These values downshift by 8 cm<sup>-1</sup> and 6 cm<sup>-1</sup> to the value calculated in gas phase CO<sub>2</sub>. The

calculated symmetric stretching modes ( $\nu_1$ ) for physisorbed CO<sub>2</sub> on MoS<sub>2</sub>-1V<sub>Mo</sub>-3N<sub>S</sub> surface, 1317 cm<sup>-1</sup>, downshifts by 11 cm<sup>-1</sup> with respect to the calculated symmetric stretching mode of gas phase CO<sub>2</sub>. The calculated symmetric stretching mode for physisorbed CO<sub>2</sub> on MoS<sub>2</sub>-1V<sub>Mo</sub>-1V<sub>S</sub> is 1315 cm<sup>-1</sup>, which downshifts by 13 cm<sup>-1</sup> with respect to the calculated symmetric stretching mode of CO<sub>2</sub> in the gas phase. The slight downshift in the vibrational frequencies of the physisorbed CO<sub>2</sub> molecule indicates that the C=O bonds are slightly weakened when the CO<sub>2</sub> molecule interact with MoS<sub>2</sub>-1V<sub>Mo</sub>-1V<sub>S</sub> and MoS<sub>2</sub>-1V<sub>Mo</sub>-3N<sub>S</sub> sites.

Moreover, upon interaction with the MoS<sub>2</sub>-1V<sub>Mo</sub>-3N<sub>S</sub> site, the CO<sub>2</sub> deformation mode ( $\nu_2$ ) of 633 cm<sup>-1</sup> remain unchanged with respect to the computed value in the gas phase. Upon interacting with the MoS<sub>2</sub>-1V<sub>Mo</sub>-1V<sub>S</sub> site, the deformation mode ( $\nu_2$ ) of CO<sub>2</sub> is 623 cm<sup>-1</sup>, which downshifts by 10 cm<sup>-1</sup> compared to the  $\nu_2$  mode in the gas phase. This downshift is responsible for the slight increase in C=O bond length as shown in **Table 5.5**. Together with the fact that the bond length and vibrational frequencies of CO<sub>2</sub> slightly changed, it can be concluded that C=O bonds are slightly weakened when the CO<sub>2</sub> molecule is physisorbed on MoS<sub>2</sub>-1V<sub>Mo</sub>-1V<sub>S</sub> and MoS<sub>2</sub>-1V<sub>Mo</sub>-3N<sub>S</sub> sites. This confirms that there is no chemical bonding, and interactions are dominated by weak vdW forces.

The vibrational mode of CO molecule formed upon CO<sub>2</sub> interaction with MoS<sub>2</sub>-1V<sub>S</sub> site is also calculated. The most intense frequency value, 2119 cm<sup>-1</sup>, corresponds to the C≡O stretching mode (**Table 5.6**), which is in excellent agreement with the experimental value [245, 272]. This value is lower than the C=O bonds in the gas phase CO<sub>2</sub>. In addition to the decrease in C–O bond length and the formation of a triple bond, we can conclude that the dissociation of CO<sub>2</sub> on the MoS<sub>2</sub>-1V<sub>S</sub> site leads to the formation CO of molecule. To

the authors' knowledge, in terms of experimental and computational comparison, there are no direct vibrational frequencies of CO<sub>2</sub> molecule physisorbed on the non-doped vacancy and tertiary N doped Mo vacancy MoS<sub>2</sub> sites. It is reasonable to compare the computed modes with CO<sub>2</sub> molecule in the gas phase, to understand how these modes shifted upon interacting with the surfaces.

**Table 5.6:** Calculated Vibrational Frequencies ( $\text{cm}^{-1}$ ) for  $\text{CO}_2$  molecule adsorption on  $\text{MoS}_2_{-1\text{V}_\text{S}}$ ,  $\text{MoS}_2_{-1\text{V}_{\text{Mo}_-1\text{V}_\text{S}}}$  and  $\text{MoS}_2_{-1\text{V}_{\text{Mo}_-3\text{N}_\text{S}}}$  sites. Calculated and Experimental values of gas-phase  $\text{CO}_2$  molecule are included for comparison.

Molecule	Gas-phase		Physisorption on	Dissociation
	Experimental	Theoretical	$\text{MoS}_2_{-1\text{V}_{\text{Mo}_-1\text{V}_\text{S}}}$ / $\text{MoS}_2_{-1\text{V}_{\text{Mo}_-3\text{N}_\text{S}}}$	on $\text{MoS}_2_{-1\text{V}_\text{S}}$
			Current	
			work	
<b>C=O</b>				
stretching	2349	[245, 2360 [236]	2361	2353/2355
Asymmetric	272]	1321 [236]	1328	1315/1317
( $\nu_3$ )	1333	[245,		
Symmetric	272]			
( $\nu_1$ )				
C=O	667 [245, 272]	638 [236]	633	623/633
bending ( $\nu_2$ )				
C≡O	2131	[245,		2119
stretching	272]			

### 5.3.3.5 Selective Adsorption of CO<sub>2</sub>, N<sub>2</sub> and H<sub>2</sub>O

An effective CO<sub>2</sub> adsorbent should selectively adsorb CO<sub>2</sub> molecule over other competitive gaseous molecules, such as N<sub>2</sub>. Since our interest is on selectivity, only the binding energies of all the molecules on pristine and defect MoS<sub>2</sub> monolayer sites are compared and discussed here. This is important for testing the trapping and catalytic activity of the MoS<sub>2</sub> sites. The highest adsorption energies between each substrate and the adsorbate (CO<sub>2</sub>, N<sub>2</sub> and H<sub>2</sub>O) are compared in **Figure 5.9a**. It can be seen that the N<sub>2</sub> adsorption is weaker than CO<sub>2</sub> adsorption for all surfaces except MoS<sub>2</sub>\_1N<sub>Mo</sub>\_1N<sub>S</sub>, in which N<sub>2</sub> is dissociated with high dissociation energy rather than adsorbing on the surface. The weaker adsorption energy of N<sub>2</sub> is attributed to its smaller quadrupole moment and polarizability properties than those of CO<sub>2</sub>. Also, MoS<sub>2</sub>\_1V<sub>S</sub> exhibits a weaker interaction with N<sub>2</sub> than pristine MoS<sub>2</sub> and the defective surfaces. The interaction between N<sub>2</sub> and MoS<sub>2</sub>\_1V<sub>S</sub> is repulsive as shown by the positive adsorption energy value, whereas CO<sub>2</sub> interacts exothermically with MoS<sub>2</sub>\_1V<sub>S</sub>, leading to dissociation of CO<sub>2</sub> molecule. This result implies that MoS<sub>2</sub>\_1V<sub>S</sub> is a good adsorbent for CO<sub>2</sub> activation and not effective for N<sub>2</sub> adsorption.

It is clear that the selective adsorption of CO<sub>2</sub> over N<sub>2</sub> is based on different binding affinities on the adsorbent surface. Therefore, the ratio and difference of the highest adsorption energies for CO<sub>2</sub> and N<sub>2</sub> can be indicators of selective adsorption (**Figure 5.9b**). From **Figure 5.9b**, MoS<sub>2</sub>\_1V<sub>S</sub> and PMoS<sub>2</sub> exhibit a relatively higher ratio of adsorption energy, while MoS<sub>2</sub>\_1N<sub>S</sub>, MoS<sub>2</sub>\_2N<sub>S</sub>, MoS<sub>2</sub>\_3N<sub>S</sub> and MoS<sub>2</sub>\_1V<sub>S</sub>\_1N<sub>S</sub> exhibit a similar ratio of adsorption energy. The highest ratio of 5.1 is obtained for the MoS<sub>2</sub>\_1V<sub>S</sub> surface, while the lowest ratio of 0.5 is obtained for MoS<sub>2</sub>\_1N<sub>Mo</sub>\_1N<sub>S</sub>. Although the highest



adsorption energies for CO<sub>2</sub> and N<sub>2</sub> molecules are obtained for, MoS<sub>2</sub>\_1V<sub>Mo</sub>\_3N<sub>S</sub> structure (see **Figure 5.6** and **Figure 5.10a**, respectively), but the smaller ratio of 1.0 compared to the values obtained for other structures. When the difference of adsorption energies for CO<sub>2</sub> and N<sub>2</sub> is compared, the MoS<sub>2</sub>\_1V<sub>S</sub> site appears to be a more suitable adsorbent for selective adsorption and separation of CO<sub>2</sub> over N<sub>2</sub>.

The adsorption of an H<sub>2</sub>O molecule on the same surfaces is also compared to CO<sub>2</sub> adsorption to predict the stability of the defect and defect free MoS<sub>2</sub> monolayers towards the H<sub>2</sub>O contaminant. **Figure 5.9c** presents the ratio and difference of the highest adsorption energies for CO<sub>2</sub> and H<sub>2</sub>O in each studied surface. Unlike the N<sub>2</sub> adsorption, H<sub>2</sub>O was found to bind more strongly on all the surfaces than CO<sub>2</sub> except on the MoS<sub>2</sub>\_1V<sub>S</sub> monolayer. The stronger adsorption of the H<sub>2</sub>O molecule is characterized by its high polarity and quadrupole moment than those of CO<sub>2</sub>. This is because the polarity of molecules adsorbed on any surface represents a very important factor that influences their interaction with the electric field of the surface. In other words, adsorbates that have the high quadrupole moment, such as H<sub>2</sub>O, interact strongly with the electric field of the MoS<sub>2</sub> monolayer and this favours their adsorption.

The highest ratio of 3.5 is obtained for MoS<sub>2</sub>\_1V<sub>S</sub>, whereas an adsorption ratio less than one is obtained for other surfaces. Also, by comparing the difference in adsorption energies for CO<sub>2</sub> and H<sub>2</sub>O, it is evident that MoS<sub>2</sub>\_1V<sub>S</sub> favours CO<sub>2</sub> adsorption over H<sub>2</sub>O. The positive difference in the adsorption energies and low ratio of adsorption energies of CO<sub>2</sub> over H<sub>2</sub>O for the pristine, N-substitutional and double vacant systems indicate that they exhibit excellent selective adsorption of H<sub>2</sub>O over CO<sub>2</sub> molecule. Therefore, the presence of H<sub>2</sub>O could significantly decrease the adsorption capacity of these MoS<sub>2</sub> monolayer

systems towards selective adsorption and separation of CO<sub>2</sub>. Although the results showed that the MoS<sub>2</sub>\_1V<sub>S</sub> site is a suitable adsorbent for selective adsorption and separation of CO<sub>2</sub>, the optimization of the MoS<sub>2</sub> monolayers structural characteristics and the experimental conditions that will ensure the removal of water vapour to the lowest value might enhance substantially their CO<sub>2</sub> adsorption capacity and thereby might give rise to the excellent adsorbents that may be used to capturing the industrial emissions of CO<sub>2</sub>. Finally, CO<sub>2</sub> appears to bind stronger on the MoS<sub>2</sub>\_1V<sub>Mo</sub>\_3N<sub>S</sub> site than N<sub>2</sub>, making it a suitable adsorbent for selective adsorption and separation of CO<sub>2</sub> over N<sub>2</sub>, but for the application of CO<sub>2</sub> storage, the existence of H<sub>2</sub>O may affect the partial charge distribution of the nitrogen-doped vacancy sites.

All the calculated results for the most stable adsorption configurations of N<sub>2</sub> and H<sub>2</sub>O molecules on different surfaces are summarized in **Table 5.7** and **Table 5.8**. Also, the adsorption energy curves of N<sub>2</sub> and H<sub>2</sub>O molecules over the studied local geometric configurations were calculated as shown in **Figure 5.10**.

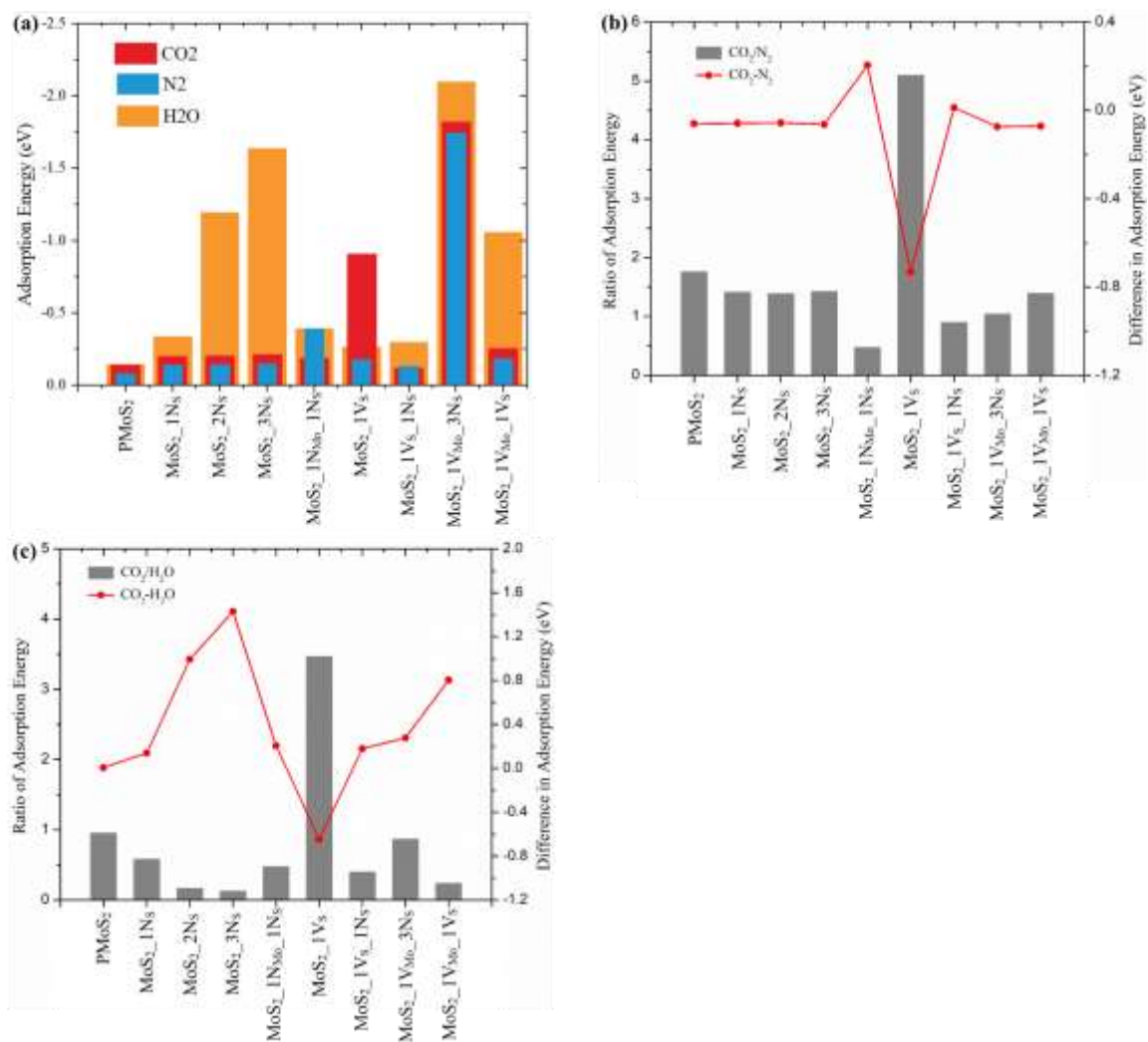


**Figure 5. 9:** Investigation of CO<sub>2</sub> adsorption selectivity over N<sub>2</sub> and the effect of moisture content (a) The adsorption energies of CO<sub>2</sub>, N<sub>2</sub> and H<sub>2</sub>O molecules for the most stable adsorption configurations compared at 2.5 Å molecular height, (b) ratio and difference of adsorption energies between CO<sub>2</sub> and N<sub>2</sub> molecules, (c) ratio and difference of adsorption energies between CO<sub>2</sub> and H<sub>2</sub>O molecules.

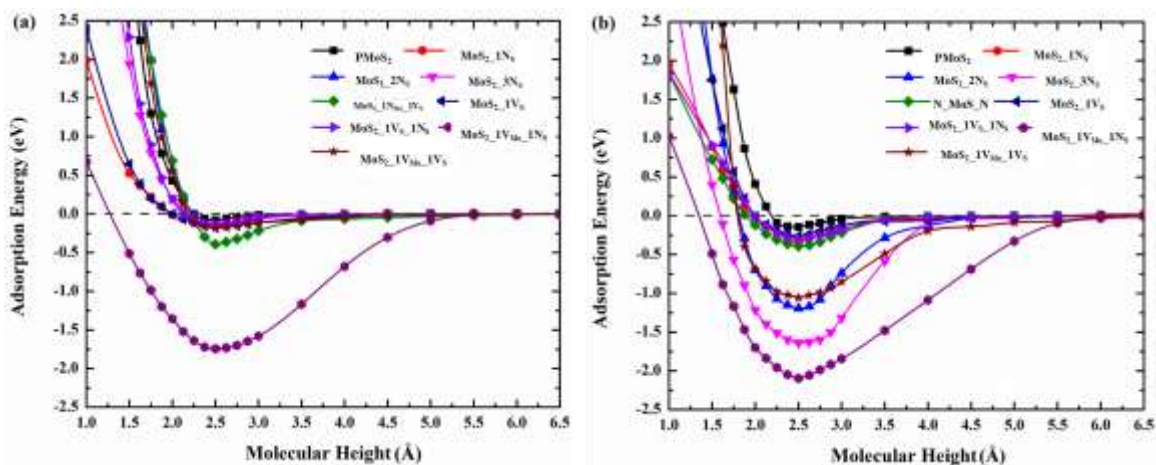


**Figure 5. 10:** Adsorption energy versus molecular height. Adsorption energy as a function of molecular height for (a) N<sub>2</sub> and (b) H<sub>2</sub>O molecules adsorbed on all the studied most stable local geometric configurations calculated by the same method applied for CO<sub>2</sub> as represented in Figure 5. [Here, molecular height is the distance between a reference atom of the MoS<sub>2</sub> surface in the basal plane in the z-direction (i.e. N atom, for N doped MoS<sub>2</sub> surface and average z plane of top S-layer atom for non-doped MoS<sub>2</sub> surface) and the (a) nearest N atom of the adsorbed N<sub>2</sub> molecule, and (b) central O atom of the adsorbed H<sub>2</sub>O molecule, respectively. Molecular Height is the same as explained in **Figure 5.6**.

**Table 5.7:** Summary of calculated results for adsorption of N<sub>2</sub> on most stable configurations of different surfaces at 2.5 Å initial molecular height.

Model	$\Delta E_{AE}$ , eV	$Q_{N_2^a}$ , e	$Q_N^b$ , e	$h_{mol-surf}^c$ , Å	$d_{Mo-S}^d$ , Å	$d_{N-Mo}^e$ , Å	$h_{N-S}^f$ , Å	$l$ , Å	$\Delta l$
PMoS <sub>2</sub>	<b>-0.079</b>	<b>-0.009</b>	-	<b>3.657</b>	<b>2.412</b>	-	-	<b>1.114</b>	<b>0.000</b>
MoS <sub>2</sub> _1N <sub>S</sub>	<b>-0.139</b>	<b>-0.012</b>	<b>-0.943</b>	<b>3.014</b>	<b>2.446</b>	<b>2.015</b>	<b>2.687</b>	<b>1.114</b>	<b>0.000</b>
MoS <sub>2</sub> _2N <sub>S</sub>	<b>-0.144</b>	<b>-0.013</b>	<b>-1.882</b>	<b>3.014</b>	<b>2.448</b>	<b>2.018</b>	<b>2.677</b>	<b>1.114</b>	<b>0.000</b>
MoS <sub>2</sub> _3N <sub>S</sub>	<b>-0.148</b>	<b>-0.012</b>	<b>-2.806</b>	<b>3.097</b>	<b>2.478</b>	<b>2.036</b>	<b>2.660</b>	<b>1.114</b>	<b>0.000</b>
MoS <sub>2</sub> _1N <sub>Mo</sub> _1N <sub>S</sub>	<b>-0.391</b>	<b>-0.152</b>	<b>-1.155</b>		<b>2.362</b>	<b>2.154</b>	<b>2.841</b>	<b>1.148</b>	<b>0.034</b>
MoS <sub>2</sub> _1V <sub>S</sub>	<b>-0.178</b>	<b>-0.242</b>	-		<b>2.386</b>	-	-	<b>1.131</b>	<b>0.017</b>
MoS <sub>2</sub> _1V <sub>S</sub> _1N <sub>S</sub>	<b>-0.132</b>	<b>-0.012</b>	<b>-0.951</b>	<b>3.054</b>	<b>2.441</b>	<b>2.019</b>	<b>2.694</b>	<b>1.114</b>	<b>0.000</b>
MoS <sub>2</sub> _1V <sub>Mo</sub> _3N <sub>S</sub>	<b>-1.744</b>	<b>-0.007</b>	<b>-2.549</b>	<b>3.031</b>	<b>2.367</b>	<b>2.044</b>	<b>**1.777</b>	<b>1.114</b>	<b>0.000</b>
MoS <sub>2</sub> _1V <sub>Mo</sub> _1V <sub>S</sub>	<b>-0.181</b>	<b>-0.016</b>	-	<b>3.687</b>	<b>2.365</b>	-	-	<b>1.114</b>	<b>0.000</b>

<sup>a</sup>  $Q_{N_2}$  and <sup>b</sup>  $Q_N$ , are total charge obtained by the  $N_2$  molecule and N dopant atom respectively. Negative charge means charge is transfer from  $MoS_2$  surface atoms to the atoms of  $N_2$  molecule, and vice versa.

<sup>c</sup>  $h_{mol-surf}$ , is the equilibrium molecular height, the equilibrium molecular height is the nearest distance between the N atom of the adsorbed  $N_2$  molecule and a reference atom of the  $MoS_2$  surface in the basal plane in the z-direction yielded by optimization (That is, N atom, for N doped  $MoS_2$  surface and average z plane of top S-layer atom, for non-doped  $MoS_2$  surface).

<sup>d</sup>  $d_{Mo-S}$ , is the average distance between Mo and S atoms close to the defect sites nearest to the adsorbed  $N_2$ .

<sup>e</sup>  $d_{N-Mo}$ , is the average distance between the N atom and its neighbouring Mo atoms nearest to the adsorbed  $N_2$ .

<sup>f</sup>  $h_{N-S}$ , is the height of the N atom with respect to the S plane (that is, S atom of the S-layer opposite to the layer doped with N atom).

<sup>‡\*</sup> 1.777 Å, is the average N-S triple bond length, that is, when  $N_2$  adsorbed on  $MoS_2-1V_{Mo}-3N_S$  surface, triple bonds were formed between opposite dangling N and S atoms in the Mo vacancy.

**Table 5.8:** Summary of calculated results for adsorption of H<sub>2</sub>O on most stable configurations of different surfaces at 2.5 Å initial molecular height.

Model	$\Delta E_{AE}$ , eV	$Q_{H_2O}^a$ , e	$Q_N^b$ , e	$h_{mol-surf}^c$ , Å	$d_{Mo-S}^d$ , Å	$d_{N-Mo}^e$ , Å	$h_{N-S}^f$ , Å	$l^g$ , Å	$\theta^h$ , °	$\Delta\theta$ , °
PMoS <sub>2</sub>	<b>-0.146</b>	<b>-0.021</b>	-	<b>3.459</b>	<b>2.413</b>	-	-	<b>0.974</b>	<b>103.777</b>	<b>0.723</b>
MoS <sub>2</sub> _1N <sub>S</sub>	<b>-0.337</b>	<b>-0.017</b>	<b>0.990</b>	<b>2.800</b>	<b>2.444</b>	<b>2.023</b>	<b>2.692</b>	<b>0.981</b>	<b>104.442</b>	<b>0.058</b>
MoS <sub>2</sub> _2N <sub>S</sub>	<b>-1.193</b>	<b>0.245</b>	<b>-1.647</b>	-	<b>2.420</b>	<b>2.115</b>	<b>2.725</b>	-	-	-
MoS <sub>2</sub> _3N <sub>S</sub>	<b>-1.639</b>	<b>-0.000</b>	<b>-2.867</b>	<b>3.041</b>	<b>2.475</b>	<b>2.035</b>	<b>2.663</b>	<b>0.977</b>	<b>102.192</b>	<b>2.308</b>
MoS <sub>2</sub> _1N <sub>Mo</sub> _1N <sub>S</sub>	<b>-0.391</b>	<b>-0.044</b>	<b>-1.174</b>	-	<b>2.465</b>	<b>2.037</b>	<b>2.713</b>	-	-	-
MoS <sub>2</sub> _1V <sub>S</sub>	<b>-0.262</b>	<b>-0.507</b>	-	-	<b>2.401</b>	-	-	-	-	-
MoS <sub>2</sub> _1V <sub>S</sub> _1N <sub>S</sub>	<b>-0.298</b>	<b>-0.020</b>	<b>-0.998</b>	<b>3.459</b>	<b>2.437</b>	<b>2.022</b>	<b>2.703</b>	<b>0.980</b>	<b>103.974</b>	<b>0.526</b>
MoS <sub>2</sub> _1V <sub>Mo</sub> _3N <sub>S</sub>	<b>-1.966</b>	<b>0.001</b>	<b>-2.637</b>	<b>2.869</b>	<b>2.366</b>	<b>2.046</b>	** <b>1.776</b>	<b>0.979</b>	<b>103.053</b>	<b>1.447</b>
MoS <sub>2</sub> _1V <sub>Mo</sub> _1V <sub>S</sub>	<b>-1.057</b>	<b>-0.754</b>	-	-	<b>2.344</b>				-	

<sup>a</sup>  $Q_{H_2O}$  and <sup>b</sup>  $Q_N$ , are total charge obtained by the H<sub>2</sub>O molecule and N dopant atom respectively. Negative charge means charge is transferred from MoS<sub>2</sub> surface atoms to the atoms of H<sub>2</sub>O molecule, and vice versa.

<sup>c</sup>  $h_{\text{mol-surf}}$ , is equilibrium molecular height, the equilibrium molecular height is the nearest distance between the central O atom of the adsorbed H<sub>2</sub>O molecule and a reference atom of the MoS<sub>2</sub> surface in the basal plane in the z-direction (That is, N atom, for N doped MoS<sub>2</sub> surface and average z plane of top S-layer atom, for non-doped MoS<sub>2</sub> surface),

<sup>d</sup>  $d_{\text{Mo-S}}$ , is the average distance between Mo and S atoms close to the defect sites nearest to the adsorbed CO<sub>2</sub>.

<sup>e</sup>  $d_{\text{N-Mo}}$ , is the average distance between the N atom and its neighbouring Mo atoms nearest to the adsorbed CO<sub>2</sub>.

$l^g$  and  $\theta^h$ , is the average bond length and bond angle of H<sub>2</sub>O after adsorption, respectively,  $\Delta\theta$  is the change in H<sub>2</sub>O bond angle

<sup>f</sup>  $h_{\text{N-S}}$ , is the height of the N atom with respect to the S plane (that is, S atom of the S-layer opposite to the layer doped with N atom).

<sup>g</sup> 1.776 Å, is the average N-S triple bond length, that is, when H<sub>2</sub>O adsorbed on MoS<sub>2</sub>-1V<sub>Mo</sub>-3N<sub>S</sub> surface, triple bonds were formed between opposite dangling N and S atoms in the Mo vacancy.



## 5.4 Summary and Conclusions

It can be concluded that all of the considered surfaces with vacancy defects and N-doping at the vacancy site exhibit superior adsorption activity, selectivity and stability except for the N-substituted Mo atom ( $\text{MoS}_2\text{-1N}_{\text{Mo}}$ ) surface. Among the 10 different surface models studied, the 1 sulphur-vacancy ( $\text{MoS}_2\text{-1V}_{\text{S}}$ ) and tertiary nitrogen-doped 1 Mo-vacancy ( $\text{MoS}_2\text{-1V}_{\text{Mo-3N}_{\text{S}}}$ ) exhibit strong binding energies of -0.908 and -1.818 eV, respectively. These values are approximately 7 and 13 times as strong as that of a pristine  $\text{MoS}_2$  surface. The results reveal that  $\text{CO}_2$  mainly adsorbs on the basal plane of pristine  $\text{MoS}_2$  surface because of vdW interactions, while the vacancy defect and N doping perturb the local electron density of  $\text{MoS}_2$  surfaces and greatly promote  $\text{CO}_2$  adsorption with covalent and electrostatic interactions. Among various vacancy defects,  $\text{MoS}_2\text{-1V}_{\text{S}}$  improved the adsorption efficiency of  $\text{CO}_2$  through dissociative chemisorption, leading to the reduction of  $\text{CO}_2$  to CO gas. This phenomenon is promoted by the perpendicular orientation of the  $\text{CO}_2$  molecule after geometric optimization, which increased the covalent attractions at the vacant site. Meanwhile, a double molybdenum and sulphur (MoS) vacancy defect ( $\text{MoS}_2\text{-1V}_{\text{Mo-1V}_{\text{S}}}$ ) facilitates  $\text{CO}_2$  physisorption by enhancing the vdW interactions between  $\text{CO}_2$  and the basal plane of the vacancy site. The promotional effects of tertiary nitrogen doping of 1 Mo-vacancy on  $\text{CO}_2$  physisorption can be attributed to the enhanced electrostatic interactions.

In addition,  $\text{MoS}_2\text{-1V}_{\text{S}}$  and  $\text{MoS}_2\text{-1V}_{\text{Mo-3N}_{\text{S}}}$  surfaces showed stronger selective adsorption of  $\text{CO}_2$  over  $\text{N}_2$ . Due to stronger adsorption, the energy of  $\text{H}_2\text{O}$  over  $\text{CO}_2$  at the tertiary nitrogen-doped 1 Mo-vacancy site, application of this material for  $\text{CO}_2$  storage may be limited by moisture, by affecting the partial charge distribution of the nitrogen species at the vacancy site. The results in this study are expected to be helpful to reveal the  $\text{CO}_2$  adsorption mechanism and develop  $\text{CO}_2$

adsorbents based on MoS<sub>2</sub> materials containing nitrogen. These will provide new insights for improved molecular adsorption on heteroatom-doped MoS<sub>2</sub> surfaces, which has been witnessed on carbon surfaces. On this note, the study of the effect of vacancy defects and nitrogen doping on the dissociation of CO<sub>2</sub> and H<sub>2</sub>O over MoS<sub>2</sub> monolayers is studied at an operating temperature of only 300 °C was achieved (see **Chapter 6 and 7**).

## CHAPTER 6

# Investigating the Effect of Vacancy Defects and Nitrogen Doping on the Adsorption and Dissociation of CO<sub>2</sub> and H<sub>2</sub>O over Mos<sub>2</sub> Monolayers

### 6.1 Introduction

Due to global climate change caused by the emission of greenhouse gases such as anthropogenic CO<sub>2</sub> [3, 35], the hydrogenation of CO<sub>2</sub> into carbon-based fuels and chemicals has become an attractive approach for mitigating CO<sub>2</sub> emissions via the utilization of CO<sub>2</sub> on a large-scale [2, 274-277]. In this approach, the dissociation of H<sub>2</sub>O plays an important role as it acts as either a hydrogen source or a reactant [275]. However, under ambient conditions, the conversion efficacy of conventional catalysts is limited by the low local concentration of CO<sub>2</sub> at the active sites and its inherent stability [2]. Under ambient conditions, H<sub>2</sub>O conversion is hindered by its thermodynamic energetics, low Faradaic efficiency (FE), and poor selectivity [24]. In both cases, these features slow down the conversion kinetics involving the transformation of CO<sub>2</sub> to CO [2, 278] and the conversion of H<sub>2</sub>O to OH\* and H\* [279]. To offset these limitations, there is a need to develop bi-functional catalysts that can simultaneously promote CO<sub>2</sub> conversion and H<sub>2</sub>O dissociation by improving the reaction kinetics at low temperatures.

Recently, metal- and metal oxide-based catalysts have been found to have the greatest catalytic efficiency for the conversion of CO<sub>2</sub> and H<sub>2</sub>O dissociation on an industrial scale [280-283].

However, the low conversion of CO<sub>2</sub> and H<sub>2</sub>O, and insufficient stability at 493-573 K restrict the application of these catalysts [280, 281, 284, 285]. Furthermore, the high cost of these precious metals [280, 281], and the high requirement of overpotential and current density [286, 287] hinder their industrial application. Therefore, there is still a need for significantly improved catalytic efficiency and selectivity to achieve viable transformation of CO<sub>2</sub> on an industrial scale [287].

Due to its layered structure and unique electronic configuration, molybdenum disulphide (MoS<sub>2</sub>) has been identified as a promising candidate for the catalytic conversion of CO<sub>2</sub> [157, 158]. However, the low electron transfer of the basal plane of MoS<sub>2</sub> can lead to slow catalytic kinetics [14, 15]. One of the methods to attenuate its catalytic sluggishness is the introduction of point defects [21], which are usually more reactive than the sites on a perfect surface. Another method of promoting its intrinsic catalytic characteristics is to create basic or redox-active surface sites by incorporating nitrogen into a surface framework [19, 22, 23] or introducing a promoter cation [24, 25]. These manipulate its conductivity and charge density to activate the inert S atoms in the basal plane, thus, promoting electron transfer [162]. Theoretical and experimental studies have shown that catalytic properties of transition-metal surfaces are improved when doped with metals (Fe, Co, Ni and Cu) [165, 275] or non-metals (N, P, O, Se, Cl) [19, 22, 23]. Generally speaking, catalytic behaviour is determined by the structure of the catalyst particle [288] and the barrier at which the reaction proceeds readily at room temperature [165]. Hence, the existence of activation barriers can impose additional constraints and poses a fundamental limitation to the catalytic efficiency of transition metal-based catalysts for CO<sub>2</sub> conversion and H<sub>2</sub>O splitting [289, 290] under ambient conditions. Therefore, to develop catalysts that are high-performance in CO<sub>2</sub> reduction and water splitting at low activation barriers and good electronic conductivity it is necessary to modify the electronic properties and boost the catalytic performance of MoS<sub>2</sub>, for example, to substitute S

atoms with N atoms [291]. By observing the impact of N dopants on various vacancies over MoS<sub>2</sub> in **Chapter 5**, it was discovered that the type of vacancy defect and the number of N active sites affect the adsorption performance of MoS<sub>2</sub>. The removal of the Mo atom from a unit cell of the MoS<sub>2</sub> surface creates a large hole with six unsaturated edge S atoms, thus making it available for substitutional doping. However, to the best of our knowledge, the tertiary N-doping of single-vacancy MoS<sub>2</sub> for CO<sub>2</sub> reduction and H<sub>2</sub>O splitting has not been reported.

In this chapter, we employ a range of computational chemistry tools to investigate the adsorption and dissociation of CO<sub>2</sub> and H<sub>2</sub>O on tertiary N-doped, single Mo vacancy MoS<sub>2</sub> (MoS<sub>2</sub>\_1V<sub>Mo</sub>\_3N<sub>S</sub>). An in-depth, first principles-based investigation of CO<sub>2</sub> reduction (CO<sub>2</sub> → CO<sup>-</sup> + H<sup>+</sup>) and water splitting (H<sub>2</sub>O → OH<sup>-</sup> + H<sup>+</sup>) mechanisms, in terms of thermodynamic stability, active sites, activation barriers and rate of reactions on MoS<sub>2</sub>\_1V<sub>Mo</sub>\_3N<sub>S</sub> are carried out.

## 6.2 Computational Methods and Models

In this section, the computational details, which include, the simulation models and methods employed to investigate the effect of vacancy defects and nitrogen doping on the adsorption and dissociation of CO<sub>2</sub> and H<sub>2</sub>O over MoS<sub>2</sub> monolayers are detailed. A range of computational chemistry tools as well as other calculation details is also discussed.

### 6.2.1 Computational Details

Computational methods and technical details of the simulations of gas adsorption on MoS<sub>2</sub> used in this study are detailed in **Chapter 5**. In **Chapter 5**, it has been found that MoS<sub>2</sub>\_1V<sub>Mo</sub>\_3N<sub>S</sub> shows excellent adsorption stability. Therefore, the present study was restricted to this adsorption site. Briefly, a MoS<sub>2</sub>\_1V<sub>Mo</sub>\_3N<sub>S</sub> site is formed by replacing three neighbouring S atoms in a unit cell with three N atoms and removing the adjacent Mo atom. A water coverage of 0.25 ML (i.e. one H<sub>2</sub>O molecule per unit cell) was used to represent water adsorption on a monolayer. The spin-polarized DFT-D2 calculations were performed for the simulated adsorption configurations using Grimme's [216] method, as implemented in the Vienna *ab initio* simulation package (VASP) [211, 212]. All calculations were performed under the same relaxation criteria.

The frequencies of the phonon modes have been calculated through the finite difference method using a displacement of 0.015, and by fixing all of the atoms of the MoS<sub>2</sub> monolayer. This approach has been shown to introduce little or no error in the computed frequencies and intensities of the adsorbed molecules and results in a significant reduction in computational cost [262]. The vibrational modes of the molecules in the gas phase were also computed to compare with the different adsorption configurations.

The evaluation of minimum-energy reaction paths (MEPs) and the transition states (TS) was performed using the climbing image nudged elastic band (CI-NEB) method [184]. The finite temperature analysis of the dissociative adsorption system at 300 K was conducted using *ab initio* molecular dynamics (AIMD) on the Born-Oppenheimer surface. A timestep of 1.0 femtoseconds (fs) was employed and the temperature of the system was maintained using a Nosé-Hoover thermostat, which normalized particle velocities every 40-time steps. Moreover, the *ab initio*

thermodynamics method [182, 183] was applied to investigate the adsorption performance under non-zero temperature and pressure of the surrounding atmosphere, to analyse the thermodynamic stability of the considered most stable adsorption surface when exposed to a given environment. Further details regarding the use of the ab initio thermodynamics method are included in Subsection 6.2.2.

### 6.2.2 Calculation Details

The adsorption energy ( $E_{AE}$ ) is calculated as,

$$E_{AE} = E_{Surf+X} - (E_{Surf} + E_X) \quad (6.1)$$

Where,  $E_{Surf}$  and  $E_{Surf+X}$  are the total energies of the surface (pristine (PMoS<sub>2</sub>) or the defect (MoS<sub>2</sub>-1V<sub>Mo</sub>-3N<sub>S</sub>) monolayer MoS<sub>2</sub> and that with the adsorbed X (CO<sub>2</sub>, N<sub>2</sub> and H<sub>2</sub>O) molecule respectively, and  $E_X$  is the total energy of the isolated X molecule. A negative value of  $E_{AE}$  indicates that the adsorption is exothermic, which means that the adsorption of X molecule on the surface of the structure is favoured energetically, vice versa.

To analyse the electronic property of the PMoS<sub>2</sub> and MoS<sub>2</sub>-1V<sub>Mo</sub>-3N<sub>S</sub> structures upon CO<sub>2</sub>, N<sub>2</sub> and H<sub>2</sub>O adsorption, the charge density difference,  $\Delta\rho_{df}$ , were calculated using Eq. (6.2)

$$\Delta\rho_{df} = \Delta\rho_{Surf+X} - (\Delta\rho_{Surf} + \Delta\rho_X) \quad (6.2)$$

Where  $\Delta\rho_{Surf+X}$ ,  $\Delta\rho_{Surf}$  and  $\Delta\rho_X$  are the charge density of X (CO<sub>2</sub>, N<sub>2</sub> and H<sub>2</sub>O)-MoS<sub>2</sub> adsorption system, MoS<sub>2</sub> substrate and X molecule, respectively.

### 6.2.3 Ab Initio Thermodynamic Calculation Details

The ab Initio thermodynamic calculations were obtained using the following equation:

$$\Delta G_{ads}(T, P) = G_{Surf+gas}(T, P) - G_{surf}(T, P) - G_{gas}(T, P) \quad (6.3)$$

where,  $G_{Surf+gas}(T, P)$ ,  $G_{surf}(T, P)$  and  $G_{gas}(T, P)$  are the Gibbs free energies as a function of temperature and pressure of the  $\text{MoS}_2\text{-1V}_{\text{Mo-3N}_S}$  surface with the adsorbed molecule, the  $\text{MoS}_2\text{-1V}_{\text{Mo-3N}_S}$  surface and the Gibbs free energy of the isolated gas phase molecule, respectively.

The  $\text{MoS}_2\text{-1V}_{\text{Mo-3N}_S}$  surface with the adsorbed gas molecule and  $\text{MoS}_2\text{-1V}_{\text{Mo-3N}_S}$  surface can be represented as a product in solid phase slab with adsorbate and solid phase slab reagents, respectively. Hence, Gibbs free energies of the solid phase reagents have relatively small variations with respect to temperature and pressure and can be approximated by the energy computed by DFT (the Helmholtz free energy at 0 K without zero-point energy correlation) [292]. Contrarily, the Gibbs free energy of the isolated gas phase molecule will be strongly affected by temperature and pressure and can be defined as [182, 292]:

$$G_{gas}(T, P) = G_g(0K, P^\circ) + \Delta H_g(T, P^\circ) - T\Delta S_{gas}(T, P^\circ) + K_B T \ln(P/P^\circ) \quad (6.4)$$

The first term,  $G_g(0K, P^\circ) \approx E_{gas}^{DFT}$ , which is the DFT calculated total energy of the isolated gas phase molecule; the second and third terms are the contribution of gas enthalpy and entropy under at atmospheric pressure ( $P^\circ = 1 \text{ atm}$ ), respectively, which could be obtained from standard thermodynamic database [293]; the fourth term is a pressure-dependent contribution [182, 292].



Combing Eq. (6.3) and (6.4), and the approximations, the different contributions to the total Gibbs free energy of adsorption can be written explicitly as:

$$\Delta G_{gas}(T, P) = \Delta E_{AE}^{DFT} + F^{vib,ads}(T) - \Delta H_g(T, P^\circ) + T\Delta S_{gas}(T, P^\circ) - K_B T \ln(P/P^\circ) \quad (6.5)$$

Where  $\Delta E_{AE}^{DFT}$  is the adsorption energy that is calculated from Eq. (6.1) and  $F^{vib,ads}(T)$  is the difference between the vibrational contribution to the free gas molecule and the free energy of the adsorbed molecule (adsorbate)

$$F^{vib,ads}(T) = F_{adsorbate}^{vib}(T) - F_{free}^{vib}(T) \quad (6.6)$$

Where the vibrational energies of the adsorbed molecule (adsorbate) and the free gas molecule can be estimated by the vibrational free energy within the harmonic approximation for n fundamental modes (with frequencies of  $\omega_i$ ) of the system as:

$$F^{vib}(T) = \sum_{i=1}^n F^{vib}(T, \hbar\omega_i) = \sum_{i=1}^n \left[ \frac{1}{2} \hbar\omega_i + K_B T \ln(1 - e^{-\frac{\hbar\omega_i}{K_B T}}) \right] \quad (6.7)$$

Here, we only considered  $n = 3N-3$  nodes, where N is the number of atoms allowed to vibrate. A detailed description of this method can be found in published works [182, 183, 294]. The adsorption (reaction) is stable when  $\Delta G_{gas}(T, P) < 0$ . It follows that if contributions from enthalpy and entropy are neglected in Eq. (6.5), the condition for stability of adatom is when  $F^{vib, ads}(T) < \Delta E_{AE}^{DFT}$ . The equilibrium is reached when  $\Delta G_{gas}(T, P) = 0$  and  $F^{vib, ads}(T) = \Delta E_{AE}^{DFT}$ .

## 6.3 Results and Discussion

### 6.3.1 Adsorption of CO<sub>2</sub>, N<sub>2</sub>, and H<sub>2</sub>O on MoS<sub>2</sub>-1V<sub>Mo</sub>-3N<sub>S</sub>

In this section, the adsorption of CO<sub>2</sub>, nitrogen (N<sub>2</sub>) and water (H<sub>2</sub>O) molecules on MoS<sub>2</sub>-1V<sub>Mo</sub>-3N<sub>S</sub> was investigated to ascertain the adsorption performance of MoS<sub>2</sub>-1V<sub>Mo</sub>-3N<sub>S</sub> sites in terms of adsorption energy and the structure of the molecule and surface upon interaction. Thereafter, Infrared (IR) spectroscopy was also performed to probe the structure of the surface adsorbates as well as the electronic properties are also discussed.

#### 6.3.1.1 Adsorption Energies and Structures

The atomic configurations and adsorption energies of CO<sub>2</sub>, N<sub>2</sub> and H<sub>2</sub>O molecules on pristine MoS<sub>2</sub> (PMoS<sub>2</sub>) and MoS<sub>2</sub>-1V<sub>Mo</sub>-3N<sub>S</sub> are shown in **Figure 6.1**, while **Table 6.1** shows the physisorption of these molecules. As shown in **Table 6.1**, MoS<sub>2</sub>-1V<sub>Mo</sub>-3N<sub>S</sub> possesses higher adsorption stability and energy ( $E_{AE}$ ) for the adsorption of CO<sub>2</sub>, N<sub>2</sub>, and H<sub>2</sub>O molecules as compared with adsorption on the perfect MoS<sub>2</sub> surface. The adsorption energies of CO<sub>2</sub>, N<sub>2</sub> and H<sub>2</sub>O are -1.818, -1.744 and -1.966 eV (as shown in **Table 6.1**), with equilibrium molecular heights of 3.313, 3.031 and 2.869 Å (as shown in **Figure 6.1** (a) to (c)), respectively. In addition, it is observed that the most stable adsorption configuration varies with different gas molecules. While CO<sub>2</sub> and N<sub>2</sub> molecules adopt a configuration that is parallel to the MoS<sub>2</sub>-1V<sub>Mo</sub>-3N<sub>S</sub> basal plane, the H<sub>2</sub>O molecule displayed a partially vertical orientation, in which one of the O-H bonds is positioned almost perpendicular to the MoS<sub>2</sub>-1V<sub>Mo</sub>-3N<sub>S</sub> basal plane with the H atom pointing to the MoS<sub>2</sub>-1V<sub>Mo</sub>-3N<sub>S</sub> surface. However, the orientation of H<sub>2</sub>O being adsorbed on the pristine surface is different, with the axis that crosses the two H atoms being parallel to the MoS<sub>2</sub> surface,

while the orientation of CO<sub>2</sub> and N<sub>2</sub> is similar to that on the MoS<sub>2</sub>\_1V<sub>Mo</sub>\_3N<sub>S</sub> surface. On the pristine surface, the adsorption energies of CO<sub>2</sub>, N<sub>2</sub> and H<sub>2</sub>O are -0.139 eV, -0.079 eV and -0.021 eV (as shown in **Table 6.1**), with equilibrium molecular heights of 3.456, 3.657 and 3.459 Å (as shown in **Figure 6.1** (d) to (f)), respectively.

**Table 6.1:** Summary of the physisorption of CO<sub>2</sub>, N<sub>2</sub> and H<sub>2</sub>O molecules on MoS<sub>2</sub>\_1V<sub>Mo</sub>\_3N<sub>S</sub> and P<sub>Mo</sub>S<sub>2</sub>.

Molecule	MoS <sub>2</sub> _1V <sub>Mo</sub> _3N <sub>S</sub>			P <sub>Mo</sub> S <sub>2</sub>		
	<i>E<sub>AE</sub></i> , eV	Q <sub>X</sub> , e	Q <sub>N</sub> , e	<i>E<sub>AE</sub></i> , eV	Q <sub>X</sub> , e	Q <sub>N</sub> , e
CO <sub>2</sub>	<b>-1.818</b>	<b>-0.012</b>	<b>-2.557</b>	<b>-0.139</b>	<b>-0.020</b>	-
N <sub>2</sub>	<b>-1.744</b>	<b>-0.007</b>	<b>-2.549</b>	<b>-0.079</b>	<b>-0.009</b>	-
H <sub>2</sub> O	<b>-1.966</b>	<b>-0.001</b>	<b>-2.637</b>	<b>-0.146</b>	<b>-0.021</b>	-

\* The values of the adsorption molecules on the P<sub>Mo</sub>S<sub>2</sub> surface are included for comparison. *E<sub>AE</sub>* is the adsorption energy and Q<sub>N</sub> is the total charge obtained by N atoms, Q<sub>X</sub> is the total charge obtained by the X (X= CO<sub>2</sub>, N<sub>2</sub> and H<sub>2</sub>O) molecule.

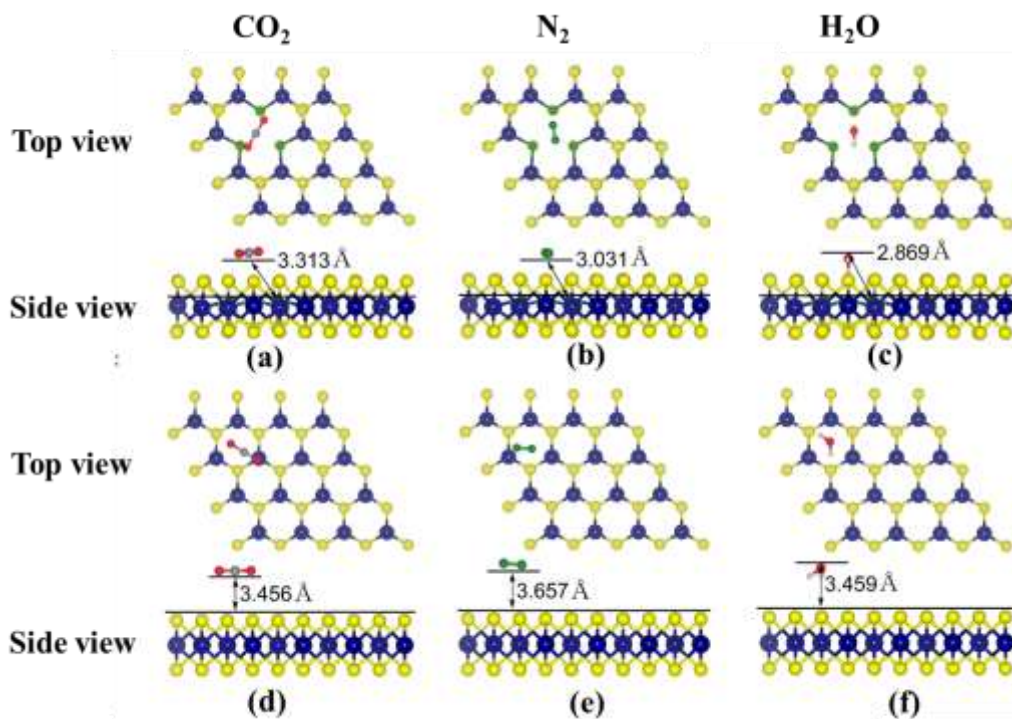


**Figure 6.1:** The most stable adsorption configurations for the adsorption of  $\text{CO}_2$ ,  $\text{N}_2$  and  $\text{H}_2\text{O}$  molecules on  $\text{MoS}_2\text{-1V}_{\text{Mo}}\text{-3N}_\text{S}$  (a-c) and  $\text{PMoS}_2$  (d-f). Colour code: Mo, blue, S, yellow, and N, green. O, C and H atoms are shown in red, grey and white, respectively. The lines define the equilibrium molecular height between the reference atoms of the molecules ( $\text{CO}_2$  (carbon),  $\text{H}_2\text{O}$  (oxygen),  $\text{N}_2$  (nitrogen)) and a reference atom of the  $\text{MoS}_2$  surface in the basal plane in the z-direction yielded by optimization (i.e. N atom for  $\text{MoS}_2\text{-1V}_{\text{Mo}}\text{-3N}_\text{S}$  surface and average z plane of S atoms, for  $\text{PMoS}_2$  surface given in Å).

These results show that the  $\text{MoS}_2\text{-1V}_{\text{Mo}}\text{-3N}_\text{S}$  surface yields stronger interactions with each adsorbate than the  $\text{PMoS}_2$  surface. Specifically, the adsorption energy of  $\text{CO}_2$  on  $\text{MoS}_2\text{-1V}_{\text{Mo}}\text{-3N}_\text{S}$  is approximately 13 times stronger than on the  $\text{PMoS}_2$ . Furthermore, the adsorption of  $\text{N}_2$  and  $\text{H}_2\text{O}$  molecules on  $\text{MoS}_2\text{-1V}_{\text{Mo}}\text{-3N}_\text{S}$  is approximately 22 and 14 times stronger than on  $\text{PMoS}_2$ , respectively. Moreover, when the equilibrium molecular height is compared, it is clear that  $\text{CO}_2$ ,

$\text{N}_2$  and  $\text{H}_2\text{O}$  molecules strongly adsorbed on the  $\text{MoS}_2\text{-1V}_{\text{Mo}}\text{-3N}_\text{S}$  site than on the  $\text{PMoS}_2$  site when the surface was fully relaxed.

The adsorption configurations and larger adsorption energy, when compared with perfect surface, can be explained by their bonding nature with  $\text{CO}_2$ ,  $\text{N}_2$  and  $\text{H}_2\text{O}$  molecules. The carbon atom and hydrogen atoms of  $\text{CO}_2$  and  $\text{H}_2\text{O}$  molecules, respectively, possess a positive charge due to their lower Pauling electronegativity compared to the oxygen atom. Therefore, are attracted electrostatically to the triangle formed by negatively charged tertiary nitrogen atoms surrounding the Mo vacancy. The absence of the Mo atom lessens the repulsive component of the interaction. As shown in **Figure 6.1**, the adsorption energetic configuration for the  $\text{CO}_2$  molecule on  $\text{MoS}_2\text{-1V}_{\text{Mo}}\text{-3N}_\text{S}$  is obtained when the linear  $\text{CO}_2$  molecular axis is placed parallel to the surface. Less or repulsive interaction is observed when linear  $\text{CO}_2$  is perpendicularly oriented to the surface, with the O atom pointing to the  $\text{MoS}_2$  basal plane, just like the adsorption on a perfect  $\text{MoS}_2$  surface. Contrarily, the  $\text{H}_2\text{O}$  molecule prefers a perpendicularly oriented configuration, with the H atom pointing to the  $\text{MoS}_2$  basal plane as shown in **Figure 6.1**. Meanwhile,  $\text{N}_2$  adsorbed strongly on  $\text{MoS}_2\text{-1V}_{\text{Mo}}\text{-3N}_\text{S}$  site, when  $\text{N}_2$  molecular axis is parallel to  $\text{MoS}_2\text{-1V}_{\text{Mo}}\text{-3N}_\text{S}$  surface, while less or repulsive interaction is observed for perpendicular orientation. Unlike  $\text{N}_2$  adsorption on  $\text{MoS}_2\text{-1V}_{\text{Mo}}\text{-3N}_\text{S}$ ,  $\text{N}_2$  adsorption on the pristine surface is relatively the same irrespective of  $\text{N}_2$  molecule orientation. The less interaction of  $\text{N}_2$  and  $\text{MoS}_2\text{-1V}_{\text{Mo}}\text{-3N}_\text{S}$  when placed perpendicularly to the surface can be ascribed to nearly the same Pauling electronegativity of the  $\text{N}_2$  molecule and surface N atoms. The similarity of adsorption configuration of  $\text{N}_2$  on pristine surface irrespective of orientation is due to lower electronegativity of S atom of the surface to diatomic  $\text{N}_2$  molecule. For  $\text{PMoS}_2$ , the adsorption of  $\text{CO}_2$ ,  $\text{H}_2\text{O}$  and  $\text{N}_2$  mainly occur on the basal plane through vdW forces. The strong interactions between  $\text{CO}_2$ ,  $\text{H}_2\text{O}$  and  $\text{N}_2$  and

MoS<sub>2</sub>\_1V<sub>Mo</sub>\_3N<sub>S</sub> can be attributed to the enhanced electrostatic interactions due to the presence of Mo vacancy and N species, except for N<sub>2</sub> adsorption, due to less electrostatic interaction with MoS<sub>2</sub>\_1V<sub>Mo</sub>\_3N<sub>S</sub>. These results demonstrate that N doping could boost the effective surface for CO<sub>2</sub>, N<sub>2</sub> and H<sub>2</sub>O adsorption by facilitating both vdW and electrostatic interactions.

### 6.3.1.2 Geometric Structure and Vibrational Frequency Predictions

The vibrational frequencies of the molecules adsorbed on MoS<sub>2</sub>\_1V<sub>Mo</sub>\_3N<sub>S</sub> surfaces were calculated and compared to the gas phase. The calculation of the infrared (IR) spectroscopy of molecules adsorbed on the surface in conjunction with the experimental measurements can provide a valuable approach to probe the structure of the surface adsorbates. As shown in **Table 6.2**, the calculated bond angle of adsorbed CO<sub>2</sub> is 178.58°, which decreases by 1.419° with respect to the gas phase linear CO<sub>2</sub> molecule [245]. Similarly, the calculated bond angle of adsorbed H<sub>2</sub>O molecule decreases by 1.471°, when compared with a H<sub>2</sub>O molecule in the gas phase. The bond lengths of adsorbed CO<sub>2</sub> and N<sub>2</sub> molecules are unchanged compared to the gas phase molecules, as shown in **Table 6.2**. For the adsorption of H<sub>2</sub>O, the bond length of the O-H bond, which is almost perpendicular to the MoS<sub>2</sub>\_1V<sub>Mo</sub>\_3N<sub>S</sub> surface increases by 0.013 Å. The other O-H bond length remains unchanged, indicating a strong interaction between the former bond and the surface. The vibrational frequencies of the asymmetric ( $\nu_3$ ) and symmetric ( $\nu_1$ ) stretching modes for gas phase CO<sub>2</sub> and H<sub>2</sub>O were calculated to be 2361, 3843 cm<sup>-1</sup> and 1328, 3729 cm<sup>-1</sup>, respectively, while the N≡N stretching mode for gas phase N<sub>2</sub> was 2424 cm<sup>-1</sup>. The bending frequencies ( $\nu_2$ ) for gas phase CO<sub>2</sub> and H<sub>2</sub>O are calculated to be 633 cm<sup>-1</sup> and 1584 cm<sup>-1</sup>, respectively. The calculated values are in good agreement with the experimental values [245, 272, 295, 296]. The computed C=O and O-H asymmetric stretching modes ( $\nu_3$ ) for adsorbed CO<sub>2</sub> and H<sub>2</sub>O molecules on the

MoS<sub>2</sub>-1V<sub>Mo</sub>-3N<sub>S</sub> surface are 2355 cm<sup>-1</sup> and 3788 cm<sup>-1</sup>, respectively. These values downshift by 6 cm<sup>-1</sup> and 55 cm<sup>-1</sup> to the values calculated in their respective gas phase. The calculated C=O symmetric stretching modes ( $\nu_1$ ) for adsorbed CO<sub>2</sub>, 1317 cm<sup>-1</sup>, downshifts by 11 cm<sup>-1</sup> with respect to the calculated symmetric stretching mode of gas phase CO<sub>2</sub>. Similarly, the calculated O-H symmetric stretching mode ( $\nu_1$ ) for adsorbed H<sub>2</sub>O, 3788 cm<sup>-1</sup>, downshifts sharply by 235 cm<sup>-1</sup> with respect to the calculated symmetric stretching mode of H<sub>2</sub>O in the gas phase. In contrast, the calculated N≡N stretching mode for adsorbed N<sub>2</sub> (2424 cm<sup>-1</sup>) is almost the same as the calculated value in the gas phase. The slight or no downshift in the vibrational frequencies of adsorbed CO<sub>2</sub> and N<sub>2</sub> molecules, indicate that the C=O and N≡N bonds are stronger when CO<sub>2</sub> and N<sub>2</sub> molecules interact with the MoS<sub>2</sub>-1V<sub>Mo</sub>-3N<sub>S</sub> site. The higher downshifts in the vibrational frequencies of adsorbed H<sub>2</sub>O molecule, shows that the O-H bond becomes weaker when the H<sub>2</sub>O molecule is adsorbed onto the MoS<sub>2</sub>-1V<sub>Mo</sub>-3N<sub>S</sub> site. Finally, upon interaction with the MoS<sub>2</sub>-1V<sub>Mo</sub>-3N<sub>S</sub> site, the CO<sub>2</sub> deformation mode ( $\nu_2$ ) of 633 cm<sup>-1</sup> remains unchanged with respect to the computed value in the gas phase. Whereas, the H<sub>2</sub>O mode ( $\nu_2$ ) of 1581 cm<sup>-1</sup> slightly downshifts by 4 cm<sup>-1</sup> compared to the  $\nu_2$  mode in the gas phase. The increase in one of the O-H bond lengths and the downshift in H<sub>2</sub>O mode suggest that the O-H bonds are weakened when the H<sub>2</sub>O molecule is adsorbed on the MoS<sub>2</sub>-1V<sub>Mo</sub>-3N<sub>S</sub> site, which would then make the reactions of H<sub>2</sub>O with other molecules easier.

**Table 6.2:** Calculated geometry and vibrational frequencies ( $\text{cm}^{-1}$ ) for adsorption of  $\text{CO}_2$ ,  $\text{N}_2$  and  $\text{H}_2\text{O}$  molecules on  $\text{MoS}_2\text{-1V}_{\text{Mo}}\text{-3N}_{\text{S}}$  sites. Calculated and experimental values of gas-phase molecules are included for comparison. The bond lengths and bond angles are in Å and degrees, respectively.

Molecule	Gas-phase			adsorption on $\text{MoS}_2\text{-1V}_{\text{Mo}}\text{-3N}_{\text{S}}$
	Experimental	Theoretical	Current work	
<b>C=O bond length</b>	1.160 [245]	1.176 [236]	1.177	1.177
<b>bond angle</b>	180 [245]	180 [236]	180	178.58
<b>C=O stretching</b>	2349 [245,			
Asymmetric ( $\nu_3$ )	272]	2360 [236]	2361	2355
Symmetric ( $\nu_1$ )	1333 [245,	1321 [236]	1328	1317
	272]			
<b>C=O bending (<math>\nu_2</math>)</b>	667 [245, 272]	638 [236]	633	633
<b><math>\text{N}\equiv\text{N}</math> bond length</b>	1.114 [245]	1.114 [160]	1.114	1.114
<b><math>\text{N}\equiv\text{N}</math> stretching</b>	1992-2625 [296]		2425	2424
<b>O-H bond length</b>	0.972 [245]	0.972 [160]	0.972	0.972/0.985
<b>bond angle</b>		104.5 [160]	104.52	103.05
<b>O-H stretching</b>				
Asymmetric ( $\nu_3$ )	3943 [295]	3713 [297]	3843	3788
Symmetric ( $\nu_1$ )	3833 [295]	3602 [297]	3729	3494
<b>O-H bending (<math>\nu_2</math>)</b>	1649 [295]	1591 [297]	1584	1580



### 6.3.1.3 Electronic Structure

The electrostatic interaction between the CO<sub>2</sub> and H<sub>2</sub>O molecules and the MoS<sub>2</sub>\_1V<sub>Mo</sub>\_3N<sub>S</sub> surface was further confirmed by Bader charge analysis. Charge analysis was focused on the atoms of the molecules and the nearest surface atoms at the adsorption locations. The result reveals that the interaction between the molecules and the MoS<sub>2</sub>\_1V<sub>Mo</sub>\_3N<sub>S</sub> surface causes charge transfer and redistribution. As shown in **Table 6.1**, a charge of 0.020 e, 0.009 e and 0.021 e is transferred to CO<sub>2</sub>, N<sub>2</sub> and H<sub>2</sub>O in P<sub>Mo</sub>S<sub>2</sub>, while only a charge of 0.012 e, 0.007 e and 0.001 e is transferred to CO<sub>2</sub>, N<sub>2</sub> and H<sub>2</sub>O, respectively, on the MoS<sub>2</sub>\_1V<sub>Mo</sub>\_3N<sub>S</sub> surface. The interaction between the molecules and the MoS<sub>2</sub>\_1V<sub>Mo</sub>\_3N<sub>S</sub> surface also supports the Lewis-acid interaction comparison but is less noticeable when compared to the pristine and non N-doped vacancy surfaces. The reactive surface N atoms gain more electrons after CO<sub>2</sub>, N<sub>2</sub> and H<sub>2</sub>O adsorption compared to the electrons gained by the N dopants before adsorption. The total number of electrons gained by the N dopant after CO<sub>2</sub>, N<sub>2</sub> and H<sub>2</sub>O adsorption is 2.557 e, 2.549 e and 2.637 e, respectively. This is ~0.371 e more than the total charge (2.21 e) the N atoms receive before adsorption (see **Table 5.3 of Chapter 5**) Thus, the N-dopants become negatively charged after adsorption. Furthermore, less charge is transferred to the molecules while the surface N atoms become negatively charged, leading to higher adsorption energy. For instance, H<sub>2</sub>O with the highest adsorption energy received less charge from the surface, with the largest amount of charge transferred to surface N atoms. This trend is different from the behaviour observed in P<sub>Mo</sub>S<sub>2</sub>. Similar behaviour was observed for CO<sub>2</sub> adsorption, while the charge received by the N<sub>2</sub> molecule from MoS<sub>2</sub>\_1V<sub>Mo</sub>\_3N<sub>S</sub> is comparable to the perfect surface. This can be attributed to the loss of an electron by the O atoms of CO<sub>2</sub> and H<sub>2</sub>O molecules. This indicates that CO<sub>2</sub> and H<sub>2</sub>O molecules bind strongly onto the N-doped vacancy site by transferring some of the electrons of their O atoms.

The charge density difference,  $\Delta\rho_{df}$  was calculated based on Eq. (6.2) as described in Subsection 6.2.2. The light blue and pink colours represent an increase and decrease of charge electron density, respectively. As shown in **Figure 6.2 (a) to (c)**, charge difference redistributes in the middle region between the molecule and MoS<sub>2</sub>-1V<sub>Mo</sub>-3N<sub>S</sub> substrate, with much more noticeable polarization of the MoS<sub>2</sub>-1V<sub>Mo</sub>-3N<sub>S</sub> nanosheet upon adsorption. This indicates a stronger covalent character, when compared to the perfect surface (**Figure 6.2 (d) and (e)**). Stronger polarization of the MoS<sub>2</sub>-1V<sub>Mo</sub>-3N<sub>S</sub> surface is observed for H<sub>2</sub>O and CO<sub>2</sub> adsorption than N<sub>2</sub> adsorption, which is consistent with the earlier Bader charge analysis.

The reason is that, when CO<sub>2</sub> is adsorbed onto the surface, the reactive surface N atoms receive electrons from the region between the CO<sub>2</sub> central carbon atom and itself to strengthen the interaction between CO<sub>2</sub> and the surface. An increase in the pink colour (decrease of electron density) in the middle region between the CO<sub>2</sub> and MoS<sub>2</sub>-1V<sub>Mo</sub>-3N<sub>S</sub> surface compared to the cases of pristine surface, indicates less charge transfer to CO<sub>2</sub> upon adsorption on MoS<sub>2</sub>-1V<sub>Mo</sub>-3N<sub>S</sub>. Also, the increase in the light blue colour (an increase of electron density) on the surface N atoms compared to MoS<sub>2</sub>-1V<sub>Mo</sub>-3N<sub>S</sub> surface before adsorption (**Figure 5.3 of Chapter 5**), shows the reactive surface N atoms gained more electrons after CO<sub>2</sub> adsorption. In addition, a big region of electron depletion appears near the oxygen atoms. Therefore, there is a lower electron density surrounding CO<sub>2</sub> compared to that of CO<sub>2</sub> on the perfect surface (**Figure 6.2 (a) and (d)**). Similar behaviour, but much stronger interaction, is also observed when the H<sub>2</sub>O molecule adsorbed on the MoS<sub>2</sub>-1V<sub>Mo</sub>-3N<sub>S</sub> surface compared to the perfect surface (**Figure 6.2 (c) and (f)**). The electron density plot of N<sub>2</sub> interaction with MoS<sub>2</sub>-1V<sub>Mo</sub>-3N<sub>S</sub> surface is similar to that of the perfect surface (**Figure 6.2 (b) and (e)**).

These results demonstrated the importance of vacancies and nitrogen doping for CO<sub>2</sub>, N<sub>2</sub> and H<sub>2</sub>O adsorptions in MoS<sub>2</sub> systems. It is found that CO<sub>2</sub>, N<sub>2</sub>, and H<sub>2</sub>O interact strongly with the Mo vacancy site when the surrounding S atoms are replaced with substituted N atoms.

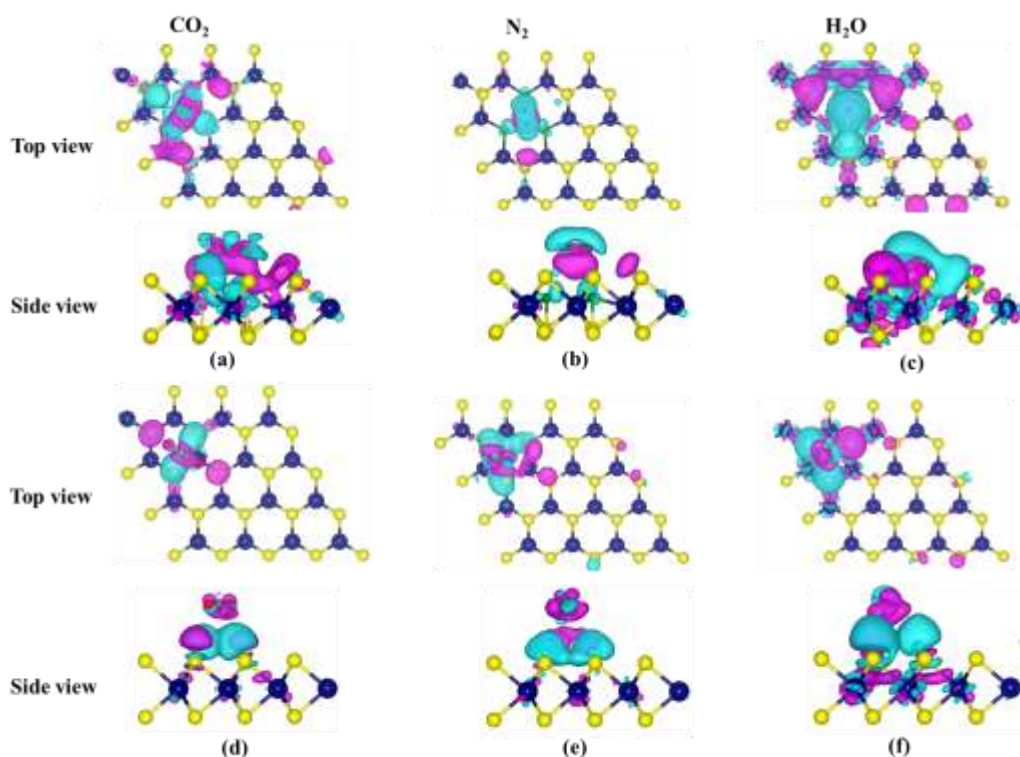


**Figure 6.2:** Top and side views of isosurfaces of spin density difference for CO<sub>2</sub>, N<sub>2</sub> and H<sub>2</sub>O molecules adsorbed on MoS<sub>2</sub>\_1V<sub>Mo</sub>\_3N<sub>S</sub> (a-c) and PMoS<sub>2</sub> (d-f). Each isosurface was taken as  $\pm 0.00015$  e/Bohr<sup>3</sup>. The light blue and pink colours represent an increase and decrease of electron density, respectively.

### 6.3.2 Dissociation of CO<sub>2</sub> and H<sub>2</sub>O on MoS<sub>2</sub>-1V<sub>Mo</sub>-3N<sub>S</sub>

The dissociation of CO<sub>2</sub> and H<sub>2</sub>O occurred when the molecules are placed close to the N-doped Mo vacancy site. For CO<sub>2</sub>, the calculations indicate that there are two stationary states for adsorption corresponding to physisorption and dissociation. CO<sub>2</sub> physisorption occurs when it is initially located at a distance of 2.5 Å or greater from the plane of the three dangling unsaturated N atoms, as explained in **Chapter 5**. Nevertheless, when CO<sub>2</sub> is initially positioned at a distance of 2.0 Å from the N-doped Mo vacant site, the molecule dissociates into CO and O fractions that remain chemisorbed at two N atoms of the vacancy site. This leads to the formation of two new double covalent bonds (C=N and O=N) of 1.229 Å and 1.209 Å, respectively. The formation of C=N and O=N bonds make this optimized state highly exothermic; ~2.136 eV, with respect to CO<sub>2</sub> in the gas phase. When comparing this dissociation state with CO<sub>2</sub> physisorbed on MoS<sub>2</sub>-1V<sub>Mo</sub>-3N<sub>S</sub> vacancy site, CO<sub>2</sub> dissociation is favoured by -0.318 eV. The C=O bond length slightly decreased to 1.176 Å, with respect to the physisorption state. The newly formed N=C=O bond is bent with an internal angle of ~178 ° similar to the bond angle of the physisorbed CO<sub>2</sub>. These covalent bonds are formed from the combination of their p-orbitals, with C=O and O=N bonds pointing up from the surface as shown in **Figure 6.3a**. The two stationary states of CO<sub>2</sub> dissociation on the MoS<sub>2</sub>-1V<sub>Mo</sub>-3N<sub>S</sub> site is similar to the CO<sub>2</sub> dissociation over a semiconducting defected graphene [237], but different from the three stationary states obtained with ones reported by literature [298] for CO<sub>2</sub> dissociation on graphene-like boron nitride with boron vacancy.

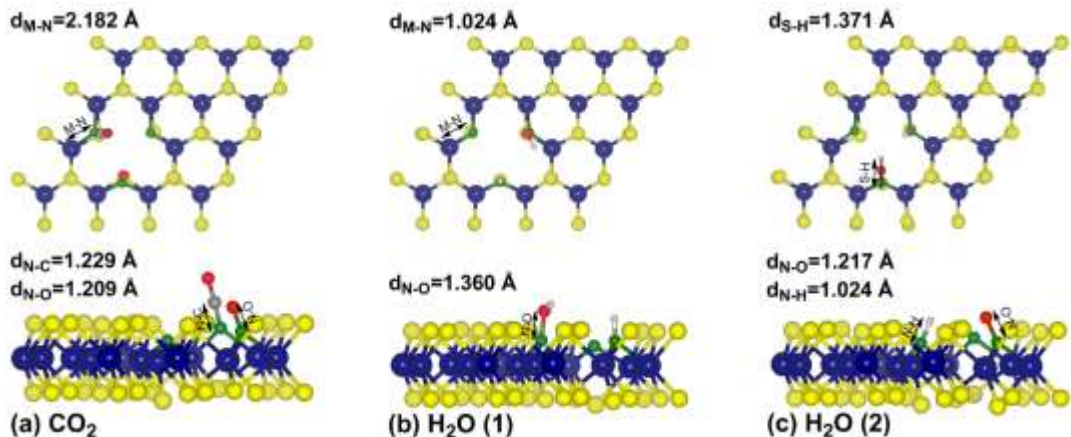


**Figure 6.3:** Top (upper panels) and side (lower panels) views of dissociated CO<sub>2</sub> and H<sub>2</sub>O molecules on MoS<sub>2</sub>\_1VMo\_3Ns site obtained from conjugate gradient energy minimization (a) CO<sub>2</sub> is partially dissociated into CO and O fractions that remain chemisorbed at two N atoms of the vacancy site, (b) first H<sub>2</sub>O dissociation state, where H<sub>2</sub>O dissociated into OH and H species that bound to two surface N atoms and (c) final H<sub>2</sub>O dissociation state, where H<sub>2</sub>O completely dissociated into O, H and H species that bound to two N atoms and one S atom of the surface.

Three stationary states were identified for H<sub>2</sub>O dissociation on the MoS<sub>2</sub>\_1VMo\_3Ns site, corresponding to physisorption and two dissociated states. The physisorption state occurs when H<sub>2</sub>O is initially placed at 2.5 Å away from the plane of the surface N atoms as mentioned in Section 6.3.1. The first dissociation state occurs at an initial molecular height of 2.0 Å, where H<sub>2</sub>O is trapped in the vacancy site by the O atom of H<sub>2</sub>O, forming bonds with one of the N atoms. As shown in **Table 6.3**, the bonded O atom receives electrons from the N atom and subsequently releases one H atom to be attached to one of the negatively charged N surface atoms, leaving behind an OH fragment. As shown in **Figure 6.3b**, the dissociation of H<sub>2</sub>O into OH and H species leads to the formation of new O-N and H-N covalent bonds with bond lengths of 1.360 Å and 1.024 Å, respectively. Again, the new bond formation makes the optimized state highly exothermic (~1.623 eV) with respect to H<sub>2</sub>O in the gas phase, but less favoured by -0.343 eV with respect to

the physisorption state. The calculated O-H bond length is 0.989 Å and the newly formed N-O-H molecule bent with an internal angle of 105.39°. This configuration is similar to the findings in ref [16] and ref [290] for H<sub>2</sub>O dissociation on MoS<sub>2</sub> triple vacancy and monolayer MoS<sub>2</sub> edges (mechanism 1), respectively. When H<sub>2</sub>O is placed at closer proximity at the start of the geometry optimization, specifically 1.5 Å from the N doped Mo vacant site, H<sub>2</sub>O dissociates into O, H and H species, with dissociation energy of -2.096 eV, with respect to free H<sub>2</sub>O. The reason is that, at closer proximity, the O atom of OH bound to the N atom receives extra electrons from the N atom. This is sufficient to release the H atom, which finally attaches to the S atom below the N atom that binds the O atom, as shown in **Figure 6.3c**.

The formation of the new H-S covalent bond of 1.371 Å makes the optimized state of the final dissociation state highly exothermic. This is favoured by 0.473 eV with respect to the initial dissociation state and 0.130 eV with respect to the physisorption state. The H-N bond remains the same while the O-N decreases to 1.217 Å. Here, the covalent bond O-N is formed from the combination of p-orbitals of O and N, whereas the N-O-H and H-N bonds are formed by p-orbitals of N and O, and the s-orbital of the H atom. Furthermore, the dissociation of H<sub>2</sub>O into OH and H species in the first dissociation state, and further dissociation of OH into O and H, suggest a possible formation of H<sub>2</sub> by simple route of the Tafel reaction ( $2\text{H}^* \rightarrow \text{H}_2$ ). Where the first dissociation state is the initiation step reaction ( $\text{H}_2\text{O} + 2^* \rightarrow \text{OH}^* + \text{H}^*$ ) and the final dissociation state is the final step reaction ( $\text{H}_2\text{O} + 3^* \rightarrow \text{O}^* + \text{H}^* + \text{H}^*$ ), with intermediate step ( $\text{OH}^* \rightarrow \text{H}^* + \text{H}^*$ , where \* represents a surface site). This route is in agreement with the one proposed by ref [290] for H<sub>2</sub>O dissociation on monolayer MoS<sub>2</sub> edges. These calculations show that the dissociation of CO<sub>2</sub> and H<sub>2</sub>O molecules on the perfect surface occurs endothermically with very high adsorption energies. In fact, CO<sub>2</sub> and H<sub>2</sub>O molecules are not attracted to the MoS<sub>2</sub> basal plane exothermically

even at a separation of 1.5 Å indicating a repulsive interaction between the free CO<sub>2</sub> and H<sub>2</sub>O molecules and the basal plane. This suggests CO<sub>2</sub> and H<sub>2</sub>O dissociation on the MoS<sub>2</sub> basal plane is unlikely. This is likely because the O atoms of the molecules cannot receive sufficient electrons to release C and H atoms of CO<sub>2</sub> and H<sub>2</sub>O molecules, respectively [16, 290]. This highlights the importance of N-doping around vacancies in the MoS<sub>2</sub> system for CO<sub>2</sub> and H<sub>2</sub>O dissociations.

Furthermore, Bader charge analysis shows that, the central C atom of CO<sub>2</sub> gains electrons from the N atom to release one O (O1) atom, which becomes positively charged (**Table 6.3**). The released O atom moves to be attached to one of the negatively charged N (N3) surface atoms, leaving behind a CO fragment that is bound to N (N2) atom. This caused the total charge obtained by the N atoms to decrease to -2.171 e. Similarly, in both H<sub>2</sub>O dissociation states, the total charge obtained by the N atoms decreases to -2.168 e and -1.895 e, as shown in **Table 6.3**. The large difference (-0.315 e) in the total charge obtained by the N atoms observed in the final H<sub>2</sub>O dissociation state, explains the strong covalent interaction between a water molecule and the N doped vacancy site. The charge analysis was focused on the atoms of the molecules and the total charge obtained by the surface N atoms.

Bader charge analysis showed that as the surrounding surface atoms (emphasis on N atoms) and adsorbate atoms exchange electrons (charges), the atoms that gain more electrons forms bonds with the atoms that lose electrons. This exchange in electrons led to the dissociation of the guest molecules and migrations of its atom to the surface atoms (N) to form covalent bonds.

**Table 6.3:** Summary of calculated results for dissociation of CO<sub>2</sub> and H<sub>2</sub>O molecules on MoS<sub>2</sub>-1V<sub>Mo</sub>-3N<sub>S</sub> sites. The values of charge transfer for the atoms of molecules and the total charge gained by the surface N atoms (Q<sub>N</sub>) are included for comparison. The bonding of the dissociated atoms is as follows: CO<sub>2</sub> (N1=C1=O2 and N3=O1), H<sub>2</sub>O<sup>a</sup> (N3-H1 and N2-O1-H2) and H<sub>2</sub>O<sup>b</sup> (N3-H1, N2-O1 and S-H2). The total charge obtained by the N atoms of the surface before adsorption is 2.21 e (see **Table 5.3** of **Chapter 5**).

Molecule	Amount of charge transferred (Q, e)							
	<i>E<sub>AE</sub></i> , eV	O1	C	O2	H1	O	H2	Q <sub>N</sub> , e
CO <sub>2</sub>	-2.136	0.614	-0.158	-0.007	-	-	-	-2.171
H <sub>2</sub> O <sup>a</sup>	-1.623	-	-	-	-0.196	0.494	-0.037	-2.168
H <sub>2</sub> O <sup>b</sup>	-2.096	-	-	-	-0.509	0.778	-0.129	-1.895

<sup>a</sup> Refers to the first water dissociation state. <sup>b</sup> Refers to the final water dissociation state.

### 6.3.3 C-NEB Analysis of CO<sub>2</sub> and H<sub>2</sub>O Dissociation on MoS<sub>2</sub>-1V<sub>Mo</sub>-3N<sub>S</sub>

Having identified the dissociated structures, the activation barrier for the dissociation reaction over the MoS<sub>2</sub>-1V<sub>Mo</sub>-3N<sub>S</sub> surface was estimated by using minimum-energy reaction paths search based on the CI-NEB method with 4 images to locate the transition states (TS), which is further confirmed by frequency analysis. For a CO<sub>2</sub> molecule, the initial state (IS) and final state (FS) are obtained from the adsorption configuration of adsorption and dissociation state obtained during geometry optimization, as shown in **Figures 6.1a** and **6.3a**, respectively. **Figure 6.4a** corresponds to the energy profile that represents the MEP between the IS and FS, along with the activation energy barrier that corresponds to the saddle point (transition state (TS)) along the MEP. The



geometries of IS, FS and TS are also shown in **Figure 6.4**. Unlike in the IS, CO<sub>2</sub> molecules are physisorbed strongly on the surface at the TS, with a separation of 1.820 Å between the nearest surface N atom and the CO<sub>2</sub> carbon atom. In the TS, CO<sub>2</sub> adopts a tilted orientation (~148° bond angle) with the two O atoms pointing up from the surface and C=O bond lengths extended to 1.217 and 1.205 Å from 1.177 Å in the IS. The calculated energy barrier ( $E_a$ ) is 0.44 eV, which is obtained by taking the difference between the energies of the TS and the IS ( $E_a = E_{TS} - E_{IS}$ ). The reaction energy ( $\Delta E$ ), which is the energy difference between the FS and the IS energies, is calculated to be -1.14 eV. The negative  $\Delta E$  indicates exothermic nature; hence, CO<sub>2</sub> dissociation on MoS<sub>2</sub>-1 V<sub>Mo</sub>-3N<sub>S</sub> is energetically favoured by -1.14 eV. Given the exponential dependence of the reaction rate on activation energy, the low activation barrier and negative reaction energy point to favourable kinetics and thermodynamics, respectively. This is far better than the best MEP obtained from previous DFT studies of CO<sub>2</sub> dissociation on defective graphene sheets [237] and graphene-like boron nitride with boron vacancy [298] and is far better than the one obtained on a metallic surface of mackinawite (FeS (011) and FeS (111)) [299]. The single imaginary frequency of 211.6 cm<sup>-1</sup> calculated at TS indicates that the searched transition state is indeed the saddle point between the two local minima (stationary states (physisorption and dissociation)) along the MEP. For H<sub>2</sub>O, only the overall reaction path is discussed. Here, the IS and FS are obtained from geometry optimization of the adsorption configuration corresponding to the adsorption and final dissociation states (**Figures 6.1c** and **6.3c**, respectively). As shown in **Figure 6.4b**, at the TS, one of the H atoms in the H<sub>2</sub>O molecule formed a bond with the adjacent surface N atom, leaving the detached OH species to move to a position intermediate between the surface bonded H atom and O atom of the OH fragment. This leads to the formation of a bond with the H atom, achieving a configuration similar to that observed in the first dissociation state (**Figure 6.3b**). The distance

between the surface bonded H atom and O atom of OH is 1.478 Å, while the OH bond length extended to 0.983 Å. The calculated  $E_a$  and  $\Delta E$  for complete dissociation of H<sub>2</sub>O into O, H and H species on the MoS<sub>2</sub>-1V<sub>Mo</sub>-3N<sub>S</sub> surface is 0.82 eV and -1.34 eV, respectively. This activation energy is significantly lower than that for H<sub>2</sub>O splitting in free space (~5 eV) and even lower than water splitting in liquid water and on the surfaces of Cu, Ni and Pd (~1 eV) [300-302]. Although water dissociation on MoS<sub>2</sub>-1V<sub>Mo</sub>-3N<sub>S</sub> is less kinetically favourable compared to the one reported by other researchers [290], its more negative reaction energy of -1.34 eV with respect to the best value of -1.29 eV of reported values [290], shows that H<sub>2</sub>O dissociation on MoS<sub>2</sub>-1V<sub>Mo</sub>-3N<sub>S</sub> surface is more thermodynamically favourable. In particular, the calculated  $E_a$  and  $\Delta E$  values compare favourably with a recent DFT study on the Pt surface that is often regarded as the best performing catalyst for water dissociation [303]. Again, the TS searched is also confirmed by a single imaginary frequency of 993.9 cm<sup>-1</sup>. These values are greater than the values obtained for reduced CeO<sub>2</sub> (111) surface [294]. All these findings show that the MoS<sub>2</sub>-1V<sub>Mo</sub>-3N<sub>S</sub> surface is a good candidate for water splitting.

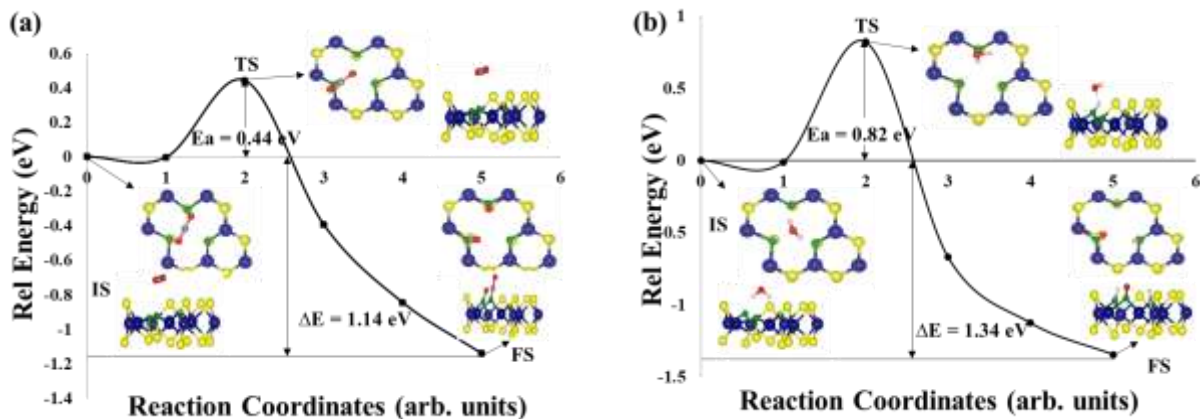


**Figure 6.4:** Energy diagram including reaction pathway and reaction barrier of single (a) CO<sub>2</sub> and (b) H<sub>2</sub>O dissociation on tertiary nitrogen doped Mo vacancy MoS<sub>2</sub> (MoS<sub>2</sub>\_1V<sub>Mo</sub>\_3Ns) from climbing image nudged elastic band (CI-NEB) simulation. Inserts are the top and side views of the initial state (IS), Transition state (TS) and final state (FS) configurations along the MEP. The colour codes for Mo, S, N, O, H and C atoms are the same as explained in **Figure 6.1**.

### 6.3.4 Energy barrier after enthalpy correction

The reported activation ( $E_a$ ) and reaction energies ( $\Delta E$ ) from NEB analysis in **Figure 6.4** correspond to the potential energy surface differences at ground state (0 K) and as a result do not account for contribution from vibrational, rotational and translation energies. Therefore, quantum corrections to the activation barrier at room temperature (300 K) were considered to explicitly analyse the room temperature effect on the activation barrier and get a more realistic view of the catalytic reaction. The zero point energy (ZPE), as well as entropic correction, were incorporated by calculating Gibbs free energy  $\Delta G_a$  between IS and TS, which is defined as:

$$\Delta G_a = E_a + \Delta ZPE - T\Delta S \quad (6.8)$$

Where  $E_a$  is the calculated activation energy obtained from NEB analysis,  $\Delta ZPE$  is the correction to the classical barrier obtained simply by taking the difference between the sum of real-valued harmonic vibrational frequencies at the TS and the IS.  $\Delta S$  is the entropic contribution obtained from the difference in the entropy of the molecules at the TS and IS, and T is the temperature. The vibrational entropy of adsorbate species can be considered very low in the adsorbed state as they are bound to a surface with little configurational freedom [304]. Hence,  $\Delta S$  can be approximated to  $S^0$ , where  $S^0$  is the entropy of CO<sub>2</sub> or H<sub>2</sub>O molecules in the gas phase at standard conditions obtained directly from the standard thermodynamic database [293]. The calculated  $\Delta G_a$  of activation for the dissociation reaction of CO<sub>2</sub> and H<sub>2</sub>O molecules on MoS<sub>2</sub>\_1V<sub>Mo</sub>\_3N<sub>S</sub> are -0.27 eV and 0.10 eV, respectively. According to a previous study, reactions with a barrier of 21 kcal/mol (~0.8 eV) or less will proceed readily at room temperature [288]. The low values of  $\Delta G_a$  suggest not only that the MoS<sub>2</sub>\_1V<sub>Mo</sub>\_3N<sub>S</sub> site has excellent catalytic property but also that dissociation of CO<sub>2</sub> and H<sub>2</sub>O molecules could be spontaneous at room temperature. This makes it a possible route for CO<sub>2</sub> activation and reduction, and H<sub>2</sub>O splitting. The exponential dependence of the kinetic rate constant on the activation energy can be estimated by transition state theory expression

$$k = \frac{K_B T}{h} e^{-\frac{\Delta G_a}{K_B T}} \quad (6.9)$$

Where  $K_B$  and  $h$  represent Boltzmann's and reduce Planck's constant, respectively. The calculated kinetic rate constants for CO<sub>2</sub> and H<sub>2</sub>O molecules at 300 K are  $1.77 \times 10^{17} \text{ s}^{-1}$  and  $1.36 \times 10^{11} \text{ s}^{-1}$ , respectively. These very high rates suggest that N doped Mo single vacant MoS<sub>2</sub> site is very favourable for the CO<sub>2</sub> and H<sub>2</sub>O dissociation reaction not only thermodynamically but also kinetically, and the reaction is likely to occur spontaneously and quickly at room temperature. Therefore, CO<sub>2</sub> and H<sub>2</sub>O dissociations observed in this study are likely not the rate limiting steps

for CO<sub>2</sub> activation and reduction, and the overall H<sub>2</sub> evolution process from H<sub>2</sub>O splitting. For H<sub>2</sub>O, the reaction path for the dissociation route with intermediate step (OH\* → H\* + O\*) is found to be thermodynamically favourable with -0.44 eV reaction energy ΔE but has a significant activation energy E<sub>a</sub> of 2.30 eV. Hence, the high E<sub>a</sub> observed in this path is likely the rate-limiting step in the overall H<sub>2</sub> evolution process from H<sub>2</sub>O splitting, which agrees well with the literature[290].

### 6.3.5 Finite Temperature Ab Initio Molecular Dynamics

To analyse the temperature effect on the dynamic evaluation of the adsorption system, finite temperature ab initio molecular dynamics (AIMD) at 300 K was conducted. The initial adsorption configurations where CO<sub>2</sub> and H<sub>2</sub>O dissociated during structural optimization were chosen as MD initial structures, which were initialized and then allowed to evolve along the Born-Oppenheimer energy surface. For CO<sub>2</sub>, three different binding configurations that correspond to different minima in the Born-Oppenheimer energy are revealed at different intermediate stages of the MD calculations as shown in **Figure 6.5a**. **Figure 6.5a (i)** corresponds to the first minima taken at  $t \approx 0.05$  ps in the dynamics, where CO<sub>2</sub> moves towards the surface and is trapped in the vacancy site by the C and one of the O atoms form single bonds with the three surface N atoms. As the simulation progresses to  $t \approx 0.10$  ps, bonded O atom separates from the C atom, leaving behind a CO fragment, with the C atom remaining bound to the two N atoms (**Figure 6.5a (ii)**). By  $\sim 0.17$  ps, the CO fragment detaches from one of the N atoms and bends towards the vacancy site, allowing the C=O bond length to decrease, as shown in **Figure 6.5a (iii)**. Interestingly, **Figure 6.5a (iii)** is quite similar to the adsorption configuration obtained from structure optimization using the conjugate gradient method, where CO<sub>2</sub> is partially dissociated into CO and O fractions, as illustrated by **Figure 6.3a**. This configuration continues to be stable for the remaining MD

simulation up to 2.0 ps, where only a small change in atomic configuration is observed, as shown in **Figure 6.5a (iv)**.

Similar behaviour is observed for H<sub>2</sub>O dissociation but with four different binding minima in the Born-Oppenheimer energy at different intermediate stages of the MD. At  $t \approx 0.01$  ps, H<sub>2</sub>O moves towards the vacancy site and tilts with the H atom pointing to the MoS<sub>2</sub> basal plane (as shown in **Figure 6.5b (i)**), achieving a configuration similar to that observed for H<sub>2</sub>O physisorption in Section 6.3.1. Eventually, at  $t \approx 0.02$  ps, the H atom pointing to the MoS<sub>2</sub> basal plane forms a bond with the nearest N atom leaving the OH fragment to physisorb at the vacancy site (as shown in **Figure 6.5b (ii)**). After this first intermediate stage, the OH fragment starts to move towards the nearest adjacent N atom and tilts to allow the O atom to form a bond with the N atom (as shown in **Figure 6.5b (iii)**) at  $t \approx 0.11$  ps. This configuration corresponds to the first dissociation state obtained through conjugate gradient energy minimization where H<sub>2</sub>O dissociates into OH and H species. Another intermediate stage is observed at  $t \approx 0.55$  ps, where the bonded O atom of the OH species releases an H atom, which moves to an intermediate position between the bonded O and the remaining adjacent N atom (as shown in **Figure 6.5b (iv)**). Finally, the intermediate H atom moves to form a bond with the N atom at  $t \approx 0.60$  ps as shown in **Figure 6.5b (v)**. This configuration remains stable for the rest of the simulation with only a small change to the atomic configurations (see **Figure 6.5b (vi)**). This configuration is similar to the final dissociation state obtained during geometry optimization, where H<sub>2</sub>O completely dissociated into O, H and H species. The difference is that the species bond only to the surface N atoms.

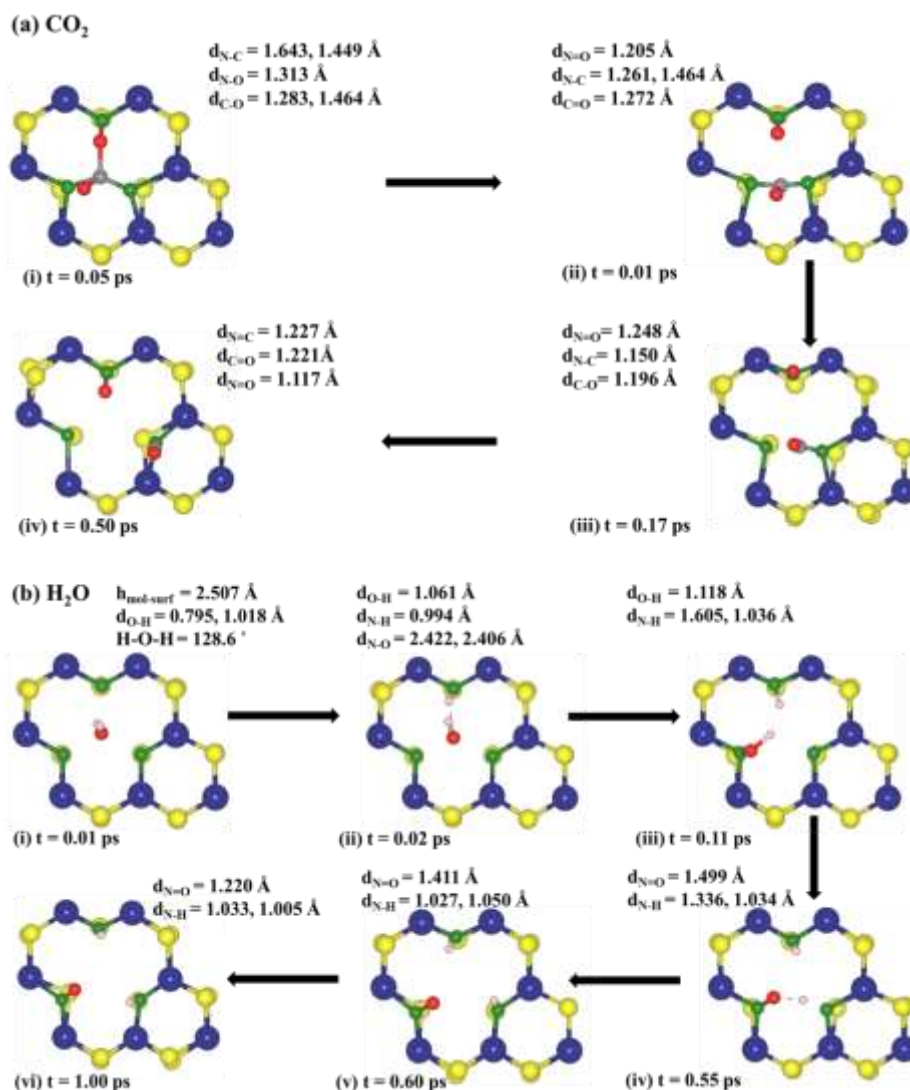


**Figure 6.5:** Reaction mechanism of single (a) CO<sub>2</sub> and (b) H<sub>2</sub>O dissociation on MoS<sub>2</sub>\_1VMo\_3Ns during AIMD simulations at 300 K. The MD reaction paths are similar to the reaction paths obtained in CI-NEB simulations.

The quick and straightforward dissociation of CO<sub>2</sub> and H<sub>2</sub>O molecules under 1.0 ps shows that the energy barrier for dissociation is below the thermal energy available at 300 K. This is a confirmation that the dissociation of these molecules on MoS<sub>2</sub>\_1VMo\_3Ns occur spontaneously at room temperature. The complete dissociation of H<sub>2</sub>O into O, H and H species on the N doped vacancy site occurs spontaneously than the ones reported by literature [16, 290] for H<sub>2</sub>O

dissociation on MoS<sub>2</sub> triple vacancy and monolayer MoS<sub>2</sub> edges, respectively, which stresses the importance of doping vacancies in MoS<sub>2</sub> systems with N atoms.

Finally, the overall evaluation of the reaction is found to be similar to the geometry optimization adsorption and NEB based results, especially the final configurations. The predicted spontaneous dissociation of the molecules happening once every 0.05 – 0.44 ps average correlates with the earlier calculated high rate constants, hence the dissociation proceeds in a roughly similar manner even with entropic and temperature effects.

### 6.3.6 Ab Initio Thermodynamic on the Surface Stability of MoS<sub>2</sub>\_1V<sub>Mo</sub>\_3N<sub>S</sub>

Having identified the relevant structures for the MoS<sub>2</sub>\_1V<sub>Mo</sub>\_3N<sub>S</sub> surface-molecule interaction systems, understanding the thermodynamic stability of each adsorption surface when exposed to a given environment is necessary. In particular, the adsorption performance under non-zero temperature and pressure of the surrounding atmosphere is of significant importance. In this case, the ab-initio thermodynamics method [182, 183] as defined in Eq. 6.3-6.7 (see Section 6.2.3) is commonly applied to illustrate the change of Gibbs free energy ( $\Delta G_{ads}(T, P)$ ) with finite temperature and pressure.

**Figure 6.6** illustrates the T-P phase diagram boundary determined by Eq. (6.5), which corresponds to temperature as a function of partial pressure above which the adsorption of CO<sub>2</sub>, N<sub>2</sub> and H<sub>2</sub>O molecule on MoS<sub>2</sub>\_1V<sub>Mo</sub>\_3N<sub>S</sub> site are stable ( $\Delta G_{gas}(T, P) < 0$ ). The temperature range of interest is between 200 K and 1200 K, while the pressure range is between  $1.5 \times 10^5$  atm and  $10^{-35}$  atm, to include experimental pressure range (1 atm and  $10^{-14}$  (ultrahigh vacuum, UHV) and any variation in pressure. From the analysis of the phase diagram, there are two important phase transitions worth investigating, the isobaric line (Line A) and isothermal (Line B, C and D) lines.



It is evident that at certain temperatures for CO<sub>2</sub> (Line B), N<sub>2</sub> (Line C) and H<sub>2</sub>O (Line D), when partial pressure is very low, there is no interaction between molecules and the surface. The molecules begin to be adsorbed when their partial pressures increase to a certain value. On the other hand, at certain partial pressures (e.g., Line A), the molecules are adsorbed on the surface at a lower temperature, and desorb at a higher temperature. At a pressure of  $\sim 10^{-31}$  atm, CO<sub>2</sub> and N<sub>2</sub> molecules, desorb from the surface after 200 K, while H<sub>2</sub>O desorb after the same temperature at a pressure of  $\sim 10^{-35}$  atm.

It is observed that at a temperature range of < 700 K, < 800 K and < 900 K, the adsorption of CO<sub>2</sub>, N<sub>2</sub> and H<sub>2</sub>O on MoS<sub>2</sub>-1V<sub>Mo</sub>-3N<sub>S</sub> surface is stable, respectively, while above these temperatures the molecules desorb into gas phase. The transition temperatures (isothermal lines) between these two phases are around 700 K (Line B), 800 K (Line C) and 900 K (Line D) for CO<sub>2</sub>, N<sub>2</sub> and H<sub>2</sub>O, respectively. The desorption temperature (200 K) of CO<sub>2</sub> at lower pressures < 1 atm, matches with the experimental data for graphene-based adsorbents for CO<sub>2</sub> capture [305]. In this study, the application range of CO<sub>2</sub> adsorption at 1 atm is better than CO<sub>2</sub> capture on N, S dual doped graphene that was reported by other researchers [228], indicating that MoS<sub>2</sub>-1V<sub>Mo</sub>-3N<sub>S</sub> is a superior adsorbent for CO<sub>2</sub> capture than the doped graphene-based material. The transition temperatures for H<sub>2</sub>O adsorption compare favourably with recent DFT results [183, 294], but H<sub>2</sub>O adsorption on MoS<sub>2</sub>-1V<sub>Mo</sub>-3N<sub>S</sub> is more stable up to 900 K than < 700 K on the stoichiometric CeO<sub>2</sub> (111) surface [294].

It has already been shown that the MoS<sub>2</sub>-1V<sub>Mo</sub>-3N<sub>S</sub> site could promote the charge transfer from the surface to CO<sub>2</sub>, N<sub>2</sub> and H<sub>2</sub>O molecule leading to enhanced adsorption performance. Considering the stronger adsorption, more energy is required to release the molecules from the

surface, indicating that the surface requires an external drive if it should adsorb gas molecules. This effect and the stability of the dissociated states will be investigated in future work.

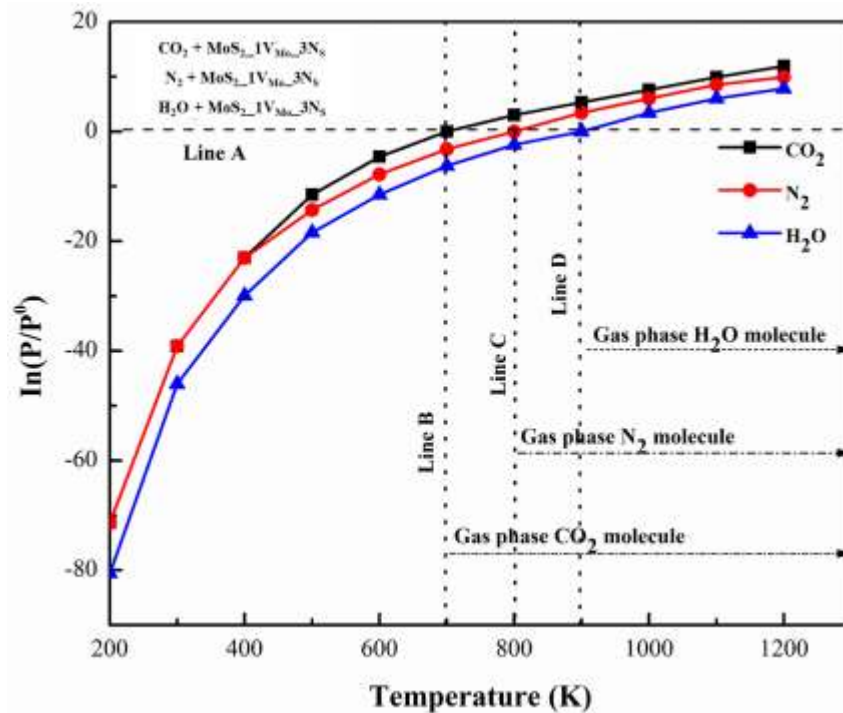


**Figure 6.6:** T-P phase diagram of CO<sub>2</sub>, N<sub>2</sub> and H<sub>2</sub>O molecules adsorption on nitrogen doped single Mo vacancy site (MoS<sub>2</sub>-1V<sub>Mo</sub>-3N<sub>S</sub>). The points on black, red and blue curves represent temperature as a function of partial pressure above which the adsorption of respective CO<sub>2</sub>, N<sub>2</sub> and H<sub>2</sub>O on the MoS<sub>2</sub>-1V<sub>Mo</sub>-3N<sub>S</sub> site is stable. Line A is the partial pressure line fixed at 1 atmospheric pressure, while Line B, Line C and Line D are the temperature lines for CO<sub>2</sub>, N<sub>2</sub> and H<sub>2</sub>O, respectively. The partial pressure and temperature lines correspond to critical point lines above which the molecules desorb into the gas phase.

## 6.4 Summary and Conclusions

MoS<sub>2</sub>\_1V<sub>Mo</sub>\_3N<sub>S</sub> is proved to be thermodynamically favourable for the adsorption of CO<sub>2</sub>, N<sub>2</sub> and H<sub>2</sub>O with adsorption energies of -1.818, -1.744 and -1.966 eV, respectively, which are approximately 13, 22 and 14 times superior to that of pristine MoS<sub>2</sub> (PMoS<sub>2</sub>) surface, respectively. The enhanced adsorption activity can be attributed to the enhanced electrostatic interactions due to the presence of Mo vacancy and N species, except for N<sub>2</sub> adsorption, where the interaction with MoS<sub>2</sub>\_1V<sub>Mo</sub>\_3N<sub>S</sub> is predominately non-covalent. It is also found that CO<sub>2</sub> dissociates into CO and O species that remain chemisorbed on two N atoms neighbouring the vacancy site, while H<sub>2</sub>O dissociates into constituent O and H atoms via a two-step route, i.e., H<sub>2</sub>O dissociates into OH and H species that are bonded on the surficial N atoms, with an energy of 1.623 eV; and, H<sub>2</sub>O dissociated into O, H and H species, with an energy of -2.096 eV. The O, H and H species are also bonded with the surface N atoms. This is different from the vdW interaction that mainly occurs on the basal plane of the PMoS<sub>2</sub> surface.

Furthermore, CI-NEB analysis reveals that the partial CO<sub>2</sub> and complete H<sub>2</sub>O dissociation processes exhibited energy barriers of 0.44 eV and 0.82 eV, respectively. In addition, the free energy of activation for the partial and complete dissociation of CO<sub>2</sub> and H<sub>2</sub>O are -0.27 eV and 0.10 eV, respectively. The reactions were found to be kinetically favourable with high reaction rate constants of  $1.77 \times 10^{17} \text{ s}^{-1}$  and  $1.36 \times 10^{11} \text{ s}^{-1}$  at 300 K for CO<sub>2</sub> and H<sub>2</sub>O molecules, respectively. These results along with the spontaneous dissociation of the molecules happening once every 0.05 – 0.44 ps average suggest that CO<sub>2</sub> and H<sub>2</sub>O dissociations will occur spontaneously at room temperature. Consequently, the rapid dissociation of CO<sub>2</sub> and H<sub>2</sub>O molecules to CO\*, O\*, OH\* and H\* radicals on the MoS<sub>2</sub>\_1V<sub>Mo</sub>\_3N<sub>S</sub> site suggest that

MoS<sub>2</sub>-1V<sub>Mo</sub>-3N<sub>S</sub> can facilitate the CO<sub>2</sub> reduction and water splitting processes, with efficacy that surpasses the performance of regular catalysts.

The ab initio thermodynamics calculation shows that at 1 atm, CO<sub>2</sub>, N<sub>2</sub> and H<sub>2</sub>O desorb at 700, 800 and 900 K, respectively. This indicates that the surface requires an external drive to desorb gas molecules.

In summary, this study suggests that MoS<sub>2</sub>-1V<sub>Mo</sub>-3N<sub>S</sub> is of great potential to be used as a catalyst for CO<sub>2</sub> reduction and water splitting.

## CHAPTER 7

# Investigating the Role of Single Sulphur Vacancy on Gaseous Adsorption and Potential Water Splitting over MoS<sub>2</sub> Edges

### 7.1 Introduction

The major sources of the current environmental problems are the use of traditional fossil fuels for the production of energy and chemicals, whereby industrial and vehicle exhaust gases (such as CO<sub>2</sub>, CH<sub>4</sub>, N<sub>2</sub>, H<sub>2</sub> and H<sub>2</sub>O ) are released into the atmosphere. Among these exhaust gases, carbon dioxide (CO<sub>2</sub>) and methane (CH<sub>4</sub>) are the main gases that cause the global warming effect. It has been reported that the primary cause of induced climate variation is the constant rise in anthropogenic CO<sub>2</sub> emission [3, 35]. Therefore, finding ideal sorbents for effective gas capture is a crucial issue for energy and environmental sciences. Because of the inert properties of these gases due to extreme stability, most of the materials show weak adsorption and are not sensitive enough to capture the gases. To date, different adsorbents, such as metal organic frameworks (MOFs) [268, 306-309], zeolites [310, 311] and carbon-based nanomaterials [312-314] have been developed for CO<sub>2</sub>, CH<sub>4</sub>, N<sub>2</sub> and H<sub>2</sub> capture. For example, the adsorption capacity of CO<sub>2</sub> and CH<sub>4</sub> can be as high as 22 wt.% on MOF-177 at 298 K and 100 bar, and 47.98 wt.% on MOF-5 at 298 K and 14 bar, respectively [268].

Alternatively, to effectively mitigate against this, traditional fossil fuels be replaced with sustainable and energy-saving platforms to store renewable energy into fuels and/or produce valuable chemicals for other uses [315, 316]. As one of the most promising platforms, the conversion of earth-abundant small molecules, such as H<sub>2</sub>O [24, 25, 317] and CO<sub>2</sub> [2, 275, 277], into energy carriers (H<sub>2</sub>) and low-carbon hydrocarbons under ambient conditions offers us an energy-saving and fossil-free pathway to produce fuels and chemicals. However, under ambient conditions, H<sub>2</sub>O conversion is hindered by the high thermodynamic energetics and low Faradaic efficiency (FE) and selectivity [24]. On the other hand, the conversion efficacy of CO<sub>2</sub> is primarily limited by its low local concentration and the extreme stability of the linear structure of CO<sub>2</sub> [2]. In both cases, these incidences slow down the initial phase conversion kinetics involving the transformation of H<sub>2</sub>O and CO<sub>2</sub> to OH\* and H\* [279] and CO [278], respectively. Therefore, to offset these limitations, suitable catalyst systems that can simultaneously promote CO<sub>2</sub> conversion and water dissociation by improving the reaction kinetics at low energetics is key.

In the recent literature review, molybdenum disulphide (MoS<sub>2</sub>) has been utilized for adsorption and conversion of gaseous molecules due to its layered structure and unique electronic configuration [157, 158]. Also, it has been the focus of considerable interest over the past two decades [108] as mentioned in the previous chapters. However, its applications have been limited due to the low electron transfer of the basal plane of MoS<sub>2</sub>, which can lead to low gaseous adsorption and conversion [14, 15]. For this reason, non-polar gas molecules, like CO<sub>2</sub> and CH<sub>4</sub>, the perfect MoS<sub>2</sub> surface cannot offer strong adsorbing sites. According to statistical thermodynamics, the presence of elemental vacancies in materials have redefined the chemical and physical properties of such material; and as such, enables the surface of the investigated material for various applications. The results from **Chapter 5** and the gaps in the literature

discussed in **Chapter 2**, single vacancy, or a missing sulphur atom in Molybdenum disulphide ( $\text{MoS}_2\text{-1V}_\text{S}$ ) is one of the most typical kinds of defects that possesses highly reactive sites, particularly for gaseous adsorption and conversion [20].

Motivation to carry out this present study stems from a notable distinction observed for the  $\text{MoS}_2\text{-1V}_\text{S}$  surface following the work presented in **Chapter 5**. In **Chapter 5**, an improved adsorption efficiency of  $\text{CO}_2$  on  $\text{MoS}_2\text{-1V}_\text{S}$  surface was obtained and was found to undergo dissociative adsorption as against the reported study, which suggested that  $\text{CO}_2$  only physisorbed on  $\text{MoS}_2\text{-1V}_\text{S}$  [160]. As mentioned in **Chapter 5**, part of the discrepancy can be attributed to the perpendicularly orientated  $\text{CO}_2$  molecule and the effect of lateral interaction between the O of  $\text{CO}_2$  pointing towards the S vacant site and the surface, and from a critical review of literature, this technique was not studied. In this chapter, the adsorption of different gas molecules ( $\text{CO}_2$ ,  $\text{CH}_4$ ,  $\text{N}_2$ ,  $\text{H}_2$  and  $\text{H}_2\text{O}$ ) on  $\text{MoS}_2\text{-1V}_\text{S}$  surface was investigated to test for cross-interference of  $\text{CO}_2$  in presence of other earth-abundant small molecules such as  $\text{N}_2$  and  $\text{H}_2\text{O}$  using first-principles calculations and Grand Canonical Monte Carlo (GCMC) simulations. First-principles simulations were performed to understand and differentiate how sulphur vacancy defects affect the adsorption of  $\text{CO}_2$ ,  $\text{CH}_4$ ,  $\text{N}_2$ ,  $\text{H}_2$  and  $\text{H}_2\text{O}$  on  $\text{MoS}_2$  in a cross-interference scenario. Classical Grand Canonical Monte-Carlo (GCMC) simulations were carried out using RASPA 2.0 [318] to simulate adsorption isotherms between 0 – 100 bar for  $\text{MoS}_2$  with and without single vacancy defects. Adsorption isotherms were simulated from 0 – 100 bar at 298 K for  $\text{CO}_2$ ,  $\text{CH}_4$ ,  $\text{N}_2$ , and  $\text{H}_2\text{O}$ , and at 298 K and 77 K for  $\text{H}_2$ . Finally, climbing image nudged elastic band (CI-NEB) calculation and a range of other computational chemistry tools were employed to investigate the adsorption and dissociation of  $\text{CO}_2$ ,  $\text{H}_2$  and  $\text{H}_2\text{O}$  on  $\text{MoS}_2\text{-1V}_\text{S}$  sites. An in-depth, first principles-based investigation of  $\text{CO}_2$  reduction ( $\text{CO}_2 \rightarrow \text{CO}^- + \text{H}^+$ ),  $\text{H}_2$  splitting ( $\text{H}_2 \rightarrow \text{H}^- + \text{H}^+$ ), and water splitting ( $\text{H}_2\text{O} \rightarrow \text{OH}^- +$

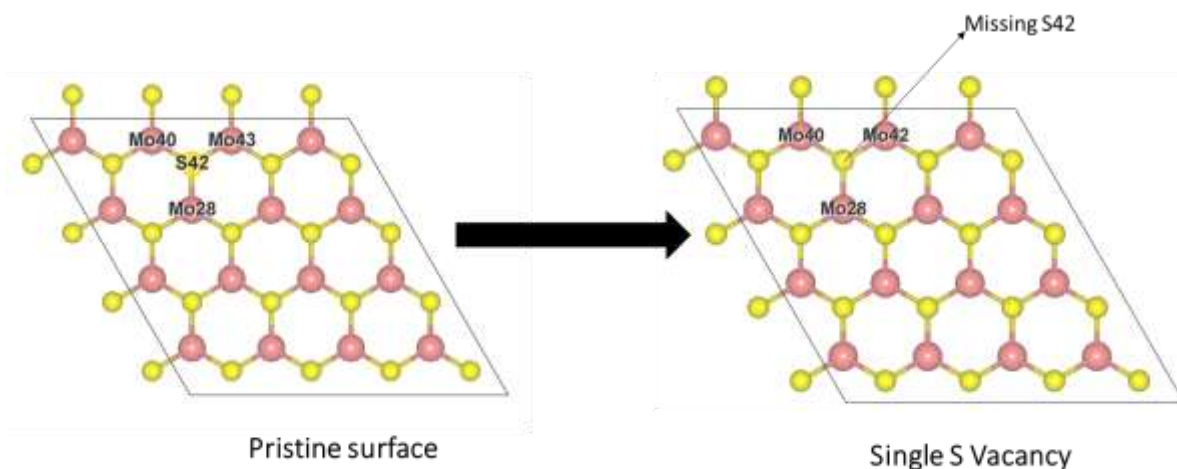
H<sup>+</sup>) mechanisms, in terms of thermodynamic stability, active sites, activation barriers and rate of reactions on MoS<sub>2</sub>\_1V<sub>S</sub> sites were carried out.

## 7.2 Simulation Details

The aim of the present section is not to provide a comprehensive review of simulations in defective and non-defective MoS<sub>2</sub>. The computational methods and technical aspects of simulations of gas adsorption in MoS<sub>2</sub> used in this study have been outlined previously (**Chapter 5 and 6**). However, it is necessary to briefly introduce some of the technical aspects of simulations of gas adsorption in MoS<sub>2</sub>. There are two broad classes of simulation available in general: approaches in which the interactions between atoms are described using quantum chemical or first-principle derivations (ab Initio approaches), and those using some combination of force fields derived empirically (classical approaches). Although, the former has been found to accurately predict adsorption energies of adsorbent-adsorbate interactions interesting target for experimental validation, but is limited due to relatively high computational cost and thus small system sizes. Therefore, adsorption properties are typically assessed using classical molecular simulations.



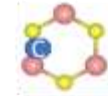

The adsorption of gas molecules in the MoS<sub>2</sub> monolayer was investigated using a simulation box of a periodic (4×4×1) supercell containing 48 atoms (16 Mo atoms and 32 S atoms) as an initial computational model. Then, a single sulphur vacancy (MoS<sub>2</sub>\_1V<sub>S</sub>) site is formed by removing one S atom in a unit cell (**Figure 7.1**). Four different orientations of the gas molecules (CO<sub>2</sub>, CH<sub>4</sub>, N<sub>2</sub>, H<sub>2</sub> and H<sub>2</sub>O) were considered for the adsorption system, which is presented in **Table 7.1**. The interaction of single gas molecules with the MoS<sub>2</sub>\_1V<sub>S</sub> site was evaluated using DFT methods. Finally, the adsorption isotherms were simulated from 0 – 100 bar for CO<sub>2</sub>, CH<sub>4</sub>, N<sub>2</sub>, H<sub>2</sub>, H<sub>2</sub>O to investigate the gas adsorption properties.





**Figure 7.1:** Single sulphur formation.

**Table 7.1:** Adsorption Energies and Orientations for the gas molecules ( $\text{CO}_2$ ,  $\text{CH}_4$ ,  $\text{N}_2$ ,  $\text{H}_2$  and  $\text{H}_2\text{O}$ ) in the four reference positions.

Position	Adsorbate	$E_{\text{ads}}$ (eV)		Orientation
		PMo52	MoS2_SV	
	$\text{H}_2$	2.490	-2.434	y
	$\text{CH}_4$	-0.059	1.222	xy
	$\text{CO}_2$	-0.139	0.004	y
	$\text{N}_2$	-0.075	0.847	y
	$\text{H}_2\text{O}$	-0.141	0.008	y
	$\text{H}_2$	-0.529	-2.435	x
	$\text{CH}_4$	-0.060	-0.106	xy
	$\text{CO}_2$	-0.116	0.003	x
	$\text{N}_2$	-0.070	0.846	x
	$\text{H}_2\text{O}$	-0.107	-0.095	x
	$\text{H}_2$	2.443	-2.434	xy
	$\text{CH}_4$	-0.057	-0.101	xy
	$\text{CO}_2$	-0.134	0.003	xy
	$\text{N}_2$	-0.075	-0.079	xy
	$\text{H}_2\text{O}$	-0.146	-0.262	xy
	$\text{H}_2$	-0.793	-2.434	-z
	$\text{CH}_4$	-0.061	1.220	-xz
	$\text{CO}_2$	-0.085	-0.908	-z
	$\text{N}_2$	-0.075	17.918	-z
	$\text{H}_2\text{O}$	-0.146	-0.093	-z

### 7.2.1 Density Functional Theory Calculations

The interaction of a single gas molecule with the MoS<sub>2</sub>\_1V<sub>s</sub> site was investigated using spin-polarized DFT-D2 calculations with Grimme dispersion correction [216] implemented in the Vienna *ab initio* simulation package (VASP) [211, 212], which adds a semi-empirical pairwise force field to conventional first-principles plane-wave DFT calculations. All other DFT calculation details are the same as explained in **Chapters 3, 5 and 6**. In addition, all calculations were performed under the same relaxation criteria as mentioned previously. The evaluation of minimum-energy reaction paths (MEPs) and the transition states (TS) was performed using the climbing image nudged elastic band (CI-NEB) methods [184].

The adsorption energy ( $E_{AE}$ ) is calculated as,

$$E_{AE} = E_{Surf+mole} - (E_{surf} + E_{mole}) \quad (1)$$

Where,  $E_{surf}$  and  $E_{Surf+mole}$  are the total energies of the surface (pristine or the defect MoS<sub>2</sub> monolayer) and that with the adsorbed gas molecule respectively, and  $E_{mole}$  is the total energy of the isolated gas molecule. A negative value of  $E_{AE}$  indicates that the adsorption is exothermic, which means that the adsorption of CO<sub>2</sub> molecule on the surface of the structure is favoured energetically, vice versa.

### 7.2.2 Force Field-Based Calculations

The Grand canonical Monte Carlo (GCMC) simulations [319] of the gas adsorption properties in idealized MoS<sub>2</sub>\_1V<sub>s</sub> surface were carried out using RASPA 2.0 [318]. A series of fixed pressure simulations were carried out at room temperature (298 K) from 0 to 100 bar for CO<sub>2</sub>, CH<sub>4</sub>, N<sub>2</sub>, and

H<sub>2</sub>O, and at 298 K and 77 K for H<sub>2</sub>. Also, in the current work, to focus on the effect of the surface defects, conditions of 298 K and 77 K (for H<sub>2</sub>) and 0-1 bar were investigated, which are relevant to gas capture applications. The Peng–Robinson equation of state was used to relate the bulk experimental pressure with the chemical potential required in the GCMC simulations. To speed up the convergence, energy-biased insertions of the sorbate molecules were employed and acceptance ratios for insertions and deletions were above 1% (slightly lower at the higher loadings) to ensure good equilibration in GCMC simulations. At each pressure, approximately 100 million GCMC moves were attempted during each GCMC simulation to allow equilibration and to sample the configuration space. Extended Charge Equilibration (EQeq) was used throughout the equilibration process. To reduce the computational time, the MoS<sub>2</sub> sorbent was assumed rigid with constrained atoms. The rigid framework assumption is because the MoS<sub>2</sub> structures have been optimized in the plane-wave DFT calculations and that the geometries of the framework were not significantly influenced by gas adsorptions.

In the current work, the adsorption of CO<sub>2</sub>, H<sub>2</sub>O, H<sub>2</sub>, CH<sub>4</sub> and N<sub>2</sub> was via only physisorption processes on the pristine (PMoS<sub>2</sub>) surface, which are predominantly associated with vdW forces (also known as dispersion-repulsion forces), while in the optimized MoS<sub>2</sub>-1V<sub>S</sub> configuration, the adsorption of CO<sub>2</sub>, H<sub>2</sub> and H<sub>2</sub>O was via dissociative chemisorption, which is predominantly associated with electrostatic forces (also known as Columbic interactions), which are sourced mainly from the permanent dipole, quadrupole, and higher induced-pole interactions. The vdW forces are present in all systems, but the electrostatic interactions are only present in systems that contain charge, such as charge due to surface functional groups or surface defects [320]. Hence, the vdW interactions between the gas molecules and the surface defect MoS<sub>2</sub> sheet field are described by the Universal force [321] but with the revised Lennard-Jones (LJ) parameters

obtained from our first-principle calculations to describe the electrostatic interaction. The CO<sub>2</sub>, CH<sub>4</sub>, and H<sub>2</sub> molecules were represented by the TraPPE model [322], a three-site rigid model that accounts for the intrinsic quadrupole moment of CO<sub>2</sub> using a partial charge at each site. The partial charges on C and O atoms are  $q(\text{C}) = 0.70 e$  and  $q(\text{O}) = -0.35 e$  ( $e = 1.6022 \times 10^{-19} \text{ C}$ ), respectively. The CO<sub>2</sub> molecule has a bond length ( $l$ ) of 1.14 Å, with a bond angle ( $\theta$ ) of 180°. The CO<sub>2</sub>–CO<sub>2</sub> interactions were modelled as a combination of Lennard-Jones (LJ) and Columbic potentials, where the vdW interactions between two Lennard-Jones (LJ) sites were calculated using the LJ 12-6 potential and the electrostatic interactions were calculated based on the Bader charge analysis. The potential energies associated with different LJ sites were calculated using standard Lorentz–Berthelot mixing rules [323]. TraPPE parameter for CH<sub>4</sub>, H<sub>2</sub> and N<sub>2</sub> was treated using united atom (UA) description [324]. Meanwhile, the H<sub>2</sub>O molecule was represented by the TIP4P-Ew model [325], a four-site rigid model that accounts for the intrinsic polarization of H<sub>2</sub>O using a partial charge at each site and adding a dummy near the O along the bisector of HOH angle of the three-site models, to improve the electrostatic distribution around the water molecule. The partial charges on the dummy atom and H atoms are  $q(\text{M}) = -1.048 e$  and  $q(\text{H}) = +0.524 e$  ( $e = 1.6022 \times 10^{-19} \text{ C}$ ), respectively. The H<sub>2</sub>O molecule has OH and OM bond lengths ( $l$ ) of 0.957 Å and 0.125 Å, respectively, with an HOH bond angle ( $\theta$ ) of 104.5°. Because of the potential existence of dangling Mo atoms in the MoS<sub>2</sub>-1V<sub>S</sub> structure, the MoS<sub>2</sub> surface becomes reactive towards existing volatile components in the adsorbed mixtures, such as water vapour. In the case that temperature and pressure conditions favour surface-bound water or various forms of dissociated water, the CO<sub>2</sub>–surface adsorption may be passivated or enhanced due to the existence of dangling Mo containing defect surface.

## 7.3 Results and Discussion

### 7.3.1 Adsorption Geometries and Energetics from DFT Calculations

In search for the most favourable adsorption configurations, four geometric sites and molecule orientations were considered for the adsorption of different gas molecules ( $\text{CO}_2$ ,  $\text{CH}_4$ ,  $\text{N}_2$ ,  $\text{H}_2$  and  $\text{H}_2\text{O}$ ) on  $\text{PMoS}_2$  and  $\text{MoS}_2_{1V_S}$  layers. The corresponding most favourable configurations for  $\text{PMoS}_2$  and  $\text{MoS}_2_{1V_S}$  are shown in **Figure 7.2**. The adsorption energies of the molecules at four different sites and orientations are summarized for both  $\text{PMoS}_2$  and  $\text{MoS}_2_{1V_S}$  surfaces in **Table 7.2**. In the current work, the most stable configurations of physisorbed  $\text{CO}_2$ ,  $\text{N}_2$  and  $\text{H}_2\text{O}$  molecules on  $\text{PMoS}_2$  and dissociated  $\text{CO}_2$  on  $\text{MoS}_2_{1V_S}$  have been investigated (**Chapter 5**). However, the adsorption energies and atomic configurations of these surfaces as references are still shown in **Table 7.2** and **Figure 7.2**, respectively. The adsorption energy ( $E_{\text{AE}}$ ) is calculated using Eq. (7.1) as described in the Computational Methods (Section 7.2.1).

**Table 7.2** and **Figure 7.2** present the summary of DFT simulation results and the strongest most stable configurations for the adsorption of  $\text{CO}_2$ ,  $\text{CH}_4$ ,  $\text{N}_2$ ,  $\text{H}_2$  and  $\text{H}_2\text{O}$  on  $\text{PMoS}_2$  and  $\text{MoS}_2_{1V_S}$  sites, respectively. In the case of adsorptions on the  $\text{PMoS}_2$  site, the adsorption energy of  $\text{CO}_2$ ,  $\text{CH}_4$ ,  $\text{N}_2$ ,  $\text{H}_2$  and  $\text{H}_2\text{O}$  is -0.14 eV, -0.06 eV, -0.08 eV, -0.79 and -0.15 eV, with an equilibrium molecular height (i.e. the distance between the reference atom of the molecule and the Mo atom) of 3.46, 3.85, 3.61, 3.24 and 3.45 Å (**Table 7.2**), respectively. Also, it is observed that in the optimized  $\text{PMoS}_2$  adsorption configuration, physisorption is the only adsorption mechanism found as evidenced by large separation heights (more than 3.1 Å) and a slight change in bond length and angle. Among these adsorbed molecules,  $\text{H}_2$  has the shortest equilibrium molecular height and largest adsorption energy, indicating a stronger interaction, which is in agreement with a previous

study [326]. Contrarily, the distance between CH<sub>4</sub> (and N<sub>2</sub>) and the Mo atom are higher than the others. Also, on the pristine surface, the adsorption energy of CH<sub>4</sub> and N<sub>2</sub> is very small (less than 0.1 eV), which correlates with the large separation heights. Therefore, these results show that PMoS<sub>2</sub> is not a good sorbent for CO<sub>2</sub>, CH<sub>4</sub>, N<sub>2</sub> and H<sub>2</sub>O molecules adsorption, especially for CH<sub>4</sub> and N<sub>2</sub> molecules, which agrees with previous studies [18].

Compared to the pristine surface, the adsorption mechanisms in optimized MoS<sub>2</sub>\_1V<sub>S</sub> configuration are via physisorption and dissociative chemisorption. We first consider the physisorbed molecules, CH<sub>4</sub> and N<sub>2</sub>, which bounded to the MoS<sub>2</sub>\_1V<sub>S</sub> surface by separation heights larger than 3.1 Å and a slight change in bond length and angle. Specifically, CH<sub>4</sub> and N<sub>2</sub> adsorptions are similar to that on the PMoS<sub>2</sub> surface, but with higher adsorption energies and shorter separation heights. On the MoS<sub>2</sub>\_1V<sub>S</sub>, the adsorption energy of CH<sub>4</sub> and N<sub>2</sub> is -0.11 eV and -0.18 eV (**Table 7.2**), with an equilibrium molecular height of 3.76 and 3.54 Å, respectively. Also, the bond length and angle of the adsorbed CH<sub>4</sub> and N<sub>2</sub> on MoS<sub>2</sub>\_1V<sub>S</sub> is the same as that of the pristine surface. On the other, CO<sub>2</sub>, H<sub>2</sub> and H<sub>2</sub>O molecules were found to undergo dissociative adsorption with -0.91, -2.44 and -0.26 eV adsorption energies, respectively. DFT simulation results reveal that CO<sub>2</sub> dissociated to yield lattice-embedded oxygen and CO molecule that desorb from the surface (**Figure 7.2f**). The full detailed discussion on the dissociation of CO<sub>2</sub> on MoS<sub>2</sub>\_1V<sub>S</sub> has been given in our previous study (**Chapter 5**). About the H<sub>2</sub> dissociation, the optimized MoS<sub>2</sub>\_1V<sub>S</sub> adsorption configuration is characterized by dissociative chemisorption of H<sub>2</sub> into H and H species that bonded with the two Mo dangling atoms at the S vacancy. This leads to the formation of three H-Mo chemical covalent bonds. As shown in **Figure 7.2i**, one of the H atoms coordinated with two unpaired surface M atoms to form two H-Mo chemical covalent bonds of 1.87 Å. While the other H atom bonded to the remaining unpaired surface M atoms to form an

H–Mo chemical covalent bond of 1.70 Å, with the H atom oriented towards the centre of the S vacant site. When comparing this dissociation state with H<sub>2</sub> physisorbed on the MoS<sub>2</sub>-1V<sub>S</sub> vacancy site, H<sub>2</sub> dissociation is favoured by -1.65 eV. H<sub>2</sub>O molecule, on the other hand, dissociated into an OH radical and an H atom that bound to the three dangling Mo atoms. As shown in **Figure 7.2j**, the dissociation of H<sub>2</sub>O into OH and H species leads to the formation of new two O–Mo and one H–Mo covalent bonds of 2.19 Å and 1.66 Å, respectively. The O of the OH radical coordinated with two unpaired surface M atoms to form the O–Mo bond, while the H atom bonded to the remaining unpaired surface M atoms to form the H–Mo bond with the H atom oriented towards the centre of the S vacant site just like in the H<sub>2</sub> dissociation. Again, the new bond formation makes the optimized state more favoured by -0.11 eV with respect to the physisorption state. The calculated O–H bond length is 0.98 Å and the newly formed Mo-O-H molecule bent with an internal angle of 113.47 °, with H atom oriented away from the centre of the S vacant site. These chemical covalent bonds are presumably formed from the combination of s-orbital of H and 4d-orbital of Mo (H–Mo) and p-orbital of O and 4d-orbital of Mo (O–Mo).

**Table 7.2:** Summary of adsorption energies ( $E_{AE}$ ), fully relaxed distances and angles of CO<sub>2</sub>, CH<sub>4</sub>, N<sub>2</sub>, H<sub>2</sub> and H<sub>2</sub>O gas molecules on PMoS<sub>2</sub> and MoS<sub>2</sub>\_1V<sub>s</sub> surface, for the most favourable adsorption configurations. Notations:  $h_{mol-suf}$  is the equilibrium molecular height, i.e. fully relaxed distance between the reference atom of the molecule and Mo atom. For CO<sub>2</sub>, CH<sub>4</sub> and H<sub>2</sub>O, the reference atoms are the central C and O, respectively, while the lowest N and H atoms are the reference atoms for N<sub>2</sub> and H<sub>2</sub>, respectively.  $l$  and  $\theta$  are the bond distances and angles, respectively. The adsorption energies, distances and angles are in eV, Å and degrees (°), respectively.

Molecule	PMoS <sub>2</sub>				MoS <sub>2</sub> _1V <sub>s</sub>			
	$E_{AE}$	$h_{mol-suf}$	$l$	$\theta$	$E_{AE}$	$h_{mol-suf}$	$l$	$\theta$
CO <sub>2</sub>	-0.14	3.46	1.18	179.7	-0.91	<sup>a</sup> 3.00	1.14	-
CH <sub>4</sub>	-0.06	3.85	1.10	109.6	-0.11	3.76	1.10	109.6
N <sub>2</sub>	-0.08	3.65	1.11	-	-0.18	3.54	1.11	-
H <sub>2</sub>	-0.79	3.24	0.75	-	-2.44	-	-	-
H <sub>2</sub> O	-0.15	3.45	0.97	103.8	-0.26	-	0.98	-

<sup>a</sup>3.00 Å, is the distance between C atom of the formed CO gas and O atom that bonded with the surface



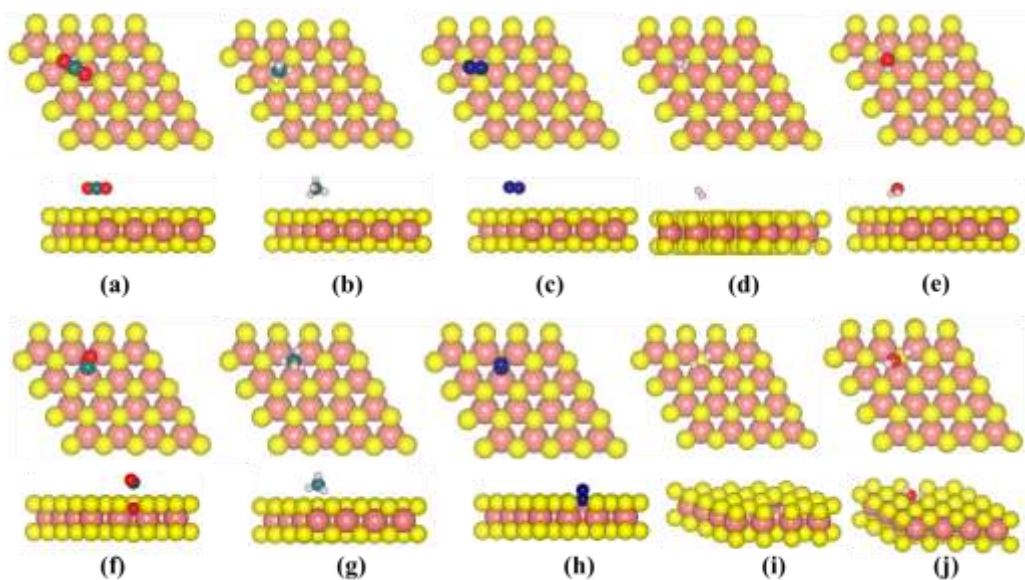


**Figure 7.2:** The schematic structure of DFT strongest most stable adsorption configurations for  $\text{CO}_2$ ,  $\text{CH}_4$ ,  $\text{N}_2$ ,  $\text{H}_2$ ,  $\text{H}_2\text{O}$  molecules adsorbed on  $\text{PMoS}_2$  (a-e) and  $\text{MoS}_2_{1\text{Vs}}$  (f-j) surfaces from the top (upper panel) and side (lower panel) views. Colour code: Mo, pink, S, yellow, O, red, C, light blue, N, dark blue and H, white.

These results reveal that,  $\text{MoS}_2_{1\text{Vs}}$  surface yields stronger interactions than the pristine  $\text{MoS}_2$  ( $\text{PMoS}_2$ ) surface. Specifically, the adsorption energy of  $\text{CO}_2$ ,  $\text{H}_2$  and  $\text{H}_2\text{O}$  molecules on  $\text{MoS}_2_{1\text{Vs}}$  is 6.5, 3.2 and 1.7 times as strong as that on a pristine  $\text{MoS}_2$  surface ( $\text{PMoS}_2$ ), respectively. On the other hand, the adsorption of  $\text{CH}_4$  and  $\text{N}_2$  molecules on  $\text{MoS}_2_{1\text{Vs}}$  is 1.8 and 2.3 times stronger than that on a pristine  $\text{MoS}_2$  surface, respectively. Also, together with the dissociated state of  $\text{CO}_2$ ,  $\text{H}_2$  and  $\text{H}_2\text{O}$  molecules and shorter separation heights of physisorbed  $\text{CH}_4$  and  $\text{N}_2$  molecules, it is clear that these molecules strongly adsorbed on the  $\text{MoS}_2_{1\text{Vs}}$  site than on the  $\text{PMoS}_2$  site when the surface was fully relaxed. Further observation (**Figure 7.3**) depicts that the adsorption of  $\text{H}_2\text{O}$  and  $\text{N}_2$  molecules on  $\text{MoS}_2_{1\text{Vs}}$  is 3.5 and 5.1 times weaker than  $\text{CO}_2$  adsorption, respectively. This suggests  $\text{MoS}_2_{1\text{Vs}}$  to be a suitable adsorbent for selective adsorption and separation of  $\text{CO}_2$

over H<sub>2</sub>O and N<sub>2</sub>. Similarly, CO<sub>2</sub> owns superior selective adsorption over CH<sub>4</sub>; in particular, the adsorption of CH<sub>4</sub> molecules on MoS<sub>2</sub>\_1V<sub>S</sub> is 8.6 times weaker than CO<sub>2</sub> adsorption. In the case of H<sub>2</sub> adsorption on the MoS<sub>2</sub>\_1V<sub>S</sub> site, H<sub>2</sub> interacts stronger than CO<sub>2</sub> as revealed by a small adsorption ratio of 0.37.

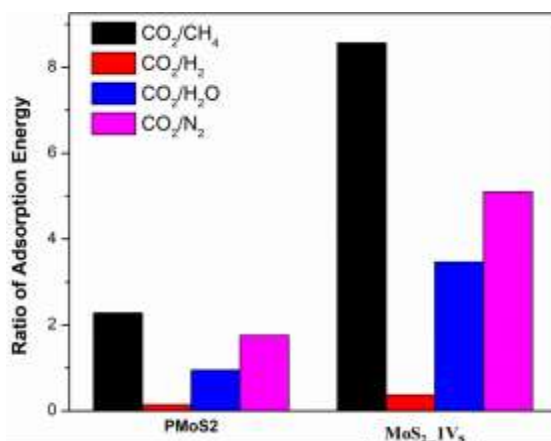


**Figure 7.3:** Ratio of adsorption energies between CO<sub>2</sub> and other molecules for pristine (PMoS<sub>2</sub>) and S vacancy (MoS<sub>2</sub>\_1V<sub>S</sub>) MoS<sub>2</sub> monolayers.

### 7.3.2 Adsorption Isotherms from GCMC Simulations

The comparison of the storage capability of MoS<sub>2</sub>\_1V<sub>S</sub> and PMoS<sub>2</sub> as an absorbent for CO<sub>2</sub>, CH<sub>4</sub>, N<sub>2</sub>, H<sub>2</sub> and H<sub>2</sub>O was determined by calculating the adsorption isotherms using GCMC calculations.

**Figure 7.4** shows the comparison of the calculated gravimetric adsorption isotherms of CO<sub>2</sub>, CH<sub>4</sub>, N<sub>2</sub>, and H<sub>2</sub>O on MoS<sub>2</sub>\_1V<sub>S</sub> and PMoS<sub>2</sub> at 298 K and different pressures. The adsorption isotherm of H<sub>2</sub> was calculated at 77 and 298 K and at the same different pressures as depicted in **Figure 7.5**.

The results reveal that the CO<sub>2</sub> capacities of MoS<sub>2</sub>\_1V<sub>S</sub> and PMoS<sub>2</sub> are enhanced with increasing pressure and gradually approaches saturation, which indicates stronger adsorption. The gravimetric adsorption density of CO<sub>2</sub> storage in MoS<sub>2</sub>\_1V<sub>S</sub> is much more than that of CO<sub>2</sub> on PMoS<sub>2</sub> (**Figure 7.4a**). For instance, the adsorption amount CO<sub>2</sub> in MoS<sub>2</sub>\_1V<sub>S</sub> at 298k and

pressures of 20, 40 and 100 bar is 24.53, 38.37, and 42.59 wt.%. For PMoS<sub>2</sub>, the values are 18.26, 30.42 and 34.05 wt.%. These results show that MoS<sub>2</sub>\_1V<sub>S</sub> enhances the adsorption of CO<sub>2</sub> relative to that of the pure surface as the pressure increases.

Unlike in CO<sub>2</sub> adsorption isotherm, little or no differences were observed for the adsorption of CH<sub>4</sub> (**Figure 7.4b**), N<sub>2</sub> (**Figure 7.4c**), and H<sub>2</sub> (**Figure 7.5a**) molecules at 298 K and different pressures across both surfaces. The gravimetric densities of these molecules on MoS<sub>2</sub>\_1V<sub>S</sub> and PMoS<sub>2</sub> are also enhanced with increasing pressure but did not approach saturation. On the other hand, an increase was observed for H<sub>2</sub> at 77 K and different pressure on the MoS<sub>2</sub>\_1V<sub>S</sub> surface and attain saturation at 90 bar (**Figure 7.5b**). For example, the H<sub>2</sub> uptake gravimetric density values of 2.10 wt.% for MoS<sub>2</sub>\_1V<sub>S</sub> and 1.73 wt.% for PMoS<sub>2</sub> were observed at the pressure of 20 bar and 2.74 wt.% for MoS<sub>2</sub>\_1V<sub>S</sub> and 2.24 wt.% for PMoS<sub>2</sub> at 40 bar. Finally, the H<sub>2</sub> uptake gravimetric density value for MoS<sub>2</sub>\_1V<sub>S</sub> and PMoS<sub>2</sub> attains 3.48 and 2.85 wt.%, respectively, at 77 K and the pressure of 100 bar. These results indicate that single sulphur vacancy plays an important role in the enhancement of H<sub>2</sub> uptake at 77 K than at room temperature.

The water isotherm (**Figure 7.4d**) show a type V shape at low pressures (**Figure 7.6b**), where the interaction between H<sub>2</sub>O molecules is stronger than their interaction with the surfaces. Very slow uptake is observed initially, which increases once the surface coverage is sufficient to induce H<sub>2</sub>O clustering, causing a step-wise increase in the gravimetric density value. For MoS<sub>2</sub>\_1V<sub>S</sub> and PMoS<sub>2</sub>, this step-wise increase occurs after 0.06 and 0.10 bar pressures, respectively. This is due to the hydrophobic characteristic of MoS<sub>2</sub> material, which is consistent with the previously reported hydrophobic nature of MoS<sub>2</sub> [327]. Also, it is observed that after the step-wise increase with increasing pressure, the gravimetric density value gradually approaches saturation. Furthermore, the amount of H<sub>2</sub>O adsorbed in MoS<sub>2</sub>\_1V<sub>S</sub> is much more than that of H<sub>2</sub>O on PMoS<sub>2</sub>

relative to the adsorption of CO<sub>2</sub> on MoS<sub>2</sub>\_1V<sub>S</sub> and PMoS<sub>2</sub> surfaces. For example, the adsorption amount of H<sub>2</sub>O in MoS<sub>2</sub>\_1V<sub>S</sub> at 298k and pressures of 20, 40 and 100 bar are 56.25, 56.65, and 57.29 wt.%. For PMoS<sub>2</sub>, the values are 45.00, 45.50 and 45.68 wt.%. The reason is that H<sub>2</sub>O being a much more polar molecule than CO<sub>2</sub> due to a strong permanent dipole moment of H<sub>2</sub>O having a stronger effect than quadrupole moment of CO<sub>2</sub>, would show a stronger effect of the single sulphur vacancy on adsorption isotherms. Hence, the H<sub>2</sub>O molecule will always preferentially adsorb over CO<sub>2</sub> to these surfaces.

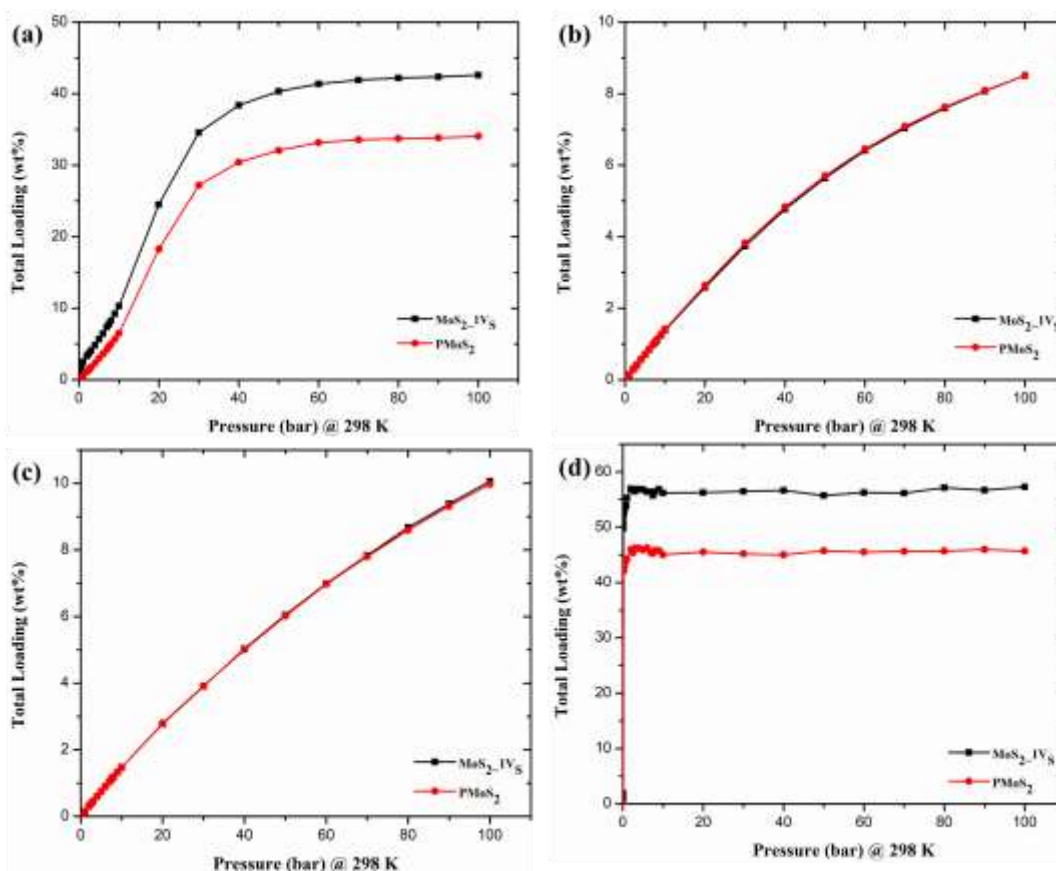


**Figure 7.4:** The gravimetric adsorption isotherms for (a) CO<sub>2</sub>, (b) CH<sub>4</sub>, (c) N<sub>2</sub>, and (d) H<sub>2</sub>O uptake on S vacancy (MoS<sub>2</sub>\_1V<sub>S</sub>) and pristine (PMoS<sub>2</sub>) MoS<sub>2</sub> monolayers at 298 K.

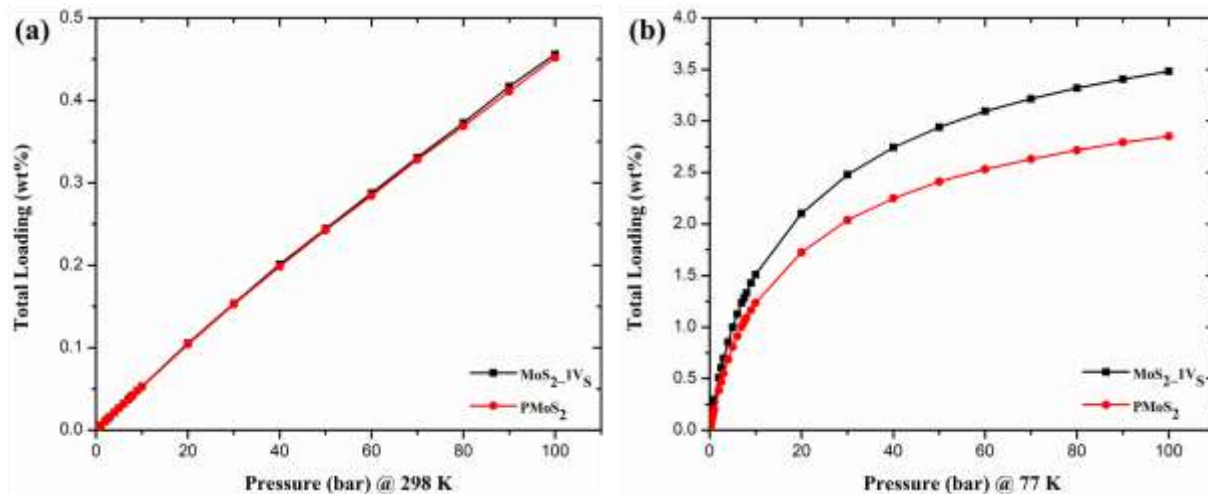


**Figure 7.5:** The gravimetric adsorption isotherms for H<sub>2</sub> uptake on S vacancy (MoS<sub>2</sub>\_1V<sub>S</sub>) and pristine (PMoS<sub>2</sub>) MoS<sub>2</sub> monolayers at (a) 298 K and (b) 77 K.

The results obtained from the simulations of CO<sub>2</sub> and H<sub>2</sub>O at 1 bar, 298 K, and that of H<sub>2</sub> at 1 bar, 77 K, reveal that the single sulphur vacancy plays an important role in low pressure regions in determining the storage capacities of MoS<sub>2</sub>\_1V<sub>S</sub>. In agreement with DFT results, the GCMC simulation demonstrated that MoS<sub>2</sub>\_1V<sub>S</sub> enhances the adsorption of CO<sub>2</sub> and H<sub>2</sub>O at 1 bar, 298 K and H<sub>2</sub> at 1 bar, 77 K relative to that of the pure surface. We observe CO<sub>2</sub> loadings of 2.49 wt.% and 0.55 wt.%, H<sub>2</sub>O loadings of 55.27 wt.% and 44.25 wt.%, and H<sub>2</sub> loadings of 0.29 wt.% and 0.20 wt.%, for the MoS<sub>2</sub>\_1V<sub>S</sub> and PMoS<sub>2</sub> surfaces respectively, as shown in **Figure 7.6a-c**. Hence, single sulphur vacancy defects can be used as an efficient adsorbent for adsorption of CO<sub>2</sub>, H<sub>2</sub>O and H<sub>2</sub> molecules, and the adsorption capability can be controlled by the density of defects in the MoS<sub>2</sub> layer. In the experiment, the synthesis of MoS<sub>2</sub> bilayer and multilayer are common and they have enough space between the layers for the gas molecules to access, therefore, these results demonstrate that modulating the density of defects in these multilayers MoS<sub>2</sub> could be more effective at capturing these gases and is subject to further investigation.

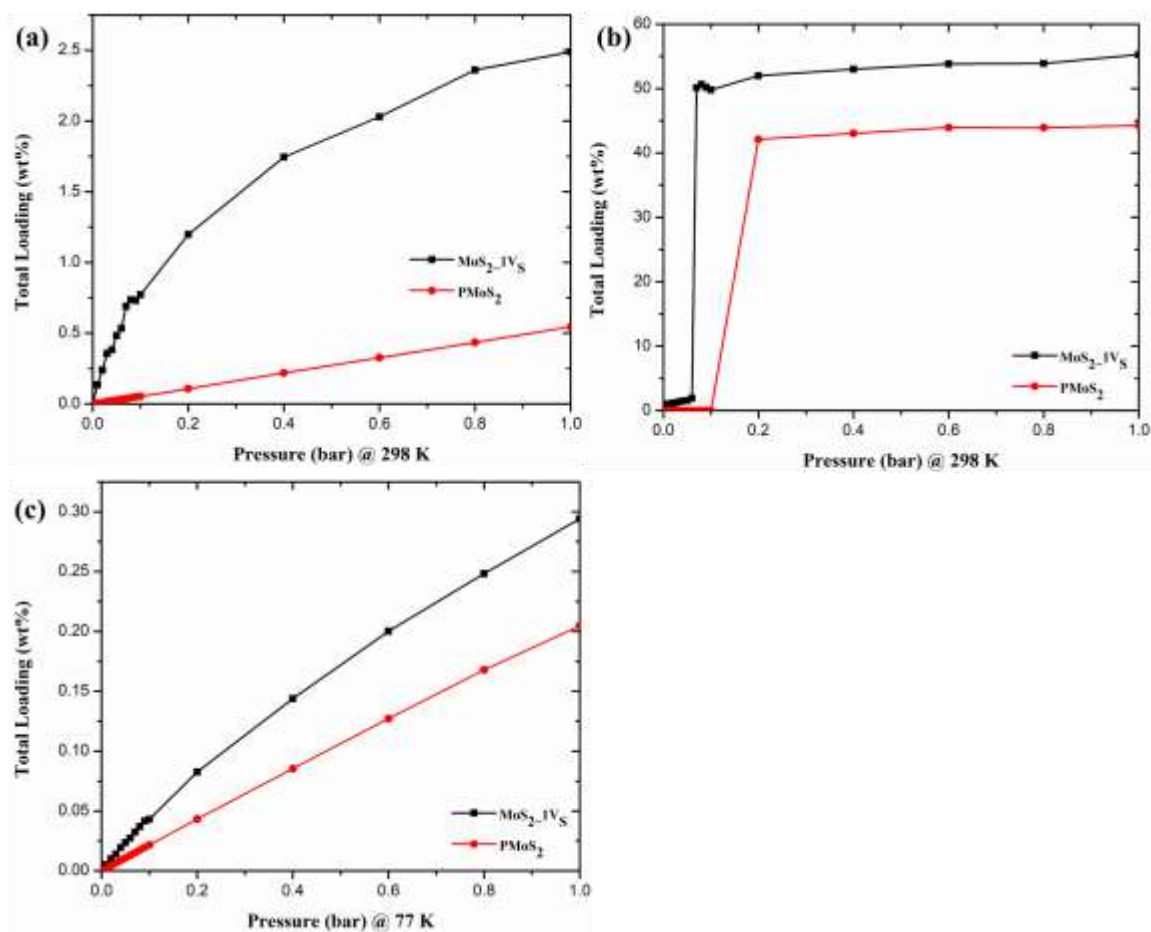


**Figure 7.6:** The gravimetric adsorption isotherms for (a) CO<sub>2</sub>, (b) H<sub>2</sub>O, and (c) H<sub>2</sub> uptake on S vacancy (MoS<sub>2</sub>\_1Vs) and pristine (PMoS<sub>2</sub>) MoS<sub>2</sub> monolayers at 298 and 77 K, calculated at 0-1 bar pressure range.

### 7.3.3 C-NEB Analysis of Dissociative Adsorption of CO<sub>2</sub>, H<sub>2</sub> and H<sub>2</sub>O on MoS<sub>2</sub>\_1Vs Site

For the CO<sub>2</sub>, H<sub>2</sub> and H<sub>2</sub>O dissociation reactions on the studied monolayer MoS<sub>2</sub>\_1Vs site, we performed CI-NEB calculations with 4 images to evaluate the MEP and transition states (TS) energy, and locate the TS. For each molecule, the initial state (IS) and final state (FS) are obtained from the adsorption configurations discussed in Section 7.1. The IS for each molecule corresponds

to the molecule physisorption, which occurred when the molecules are placed initially at about 3.0 Å away from the plane of the S vacancy site, while the FS corresponds to dissociated CO<sub>2</sub>, H<sub>2</sub> and H<sub>2</sub>O molecules (**Figures 7.2f, 7.2i and 7.4j**, respectively). **Figure 7.7** presents the summary of CI-NEB simulation results, which includes the energy profile that represents MEP between the IS and FS, the activation energy barrier that corresponds to the saddle point (TS) along the MEP, and the geometries of IS, TS and FS. The chosen TS configuration is the geometry of the highest energy point along the MEP. All the dissociations are energetically downward processes. In the case of CO<sub>2</sub> dissociation on MoS<sub>2</sub>\_1V<sub>S</sub>, CO<sub>2</sub> molecule chemisorbed on the surface at the TS, with the O atom forming a bond (2.22 Å) with one of the Mo dangling atoms at the S vacancy. The chemisorbed CO<sub>2</sub> adopts a tilted orientation (~148 ° bond angle) with the unbounded O atom pointing up from the surface. The C=O bond length of the bonded O extended to 1.25 Å from 1.18 Å in the IS, while that of the free O atom remains unchanged. Eventually, the CO detached from the bonded O atom to form a CO molecule that desorbs from the surface, with the bonded O atom forming lattice-embedded oxygen in the FS. This configuration is similar to the dissociation state obtained during geometry optimization in **Chapter 5**. The calculated activation energy barrier (E<sub>a</sub>) is 1.11 eV and the dissociation is energetically favoured by 0.79 eV reaction energy (ΔE). The low activation barrier and negative reaction energy point to favourable kinetics and thermodynamics, respectively, given the exponential dependence of reaction rate. This beats the best MEP obtained from previous DFT studies of CO<sub>2</sub> dissociation on defective graphene sheets [237] and a metallic surface of mackinawite (FeS (011)) [299], but close to the results of graphene-like boron nitride with boron vacancy [298]. The single imaginary frequency of 219.59 cm<sup>-1</sup> calculated at TS indicates that the searched transition state is indeed the saddle point between the two local minima (stationary states (physisorption and dissociation)) along the MEP.

For H<sub>2</sub> molecule dissociation on MoS<sub>2</sub>\_1V<sub>S</sub>, H<sub>2</sub> molecule strongly adsorbed on the surface at the TS, with a separation of 0.35 Å between the nearest surface S atom and an H atom. The H<sub>2</sub> molecule tilted towards the S plane and the H–H bond length extended to 0.78 Å from 0.75 Å in the IS. In the FS, H<sub>2</sub> dissociated and the H atoms eventually draw close to the surface and form bonds with the two Mo dangling atoms at the S vacancy just like explained in Section 7.1. The calculated activation energy barrier (E<sub>a</sub>) is 0.65 eV and the dissociation is energetically favoured by 0.32 eV. These results are closed to the reported results [160, 260], but different from the reported results where H<sub>2</sub> was found to move away from MoS<sub>2</sub> with an S vacancy row no matter where it is placed initially [264]. Again, the TS searched is also confirmed by a single imaginary frequency of 671.68 cm<sup>-1</sup>.

The reaction path of the dissociation of H<sub>2</sub>O molecule on MoS<sub>2</sub>\_1V<sub>S</sub> was found to be similar to the CO<sub>2</sub> dissociation. In TS, the H<sub>2</sub>O molecule is chemisorbed on the surface to allow the O atom to form bonds (2.27 Å each) with two of the Mo dangling atoms at the S vacancy. The H<sub>2</sub>O molecule adopts a tilted orientation with one of the H atoms pointing up from the surface while the other tilted towards the S plane. This extended the O–H bond lengths and bond angle to 0.99 and 1.19 Å, and ~126 ° from 0.97 Å and ~104 °, respectively, in the IS. Finally, the H atom that tilted towards the S plane detached from OH species to form a bond with one of the Mo dangling atoms at the S vacancy in the FS, achieving the same configuration that was observed in Section 7.3.1. The calculated E<sub>a</sub> and ΔE is 0.18 eV and -0.05 eV, respectively. This activation energy is significantly lower than that for H<sub>2</sub>O splitting on Mo-edge (0.54 eV) reported by Ref [290]. On the other hand, H<sub>2</sub>O dissociation on the MoS<sub>2</sub>\_1V<sub>S</sub> surface is less thermodynamically favourable due to its small reaction energy compared to more negative reaction energy of -1.29 eV of Ref [290]. The single imaginary frequency calculated at 914.50 cm<sup>-1</sup> confirms the TS searched.



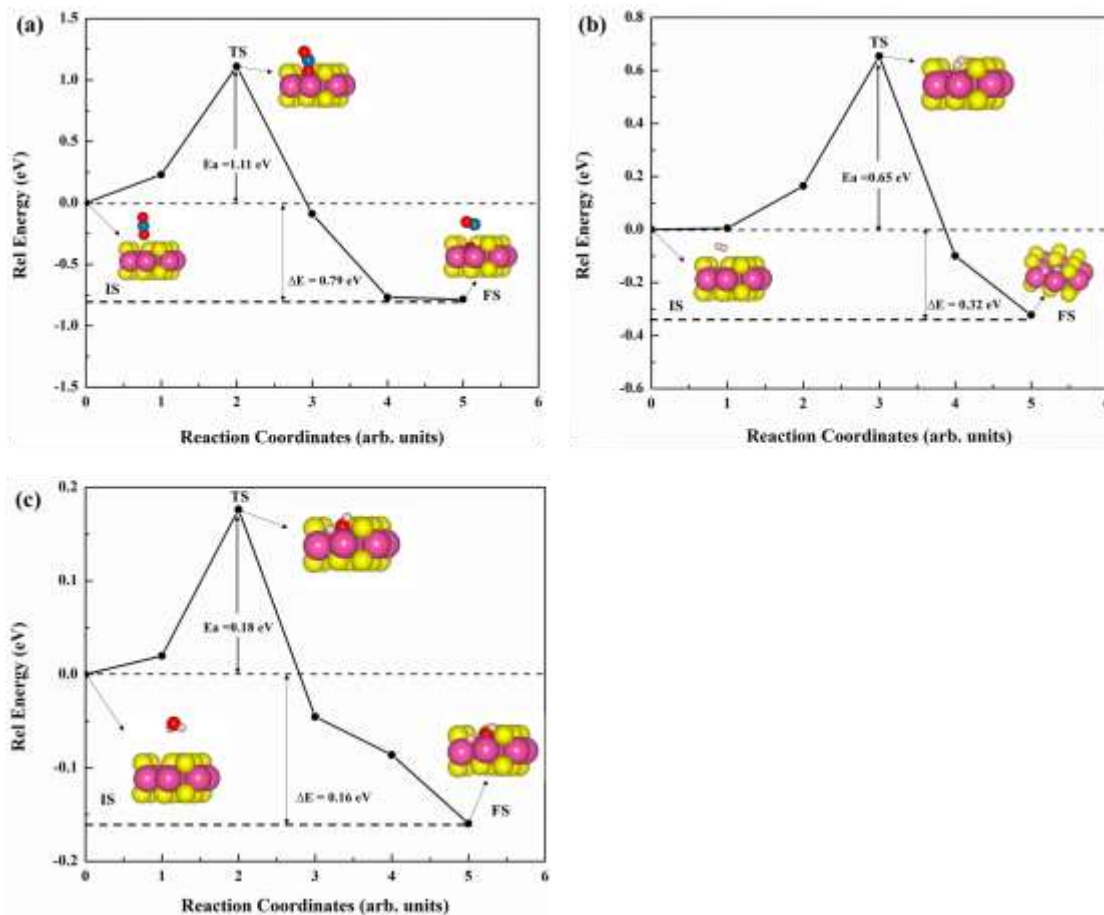


**Figure 7.7:** Energy diagram including reaction pathway and reaction barrier of single (a) CO<sub>2</sub>, (b) H<sub>2</sub> and (c) H<sub>2</sub>O dissociation on MoS<sub>2</sub>\_1V<sub>s</sub> from climbing image nudged elastic band (CI-NEB) simulation. Inserts are the top views of the initial state (IS); Transition state (TS) and final state (FS) configurations along the MEP. The colour codes for Mo, S, O, H and C atoms are the same as explained in **Figure 7.2**.

### 7.3.4 Energy Barrier after Enthalpy Correction

The reported  $E_a$  and  $\Delta E$  from NEB analysis in **Figure 7.7** correspond to the potential energy surface differences at ground state (0 K) and as a result do not account for contribution from

vibrational, rotational and translation energies. Therefore, quantum corrections to the activation barrier at room temperature (300 K) were considered to explicitly analyse the room temperature effect on the activation barrier and get a more realistic view of the catalytic reaction. The zero point energy (ZPE), as well as entropic correction, were incorporated by calculating Gibbs free energy ( $\Delta G_a$ ) between IS and TS as defined in **Chapter 6**. The calculated  $\Delta G_a$  of activation for the dissociation reaction of CO<sub>2</sub>, H<sub>2</sub> and H<sub>2</sub>O molecules on MoS<sub>2</sub>\_1V<sub>S</sub> are 0.35 eV, 0.30 eV and -0.66 eV, respectively. According to a previous study, the threshold for reactions to proceed readily at room temperature is a barrier of 21 kcal/mol (~0.8 eV) or less will [288]. The corrected reaction barriers are within this threshold, indicating that the predicted reactions should be feasible at room temperature. The low values of  $\Delta G_a$  suggest not only that the MoS<sub>2</sub>\_1V<sub>S</sub> site has excellent catalytic property but also that dissociation of CO<sub>2</sub>, H<sub>2</sub> and H<sub>2</sub>O molecules could be spontaneous at room temperature. This makes it a possible route for CO<sub>2</sub> activation and reduction, H<sub>2</sub> and H<sub>2</sub>O splitting. When Gibbs free energies are compared, it is obvious that water dissociation on MoS<sub>2</sub>\_1V<sub>S</sub> occurs more spontaneously at room temperature, since it has the lowest  $\Delta G_a$ .

The exponential dependence of the kinetic rate constant on the activation energy can be estimated by transition state theory expression explained in **Chapter 6**. The calculated kinetic rate constants for CO<sub>2</sub>, H<sub>2</sub> and H<sub>2</sub>O molecules at 300 K are  $7.09 \times 10^6 \text{ s}^{-1}$ ,  $5.20 \times 10^7 \text{ s}^{-1}$  and  $6.79 \times 10^{23} \text{ s}^{-1}$ , respectively. These very high rates suggest that a single S vacant MoS<sub>2</sub> site is very favourable for the CO<sub>2</sub>, H<sub>2</sub> and H<sub>2</sub>O dissociation reaction not only thermodynamically but also kinetically, and the reaction is likely to occur spontaneously and quickly at room temperature. Therefore, CO<sub>2</sub>, H<sub>2</sub> and H<sub>2</sub>O dissociations observed in this study is likely not the rate-limiting step for CO<sub>2</sub> activation and reduction, and overall H<sub>2</sub> evolution process from H<sub>2</sub> and H<sub>2</sub>O splitting, therefore further steps will be studied in our further study.

## 7.4 Summary and Conclusions

Single vacancy or a missing sulphur atom in Molybdenum disulphide ( $\text{MoS}_2\text{-1V}_\text{S}$ ) is demonstrated to be thermodynamically and statistically favourable for the adsorption of  $\text{CO}_2$ ,  $\text{CH}_4$ ,  $\text{N}_2$ ,  $\text{H}_2$  and  $\text{H}_2\text{O}$  with adsorption energies of -0.91, -0.11, -0.18, -2.44 and -0.26 eV, respectively, which are approximately 6.5, 1.8, 2.3, 3.2 and 1.7 times superior to that of pristine  $\text{MoS}_2$  ( $\text{PMoS}_2$ ) surface, respectively. DFT and statistical thermodynamics results show that the presence of elemental sulphur vacancy in  $\text{MoS}_2$  redefined the chemical and physical properties of the  $\text{MoS}_2$  surface; thus improving its gaseous adsorption and conversion applications. DFT simulation reveals that the highest  $\text{CO}_2$  adsorption energies obtained after geometry optimization were -0.14 eV and -0.91 eV for perfect  $\text{MoS}_2$  surface ( $\text{PMoS}_2$ ) and  $\text{MoS}_2\text{-1V}_\text{S}$  respectively. Further observation depicts that the adsorption of  $\text{H}_2\text{O}$  and  $\text{N}_2$  molecules on  $\text{MoS}_2\text{-1V}_\text{S}$  is 3.5 and 5.1 times weaker than  $\text{CO}_2$  adsorption, respectively. This suggests  $\text{MoS}_2\text{-1V}_\text{S}$  to be a suitable adsorbent for selective adsorption and separation of  $\text{CO}_2$  over  $\text{H}_2\text{O}$  and  $\text{N}_2$ . Moreover, optimized  $\text{MoS}_2\text{-1V}_\text{S}$  configuration stipulates that adsorption of  $\text{CO}_2$ ,  $\text{H}_2$  and  $\text{H}_2\text{O}$  was via dissociative chemisorption, in contrast to optimized  $\text{PMoS}_2$  configuration, for which physisorption was the only adsorption mechanism.

Classical GCMC simulations further investigated the adsorption properties of  $\text{PMoS}_2$  and  $\text{MoS}_2\text{-1V}_\text{S}$  between 0 – 100 bar. Little or no differences were observed for the adsorption of  $\text{N}_2$ ,  $\text{H}_2$  and  $\text{CH}_4$  molecules across both surfaces. An increase of 0.63 wt.% was observed for  $\text{H}_2$  at 77K on the  $\text{MoS}_2\text{-1V}_\text{S}$  surface. In agreement with DFT results, the GCMC simulation also demonstrated that  $\text{MoS}_2\text{-1V}_\text{S}$  enhances the adsorption of  $\text{CO}_2$  and  $\text{H}_2\text{O}$  at 1 bar, 298 K, and  $\text{H}_2$  at 1 bar, 77 K relative to that of the pure surface. We observe  $\text{CO}_2$  loadings of 2.49 wt.% and 0.55

wt.%, H<sub>2</sub>O loadings of 55.27 wt.% and 44.25 wt.%, and H<sub>2</sub> loadings of 0.29 wt.% and 0.20 wt.%, for the MoS<sub>2</sub>\_1V<sub>S</sub> and PMoS<sub>2</sub> surfaces, respectively.

Furthermore, in agreement with the conjugate gradient energy minimization (DFT geometry optimization), CI-NEB analysis reveals that the partial CO<sub>2</sub> and H<sub>2</sub>O dissociation, and complete H<sub>2</sub> splitting processes exhibited energy barriers of 1.11 eV, 0.65 eV and 0.18 eV, respectively. In addition, the free energy of activation for the partial and complete dissociation of CO<sub>2</sub> and H<sub>2</sub>O, and H<sub>2</sub> are 0.35 eV, 0.30 eV, and -0.66 eV, respectively. The reactions were found to be kinetically favourable with high reaction rate constants of  $7.09 \times 10^6 \text{ s}^{-1}$ ,  $5.20 \times 10^7 \text{ s}^{-1}$ , and  $6.79 \times 10^{23} \text{ s}^{-1}$  at 300 K for CO<sub>2</sub>, H<sub>2</sub> and H<sub>2</sub>O molecules, respectively.

Conclusively, this study suggests the potential application of MoS<sub>2</sub>\_1V<sub>S</sub> for carbon capture, CO<sub>2</sub> activation and reduction, water and H<sub>2</sub> splitting, and demonstrates the great potential applicability of a catalyst overall H<sub>2</sub> evolution process from water splitting.

# CHAPTER 8

## Conclusions and Future Work

In this chapter, the summary of conclusions of the work presented in the thesis and recommendations for future work are discussed.

### 8.1 Conclusions

The work presented in this thesis has dealt extensively with broadening the calculation of molecular interactions with 2D nanomaterials by making them as accurate as possible, with an extension of the methods studied towards the calculation of structural and electronic properties, Infrared (IR) Spectroscopy, and the barrier energies, thermodynamics properties and molecular dynamics (MD) of the dissociated states. This has been done exclusively using DFT based approaches implemented in the Vienna ab initio simulation package (VASP).

The accuracy of a wide range of different dispersion schemes has been employed to understand the effects of vdW forces on the adsorption properties for pristine and modified surfaces. The DFT-D2 calculations using Grimme's method have been found to perform well, especially within the spin-polarized framework. Speed has been explored for cutoff energy and k-point grid, which is required for convergence. Hence, a test for cutoff and k-point grid was carried and the results were compared for several selected parameters. It was found that the results from 5x5x1 Monkhorst-Pack grids were very similar to those for the 6x6x1 and 7x7x1 Monkhorst-Pack grids. The total energy was converged to <10 meV. Hence, it was believed that 5x5x1 Monkhorst-Pack is dense enough for the selected systems and that 500 eV cutoff energy is suitable for the plane-wave basis

set. Finer k-point of  $9 \times 9 \times 1$  Monkhorst-Pack were used for sampling the Brillouin zone density of state calculations to ensure accurate prediction of the DOS of the semiconductors and that significant increases in computational efficiency are possible for the selected systems, following the work presented in **Chapter 4**. Furthermore, different calculations have been performed with a wide range of supercell and a  $4 \times 4 \times 1$  supercell of monolayer  $\text{MoS}_2$  (1H- $\text{MoS}_2$ ) containing (16 Mo atoms and 32 S atoms) and  $5 \times 5 \times 1$  supercell of monolayer graphene containing 50 C atoms for the monolayers have been found to perform well. A large vacuum layer of 15 Å has been used in the direction to the interface as an isolated slab boundary condition to avoid interlayer interactions in all calculations.

This thesis work started with an aim of developing finely tailored 2D nanomaterials that will describe the behaviour of  $\text{CO}_2$  on the adsorption sites, which are sensitive and selective to  $\text{CO}_2$ . During the course of this work, 2D nanostructure layered materials namely graphene and  $\text{MoS}_2$  with 4 novel materials for  $\text{CO}_2$  adsorption (graphene/ $\text{MoS}_2$  ( $\text{GMoS}_2$ ) and  $\text{MoS}_2$ /graphene ( $\text{MoS}_2\text{G}$ ) hybrids (**Chapter 4**), N atoms surrounding a single Mo vacancy site ( $\text{MoS}_2\text{-1V}_{\text{Mo}}\text{-3N}_\text{S}$ ) (**Chapter 5 and 6**) and single sulphur vacancy  $\text{MoS}_2$  (**Chapter 7**) were developed. **Chapter 4** explored the effect of interlayer distance between 2D materials, graphene/graphene (GrapheneB) and  $\text{MoS}_2$ / $\text{MoS}_2$  ( $\text{MoS}_2\text{B}$ ) bilayers as well as graphene/ $\text{MoS}_2$  ( $\text{GMoS}_2$ ) and  $\text{MoS}_2$ /graphene ( $\text{MoS}_2\text{G}$ ) hybrids, on  $\text{CO}_2$  adsorption mechanisms from first principles, intending to find the most stable conformation for  $\text{CO}_2$  adsorptions. The findings show that the modification of interlayer spacing and structural configuration during the synthesis route is the key to enhancing the adsorption performance of these nanocomposites. **Chapters 5, 6, and 7** have then looked at calculating the adsorption performance and catalytic activity of the developed N-doped and vacancy-containing  $\text{MoS}_2$  material towards  $\text{CO}_2$  adsorption and activation in some instant at various temperatures and

pressure. The findings reveal that N atoms and vacancy defects have effects on the structural properties of the MoS<sub>2</sub> surface and that the N-doping enabled defect engineering of MoS<sub>2</sub> proved to be an effective approach for the enhanced selective adsorption of CO<sub>2</sub>. The enhanced adsorption of CO<sub>2</sub> on the N-doped vacancy-containing MoS<sub>2</sub> surface was tested for cross-interference in presence of N<sub>2</sub> and H<sub>2</sub>O. This was crucial since the adsorption phenomenon of vacancy defect and nitrogen doping facilitates CO<sub>2</sub> and H<sub>2</sub>O dissociations at room temperature leading to the formation of CO\* and O\*, and OH\* and H\* radicals. From a critical review of literature, this technique was only conducted for carbon surfaces (e.g. graphene). In addition, the single S vacancy defect was identified for dissociative chemisorption of CO<sub>2</sub> at the vacant site during CO<sub>2</sub> adsorption to yield lattice-embedded oxygen and CO molecule that desorb from the surface. The reason can be associated with the perpendicular orientation of the CO<sub>2</sub> molecule and the increased covalent attractions, which was not considered in previously reported studies. Further, infrared (IR) spectroscopy of molecules adsorbed on the surface was calculated to analyse the structure of the surface adsorbates, and to show how calculated vibrational frequencies of molecules adsorbed on the surface can be used as an important complement to experimental measurements.

Finally, **Chapter 6** and **7**, make use of a range of computational chemistry tools to investigate the adsorption and dissociation of CO<sub>2</sub>, H<sub>2</sub> and H<sub>2</sub>O on tertiary N-doped, single Mo vacancy MoS<sub>2</sub> (MoS<sub>2</sub>\_1V<sub>Mo</sub>\_3N<sub>S</sub>) and single S-vacancy MoS<sub>2</sub> (MoS<sub>2</sub>\_1V<sub>S</sub>). An in-depth, first principles-based investigation of CO<sub>2</sub> reduction (CO<sub>2</sub> → CO<sup>-</sup> + H<sup>+</sup>) and water splitting (H<sub>2</sub>O → OH<sup>-</sup> + H<sup>+</sup>) mechanisms, in terms of thermodynamic stability, active sites, activation barriers and rate of reactions on MoS<sub>2</sub>\_1V<sub>Mo</sub>\_3N<sub>S</sub> and MoS<sub>2</sub>\_1V<sub>S</sub> were carried out. The findings show that while MoS<sub>2</sub>\_1V<sub>Mo</sub>\_3N<sub>S</sub> is of great potential to be used as a catalyst for CO<sub>2</sub> reduction and water splitting, MoS<sub>2</sub>\_1V<sub>S</sub> performs well for CO<sub>2</sub> reduction, H<sub>2</sub>, and water splitting. In agreement with DFT

results, the GCMC simulation also demonstrated that MoS<sub>2</sub>-1V<sub>S</sub> enhances the adsorption of CO<sub>2</sub> and H<sub>2</sub>O at 1 bar, 298 K relative to that of the pure surface, following the work presented in **Chapter 7**. Conclusively, this study suggests the potential application of MoS<sub>2</sub>-1V<sub>S</sub> for carbon capture, CO<sub>2</sub> activation and reduction, water and H<sub>2</sub> splitting, and demonstrates the great potential applicability of a catalyst overall H<sub>2</sub> evolution process from water splitting.

## 8.2 Recommended Future Work

All through the course of this thesis work, several novel concepts showing tremendous research potential were identified which could be recommended for future work. Some of these areas of interest can be summarized as below:

1. In the case of hybrid nanostructured, to attain the modification of interlayer spacing and structural configuration in preparation of graphene-MoS<sub>2</sub> nanosheets for improved adsorption performance of CO<sub>2</sub>, the combination of improved atomic level studies and design of experiments like nanoparticle tracking analysis could serve as useful guidance.
2. The effect of metal-doped such as Cu and Co vacancy defect MoS<sub>2</sub> adsorption stability can be undertaken. The materials have been shown to offer exceptional electron conductivity to catalytically activate CO<sub>2</sub> conversion and water splitting processes for a better catalysts design. Thermodynamic results from such studies will provide bright insight into CO<sub>2</sub> reduction and water splitting.
3. The study of photochemical and electrochemical performances of this doped MoS<sub>2</sub> surface for dissociation of CO<sub>2</sub>, H<sub>2</sub>, H<sub>2</sub>O and other interfering gases, can be carried out using Computational Hydrogen Electrode (CHE) model and experimental approach and will provide further evidence of the feasibility of the doped MoS<sub>2</sub> in the industrial application.



4. Furthermore, the insight of DFT and ab initio atomistic thermodynamics on the surface stability and morphology of doped MoS<sub>2</sub> surface can be investigated, to show remarkable activity and selectivity in the sustainable production of fuels and chemicals through the highly efficient dissociation of inert CO<sub>2</sub> and H<sub>2</sub>O.

## REFERENCES

- [1] D. G. Kaufman and C. M. Franz, *Biosphere 2000: Protecting Our Global Environment* (Kendall/Hunt Publishing Company, 2011), retrieved 11 October 2011.
- [2] M. Ma, B.J. Trześniewski, J. Xie, W.A. Smith, Selective and Efficient Reduction of Carbon Dioxide to Carbon Monoxide on Oxide-Derived Nanostructured Silver Electrocatalysts, *Angewandte Chemie International Edition*, 55 (2016) 9748-9752.
- [3] N.O.A.A. (NOAA), Trends in Carbon Dioxide: Globally averaged marine surface monthly mean data, Earth System Research Laboratory (ESRL), DOI (2017).
- [4] H.C. Kinney, B.T. Thach, The Sudden Infant Death Syndrome, *New England Journal of Medicine*, 361 (2009) 795-805.
- [5] E. Gellhorn, THE EFFECT OF O<sub>2</sub>-LACK, VARIATIONS IN THE CO<sub>2</sub>-CONTENT OF THE INSPIRED AIR, AND HYPERPNEA ON VISUAL INTENSITY DISCRIMINATION, *American Journal of Physiology-Legacy Content*, 115 (1936) 679-684.
- [6] M.L.S. C. D. Farrar, W. C. Evans, J. F. Howle, B. D. Kerr, B. M. Kennedy, C., Y.K.a.J.R. Southon, Forest-killing diffuse CO<sub>2</sub> emission at Mammoth Mountain as a sign of magmatic unrest, *Nature*, 376 (1995).
- [7] A.B. Rao, A.R. Rubin, *Environ. Sci. Technol.*, p. 4467, A Technical, Economic, and Environmental Assessment of Amine-Based CO<sub>2</sub> Capture Technology for Power Plant Greenhouse Gas Control, *Environ. Sci. Technol.*, 36 (2002) 4467-4475.
- [8] J.Y. Wong, R.L. Anderson, *Non-Dispersive Infrared Gas Measurement*, International Frequency Sensor Association Publishing, USA, 2012.
- [9] S. Budinis, S. Krevor, N.M. Dowell, N. Brandon, A. Hawkes, An assessment of CCS costs, barriers and potential, *Energy Strategy Reviews*, 22 (2018) 61-81.
- [10] C. Cazorla, The role of density functional theory methods in the prediction of nanostructured gas-adsorbent materials, *Coordination Chemistry Reviews*, 300 (2015) 142-163.
- [11] L. Ci, L. Song, C. Jin, D. Jariwala, D. Wu, Y. Li, A. Srivastava, Z.F. Wang, K. Storr, L. Balicas, F. Liu, P.M. Ajayan, Atomic layers of hybridized boron nitride and graphene domains, *Nature Materials*, 9 (2010) 430.
- [12] C. Lee, Q. Li, W. Kalb, X.-Z. Liu, H. Berger, R.W. Carpick, J. Hone, Frictional Characteristics of Atomically Thin Sheets, *Science*, 328 (2010) 76-80.
- [13] K.S. Novoselov, D. Jiang, F. Schedin, T.J. Booth, V.V. Khotkevich, S.V. Morozov, A.K. Geim, Two-dimensional atomic crystals, *Proceedings of the National Academy of Sciences of the United States of America*, 102 (2005) 10451-10453.
- [14] H. Li, C. Tsai, A.L. Koh, L. Cai, A.W. Contryman, A.H. Fragapane, J. Zhao, H.S. Han, H.C. Manoharan, F. Abild-Pedersen, J.K. Nørskov, X. Zheng, Activating and optimizing MoS<sub>2</sub> basal planes for hydrogen evolution through the formation of strained sulphur vacancies, *Nature Materials*, 15 (2016) 48-53.
- [15] X.-Y. Yu, H. Hu, Y. Wang, H. Chen, X.W. Lou, Ultrathin MoS<sub>2</sub> Nanosheets Supported on N-doped Carbon Nanoboxes with Enhanced Lithium Storage and Electrocatalytic Properties, *Angewandte Chemie International Edition*, 54 (2015) 7395-7398.
- [16] C. Ataca, S. Ciraci, Dissociation of H<sub>2</sub>O at the vacancies of single-layer MoS<sub>2</sub>, *Physical Review B*, 85 (2012) 195410.

- [17] D. Ma, W. Ju, T. Li, G. Yang, C. He, B. Ma, Y. Tang, Z. Lu, Z. Yang, Formaldehyde molecule adsorption on the doped monolayer MoS<sub>2</sub>: A first-principles study, *Applied Surface Science*, 371 (2016) 180-188.
- [18] N. Yu, L. Wang, M. Li, X. Sun, T. Hou, Y. Li, Molybdenum disulfide as a highly efficient adsorbent for non-polar gases, *Physical Chemistry Chemical Physics*, 17 (2015) 11700-11704.
- [19] V.P. Pham, G.Y. Yeom, Recent Advances in Doping of Molybdenum Disulfide: Industrial Applications and Future Prospects, *Advanced Materials*, 28 (2016) 9024-9059.
- [20] S.-Y. Cho, S.J. Kim, Y. Lee, J.-S. Kim, W.-B. Jung, H.-W. Yoo, J. Kim, H.-T. Jung, Highly Enhanced Gas Adsorption Properties in Vertically Aligned MoS<sub>2</sub> Layers, *ACS Nano*, 9 (2015) 9314-9321.
- [21] B.H.R. Suryanto, D. Wang, L.M. Azofra, M. Harb, L. Cavallo, R. Jalili, D.R.G. Mitchell, M. Chatti, D.R. MacFarlane, MoS<sub>2</sub> Polymorphic Engineering Enhances Selectivity in the Electrochemical Reduction of Nitrogen to Ammonia, *ACS Energy Letters*, 4 (2019) 430-435.
- [22] O.G. Sánchez, Y.Y. Birdja, M. Bulut, J. Vaes, T. Breugelmans, D. Pant, Recent advances in industrial CO<sub>2</sub> electroreduction, *Current Opinion in Green and Sustainable Chemistry*, 16 (2019) 47-56.
- [23] H. Wang, Z. Cheng, Y. Liao, J. Li, J. Weber, A. Thomas, C.F.J. Faul, Conjugated Microporous Polycarbazole Networks as Precursors for Nitrogen-Enriched Microporous Carbons for CO<sub>2</sub> Storage and Electrochemical Capacitors, *Chemistry of Materials*, 29 (2017) 4885-4893.
- [24] K. Lv, C. Teng, M. Shi, Y. Yuan, Y. Zhu, J. Wang, Z. Kong, X. Lu, Y. Zhu, Hydrophobic and Electronic Properties of the E-MoS<sub>2</sub> Nanosheets Induced by FAS for the CO<sub>2</sub> Electroreduction to Syngas with a Wide Range of CO/H<sub>2</sub> Ratios, *Advanced Functional Materials*, 28 (2018) 1802339.
- [25] H. Zhang, L. Yu, T. Chen, W. Zhou, X.W. Lou, Surface Modulation of Hierarchical MoS<sub>2</sub> Nanosheets by Ni Single Atoms for Enhanced Electrocatalytic Hydrogen Evolution, *Advanced Functional Materials*, 28 (2018) 1807086.
- [26] A.K. Geim, I.V. Grigorieva, Van der Waals heterostructures, *Nature*, 499 (2013) 419.
- [27] N.N. Greenwood, A. Earnshaw, *Chemistry of the Elements*, 2nd ed. ed., Butterworth-Heinemann., Oxford (UK) 1997.
- [28] K.R. Hahn, M. Iannuzzi, A.P. Seitsonen, J. Hutter, Coverage Effect of the CO<sub>2</sub> Adsorption Mechanisms on CeO<sub>2</sub>(111) by First Principles Analysis, *The Journal of Physical Chemistry C*, 117 (2013) 1701-1711.
- [29] C. Energy Institute, Good plant design and operation for onshore carbon capture installations and onshore pipelines, First edition ed., ENERGY INSTITUTE, LONDON, England, 2010.
- [30] K.L. Denman, G. Brasseur, A. Chidthaisong, P. Ciais, P.M. Cox, R.E. Dickinson, D. Hauglustaine, C. Heinze, E. Holland, D. Jacob, U. Lohmann, S. Ramachandran, P.L. da Silva Dias, S.C. Wofsy, X. Zhang, "Couplings between Changes in the Climate System and Biogeochemistry". In: *Climate Change 2007: The Physical Science Basis. Contribution of Working Group I to the Fourth Assessment Report of the Intergovernmental Panel on Climate Change.*, Cambridge University Press, Cambridge, United Kingdom and New York, NY, USA, 2007.
- [31] J.W. Manning, V.A. Tiedermann, CLIMATE CHANGE: POTENTIAL EFFECTS OF INCREASED ATMOSPHERIC CARBON DIOXIDE (CO<sub>2</sub>) AND OZONE (O<sub>3</sub>), AND ULTRAVIOLET-B (UV-B) RADIATION ON PLANT DISEASES *Env Pollut.*, 88 (1995) 219-245

- [32] C. Energy Institute, General Properties and Uses of Carbon Dioxide, Good Plant Design and Operation for Onshore Carbon Capture Installations and Onshore Pipelines, Global Carbon Capture and Sequestration (CCS) Institute, Australia, 2012.
- [33] D. Department of Energy, Carbon Cycling and Biosequestration: Integrating Biology and Climate Through Systems Science; Report from the March 2008 Workshop, U.S. Department of Energy Office of Science, 2008, pp. DOE/SC-108.
- [34] T. Gerlach, Volcanic versus anthropogenic carbon dioxide, *Eos, Transactions American Geophysical Union*, 92 (2011) 201-202.
- [35] M.R. Allen, D.J. Frame, C. Huntingford, C.D. Jones, J.A. Lowe, M. Meinshausen, N. Meinshausen, Warming caused by cumulative carbon emissions towards the trillionth tonne, *Nature*, 458 (2009) 1163.
- [36] C. Le Quéré, A.K. Jain, M.R. Raupach, J. Schwinger, S. Sitch, B.D. Stocker, N. Viovy, S. Zaehle, C. Huntingford, P. Friedlingstein, R.J. Andres, T. Boden, C. Jourdain, T. Conway, R.A. Houghton, J.I. House, G. Marland, G.P. Peters, G. Van Der Werf, A. Ahlström, R.M. Andrew, L. Bopp, J.G. Canadell, E. Kato, P. Ciais, S.C. Doney, C. Enright, N. Zeng, R.F. Keeling, K. Klein Goldewijk, S. Levis, P. Levy, M. Lomas, B. Poulter, “The global carbon budget 1959-2011”, *Earth System Science Data Discussions* 5, 2 (2012).
- [37] R.A. Houghton, How well do we know the flux of CO<sub>2</sub> from land-use change?, *Tellus B*, 62 (2010) 337-351.
- [38] G.D. Kaufman, M.C. Franz, *Biosphere 2000: protecting our global environment.*, 2nd edn. ed., Kendall/Hunt Publishing Company, Dubuque, Dubuque, 1996.
- [39] S.A. Rice, Carbon dioxide in Mississippian rocks of the Paradox and adjacent areas, Colorado, Third Annual Conference on Carbon Sequestration, US Department of Energy, US Department of Energy, Alexandria, Virginia, USA., 2004.
- [40] Global Environment Division Greenhouse Gas Assessment Handbook, – A Practical Guidance Document for the Assessment of Project-level Greenhouse Gas Emissions., World Bank. Archived from the original on 2016-06-03. Retrieved 2007-11-10.2016.
- [41] L.R. Kump, T.J. Bralower, A. A. Ridgwell, OCEAN ACIDIFICATION IN DEEP TIME. Special Issue On The Future of Ocean Biogeochemistry in a High-CO<sub>2</sub>World, *Oceanography*, Vol. 22 (2009) pp. 94-107.
- [42] National Institute for Occupational Safety and Health (NIOSH), Carbon dioxide, Immediately Dangerous to Life and Health. , NIOSH, NIOSH.
- [43] The Control of Substances Hazardous to Health Regulations 2002, Approved Code of Practice and guidance, COSHH, COSHH, 2013.
- [44] EH40/2005, Workplace exposure limits, containing the list of workplace exposure limits for use with the Control of Substances Hazardous to Health Regulations 2002, ISBN: 9780717664467, 2011.
- [45] G.K. Inouye, T. Nagaya, Y. Shigematsu, EFFECT OF HIGH CARBON DIOXIDE CONCENTRATION ON MENTAL PERFORMANCE AND SOME SENSORY FUNCTIONS, *The Japanese Journal of Physiology*, 5 (1955) 109-121.
- [46] S. Choi, J.H. Drese, C.W. Jones, Adsorbent Materials for Carbon Dioxide Capture from Large Anthropogenic Point Sources, *ChemSusChem*, 2 (2009) 796-854.
- [47] C.-H. Yu, C.-H. Huang, C.-S. Tan, A Review of CO<sub>2</sub> Capture by Absorption and Adsorption, *Aerosol and Air Quality Research*, 12 (2012) 745-769.
- [48] G.T. Rochelle, Amine Scrubbing for CO<sub>2</sub> Capture, *Science*, 325 (2009) 1652–1654.

- [49] T.C. Drage, C.E. Snape, L.A. Stevens, J. Wood, J. Wang, A.I. Cooper, R. Dawson, X. Guo, C. Satterley, R. Irons, Materials challenges for the development of solid sorbents for post-combustion carbon capture, *Journal of Materials Chemistry*, 22 (2012) 2815.
- [50] S.A. Rackley, *Carbon Capture and Storage* Oxford: Elsevier Inc., DOI (2010 ) p. 392.
- [51] R. Maceiras, E. Álvarez, M.Á. Cancela, Effect of temperature on carbon dioxide absorption in monoethanolamine solutions, *Chemical Engineering Journal*, 138 (2008) 295-300.
- [52] I. Hadjipaschalis, G. Kourtis, A. Poullikkas, Assessment of oxyfuel power generation technologies, *Renewable and Sustainable Energy Reviews*, 13 (2009) 2637-2644.
- [53] S.D. Kenarsari, D. Yang, G. Jiang, S. Zhang, J. Wang, A.G. Russell, Q. Wei, M. Fan, Review of recent advances in carbon dioxide separation and capture, *RSC Advances*, 3 (2013) 22739.
- [54] V. Scott, S. Gilfillan, N. Markusson, H. Chalmers, R.S. Haszeldine, Last chance for carbon capture and storage, *Nature Climate Change*, 3 (2012) 105-111.
- [55] M. Pera-Titus, Porous Inorganic Membranes for CO<sub>2</sub> Capture: Present and Prospects, *Chem. Rev.*, 114 (2014) pp1413-1492.
- [56] L. Rectisol, The Challenge Conditions for Capture., 7th European Gasification Conference., Barcelona., 2006.
- [57] H.W. Granite, E.J. Pennline, Photochemical Removal of Mercury from Flue Gas. , Department of Energy., National Energy Technology Laboratory, United States Department of Energy. Pittsburgh, 2012.
- [58] W. Liu, H. An, C. Qin, J. Yin, G. Wang, B. Feng, M. Xu, Performance Enhancement of Calcium Oxide Sorbents for Cyclic CO<sub>2</sub> Capture—A Review, *Energy & Fuels*, 26 (2012) 2751-2767.
- [59] D.M. D'Alessandro, B. Smit, J.R. Long, Carbon Dioxide Capture: Prospects for New Materials, *Angewandte Chemie International Edition*, 49 (2010) 6058-6082.
- [60] A.M. Kierzkowska, C.R. Müller, Development of calcium-based, copper-functionalised CO<sub>2</sub> sorbents to integrate chemical looping combustion into calcium looping, *Energy & Environmental Science*, 5 (2012) 6061.
- [61] A. Pulido, M.R. Delgado, O. Bludský, M. Rubeš, P. Nachtigall, C.O. Areán, Combined DFT/CC and IR spectroscopic studies on carbon dioxide adsorption on the zeolite H-FER, *Energy & Environmental Science*, 2 (2009) 1187.
- [62] R. Sabouni, H. Kazemian, S. Rohani, Carbon dioxide capturing technologies: a review focusing on metal organic framework materials (MOFs), *Environmental Science and Pollution Research*, 21 (2014) 5427-5449.
- [63] FaradayDiscussion, New Advances in Carbon Nanomaterials: Faraday Discussion 173, Royal Society of Chemistry (RSC) Publishing, <http://www.rsc.org/events/detail/11555/new-advances-in-carbon-nanomaterials-faraday-discussion-173>, DOI (2014).
- [64] A.K. Mishra, S. Ramaprabhu, Carbon dioxide adsorption in graphene sheets, *AIP Advances*, 1 (2011) 032152.
- [65] S.C. Xu, S. Irlle, D.G. Musaev, M.C. Lin, Quantum Chemical Prediction of Reaction Pathways and Rate Constants for Dissociative Adsorption of CO<sub>x</sub> and NO<sub>x</sub> on the Graphite (0001) Surface, *J. Phys. Chem. B*, Vol. 110 (2006) pp 21135-21144.
- [66] D. Quiñero, A. Frontera, P.M. Deyà, Feasibility of Single-Walled Carbon Nanotubes as Materials for CO<sub>2</sub> Adsorption: A DFT Study, *The Journal of Physical Chemistry C*, 116 (2012) 21083-21092.
- [67] M. Bienfait, P. Zeppenfeld, N. Dupont-Pavlovsky, M. Muris, M.R. Johnson, T. Wilson, M. DePies, O.E. Vilches, Thermodynamics and structure of hydrogen, methane, argon, oxygen, and

carbon dioxide adsorbed on single-wall carbon nanotube bundles, *Physical Review B*, 70 (2004) 035410.

[68] Z. Jijun, B. Alper, H. Jie, L. Jian Ping, Gas molecule adsorption in carbon nanotubes and nanotube bundles, *Nanotechnology*, 13 (2002) 195.

[69] B. Szczeńśniak, J. Choma, M. Jaroniec, Gas adsorption properties of graphene-based materials, *Advances in Colloid and Interface Science*, 243 (2017) 46-59.

[70] H.P. Boehm, R. Setton, E. Stumpp, Nomenclature and terminology of graphite intercalation compounds, *Carbon*, 24 (1986) 241-245.

[71] R.R. Nair, P. Blake, A.N. Grigorenko, K.S. Novoselov, T.J. Booth, T. Stauber, N.M.R. Peres, A.K. Geim, Fine structure constant defines visual transparency of graphene, *Science*, 320 (2008) 1308.

[72] C. Lee, X. Wei, J.W. Kysar, J. Hone, Measurement of the elastic properties and intrinsic strength of monolayer graphene, *Science*, 321 (2008) 385-388.

[73] C.R. Dean, A.F. Young, I. Meric, C. Lee, L. Wang, S. Sorgenfrei, K. Watanabe, T. Taniguchi, P. Kim, K.L. Shepard, J. Hone, Boron nitride substrates for high-quality graphene electronics, *Nature Nanotechnology*, 5 (2010) 722.

[74] A.K. Geim, K.S. Novoselov, The rise of graphene, *Nature Materials*, 6 (2007) 183.

[75] Y.-H. Zhang, W.-J. Ruan, Z.-Y. Li, Y. Wu, J.-Y. Zheng, DFT study on the influence of meso-phenyl substitution on the geometric, electronic structure and vibrational spectra of free base porphyrin, *Chemical Physics*, 315 (2005) 201-213.

[76] N. Levy, S.A. Burke, K.L. Meaker, M. Panlasigui, A. Zettl, F. Guinea, A.H. Castro Neto, M.F. Crommie, Strain-induced pseudo-magnetic fields greater than 300 tesla in graphene nanobubbles, *Science*, 329 (2010) 544-547.

[77] H.M. Jeong, J.W. Lee, W.H. Shin, Y.J. Choi, H.J. Shin, J.K. Kang, J.W. Choi, Nitrogen-Doped Graphene for High-Performance Ultracapacitors and the Importance of Nitrogen-Doped Sites at Basal Planes, *Nano Letters*, 11 (2011) 2472-2477.

[78] X. Ma, G. Ning, C. Qi, C. Xu, J. Gao, Phosphorus and Nitrogen Dual-Doped Few-Layered Porous Graphene: A High-Performance Anode Material for Lithium-Ion Batteries, *ACS Applied Materials & Interfaces*, 6 (2014) 14415-14422.

[79] D. Iruretagoyena, M.S.P. Shaffer, D. Chadwick, Layered Double Oxides Supported on Graphene Oxide for CO<sub>2</sub> Adsorption: Effect of Support and Residual Sodium, *Industrial & Engineering Chemistry Research*, 54 (2015) 6781-6792.

[80] F.D. Iruretagoyena, Supported Layered Double Hydroxides as CO<sub>2</sub> Adsorbents for Sorption-enhanced H<sub>2</sub> Production, Springer International Publishing, London, UK, 2016.

[81] M.D. Stoller, S. Park, Y. Zhu, J. An, R.S. Ruoff, Graphene-Based Ultracapacitors, *Nano Letters*, 8 (2008) 3498-3502.

[82] A. Garcia-Gallastegui, D. Iruretagoyena, V. Gouvea, M. Mokhtar, A.M. Asiri, S.N. Basahel, S.A. Al-Thabaiti, A.O. Alyoubi, D. Chadwick, M.S.P. Shaffer, Graphene Oxide as Support for Layered Double Hydroxides: Enhancing the CO<sub>2</sub> Adsorption Capacity, *Chemistry of Materials*, 24 (2012) 4531-4539.

[83] I.A. Baburin, A. Klechikov, G. Mercier, A. Talyzin, G. Seifert, Hydrogen adsorption by perforated graphene, *International Journal of Hydrogen Energy*, 40 (2015) 6594-6599.

[84] K.S. Novoselov, V. Fal, L. Colombo, P. Gellert, M. Schwab, K. Kim, A roadmap for graphene, *nature*, 490 (2012) 192-200.

[85] C. Soldano, A. Mahmood, E. Dujardin, Production, properties and potential of graphene, *Carbon*, 48 (2010) 2127-2150.

- [86] D. Wei, Y. Liu, Controllable synthesis of graphene and its applications, *Advanced Materials*, 22 (2010) 3225-3241.
- [87] Y. Zhu, S. Murali, W. Cai, X. Li, J.W. Suk, J.R. Potts, R.S. Ruoff, Graphene and graphene oxide: synthesis, properties, and applications, *Advanced materials*, 22 (2010) 3906-3924.
- [88] K.S. Novoselov, A.K. Geim, S.V. Morozov, D. Jiang, Y. Zhang, S.V. Dubonos, I.V. Grigorieva, A.A. Firsov, Electric field effect in atomically thin carbon films, *science*, 306 (2004) 666-669.
- [89] J. Hedberg, Images of C60 and Carbon nanotubes [www.jameshedberg.com](http://www.jameshedberg.com), DOI (2015).
- [90] M.E. Wieser, Rendering of a Multi-walled carbon nanotube, *Wikimedia Commons* [wikimedia.org/wiki/File:Multiwalled Carbon Nanotube](http://wikimedia.org/wiki/File:Multiwalled_Carbon_Nanotube), DOI (2010).
- [91] P. Lazar, F.e. Karlický, P. Jurečka, M.s. Kocman, E. Otyepková, K.r. Šafářová, M. Otyepka, Adsorption of small organic molecules on graphene, *Journal of the American Chemical Society*, 135 (2013) 6372-6377.
- [92] P.V. Medeiros, G.K. Gueorguiev, S. Stafström, Bonding, charge rearrangement and interface dipoles of benzene, graphene, and PAH molecules on Au (111) and Cu (111), *Carbon*, 81 (2015) 620-628.
- [93] R. Podeszwa, Interactions of graphene sheets deduced from properties of polycyclic aromatic hydrocarbons, *The Journal of chemical physics*, 132 (2010) 044704.
- [94] M. Rubeš, P. Nachtigall, J.i. Vondrášek, O. Bludský, Structure and stability of the water-graphite complexes, *The Journal of Physical Chemistry C*, 113 (2009) 8412-8419.
- [95] G.R. Jenness, O. Karalti, K.D. Jordan, Benchmark calculations of water-acene interaction energies: Extrapolation to the water-graphene limit and assessment of dispersion-corrected DFT methods, *Physical Chemistry Chemical Physics*, 12 (2010) 6375-6381.
- [96] Y. Zhao, D.G. Truhlar, A prototype for graphene material simulation: structures and interaction potentials of coronene dimers, *The Journal of Physical Chemistry C*, 112 (2008) 4061-4067.
- [97] V.V. Gobre, A. Tkatchenko, Scaling laws for van der Waals interactions in nanostructured materials, *Nature Communications*, 4 (2013) 2341.
- [98] M. Pykal, K. Šafářová, K. Machalová Šišková, P. Jurečka, A.B. Bourlinos, R. Zbořil, M. Otyepka, Lipid Enhanced Exfoliation for Production of Graphene Nanosheets, *The Journal of Physical Chemistry C*, 117 (2013) 11800-11803.
- [99] R. Lv, J.A. Robinson, R.E. Schaak, D. Sun, Y. Sun, T.E. Mallouk, M. Terrones, Transition Metal Dichalcogenides and Beyond: Synthesis, Properties, and Applications of Single- and Few-Layer Nanosheets, *Accounts of Chemical Research*, 48 (2015) 56-64.
- [100] B.K. Miremedi, S.R. Morrison, High activity catalyst from exfoliated MoS<sub>2</sub>, *Journal of Catalysis*, 103 (1987) 334-345.
- [101] C. Lee, H. Yan, L.E. Brus, T.F. Heinz, J. Hone, S. Ryu, Anomalous Lattice Vibrations of Single- and Few-Layer MoS<sub>2</sub>, *ACS Nano*, 4 (2010) 2695-2700.
- [102] K.F. Mak, C. Lee, J. Hone, J. Shan, T.F. Heinz, Atomically Thin MoS<sub>2</sub>: A New Direct-Gap Semiconductor, *Physical Review Letters*, 105 (2010) 136805.
- [103] B. Radisavljevic, A. Radenovic, J. Brivio, V. Giacometti, A. Kis, Single-layer MoS<sub>2</sub> transistors, *Nature Nanotechnology*, 6 (2011) 147.
- [104] Y. Zhang, J. Ye, Y. Matsuhashi, Y. Iwasa, Ambipolar MoS<sub>2</sub> Thin Flake Transistors, *Nano Letters*, 12 (2012) 1136-1140.
- [105] Q. He, Z. Zeng, Z. Yin, H. Li, S. Wu, X. Huang, H. Zhang, Fabrication of Flexible MoS<sub>2</sub> Thin-Film Transistor Arrays for Practical Gas-Sensing Applications, *Small*, 8 (2012) 2994-2999.

- [106] H. Li, Z. Yin, Q. He, H. Li, X. Huang, G. Lu, D.W.H. Fam, A.I.Y. Tok, Q. Zhang, H. Zhang, Fabrication of Single- and Multilayer MoS<sub>2</sub> Film-Based Field-Effect Transistors for Sensing NO at Room Temperature, *Small*, 8 (2012) 63-67.
- [107] H. Zhao, X. Mu, C. Zheng, S. Liu, Y. Zhu, X. Gao, T. Wu, Structural defects in 2D MoS<sub>2</sub> nanosheets and their roles in the adsorption of airborne elemental mercury, *Journal of Hazardous Materials*, 366 (2019) 240-249.
- [108] M. Chhowalla, H.S. Shin, G. Eda, L.-J. Li, K.P. Loh, H. Zhang, The chemistry of two-dimensional layered transition metal dichalcogenide nanosheets, *Nature Chemistry*, 5 (2013) 263.
- [109] X. Chia, A. Adriano, P. Lazar, Z. Sofer, J. Luxa, M. Pumera, Layered Platinum Dichalcogenides (PtS<sub>2</sub>, PtSe<sub>2</sub>, and PtTe<sub>2</sub>) Electrocatalysis: Monotonic Dependence on the Chalcogen Size, *Advanced Functional Materials*, 26 (2016) 4306-4318.
- [110] K.F. Mak, C. Lee, J. Hone, J. Shan, T.F. Heinz, Atomically Thin  $\{\mathrm{MoS}\}_2$ : A New Direct-Gap Semiconductor, *Physical Review Letters*, 105 (2010) 136805.
- [111] D. Boukhvalov, M. Katsnelson, Chemical functionalization of graphene, *Journal of Physics: Condensed Matter*, 21 (2009) 344205.
- [112] V. Georgakilas, M. Otyepka, A.B. Bourlinos, V. Chandra, N. Kim, K.C. Kemp, P. Hobza, R. Zboril, K.S. Kim, Functionalization of graphene: covalent and non-covalent approaches, derivatives and applications, *Chem. Rev.*, 112 (2012) 6156-6214.
- [113] H.P. Boehm, Some aspects of the surface chemistry of carbon blacks and other carbons, *Carbon*, 32 (1994) 759-769.
- [114] Z.-Q. Bai, Z.-J. Li, C.-Z. Wang, L.-Y. Yuan, Z.-R. Liu, J. Zhang, L.-R. Zheng, Y.-L. Zhao, Z.-F. Chai, W.-Q. Shi, Interactions between Th(IV) and graphene oxide: experimental and density functional theoretical investigations, *RSC Adv.*, 4 (2014) 3340-3347.
- [115] Z. Jin, X. Wang, Y. Sun, Y. Ai, X. Wang, Adsorption of 4-n-Nonylphenol and Bisphenol-A on Magnetic Reduced Graphene Oxides: A Combined Experimental and Theoretical Studies, *Environ Sci Technol*, 49 (2015) 9168-9175.
- [116] A.K. Mishra, S. Ramaprabhu, Nano magnetite decorated multiwalled carbon nanotubes: a robust nanomaterial for enhanced carbon dioxide adsorption, *Energy Environ. Sci.*, 4 (2011) 889-895.
- [117] K.K. Paulla, A.J. Hassan, C.R. Knick, A.A. Farajian, Ab-initio assessment of graphene nanoribbons reactivity for molecule adsorption and conductance modulation: nitrogen dioxide nanosensor, *RSC Adv.*, 4 (2014) 2346-2354.
- [118] Y. Sun, S. Yang, Y. Chen, C. Ding, W. Cheng, X. Wang, Adsorption and desorption of U(VI) on functionalized graphene oxides: a combined experimental and theoretical study, *Environ Sci Technol*, 49 (2015) 4255-4262.
- [119] N. Tit, K. Said, N.M. Mahmoud, S. Kouser, Z.H. Yamani, Ab-initio investigation of adsorption of CO and CO<sub>2</sub> molecules on graphene: Role of intrinsic defects on gas sensing, *Applied Surface Science*, 394 (2017) 219-230.
- [120] Q.Y. Wu, J.H. Lan, C.Z. Wang, C.L. Xiao, Y.L. Zhao, Y.Z. Wei, Z.F. Chai, W.Q. Shi, Understanding the bonding nature of uranyl ion and functionalized graphene: a theoretical study, *J Phys Chem A*, 118 (2014) 2149-2158.
- [121] Q.Y. Wu, J.H. Lan, C.Z. Wang, Y.L. Zhao, Z.F. Chai, W.Q. Shi, Understanding the interactions of neptunium and plutonium ions with graphene oxide: scalar-relativistic DFT investigations, *J Phys Chem A*, 118 (2014) 10273-10280.
- [122] H.J. Yoon, D.H. Jun, J.H. Yang, Z. Zhou, S.S. Yang, M.M.-C. Cheng, Carbon dioxide gas sensor using a graphene sheet, *Sensors and Actuators B: Chemical*, 157 (2011) 310-313.



- [123] G. Zhao, L. Jiang, Y. He, J. Li, H. Dong, X. Wang, W. Hu, Sulfonated Graphene for Persistent Aromatic Pollutant Management, *Advanced Materials*, 23 (2011) 3959-3963.
- [124] A. Hashimoto, K. Suenaga, A. Gloter, K. Urita, S. Iijima, Direct evidence for atomic defects in graphene layers, *Nature*, 430 (2004) 870.
- [125] K.N. Kudin, B. Ozbas, H.C. Schniepp, R.K. Prud'Homme, I.A. Aksay, R. Car, Raman spectra of graphite oxide and functionalized graphene sheets, *Nano letters*, 8 (2008) 36-41.
- [126] J. Kushmerick, K. Kelly, H.-P. Rust, N. Halas, P. Weiss, Observations of anisotropic electron scattering on graphite with a low-temperature scanning tunneling microscope, *The Journal of Physical Chemistry B*, 103 (1999) 1619-1622.
- [127] J. Hahn, H. Kang, Vacancy and interstitial defects at graphite surfaces: Scanning tunneling microscopic study of the structure, electronic property, and yield for ion-induced defect creation, *Physical Review B*, 60 (1999) 6007.
- [128] P. Cabrera-Sanfeliix, Adsorption and reactivity of CO<sub>2</sub> on defective graphene sheets, *The Journal of Physical Chemistry A*, 113 (2009) 493-498.
- [129] Y. Liu, J. Wilcox, CO<sub>2</sub> adsorption on carbon models of organic constituents of gas shale and coal, *Environmental science & technology*, 45 (2010) 809-814.
- [130] J. Campos-Delgado, J.M. Romo-Herrera, X. Jia, D.A. Cullen, H. Muramatsu, Y.A. Kim, T. Hayashi, Z. Ren, D.J. Smith, Y. Okuno, Bulk production of a new form of sp<sup>2</sup> carbon: crystalline graphene nanoribbons, *Nano letters*, 8 (2008) 2773-2778.
- [131] L. Cancado, M. Pimenta, B. Neves, M. Dantas, A. Jorio, Influence of the atomic structure on the Raman spectra of graphite edges, *Physical review letters*, 93 (2004) 247401.
- [132] L. Cançado, M. Pimenta, B. Neves, G. Medeiros-Ribeiro, T. Enoki, Y. Kobayashi, K. Takai, K.-i. Fukui, M. Dresselhaus, R. Saito, Anisotropy of the Raman spectra of nanographite ribbons, *Physical review letters*, 93 (2004) 047403.
- [133] L.A. Jauregui, H. Cao, W. Wu, Q. Yu, Y.P. Chen, Electronic properties of grains and grain boundaries in graphene grown by chemical vapor deposition, *Solid State Communications*, 151 (2011) 1100-1104.
- [134] X. Jia, M. Hofmann, V. Meunier, B.G. Sumpter, J. Campos-Delgado, J.M. Romo-Herrera, H. Son, Y.-P. Hsieh, A. Reina, J. Kong, Controlled formation of sharp zigzag and armchair edges in graphitic nanoribbons, *Science*, 323 (2009) 1701-1705.
- [135] K. Kim, Z. Lee, W. Regan, C. Kisielowski, M. Crommie, A. Zettl, Grain boundary mapping in polycrystalline graphene, *ACS nano*, 5 (2011) 2142-2146.
- [136] K. Nakada, M. Fujita, G. Dresselhaus, M.S. Dresselhaus, Edge state in graphene ribbons: Nanometer size effect and edge shape dependence, *Physical Review B*, 54 (1996) 17954.
- [137] C.S. Ruiz-Vargas, H.L. Zhuang, P.Y. Huang, A.M. van der Zande, S. Garg, P.L. McEuen, D.A. Muller, R.G. Hennig, J. Park, Softened elastic response and unzipping in chemical vapor deposition graphene membranes, *Nano Letters*, 11 (2011) 2259-2263.
- [138] R. Saito, M. Hofmann, G. Dresselhaus, A. Jorio, M. Dresselhaus, Raman spectroscopy of graphene and carbon nanotubes, *Advances in Physics*, 60 (2011) 413-550.
- [139] L. Yang, C.-H. Park, Y.-W. Son, M.L. Cohen, S.G. Louie, Quasiparticle energies and band gaps in graphene nanoribbons, *Physical Review Letters*, 99 (2007) 186801.
- [140] Q. Yu, L.A. Jauregui, W. Wu, R. Colby, J. Tian, Z. Su, H. Cao, Z. Liu, D. Pandey, D. Wei, Control and characterization of individual grains and grain boundaries in graphene grown by chemical vapour deposition, *Nature materials*, 10 (2011) 443-449.
- [141] A. Montoya, F. Mondragon, T.N. Truong, CO<sub>2</sub> adsorption on carbonaceous surfaces: a combined experimental and theoretical study, *Carbon*, 41 (2003) 29-39.

- [142] T. Ohba, H. Kanoh, Intensive edge effects of nanographenes in molecular adsorptions, *The journal of physical chemistry letters*, 3 (2012) 511-516.
- [143] D. Umadevi, G.N. Sastry, Molecular and ionic interaction with graphene nanoflakes: a computational investigation of CO<sub>2</sub>, H<sub>2</sub>O, Li, Mg, Li<sup>+</sup>, and Mg<sup>2+</sup> interaction with polycyclic aromatic hydrocarbons, *The Journal of Physical Chemistry C*, 115 (2011) 9656-9667.
- [144] A. Rochefort, J.D. Wuest, Interaction of substituted aromatic compounds with graphene, *Langmuir*, 25 (2008) 210-215.
- [145] J.-R. Li, R.J. Kuppler, H.-C. Zhou, Selective gas adsorption and separation in metal-organic frameworks, *Chemical Society Reviews*, 38 (2009) 1477-1504.
- [146] T. Dasgupta, S.N. Punnathanam, K. Ayappa, Effect of functional groups on separating carbon dioxide from CO<sub>2</sub>/N<sub>2</sub> gas mixtures using edge functionalized graphene nanoribbons, *Chemical Engineering Science*, 121 (2015) 279-291.
- [147] L.S. L.S. Panchakala, K.S. Subrahmanyam, S.K. Saha, A. Govindaraj, H.R. Krishnamurthy, U.V. Waghmare, C.N.R. Rao, Synthesis, Structure, and Properties of Boron- and Nitrogen-Doped Graphene, *Adv. Mater.*, 21 (2009) 4726-4730.
- [148] L. Ci, L. Song, C. Jin, D. Jariwala, D. Wu, Y. Li, A. Srivastava, Z.F. Wang, K. Storr, L. Balicas, F. Liu, P.M. Ajayan, Atomic layers of hybridized boron nitride and graphene domains, *Nature Materials*; London, 9 (2010) 430-435.
- [149] P.A. Denis, Band gap opening of monolayer and bilayer graphene doped with aluminium, silicon, phosphorus, and sulfur, *Chemical Physics Letters*, 492 (2010) 251-257.
- [150] J. Kotakoski, A.V. Krashenninnikov, Y. Ma, A.S. Foster, K. Nordlund, R.M. Nieminen, B and N ion implantation into carbon nanotubes: Insight from atomistic simulations, *Physical Review B*, 71 (2005).
- [151] T.B. Martins, R.H. Miwa, A.J. da Silva, A. Fazzio, Electronic and transport properties of boron-doped graphene nanoribbons, *Phys Rev Lett*, 98 (2007) 196803.
- [152] S. Yu, W. Zheng, C. Wang, Q. Jiang, Nitrogen/Boron Doping Position Dependence of the Electronic Properties of a Triangular Graphene, *Acs Nano* 4(2010) 7619-7629.
- [153] K. Gong, F. Du, Z. Xia, M. Duratock, L. Dai, Nitrogen-Doped Carbon Nanotube Arrays with High Electrocatalytic Activity for Oxygen Reduction, *Science*, 323 (2009) 760-764.
- [154] S.U. Lee, R.V. Belosludov, H. Mizuseki, Y. Kawazoe, Designing Nanogadgets for Nanoelectronic Devices with Nitrogen-Doped Capped Carbon Nanotubes, *Small*, 5 (2009) 1769-1775.
- [155] B. Guo, Q. Liu, E. Chen, H. Zhu, L. Fang, J.R. Gong, Controllable N-doping of graphene, *Nano Lett*, 10 (2010) 4975-4980.
- [156] D. Cortés-Arriagada, N. Villegas-Escobar, D.E. Ortega, Fe-doped graphene nanosheet as an adsorption platform of harmful gas molecules (CO, CO<sub>2</sub>, SO<sub>2</sub> and H<sub>2</sub>S), and the co-adsorption in O<sub>2</sub> environments, *Applied Surface Science*, 427 (2018) 227-236.
- [157] K. Chang, X. Hai, H. Pang, H. Zhang, L. Shi, G. Liu, H. Liu, G. Zhao, M. Li, J. Ye, Targeted Synthesis of 2H- and 1T-Phase MoS<sub>2</sub> Monolayers for Catalytic Hydrogen Evolution, *Advanced Materials*, 28 (2016) 10033-10041.
- [158] L. Yu, B.Y. Xia, X. Wang, X.W. Lou, General Formation of M-MoS<sub>3</sub> (M = Co, Ni) Hollow Structures with Enhanced Electrocatalytic Activity for Hydrogen Evolution, *Advanced Materials*, 28 (2016) 92-97.
- [159] J. Hong, Z. Hu, M. Probert, K. Li, D. Lv, X. Yang, L. Gu, N. Mao, Q. Feng, L. Xie, J. Zhang, D. Wu, Z. Zhang, C. Jin, W. Ji, X. Zhang, J. Yuan, Z. Zhang, Exploring atomic defects in molybdenum disulphide monolayers, *Nature Communications*, 6 (2015) 6293.

- [160] H. Li, M. Huang, G. Cao, Markedly different adsorption behaviors of gas molecules on defective monolayer MoS<sub>2</sub>: a first-principles study, *Physical Chemistry Chemical Physics*, 18 (2016) 15110-15117.
- [161] H. Schweiger, P. Raybaud, G. Kresse, H. Toulhoat, Shape and Edge Sites Modifications of MoS<sub>2</sub> Catalytic Nanoparticles Induced by Working Conditions: A Theoretical Study, *Journal of Catalysis*, 207 (2002) 76-87.
- [162] H. Li, J. Li, A. Thomas, Y. Liao, Ultra-High Surface Area Nitrogen-Doped Carbon Aerogels Derived From a Schiff-Base Porous Organic Polymer Aerogel for CO<sub>2</sub> Storage and Supercapacitors, *Advanced Functional Materials*, 29 (2019) 1904785.
- [163] D. Kong, J.J. Cha, H. Wang, H.R. Lee, Y. Cui, First-row transition metal dichalcogenide catalysts for hydrogen evolution reaction, *Energy & Environmental Science*, 6 (2013) 3553-3558.
- [164] C.W. Li, M.W. Kanan, CO<sub>2</sub> Reduction at Low Overpotential on Cu Electrodes Resulting from the Reduction of Thick Cu<sub>2</sub>O Films, *Journal of the American Chemical Society*, 134 (2012) 7231-7234.
- [165] X. Hong, K. Chan, C. Tsai, J.K. Nørskov, How Doped MoS<sub>2</sub> Breaks Transition-Metal Scaling Relations for CO<sub>2</sub> Electrochemical Reduction, *ACS Catalysis*, 6 (2016) 4428-4437.
- [166] M. Kuang, P. Han, L. Huang, N. Cao, L. Qian, G. Zheng, Electronic Tuning of Co, Ni-Based Nanostructured (Hydr)oxides for Aqueous Electrocatalysis, *Advanced Functional Materials*, 28 (2018) 1804886.
- [167] J. Wang, W. Cui, Q. Liu, Z. Xing, A.M. Asiri, X. Sun, Recent Progress in Cobalt-Based Heterogeneous Catalysts for Electrochemical Water Splitting, *Advanced Materials*, 28 (2016) 215-230.
- [168] H. Wang, H.S. Casalongue, Y. Liang, H. Dai, Ni(OH)<sub>2</sub> Nanoplates Grown on Graphene as Advanced Electrochemical Pseudocapacitor Materials, *Journal of the American Chemical Society*, 132 (2010) 7472-7477.
- [169] X. Wang, X. Zhou, K. Yao, J. Zhang, Z. Liu, A SnO<sub>2</sub>/graphene composite as a high stability electrode for lithium ion batteries, *Carbon*, 49 (2011) 133-139.
- [170] D. Wang, W. Xing, L. Song, Y. Hu, Space-Confined Growth of Defect-Rich Molybdenum Disulfide Nanosheets Within Graphene: Application in The Removal of Smoke Particles and Toxic Volatiles, *ACS Appl Mater Interfaces*, 8 (2016) 34735-34743.
- [171] K. Chang, W. Chen, In situ synthesis of MoS<sub>2</sub>/graphene nanosheet composites with extraordinarily high electrochemical performance for lithium ion batteries, *Chemical Communications*, 47 (2011) 4252-4254.
- [172] R. Mu, Q. Fu, L. Jin, L. Yu, G. Fang, D. Tan, X. Bao, Visualizing chemical reactions confined under graphene, *Angew Chem Int Ed Engl*, 51 (2012) 4856-4859.
- [173] X. Pan, X. Bao, The Effects of Confinement inside Carbon Nanotubes on Catalysis, *Accounts of Chemical Research*, 44 (2011) 553-562.
- [174] B. Smit, T.L.M. Maesen, Towards a molecular understanding of shape selectivity, *Nature*, 451 (2008) 671.
- [175] J.M. Thomas, R. Raja, Exploiting Nanospace for Asymmetric Catalysis: Confinement of Immobilized, Single-Site Chiral Catalysts Enhances Enantioselectivity, *Accounts of Chemical Research*, 41 (2008) 708-720.
- [176] J.-R. Li, Y. Ma, M.C. McCarthy, J. Sculley, J. Yu, H.-K. Jeong, P.B. Balbuena, H.-C. Zhou, Carbon dioxide capture-related gas adsorption and separation in metal-organic frameworks, *Coordination Chemistry Reviews*, 255 (2011) 1791-1823.

- [177] R.B. Getman, Y.-S. Bae, C.E. Wilmer, R.Q. Snurr, Review and analysis of molecular simulations of methane, hydrogen, and acetylene storage in metal–organic frameworks, *Chem. Rev.*, 112 (2012) 703-723.
- [178] Shijun Zhao, Jianming Xue, W. Kang, Gas adsorption on MoS<sub>2</sub> monolayer from first-principles calculations, *Chemical Physics Letters*, Vol. 595-596 (2014) pp 35-42.
- [179] Q. Yue, Z. Shao, S. Chang, J. Li, Adsorption of gas molecules on monolayer MoS<sub>2</sub> and effect of applied electric field, *Nanoscale Research Letters*, 8 (2013) 1-7.
- [180] M. Mueller, *Fundamentals of Quantum Chemistry : Molecular Spectroscopy and Modern Electronic Structure Computations*, Kluwer Academic/Plenum Publisher, New York, 2001.
- [181] P. Hohenberg, W. Kohn, Inhomogeneous Electron Gas, *Physical Review*, 136 (1964) B864-B871.
- [182] J.R. Rogal, K., *Ab Initio Atomistic Thermodynamics for Surfaces: A Primer*. In *Experiment, Modeling and Simulation of Gas-Surface Interactions for Reactive Flows in Hypersonic Flights.*, Educational Notes RTO-EN-AVT, Paper 2 (2007) 2-1 – 2-18.
- [183] Z. Yang, Q. Wang, S. Wei, D. Ma, Q. Sun, The Effect of Environment on the Reaction of Water on the Ceria(111) Surface: A DFT+U Study, *The Journal of Physical Chemistry C*, 114 (2010) 14891-14899.
- [184] G. Henkelman, H. Jónsson, Improved tangent estimate in the nudged elastic band method for finding minimum energy paths and saddle points, *The Journal of Chemical Physics*, 113 (2000) 9978-9985.
- [185] A. Seitsonen, *Theoretical Investigations into Adsorption and Co-adsorption on Transition-metal surfaces as models to Heterogeneous Catalysis*, Vom Fachbereich 4 (Physik), der Technischen Universität, Berlin, Berlin, 2002, pp. 124.
- [186] D. CEPERLEY, B. ALDER, Quantum Monte Carlo, *Science*, 231 (1986) 555-560.
- [187] D.M. Ceperley, L. Mitas, Quantum Monte Carlo Methods in Chemistry, in *New Methods in Computational Quantum Mechanics*, Advances in Chemical Physics, Editors I Prigogine and S A Rice, XCIII (1996).
- [188] B.L. Hammond, W.A.J. Lester, P.J. Reynolds, *Monte Carlo Methods in ab initio Quantum Chemistry*, , World Scientific, Singapore, DOI (1994).
- [189] L. Mitas, *Electronic structure by quantum Monte Carlo: atoms, molecules and solids*, *Computer Physics Communications*, 96 (1996) 107-117.
- [190] A. Szabo, N.S. Ostlund, *Modern Quantum Chemistry*, McGraw-Hill, New York, 1989.
- [191] P. Fulde, *Electron Correlations in Molecules and Solids*, Vol. 100 aus der Reihe: Springer Series in Solid-State Sciences, Springer-Verlag, Berlin, Heidelberg, New York 1991, ISBN 3–540–553623-X, 422 Seiten, Preis: DM 98,—, *Berichte der Bunsengesellschaft für physikalische Chemie*, 96 (1992) 1895-1896.
- [192] K.E. Schmidt, M.H. Kalos, *Monte Carlo Methods in Statistical Physics II Topics in Current Physics* 1984.
- [193] J.B. Anderson, Fixed-node quantum Monte Carlo, *International Reviews in Physical Chemistry*, 14 (1995) 85-112.
- [194] A. Harju, B. Barbiellini, S. Siljamäki, R.M. Nieminen, G. Ortiz, Stochastic Gradient Approximation: An Efficient Method to Optimize Many-Body Wave Functions, *Physical Review Letters*, 79 (1997) 1173-1177.
- [195] C.J. Umrigar, Accelerated Metropolis method, *Physical Review Letters*, 71 (1993) 408-411.
- [196] C.J. Umrigar, M.P. Nightingale, K.J. Runge, A diffusion Monte Carlo algorithm with very small time-step errors, *The Journal of Chemical Physics*, 99 (1993) 2865-2890.

- [197] E. Schrödinger, An Undulatory Theory of the Mechanics of Atoms and Molecules, *Physical Review*, 28 (1926) 1049-1070.
- [198] M. Born, J.R. Oppenheimer, On the Quantum Theory of Molecules, *Ann. Phys.*, 84 (1927).
- [199] B.O. Roos, K. Andersson, M.P. Fulscher, P.A. Malmqvist, L. SerranoAndres, K. Pierloot, M. Merchán, *Adv. Chem. Phys.*, 93 (1996) 219-331.
- [200] E.H. Lieb, B. Simon, The Hartree-Fock theory for Coulomb systems, *Communications in Mathematical Physics*, 53 (1977) 185-194.
- [201] J.C. Slater, Note on Hartree's Method, *Physical Review*, 35 (1930) 210-211.
- [202] P. Hohenberg, W. Kohn, Inhomogeneous electron gas, *Physical review*, 136 (1964) B864.
- [203] W. Kohn, L.J. Sham, Self-Consistent Equations Including Exchange and Correlation Effects, *Physical Review*, 140 (1965) A1133-A1138.
- [204] D.C. Langreth, J.P. Perdew, Theory of nonuniform electronic systems. I. Analysis of the gradient approximation and a generalization that works, *Physical Review B*, 21 (1980) 5469-5493.
- [205] G.I. Csonka, J.P. Perdew, A. Ruzsinszky, P.H.T. Philipsen, S. Lebègue, J. Paier, O.A. Vydrov, J.G. Ángyán, Assessing the performance of recent density functionals for bulk solids, *Physical Review B*, 79 (2009) 155107.
- [206] J. Heyd, J.E. Peralta, G.E. Scuseria, R.L. Martin, Energy band gaps and lattice parameters evaluated with the Heyd-Scuseria-Ernzerhof screened hybrid functional, *J Chem Phys*, 123 (2005) 174101.
- [207] A. Rohrbach, J. Hafner, G. Kresse, Electronic correlation effects in transition-metal sulfides, *Journal of Physics: Condensed Matter*, 15 (2003) 979.
- [208] I.A. Vladimir, F. Aryasetiawan, A.I. Lichtenstein, First-principles calculations of the electronic structure and spectra of strongly correlated systems: the LDA + U method, *Journal of Physics: Condensed Matter*, 9 (1997) 767.
- [209] F. Zhou, M. Cococcioni, C.A. Marianetti, D. Morgan, G. Ceder, First-principles prediction of redox potentials in transition-metal compounds with  $\text{LDA}+U$ , *Physical Review B*, 70 (2004) 235121.
- [210] J.P. Merrick, D. Moran, L. Radom, An Evaluation of Harmonic Vibrational Frequency Scale Factors, *The Journal of Physical Chemistry A*, 111 (2007) 11683-11700.
- [211] G. Kresse, J. Furthmüller, Efficient iterative schemes for ab initio total-energy calculations using a plane-wave basis set, *Physical Review B*, 54 (1996) 11169-11186.
- [212] G. Kresse, J. Furthmüller, Efficiency of ab-initio total energy calculations for metals and semiconductors using a plane-wave basis set, *Computational Materials Science*, 6 (1996) 15-50.
- [213] P.E. Blöchl, Projector augmented-wave method, *Physical Review B*, 50 (1994) 17953-17979.
- [214] G. Kresse, D. Joubert, From ultrasoft pseudopotentials to the projector augmented-wave method, *Physical Review B*, 59 (1999) 1758-1775.
- [215] J.P. Perdew, K. Burke, M. Ernzerhof, Generalized Gradient Approximation Made Simple, *Physical Review Letters*, 77 (1996) 3865-3868.
- [216] S. Grimme, Semiempirical GGA-type density functional constructed with a long-range dispersion correction, *Journal of Computational Chemistry*, 27 (2006) 1787-1799.
- [217] M. Dion, H. Rydberg, E. Schröder, D.C. Langreth, B.I. Lundqvist, Van der Waals Density Functional for General Geometries, *Physical Review Letters*, 92 (2004) 246401.
- [218] J. Klimeš, D.R. Bowler, A. Michaelides, Van der Waals density functionals applied to solids, *Physical Review B*, 83 (2011) 195131.

- [219] G. Román-Pérez, J.M. Soler, Efficient Implementation of a van der Waals Density Functional: Application to Double-Wall Carbon Nanotubes, *Physical Review Letters*, 103 (2009) 096102.
- [220] K. Jiří, R.B. David, M. Angelos, Chemical accuracy for the van der Waals density functional, *Journal of Physics: Condensed Matter*, 22 (2010) 022201.
- [221] I. Hamada, van der Waals density functional made accurate, *Physical Review B*, 89 (2014) 121103.
- [222] K. Lee, É.D. Murray, L. Kong, B.I. Lundqvist, D.C. Langreth, Higher-accuracy van der Waals density functional, *Physical Review B*, 82 (2010) 081101.
- [223] S.E. Mason, P.H. Beton, N.A. Besley, AIRBED: A Simplified Density Functional Theory Model for Physisorption on Surfaces, *Journal of Chemical Theory and Computation*, 15 (2019) 5628-5634.
- [224] H.J. Monkhorst, J.D. Pack, Special points for Brillouin-zone integrations, *Physical Review B*, 13 (1976) 5188-5192.
- [225] G. Henkelman, A. Arnaldsson, H. Jónsson, A fast and robust algorithm for Bader decomposition of charge density, *Computational Materials Science*, 36 (2006) 354-360.
- [226] C. Ataca, S. Ciraci, Functionalization of Single-Layer MoS<sub>2</sub> Honeycomb Structures, *The Journal of Physical Chemistry C*, 115 (2011) 13303-13311.
- [227] W. Yang, Direct calculation of electron density in density-functional theory, *Physical Review Letters*, 66 (1991) 1438-1441.
- [228] J. Li, M. Hou, Y. Chen, W. Cen, Y. Chu, S. Yin, Enhanced CO<sub>2</sub> capture on graphene via N, S dual-doping, *Applied Surface Science*, 399 (2017) 420-425.
- [229] S.A. Tawfik, X.Y. Cui, S.P. Ringer, C. Stampfl, Multiple CO<sub>2</sub> capture in stable metal-doped graphene: a theoretical trend study, *RSC Advances*, 5 (2015) 50975-50982.
- [230] B.B. Kappes, A. Ebnonnasir, S. Kodambaka, C.V. Ciobanu, Orientation-dependent binding energy of graphene on palladium, *Applied Physics Letters*, 102 (2013) 051606.
- [231] Y. Murata, E. Starodub, B.B. Kappes, C.V. Ciobanu, N.C. Bartelt, K.F. McCarty, S. Kodambaka, Orientation-dependent work function of graphene on Pd(111), *Applied Physics Letters*, 97 (2010) 143114.
- [232] Y. Murata, S. Nie, A. Ebnonnasir, E. Starodub, B.B. Kappes, K.F. McCarty, C.V. Ciobanu, S. Kodambaka, Growth structure and work function of bilayer graphene on Pd(111), *Physical Review B*, 85 (2012) 205443.
- [233] Y. Ma, Y. Dai, M. Guo, C. Niu, B. Huang, Graphene adhesion on MoS<sub>2</sub> monolayer: an ab initio study, *Nanoscale*, 3 (2011) 3883-3887.
- [234] A. Bostwick, T. Ohta, T. Seyller, K. Horn, E. Rotenberg, Quasiparticle dynamics in graphene, *Nature Physics*, 3 (2006) 36.
- [235] C. Ataca, M. Topsakal, E. Aktürk, S. Ciraci, A Comparative Study of Lattice Dynamics of Three- and Two-Dimensional MoS<sub>2</sub>, *The Journal of Physical Chemistry C*, 115 (2011) 16354-16361.
- [236] Y. Liu, J. Wilcox, CO<sub>2</sub> Adsorption on Carbon Models of Organic Constituents of Gas Shale and Coal, *Environ Sci Technol*, Vol. 45 (2011) 809-814.
- [237] P. Cabrera-Sanfelix, Adsorption and Reactivity of CO<sub>2</sub> on Defective Graphene Sheets, *J. Phys. Chem. A*, Vol. 113 (2009) 493-498.
- [238] A.F. Ismail, K. Khulbe, T. Matsuura, *Gas Separation Membranes: Polymeric and Inorganic, Membrane Technology and Applications*, Springer 2015 pp. p.14.

- [239] B. Sachs, L. Britnell, T.O. Wehling, A. Eckmann, R. Jalil, B.D. Belle, A.I. Lichtenstein, M.I. Katsnelson, K.S. Novoselov, Doping mechanisms in graphene-MoS<sub>2</sub> hybrids, *Applied Physics Letters*, 103 (2013) 251607.
- [240] A.F. Holleman, E. Wiberg, *Inorganic Chemistry*; Wiberg, N., Ed. , Academic Press, San Diego, CA, USA, , 2001.
- [241] J. Deng, H. Li, J. Xiao, Y. Tu, D. Deng, H. Yang, H. Tian, J. Li, P. Ren, X. Bao, Triggering the electrocatalytic hydrogen evolution activity of the inert two-dimensional MoS<sub>2</sub> surface via single-atom metal doping, *Energy & Environmental Science*, 8 (2015) 1594-1601.
- [242] T.F. Jaramillo, K.P. Jørgensen, J. Bonde, J.H. Nielsen, S. Horch, I. Chorkendorff, Identification of Active Edge Sites for Electrochemical H<sub>2</sub> Evolution from MoS<sub>2</sub> Nanocatalysts, *Science*, 317 (2007) 100-102.
- [243] J. Li, M. Hou, Y. Chen, W. Cen, Y. Chu, S. Yin, Enhanced CO<sub>2</sub> capture on graphene via N, S dual-doping, *Applied Surface Science*, 399 (2017) 420-425.
- [244] W.-L. Yim, O. Byl, J.T.Y. Jr., J.K. Johnson, Vibrational behavior of adsorbed CO<sub>2</sub> on single-walled carbon nanotubes, *The Journal of Chemical Physics*, 120 (2004) 5377-5386.
- [245] CRC, *CRC Handbook of Chemistry and Physics*, 90th ed., CRC Press, Boca Raton, FL, 2009-2010.
- [246] C. Tayran, S. Aydin, M. Çakmak, Ş. Ellialtıođlu, Structural and electronic properties of AB- and AA-stacking bilayer-graphene intercalated by Li, Na, Ca, B, Al, Si, Ge, Ag, and Au atoms, *Solid State Communications*, 231-232 (2016) 57-63.
- [247] S. Yang, S. Li, S. Tang, W. Dong, W. Sun, D. Shen, M. Wang, Sodium adsorption and intercalation in bilayer graphene from density functional theory calculations, *Theoretical Chemistry Accounts*, 135 (2016) 164.
- [248] A.M. Ukpong, First principles study of van der Waals heterobilayers, *Computational Condensed Matter*, 2 (2015) 1-10.
- [249] R. Gatensby, N. McEvoy, K. Lee, T. Hallam, N.C. Berner, E. Rezvani, S. Winters, M. O'Brien, G.S. Duesberg, Controlled synthesis of transition metal dichalcogenide thin films for electronic applications, *Applied Surface Science*, 297 (2014) 139-146.
- [250] A.B. Kaul, Two-dimensional layered materials: Structure, properties, and prospects for device applications, *Journal of Materials Research*, 29 (2014) 348-361.
- [251] H. Terrones, F. López-Urías, M. Terrones, Novel hetero-layered materials with tunable direct band gaps by sandwiching different metal disulfides and diselenides, *Scientific Reports*, 3 (2013) 1549.
- [252] A.S. Rad, First principles study of Al-doped graphene as nanostructure adsorbent for NO<sub>2</sub> and N<sub>2</sub>O: DFT calculations, *Applied Surface Science*, 357 (2015) 1217-1224.
- [253] A.S. Rad, E. Abedini, Chemisorption of NO on Pt-decorated graphene as modified nanostructure media: A first principles study, *Applied Surface Science*, 360 (2016) 1041-1046.
- [254] A.S. Rad, O.R. Kashani, Adsorption of acetyl halide molecules on the surface of pristine and Al-doped graphene: Ab initio study, *Applied Surface Science*, 355 (2015) 233-241.
- [255] A. Shokuhi Rad, D. Zareyee, M. Peyravi, M. Jahanshahi, Surface study of gallium- and aluminum- doped graphenes upon adsorption of cytosine: DFT calculations, *Applied Surface Science*, 390 (2016) 444-451.
- [256] A.S. Rad, S.S. Shabestari, S.A. Jafari, M.R. Zardoost, A. Mirabi, N-doped graphene as a nanostructure adsorbent for carbon monoxide: DFT calculations, *Molecular Physics*, 114 (2016) 1756-1762.

- [257] S. Muhammad Hafiz, R. Ritikos, T.J. Whitcher, N. Md. Razib, D.C.S. Bien, N. Chanlek, H. Nakajima, T. Saisopa, P. Songsiriritthigul, N.M. Huang, S.A. Rahman, A practical carbon dioxide gas sensor using room-temperature hydrogen plasma reduced graphene oxide, *Sensors and Actuators B: Chemical*, 193 (2014) 692-700.
- [258] S. Zhao, J. Xue, W. Kang, Gas adsorption on MoS<sub>2</sub> monolayer from first-principles calculations, *Chemical Physics Letters*, 595-596 (2014) 35-42.
- [259] A. Shokri, N. Salami, Gas sensor based on MoS<sub>2</sub> monolayer, *Sensors and Actuators B: Chemical*, 236 (2016) 378-385.
- [260] E.W. Keong Koh, C.H. Chiu, Y.K. Lim, Y.-W. Zhang, H. Pan, Hydrogen adsorption on and diffusion through MoS<sub>2</sub> monolayer: First-principles study, *International Journal of Hydrogen Energy*, 37 (2012) 14323-14328.
- [261] Y. Wang, S. Li, J. Yi, Electronic and magnetic properties of Co doped MoS<sub>2</sub> monolayer, *Scientific Reports*, 6 (2016) 24153.
- [262] N.A. Besley, J.A. Bryan, Partial Hessian Vibrational Analysis of Organic Molecules Adsorbed on Si(100), *The Journal of Physical Chemistry C*, 112 (2008) 4308-4314.
- [263] P. Joensen, E.D. Crozier, N. Alberding, R.F. Frindt, A study of single-layer and restacked MoS<sub>2</sub> by X-ray diffraction and X-ray absorption spectroscopy, *Journal of Physics C: Solid State Physics*, 20 (1987) 4043.
- [264] D. Le, T.B. Rawal, T.S. Rahman, Single-Layer MoS<sub>2</sub> with Sulfur Vacancies: Structure and Catalytic Application, *The Journal of Physical Chemistry C*, 118 (2014) 5346-5351.
- [265] F.M. Enejkwu, C.I. Ezeh, M.W. George, M. Xu, H. Do, Y. Zhang, H. Zhao, T. Wu, A comparative study of mechanisms of the adsorption of CO<sub>2</sub> confined within graphene–MoS<sub>2</sub> nanosheets: a DFT trend study, *Nanoscale Advances*, DOI 10.1039/C8NA00314A(2019).
- [266] A.L. Allred, Electronegativity values from thermochemical data, *Journal of Inorganic and Nuclear Chemistry*, 17 (1961) 215-221.
- [267] A. Azcatl, X. Qin, A. Prakash, C. Zhang, L. Cheng, Q. Wang, N. Lu, M.J. Kim, J. Kim, K. Cho, R. Addou, C.L. Hinkle, J. Appenzeller, R.M. Wallace, Covalent Nitrogen Doping and Compressive Strain in MoS<sub>2</sub> by Remote N<sub>2</sub> Plasma Exposure, *Nano Letters*, 16 (2016) 5437-5443.
- [268] D. Saha, Z. Bao, F. Jia, S. Deng, Adsorption of CO<sub>2</sub>, CH<sub>4</sub>, N<sub>2</sub>O, and N<sub>2</sub> on MOF-5, MOF-177, and Zeolite 5A, *Environmental Science & Technology*, 44 (2010) 1820-1826.
- [269] Y. Zheng, S. Zheng, H. Xue, H. Pang, Metal-Organic Frameworks/Graphene-Based Materials: Preparations and Applications, *Advanced Functional Materials*, 28 (2018) 1804950.
- [270] A.A. Kistanov, S.K. Khadiullin, S.V. Dmitriev, E.A. Korznikova, Effect of oxygen doping on the stability and band structure of borophene nanoribbons, *Chemical Physics Letters*, 728 (2019) 53-56.
- [271] D. Ma, Q. Wang, T. Li, C. He, B. Ma, Y. Tang, Z. Lu, Z. Yang, Repairing sulfur vacancies in the MoS<sub>2</sub> monolayer by using CO, NO and NO<sub>2</sub> molecules, *Journal of Materials Chemistry C*, 4 (2016) 7093-7101.
- [272] W.B. Person, G. Zerbi, *Vibrational intensities in infrared and Raman spectroscopy*, Amsterdam : Elsevier scientific 1982.
- [273] D.S. Sholl, J.A. Steckel, *Accuracy and Methods beyond “Standard” Calculations, Density Functional Theory: A Practical Introduction*, John Wiley & Sons, Inc., Hoboken, NJ, 2009, pp. 209-233.
- [274] K.P. Kuhl, E.R. Cave, D.N. Abram, T.F. Jaramillo, New insights into the electrochemical reduction of carbon dioxide on metallic copper surfaces, *Energy & Environmental Science*, 5 (2012) 7050-7059.



- [275] K.P. Kuhl, T. Hatsukade, E.R. Cave, D.N. Abram, J. Kibsgaard, T.F. Jaramillo, Electrocatalytic Conversion of Carbon Dioxide to Methane and Methanol on Transition Metal Surfaces, *Journal of the American Chemical Society*, 136 (2014) 14107-14113.
- [276] N. Kornienko, Y. Zhao, C.S. Kley, C. Zhu, D. Kim, S. Lin, C.J. Chang, O.M. Yaghi, P. Yang, Metal–Organic Frameworks for Electrocatalytic Reduction of Carbon Dioxide, *Journal of the American Chemical Society*, 137 (2015) 14129-14135.
- [277] J. Qiao, Y. Liu, F. Hong, J. Zhang, A review of catalysts for the electroreduction of carbon dioxide to produce low-carbon fuels, *Chemical Society Reviews*, 43 (2014) 631-675.
- [278] J. Schneider, H. Jia, J.T. Muckerman, E. Fujita, Thermodynamics and kinetics of CO<sub>2</sub>, CO, and H<sup>+</sup> binding to the metal centre of CO<sub>2</sub> reduction catalysts, *Chemical Society Reviews*, 41 (2012) 2036-2051.
- [279] J. Rossmeisl, Z.W. Qu, H. Zhu, G.J. Kroes, J.K. Nørskov, Electrolysis of water on oxide surfaces, *Journal of Electroanalytical Chemistry*, 607 (2007) 83-89.
- [280] N. Mahmood, Y. Yao, J.-W. Zhang, L. Pan, X. Zhang, J.-J. Zou, Electrocatalysts for Hydrogen Evolution in Alkaline Electrolytes: Mechanisms, Challenges, and Prospective Solutions, *Advanced Science*, 5 (2018) 1700464.
- [281] L. Zhang, L. Han, H. Liu, X. Liu, J. Luo, Back Cover: Potential-Cycling Synthesis of Single Platinum Atoms for Efficient Hydrogen Evolution in Neutral Media (*Angew. Chem. Int. Ed.* 44/2017), *Angewandte Chemie International Edition*, 56 (2017) 13900-13900.
- [282] L.C. Grabow, M. Mavrikakis, Mechanism of Methanol Synthesis on Cu through CO<sub>2</sub> and CO Hydrogenation, *ACS Catalysis*, 1 (2011) 365-384.
- [283] F. Arena, K. Barbera, G. Italiano, G. Bonura, L. Spadaro, F. Frusteri, Synthesis, characterization and activity pattern of Cu–ZnO/ZrO<sub>2</sub> catalysts in the hydrogenation of carbon dioxide to methanol, *Journal of Catalysis*, 249 (2007) 185-194.
- [284] E.L. Kunkes, F. Studt, F. Abild-Pedersen, R. Schlögl, M. Behrens, Hydrogenation of CO<sub>2</sub> to methanol and CO on Cu/ZnO/Al<sub>2</sub>O<sub>3</sub>: Is there a common intermediate or not?, *Journal of Catalysis*, 328 (2015) 43-48.
- [285] F. Studt, M. Behrens, E.L. Kunkes, N. Thomas, S. Zander, A. Tarasov, J. Schumann, E. Frei, J.B. Varley, F. Abild-Pedersen, J.K. Nørskov, R. Schlögl, The Mechanism of CO and CO<sub>2</sub> Hydrogenation to Methanol over Cu-Based Catalysts, *ChemCatChem*, 7 (2015) 1105-1111.
- [286] Y. Fang, J.C. Flake, Electrochemical Reduction of CO<sub>2</sub> at Functionalized Au Electrodes, *Journal of the American Chemical Society*, 139 (2017) 3399-3405.
- [287] E.E. Benson, C.P. Kubiak, A.J. Sathrum, J.M. Smieja, Electrocatalytic and homogeneous approaches to conversion of CO<sub>2</sub> to liquid fuels, *Chemical Society Reviews*, 38 (2009) 89-99.
- [288] D.C. Young, *Computational Chemistry: A Practical Guide for Applying Techniques to Real-World Problems*, John Wiley & Sons, Inc., New York, 2001.
- [289] A.A. Peterson, F. Abild-Pedersen, F. Studt, J. Rossmeisl, J.K. Nørskov, How copper catalyzes the electroreduction of carbon dioxide into hydrocarbon fuels, *Energy & Environmental Science*, 3 (2010) 1311-1315.
- [290] K.K. Ghuman, S. Yadav, C.V. Singh, Adsorption and Dissociation of H<sub>2</sub>O on Monolayered MoS<sub>2</sub> Edges: Energetics and Mechanism from ab Initio Simulations, *The Journal of Physical Chemistry C*, 119 (2015) 6518-6529.
- [291] R. Li, L. Yang, T. Xiong, Y. Wu, L. Cao, D. Yuan, W. Zhou, Nitrogen doped MoS<sub>2</sub> nanosheets synthesized via a low-temperature process as electrocatalysts with enhanced activity for hydrogen evolution reaction, *Journal of Power Sources*, 356 (2017) 133-139.

- [292] K. Reuter, M. Scheffler, Composition, structure, and stability of RuO<sub>2</sub>(110) as a function of oxygen pressure, *Physical Review B*, 65 (2001) 035406.
- [293] N.C. Webbook, NIST-JANAF Thermochemical Tables, NIST.
- [294] M. Fronzi, S. Piccinin, B. Delley, E. Traversa, C. Stampfl, Water adsorption on the stoichiometric and reduced CeO<sub>2</sub>(111) surface: a first-principles investigation, *Physical Chemistry Chemical Physics*, 11 (2009) 9188-9199.
- [295] D.A. Clabo, W.D. Allen, R.B. Remington, Y. Yamaguchi, H.F. Schaefer, A systematic study of molecular vibrational anharmonicity and vibration—rotation interaction by self-consistent-field higher-derivative methods. Asymmetric top molecules, *Chemical Physics*, 123 (1988) 187-239.
- [296] R.V. Kochanov, I.E. Gordon, L.S. Rothman, P. Wcisło, C. Hill, J.S. Wilzewski, HITRAN Application Programming Interface (HAPI): A comprehensive approach to working with spectroscopic data, *Journal of Quantitative Spectroscopy and Radiative Transfer*, 177 (2016) 15-30.
- [297] M. Hartnett, S. Fahy, Vibrational mode frequencies of H<sub>2</sub>S and H<sub>2</sub>O adsorbed on Ge(001)-(2×1) surfaces, *Applied Surface Science*, 329 (2015) 363-370.
- [298] Y. Jiao, A. Du, Z. Zhu, V. Rudolph, G.Q. Lu, S.C. Smith, A density functional theory study on CO<sub>2</sub> capture and activation by graphene-like boron nitride with boron vacancy, *Catalysis Today*, 175 (2011) 271-275.
- [299] N.Y. Dzade, A. Roldan, N.H.d. Leeuw, Activation and dissociation of CO<sub>2</sub> on the (001), (011), and (111) surfaces of mackinawite (FeS): A dispersion-corrected DFT study, *The Journal of Chemical Physics*, 143 (2015) 094703.
- [300] M.A. Henderson, The interaction of water with solid surfaces: fundamental aspects revisited, *Surface Science Reports*, 46 (2002) 1-308.
- [301] M.K.S. Kostov, E. E.; George, A. M.; Gubbins, K. E.; Nardelli, M. B., Dissociation of Water on Defective Carbon Substrates., *Phys. Rev. Lett.*, DOI (2005) 136105.
- [302] A.A. Phatak, W.N. Delgass, F.H. Ribeiro, W.F. Schneider, Density Functional Theory Comparison of Water Dissociation Steps on Cu, Au, Ni, Pd, and Pt, *The Journal of Physical Chemistry C*, 113 (2009) 7269-7276.
- [303] J.L.C. Fajín, M.N. D. S. Cordeiro, J.R.B. Gomes, Density Functional Theory Study of the Water Dissociation on Platinum Surfaces: General Trends, *The Journal of Physical Chemistry A*, 118 (2014) 5832-5840.
- [304] J.K.B. Norskov, T.; Logadottir, A.; Kitchin, J. R.; Chen, J. G.; Pandalov, S.; Stimming, U., Trends in the Exchange Current for Hydrogen Evolution. , *J. Electrochem. Soc.* , 152 (2005) J23–J26.
- [305] R. Balasubramanian, S. Chowdhury, Recent advances and progress in the development of graphene-based adsorbents for CO<sub>2</sub> capture, *J. Mater. Chem. A*, 3 (2015) 21968-21989.
- [306] T. Ghanbari, F. Abnisa, W.M.A. Wan Daud, A review on production of metal organic frameworks (MOF) for CO<sub>2</sub> adsorption, *Science of The Total Environment*, 707 (2020) 135090.
- [307] J. Möllmer, M. Lange, A. Möller, C. Patzschke, K. Stein, D. Lässig, J. Lincke, R. Gläser, H. Krautscheid, R. Staudt, Pure and mixed gas adsorption of CH<sub>4</sub> and N<sub>2</sub> on the metal–organic framework Basolite® A100 and a novel copper-based 1,2,4-triazolyl isophthalate MOF, *Journal of Materials Chemistry*, 22 (2012) 10274-10286.
- [308] S. Vandenbrande, T. Verstraelen, J.J. Gutiérrez-Sevillano, M. Waroquier, V. Van Speybroeck, Methane Adsorption in Zr-Based MOFs: Comparison and Critical Evaluation of Force Fields, *The Journal of Physical Chemistry C*, 121 (2017) 25309-25322.

- [309] A. Ahmed, S. Seth, J. Purewal, A.G. Wong-Foy, M. Veenstra, A.J. Matzger, D.J. Siegel, Exceptional hydrogen storage achieved by screening nearly half a million metal-organic frameworks, *Nature Communications*, 10 (2019) 1568.
- [310] J. Vermesse, D. Vidal, P. Malbrunot, Gas Adsorption on Zeolites at High Pressure, *Langmuir*, 12 (1996) 4190-4196.
- [311] R. Krishna, J.M. van Baten, Investigating Cluster Formation in Adsorption of CO<sub>2</sub>, CH<sub>4</sub>, and Ar in Zeolites and Metal Organic Frameworks at Subcritical Temperatures, *Langmuir*, 26 (2010) 3981-3992.
- [312] F. Schedin, A.K. Geim, S.V. Morozov, E.W. Hill, P. Blake, M.I. Katsnelson, K.S. Novoselov, Detection of individual gas molecules adsorbed on graphene, *Nature Materials*, 6 (2007) 652-655.
- [313] B. Huang, Z. Li, Z. Liu, G. Zhou, S. Hao, J. Wu, B.-L. Gu, W. Duan, Adsorption of Gas Molecules on Graphene Nanoribbons and Its Implication for Nanoscale Molecule Sensor, *The Journal of Physical Chemistry C*, 112 (2008) 13442-13446.
- [314] R. Arsat, M. Breedon, M. Shafiei, P.G. Spizziri, S. Gilje, R.B. Kaner, K. Kalantar-zadeh, W. Wlodarski, Graphene-like nano-sheets for surface acoustic wave gas sensor applications, *Chemical Physics Letters*, 467 (2009) 344-347.
- [315] Z.W. Seh, J. Kibsgaard, C.F. Dickens, I. Chorkendorff, J.K. Nørskov, T.F. Jaramillo, Combining theory and experiment in electrocatalysis: Insights into materials design, *Science*, 355 (2017) eaad4998.
- [316] M.G. Walter, E.L. Warren, J.R. McKone, S.W. Boettcher, Q. Mi, E.A. Santori, N.S. Lewis, Solar Water Splitting Cells, *Chemical Reviews*, 110 (2010) 6446-6473.
- [317] H. Zhang, J. Nai, L. Yu, X.W. Lou, Metal-Organic-Framework-Based Materials as Platforms for Renewable Energy and Environmental Applications, *Joule*, 1 (2017) 77-107.
- [318] D. Dubbeldam, S. Calero, D.E. Ellis, R.Q. Snurr, RASPA: molecular simulation software for adsorption and diffusion in flexible nanoporous materials, *Molecular Simulation*, 42 (2016) 81-101.
- [319] D. Frenkel, B. Smit, J. Tobochnik, S.R. McKay, W. Christian, Understanding Molecular Simulation, *Computers in Physics*, 11 (1997) 351-354.
- [320] J. Wilcox, Carbon Capture, Springer Publishing, New York, 2012.
- [321] A.K. Rappe, C.J. Casewit, K.S. Colwell, W.A. Goddard, W.M. Skiff, UFF, a full periodic table force field for molecular mechanics and molecular dynamics simulations, *Journal of the American Chemical Society*, 114 (1992) 10024-10035.
- [322] J.J. Potoff, J.I. Siepmann, Vapor-liquid equilibria of mixtures containing alkanes, carbon dioxide, and nitrogen, *AIChE Journal*, 47 (2001) 1676-1682.
- [323] M.P.T. Allen, D. J. , Computer simulation of liquids, Clarendon Press 1989.
- [324] M.G. Martin, J.I. Siepmann, Transferable Potentials for Phase Equilibria. 1. United-Atom Description of n-Alkanes, *The Journal of Physical Chemistry B*, 102 (1998) 2569-2577.
- [325] J.D. Bernal, R.H. Fowler, A Theory of Water and Ionic Solution, with Particular Reference to Hydrogen and Hydroxyl Ions, *Journal of Chemical Physics*, 1 (1933) 515.
- [326] F. Ferreira, A. Carvalho, Í.J.M. Moura, J. Coutinho, R.M. Ribeiro, Adsorption of H<sub>2</sub>, O<sub>2</sub>, H<sub>2</sub>O, OH and H on monolayer MoS<sub>2</sub>, *Journal of Physics: Condensed Matter*, 30 (2017) 035003.
- [327] P. Bampoulis, V.J. Teernstra, D. Lohse, H.J.W. Zandvliet, B. Poelsema, Hydrophobic Ice Confined between Graphene and MoS<sub>2</sub>, *The Journal of Physical Chemistry C*, 120 (2016) 27079-27084.